Metallo-supramolecular Architectures based on Multifunctional N-Donor Ligands

DISSERTATION

zur Erlangung des akademischen Grades

Doctor rerum naturalium

(Dr. rer. nat.)

vorgelegt

der Fakultät Mathematik und Naturwissenschaften

der Technischen Universität Dresden

von

MSc. Harold Brice Tanh Jeazet

geboren am 22.11.1979 in Bafoussam / Kamerun

Eingereicht am: 23. 06. 2010

Die Dissertation wurde in der Zeit von Dezember 2006 bis Mai 2010 an der Professur Koordinationschemie der Fachrichtung Chemie und Lebensmittelchemie der TU Dresden sowie im Institut für Radiochemie des Forschungszentrums Dresden-Rossendorf angefertigt.

To my daugther

“Scio me nihil scire“

(I know that I know nothing)

Sokrates

(469 BC - 399 BC)

Acknowledgements

First I wish to thank my both supervisors Prof. Dr. Karsten Gloe, chair of Coordination Chemistry at TU Dresden, and Prof. Dr. Gert Bernhard, director of the Institute of Radiochemistry at Forschungszentrum Dresden-Rossendorf (FZD), for giving me the opportunity to carry out this research at their respective groups as well as for their constant supervision and guidance throughout my stay. They always had time for discussions during this work and supported me with their immense theoretical and practical knowledges. Their extensive knowledges in many fields and their patience in helping me have not only driven me to complete my research projects, but also fueled my passion for pursuing future scientific endeavors in a variety of subjects.

I acknowledge the strong support given by Dr. Kerstin Gloe. Her constant guidance, valuable advice and encouragement help me a lot.

I am very grateful to several colleagues who provided technical support to this work. Dr. Gerhard Geipel supported me beside his tutor role with TRLFS measurements. His advices, comments and suggestions were crucial. I wish to thank Dr. Olga Kataeva and Mrs. Anne Jäger for their collaboration with crystal structure measurements and characterization. In particular, special thanks go to Dr. Thomas Doert for his very fruitful collaboration on X-ray structures. I also wish to thank Prof. Dr. Satoru Tsushima for DFT calculations, Dr. Harald Foerstendorf and Mrs. Inge Schubert for IR measurements. I thank Dr. Karim Fahmy, Dr. Olesya Savchuk and Stefanie Eichler for their cooperation in DNA-binding studies and valuable comments, Dr. Bernd Schwenzer and Anja Drose for experiments and discussions on cancer cells activity.

I thank Dr. Margret Acker, Mrs. Martina Kobus, Dr. Steffen Taut and Wolfgang Krause for the good working atmosphere as well as for their scientific support and organisational tasks in the radiochemical laboratory at the TU Dresden.

Furthermore, I would like to extent my thanks to the members of our group. Several of them acted as friends, advisors or assistants. Though numerous to mention all, I would like to single out Dr. Marco Wenzel whose presence was invaluable. Beside his great assistance at the beginning of my work he was involved in proof-reading of the first draft

of my thesis and he has very constructive comments. I express also my sincere gratitude to Axel Heine, Katja Schreppel, Jens Mizera and Linda Götzke for their fruitful cooperation. I enjoyed the good working climate and the fun during our seminars, coffeebreaks and Christmas lectures.

I sincerely thank Ejaz Ahmed for his friendship, his timely help, a fruitful discussion on X-ray crystallography and for reading of the first draft of this thesis.

I am grateful to all my colleagues who made and make me have good time in both research groups.

I am also grateful to Mrs Claudia Kirmes who make my stay at the FZD comfortable through easy and quick administrative treatment records.

I also take this opportunity to express my gratitude to Dr. Julien Makongo for the great support and encouragement. He have facilitated my integration in Germany and assisted me during my initial stages.

My heart-felt thanks go to my girl-friend Marie-laure Kapim, whose moral support, generosity, advice, patience, encouragement and permanent contact contributed emensely to the realisation of this work.

On a final note I wish to thank my parents my brothers and sisters for their never-ending love and support. All other friends and relatives are also acknowledged.

And most of all, I thank GOD.

Table of content

1 Introduction and motivation of the studies

Supramolecular chemistry is a young discipline, which investigates (supra)molecular phenomena between the traditional fields of chemistry (organic, inorganic, and physical chemistry). As a matter of course it is strongly influenced by other sciences like biology biochemistry physics and material sciences.

Supramolecular chemistry is one of the actively pursued areas of research in chemistry. The concepts and the term of “supramolecular chemistry” were introduced in 1978 by Lehn [1] and it was defined in words, “just as there is a field of molecular chemistry based on the covalent bond, there is a field of supramolecular chemistry, the chemistry of molecular assemblies and of the intermolecular bond”. It is often defined as “the chemistry of the noncovalent bond” [2-4]. This means that not only an isolated molecule (either as a single species or as bulk material) but also the assembly of at least two molecules is studied [5-7]. Molecular recognition between the molecular building blocks is important to enable an effective aggregation by noncovalent interactions. The reversible self-assembly processes [8] leads to stable and well-defined supramolecular species. Aggregation of the components might result in new properties, which are expressed in a supramolecular function [4, 9]. By the use of this principle to construct large ensembles of molecules, supramolecular chemistry bridges the gap between the picometer dimensions of molecules and the nanoworld. Therefore, the understanding of its fundamental basics is crucial for a successful chemical “bottom–up” approach toward nanotechnology [10].

Essential biological processes, e.g., reproduction, signal transduction, biocatalysis, information storage, and processing, are all based on supramolecular interactions between molecular components. Enzymes, viruses, membranes, and many other complicated structures with biologically relevant functions are mainly built up by simple self-assembly processes [11, 12]. The processes can be mimicked in small artificial supramolecular derivatives. Recently, major chemistry research activities are devoted to the development of chemical tools for the self-assembly of structurally rich supramolecular arrays [13-17]. Several strategies, such as the mutual complementary

approach (based on hydrogen bonded assemblies), directional bonding, weak-link have been designed to fabricate self-assembled architectures using bio-inspired noncovalent interactions, such as hydrogen bonds, π-π stacking, donor-acceptor interactions, and metal coordination chemistry. As a result, supramolecular chemistry was able to produce spectacular architectures possessing various functionalities. Over the past several decades, the self-assembly process has motivated countless chemists, physicists, and engineers to construct self-assembling systems at scales from the molecular to the macroscopic. This effort has met with considerable success. In molecular sciences, self-assembly provides the basis for crystallization of organic [18, 19] and inorganic [20, 21] molecules and is at the heart of supramolecular chemistry, where the "instructions" of how to assemble larger entities are "coded" in the structural motifs of individual molecules. In nanotechnology, self-assembly underlies various types of molecular structures (*e.g.*, Langmuir-Blodgett films [22], self-assembled monolayers [23-25], amphiphilic fibers [26, 27] as well as higher-order architectures built from nanoparticles [28-31], nanotubes [32], or nanorods [33]. At the microscale, there are currently self-assembling fluidic machines [34] and micromixers [35], complex microparticles building themselves from prepolymer patches [36], and artificial opals comprising millions of colloidal particles [37, 38]. Some of the macroscopic manifestations of self-assembly include 2D and 3D structures driven by capillary forces [39, 40], self-assembling electronic circuits [41, 42], and unusual crystals of charged components [43, 44]. Some of the self-assembly strategies are already finding industrial applications. For example, Alien Technologies has developed fluidic self-assembly methods to fabricate radio-frequency identification (RFID) tags, by using shape recognition and fluid transport on the microscale [45, 46]. Nanogen employs electric-field mediated self-assembly to bring together DNA nanocomponents for electronic and diagnostic devices [47]. IBM, too, has recently harnessed the power of self-assembly to create trillions of nanometre-sized holes across the length of a 300 millimetre computer chip, thus creating new insulators that increase the speed (by 35%) and efficiency (by 15%) of electrical signal transmission [48].

In many of the above examples, self-assembly capitalizes on the fact that with the current state of chemistry/material science it is often easier to fine tune the interparticle forces that bring small components together than to manipulate or modify these components by optical tweezers [49], atomic traps [50], or other high-end techniques. Of course, this is not always the case, and "programming" the correct interactions into self-assembling molecules or particles is often based on intuition rather than predictive formulas. Consequently, identification of reverse-engineering strategies that would identify the necessary interactions required for a specific mode of self-assembly is one of the holy grails of self-assembly research.

Three general factors determine the self-assembly of metallosupramolecular architectures. First, the process according to the principle of maximum occupation of binding sites for control of the desired end product. Secondly, the internal orientation factors such as steric effects that prevent formation of undesirable Products. Additional stabilizing interactions, such as electrostatic interactions, hydrogen bonds, van der Waals or π interactions, are favoring the formation of a stable product. Third, ensure external factors such as the additional coordination of solvent molecules, counter ions or other ligands, for fine-tuning of the building process. Through directional coordinative bonding, two- and three-dimensional self-assemblies are readily available by the spontaneous combination of electron-deficient metal centers with appropriate organic electron-donor ligands, such as Lewis bases (Figure 1) [51].

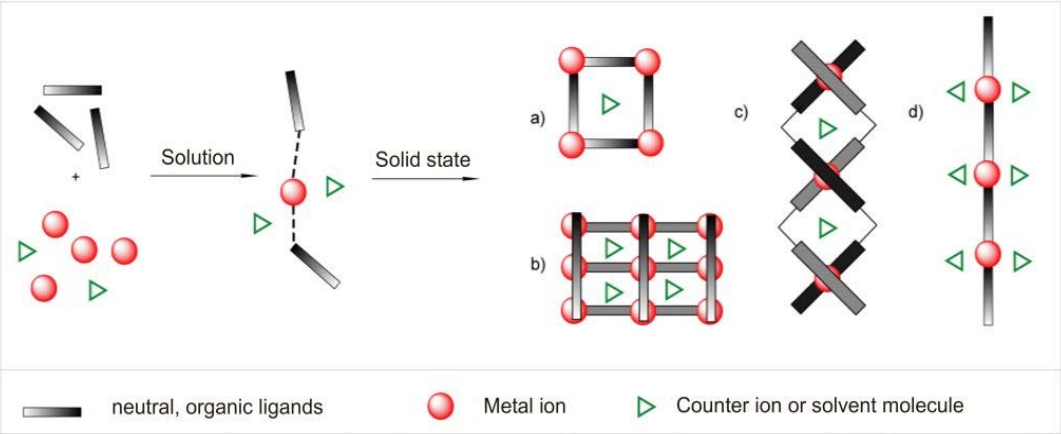

Figure 1. Formation of different architectures of supramolecular coordination compounds from neutral organic ligands and metal salts: a) rings, b) grids, c) helicates and d) linear coordination polymers.

The ligands influence the complex architecture and their properties in different ways and a prediction is difficult in many cases. The properties of the metal ions and the external conditions also play an important role besides the nature, the number and the arrangement of the donor atoms. Thus, a frequent objective of metallo-supramolecular chemistry has been the design of ligands which can be directed, with the aid of a suitable metal ion, to form pre-determined new architectures [52]. For the construction of supramolecular structures on the basis of specific metal-ligand interactions, three different synthetic strategies have been proved successfully: the “directional-bonding approach”, the “weak-bonding approach” and the “symmetry-interaction approach” [13]. So by carefully selecting the organic ligand and metal ion, one also aims to tune the physical properties and, thus, realize various applications, such as those mentioned above. Generally, nitrogen- and oxygen-donor ligands feature prominently in the construction of a range of functional supramolecules [53]. Supramolecular chemistry is equilibrium-controlled, and thus dynamically generates the most thermodynamically stable molecular assembly. Since supramolecular chemistry have a set of parameters that can be tuned according to the desired product, the chemist can play the part of an engineer in judiciously designing the construction of a molecular architecture by considering the structural features of the

building blocks of the superstructure, as well as the ideal combination of conditions that will most efficiently form the desired product.

In view of these developments, the aim of the present thesis is to rationally design multifunctional N-donor ligands and study their properties. Three distinct parts are presented.

The focus of the first part is directed on the synthesis and characterization of Schiff base ligands with pyridine groups as additional coordinative functions groups and their use for the self-assembly of supramolecular architectures. Pyridylimine compounds are classical neutral ligands for transition metal ions. So the main goal is to study the reactivity of the synthesized structurally analogous bis-pyridylimine ligands shown in Figure 2 towards *d*-block metal ions like Mn(II), Fe(II), Ni(II), Cu(II), Ag(I) and Hg(II). These ligands differ from each other in the linking element (–CH_2–, –O–, –S–, –NH–, –C_6H_{10}–) present between the two bidentate chelating subunits. Besides the characterization of the new molecules a topic of the investigations is the structural analysis of isolated crystalline compounds. Another point of view consists in the test of the reactivity of relevant complexes towards DNA or cells.

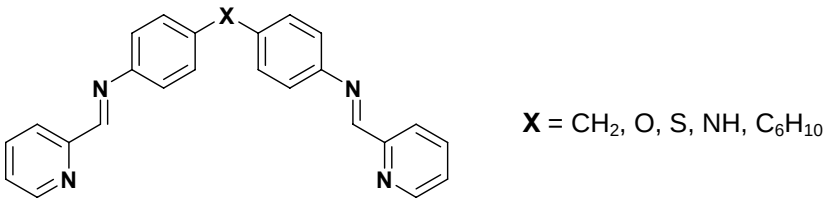

Figure 2. Structures of bis-pyridylimine ligands.

In nuclear waste treatment and extraction processes there is a need for improved ligands for U(VI) and other actinides binding with pronounced selectivity in comparison to lanthanides. The introduction of soft heteroatoms, as imine nitrogen, in the ligand system could be used as a tool for more selective and effective binding and extraction. Therefore the combination of the hydroxy group with the imine function and the use of different spacer units in one molecule should lead to interesting candidates with optimum

coordination of uranyl ions. This second part is focused on the synthesis and characterization of bis(2-hydroxyaryl) imine ligands (Figure 3) as well as their U(VI) complexes. It is also an intention of this part to discuss not only the structure of these complexes but also their extraction ability towards Eu(III) and U(VI).

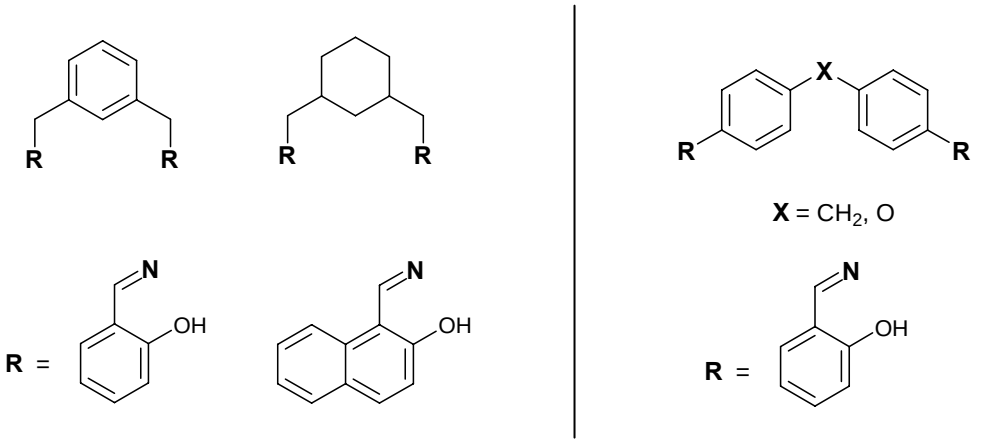

Figure 3. Structures of bis(2-hydroxyaryl) imine ligands.

In the third part of the thesis tripodal amine and imine ligands as well as platform controlled multifunctional ligands with additional OH or pyridine functions are discussed (Figure 4 and 5). The main topics are related to their synthesis, characterization, metal complexation [Nd(III), Eu(III), Yb(III) and U(VI)] and extraction as well as structural aspects of these ligands systems.

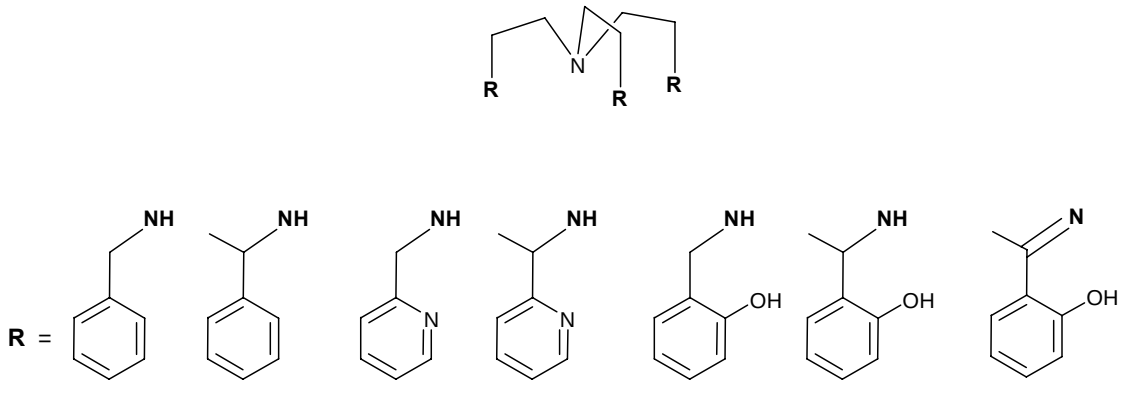

Figure 4. Structures of tripodal amine ligands.

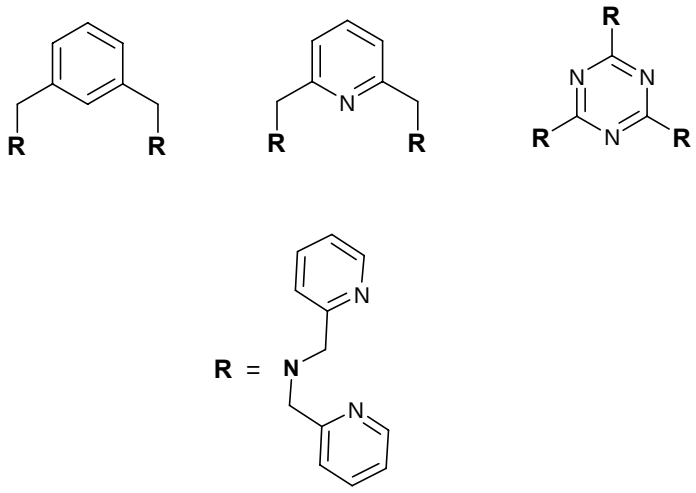

Figure 5. Multifunctional platform controlled ligand systems.

In general the motivation of the studies presented is especially directed to a better understanding of selected factors of influence on supramolecular self-assembly processes of mixed donors ligand systems and their use for selective metal ion binding and extraction.

2 The bis-pyridylimine ligand approach

The reversible condensation between amino and carbonyl groups to form imine bonds is one of the most fundamental and ubiquitous reactions in chemistry [54, 55].

The rapid development of these ligands resulted in an enhanced research activity in the field of coordination chemistry leading to very interesting conclusions. Schiff bases form stable complexes with a range of transition metal ions with very interesting properties. Many biologically important Schiff bases and their complexes have been reported in the literature possessing antibacterial [56-58], antifungal [59, 60], antimicrobial [61, 62], anticonvulsant [63], anti HIV [64], anti inflammatory [65], and antitumor [66-69] activities. So the background about the supramolecular coordination chemistry of N-pyridylimine-Donor ligands will certainly help for better understanding the chemistry behind their complex formation.

The starting point of supramolecular coordination chemistry of transition metal ions is the typical coordinative interaction with appropriate ligands. Also additional weak non-covalent interactions such as electrostatic, van der Walls, π interactions and hydrogen bonding play an important role in the structure building process [21, 70-73]. In the following significant interactions and their role in the construction of supramolecular coordination compounds using the ligands types of this thesis will be discussed in detail. Pyridylimine ligands are interesting building blocks in supramolecular chemistry. Pyridine and imine nitrogen atoms act as a soft σ-bases (donor) and form many different structures with metal ions. Such complexes are often stabilized by an additional back-donation from d–Orbitals of the metal center to empty π*–Orbitals of pyridine.

The popularity of supramolecular interaction of metal ions with azaligands is not only due to structure diversity but also to their interesting physical-chemical properties, for example, in view of possible applications in medicine [74, 75] or materials with special electronic and magnetic properties [76, 77].

The self-assembly of $AgClO_4$ with two highly conjugated Schiff bases **I** and **II** leads to the formation of one zigzag polymeric network $\{[Ag_2(\mathbf{I})_2](ClO_4)_2(CH_3CN)\}_n$ and one discrete rectangular compound $[Ag_2(\mathbf{II})_2](ClO_4)_2$ (Figure 6) [78]. The spacers in the conjugated Schiff-base ligands and the π–π interactions are important determinants of the architectures of the final products. Interestingly, the 1D zigzag Ag(I)-containing coordination polymer form with **I** is not stable in solution. The degradation and reorganization of the compound occurs to form a [2 × 2] grid architecture (Figure 7). These Ag(I) Schiff base compounds exhibit unusual luminescence at room temperature that is significantly red-shifted compared to other reported Ag(I) polymers, indicating that such electronic excited-state properties can be moified by the combination of electron-rich Ag metal centers and highly conjugated Schiff bases.

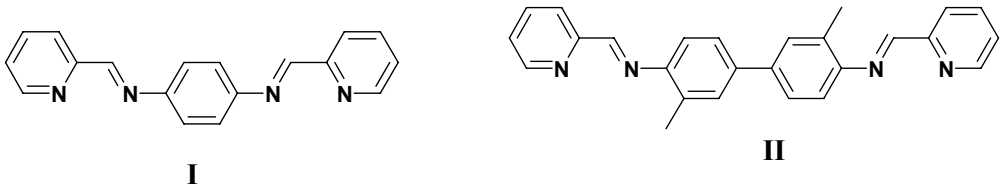

I

II

a)

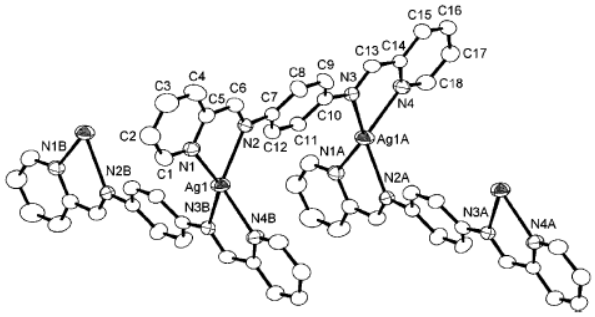

b)

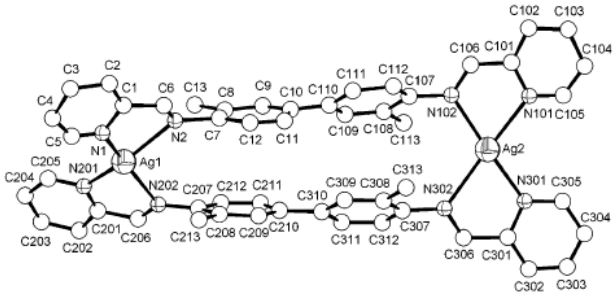

Figure 6. Local coordination environment of Ag(I) complexes formed with **I** and **II:** a) $[Ag_2(\mathbf{I})_2]_n$, b) $[Ag_2(\mathbf{II})_2]^{2+}$.

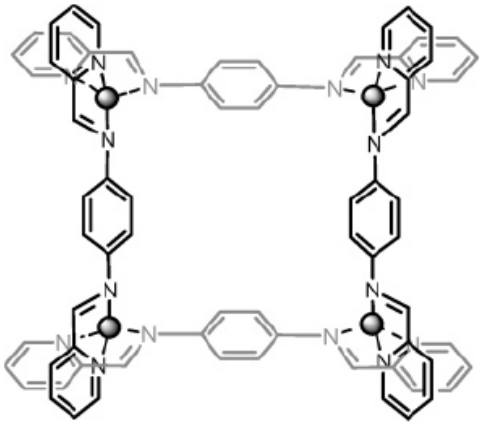

Figure 7. [2 × 2] grid-type structure of $\{[Ag_2(\mathbf{I})_2](ClO_4)_2(CH_3CN)\}_n$ in solution.

The Silver complex formation with $\mathbf{L^2}$ was studied by Stoeckli-Evans *et al.* and Cheng et al. This ligand forms an ionic complex $[Ag\mathbf{L^2}]^+$ with $Ag(CF_3SO_3)$ consisting of a one-dimensional zigzag coordination polymer $\{[Ag(\mathbf{L^2})]CF_3SO_3{\cdot}0.4H_2\}_n$ [79]. On changing the $CF_3SO_3^-$ anion to BF_4^- the molecular box $[Ag_2(\mathbf{L^2})_2]^{2+}$ is formed in methanolic solution [80].

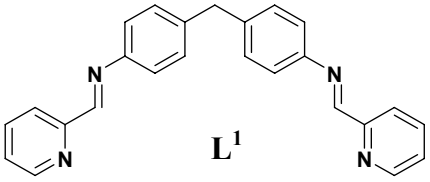

$\mathbf{L^1}$

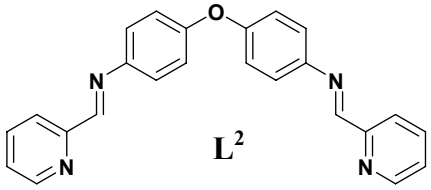

$\mathbf{L^2}$

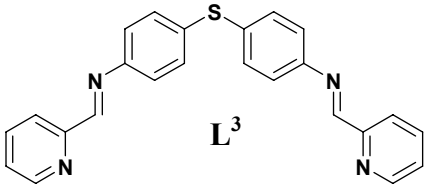

$\mathbf{L^3}$

There is a large variety of coordination compounds whose molecular structure may be loosely described as helical. Pseudotetrahedral complexes possessing two unsymmetrical bidentate AB-type ligands coordinated to a central metal ion $[M(AB)_2]$ (Figure 8a) or pseudooctahedral complexes $[M(AB)_3]$ or $[M(AA)_3]$ (Figure 8b) correspond to helical complexes since the absolute configuration of the metal ion produces right-handed (Δ = P) or left-handed (Λ = M) helicity along their principal C_2 or C_3 axes [81].

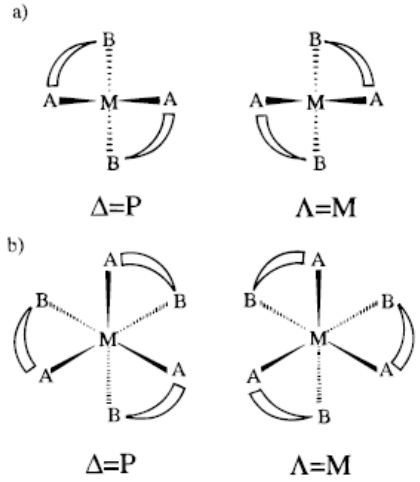

Figure 8. Absolute configurations of (a) bis-chelate complexes viewed down the C_2 axis and (b) tris-chelate complexes viewed down the C_3 axis. Δ corresponds to a right-handed helix (symbol P according to Cahn-Ingold- Prelog notation), [82] and Λ to a left-handed helix (M) along the principal axis.

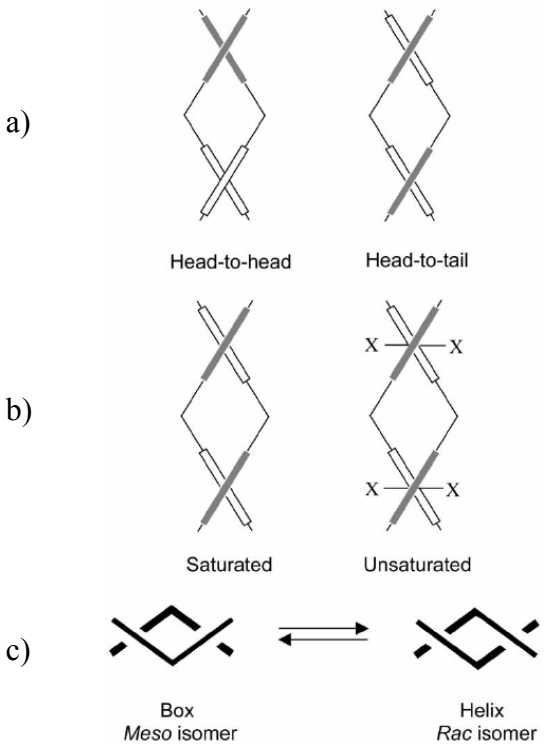

Figure 9. Representation of a) Head-to-head (HH) and Head-to-tail (HT) helicates b) saturated and unsaturated helicates and c) cyclophane (box) and helicate conformations. X is additional ligand [83].

Reaction of $\mathbf{L^1}$ with copper(I) and silver(I) gives dinuclear double-stranded helicates [84] or a molecular box [85]. The two metal binding sites are sterically prevented from coordinating to the same metal centre because of the phenylenes in the spacer unit while the central methylene unit introduces sufficient flexibility into the ligand to allow helicate formation. The dimeric complexes formed between ligand $\mathbf{L^1}$ and tetrahedral metal ions exist in two possible conformations, the cyclophane (box) and helicate (Figure 9c).

The complex $[Ag_2(\mathbf{III})_2]^{2+}$ also adopts two conformations in solution. In the solid state a helix is observed with the face-edge π-stacking interactions between the strands creating a major and minor groove in the double-helical array [86]. Using the imine technology, it was demonstrated that it is possible to impose directionality in a helical array [87] by introducing an asymmetric spacer into the ligand (**IV**). Two conformations shown in Figure 9 are possible for complexes of ligand **IV** (HH and HT); however, only a double-helicate of HT configuration is obtained when tetrahedral metals are used.

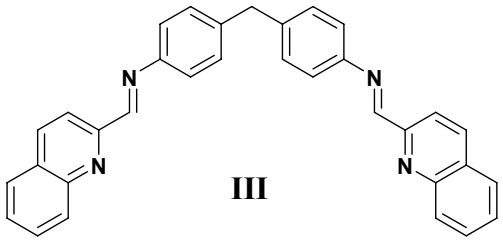

III

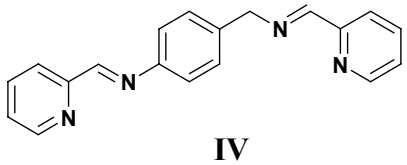

IV

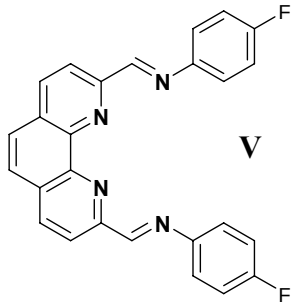

V

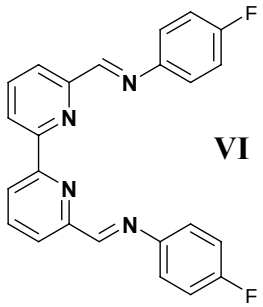

VI

Ligands **V** and **VI** were synthesized by Ziessel et al. [88] Both ligands lead to helical complexes $[Cu_2(\mathbf{V})_2]^{2+}$ and $[Cu_2(\mathbf{VI})_2]^{2+}$ when reacted with Cu(I) ions. In both helicates each Cu(I) ion is coordinated to four nitrogen atoms of two pyridylimine units from two ligand strands.

Oligopyridine ligands with imine bridging units (**VII** and **VIII**) have been synthesized by Lehn et al. The rigid double bond does not prevent helicate formation when the ligands are treated with metal ions of tetrahedral coordination geometry and coordination occurs through the pyridine nitrogen atoms only [89]. Competition experiments with a mixture of the two ligands demonstrated that self-recognition occurs; each ligand self-assembles into a helicate with an identical ligand, resulting in homostranded helicates.

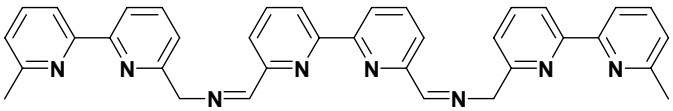

VII

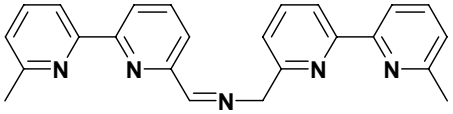

VIII

Ligand $\mathbf{L^1}$ has already been shown to form double helicates with Cu(I) and Ag(I). This ligand and his analogues $\mathbf{L^2}$ and $\mathbf{L^3}$ also self-assemble into dinuclear triple helical architectures with Fe(II), Co(II), Ni(II) Cu(II) and Ru(II) (Figure 10) [80, 84, 85, 90, 91]. Spectroscopic studies reveal that the tetracationic complexes bind to the major groove of DNA (Figure 11) [92-93] causing the DNA to wrap up in an intramolecular fashion (*vide infra*) [92, 94]. The two enantiomers of these triple helicates can be separated by paper chromatography and the DNA binding of each enantiomer is distinct [93-96]. The binding process shows chiral discrimination, with the M enantiomer bound strongly than the P enantiomer. The ability of $[Fe_2(\mathbf{L^1})_3]^{4+}$ to "wrap up" DNA in an intramolecular fashion is unprecedented for traditional small molecule DNA condensation agents and reminiscent of protein recognition of DNA. The helicates represent chiral supramolecular cylinders of similar size to natural protein cylindrical DNA recognition units such as zinc fingers, and this may provide a rich seam for application of helicate technology. As a consequence Fe(II) and Ru(II) triple-helical complexes of $\mathbf{L^1}$ were proved to exhibit activities against cancer cell lines [90, 97] and this may represent a significant step

toward therapeutic advancement compared to traditional agents such as cisplatin which induce cell death through covalent modification to DNA and genotoxicity.

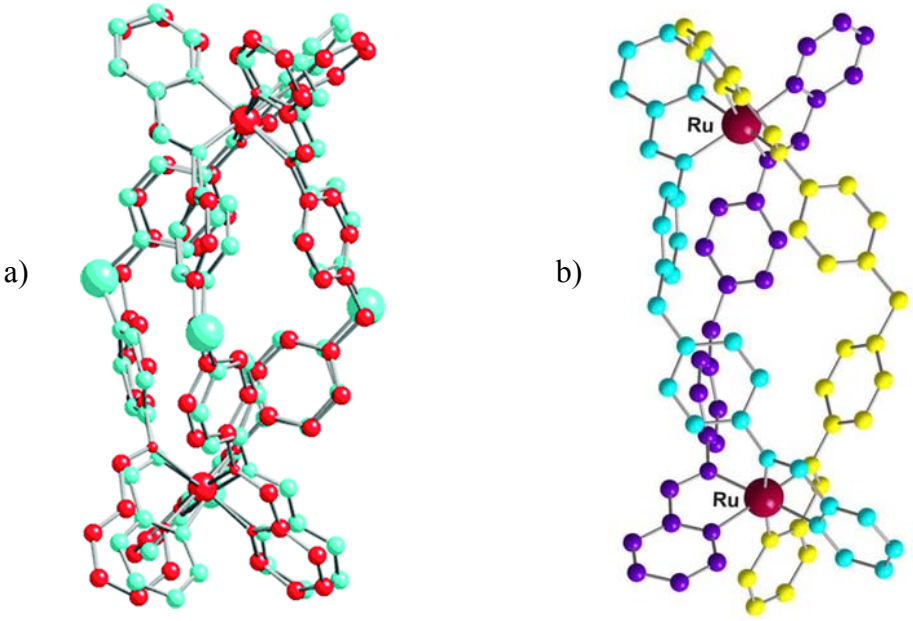

Figure 10. a) Comparison of the triple-stranded cylindrical cations $[Fe_2(\mathbf{L^3})_3]^{4+}$ (green) and $[Fe_2(\mathbf{L^1})_3]^{4+}$ (red). b) Structure of $[Ru_2(\mathbf{L^1})_3]^{4+}$ cation.

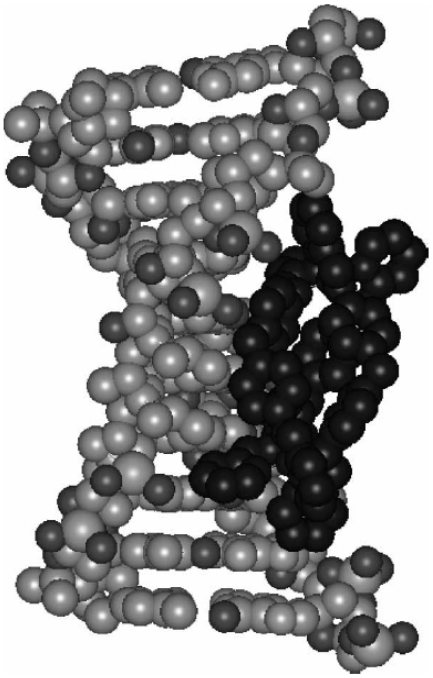

Figure 11. Representation of $[Fe_2(\mathbf{L^1})_3]^{4+}$ binding to major groove of DNA.

Silver(I) coordination chemistry of ligand **IX** which contains a 1,5-naphthalene spacer, has been investigated. Isotactic, helical and syndiotactic, achiral coordination polymers are formed with a range of different anions with the isotactic polymers displaying long-range ordering of the metal centres [98].

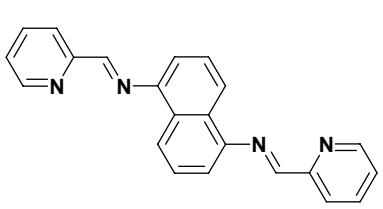

IX

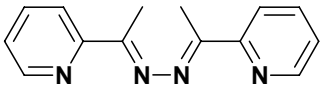

X

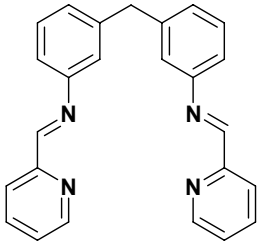

XI

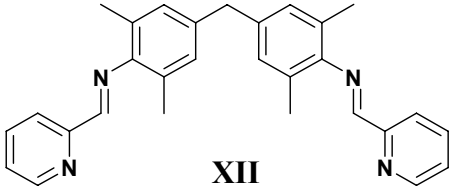

XII

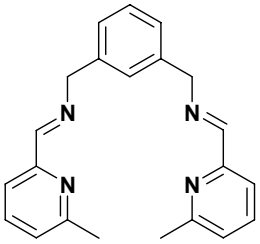

XIII

Copper(I) chemistry with the pyridine–azine ligand **X** has been investigated and an X-ray structure obtained. The structure reveals a trinuclear circular helicate (Figure 12) whilst solution data support the existence of an equilibrium mixture of species with a dimer and trimer being dominant [99].

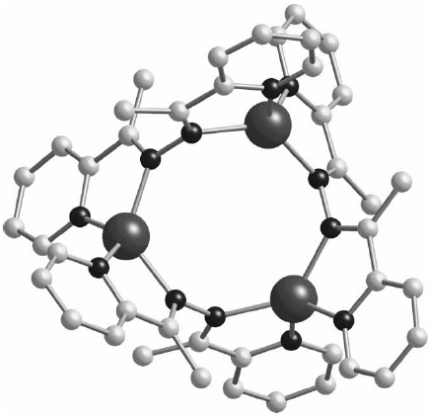

Figure 12. X-ray crystal structure of trinuclear circular helicate $[Cu_3(\mathbf{X})_3]^{3+}$.

Pyridyl-imine ligand **XI** forms a "bowed" (arcshaped) helicate when reacted with Cu(I) ions [100]. The crystal structure reveals that in the solid state the arc-shaped helicates aggregate to form a cyclic array of four metallo-supramolecular units held together by π–π interactions (Figure 13). The diameter of the circular aggregate is approximately 2.5 nm and four BF_4^- counteranions are located in the internal cavity. The chirality of each helicate alternates around the circle so that the overall structure is achiral. The nanoscale structure, nevertheless, bears a striking resemblance to the circular helical arrays but it is achieved without the need for extensive covalent ligand synthesis.

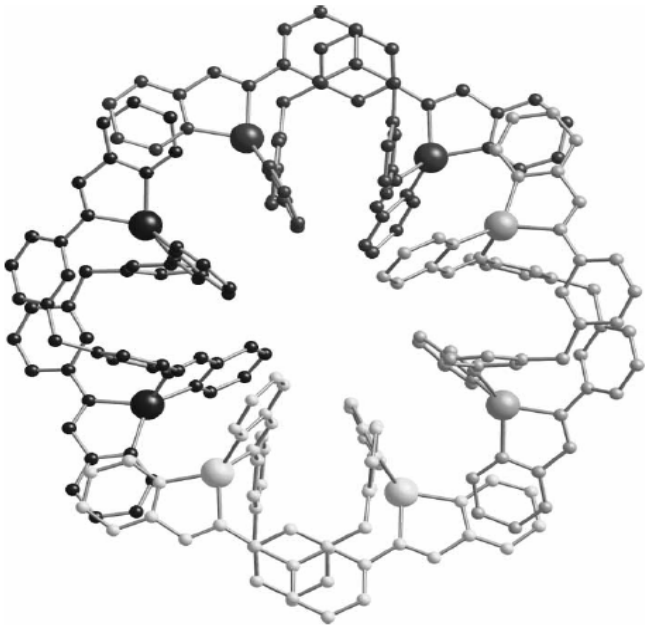

Figure 13. Crystal structure showing the cyclic aggregation of $[Cu_2(\mathbf{XI})_2]^{3+}$.

Aggregation of circular helicates to 3D arrangements has also been described. Ligand **XII** has been reacted with copper(I) and an X-ray crystal structure was determined [101]. The solid state structure reveals a chiral helical trimer $[Cu_3(\mathbf{XII})_3]^{3+}$ with each copper(I) centre occupying a four coordinate pseudo-tetrahedral environment bound to two pyridylimine units from two different ligands. The side view of this triangle reveals that the triangle is not planar but instead slightly bent over towards one face to provide a bowl-shaped motif (Figure 14a). This bowlshaped distortion arises to accommodate the

CH–π interactions and is a consequence of the desirability of the methyl groups forming CH–π interactions coupled with the constraints of the ligand connectivity. Three pyridyl rings (one from each ligand) point up towards the cavity of the bowl and are arranged like the blades of a propeller. Four of the bowl-shaped triangles aggregate together to form a nanoscale tetrahedral ball-shaped structure (Figure 14b) with three pyridyl rings from each triangle pointing into the cavity of the tetrahedron.

a)

b)

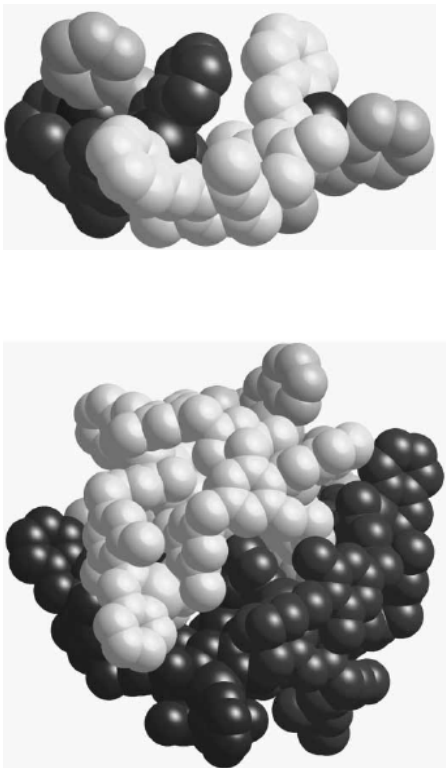

Figure 14. Crystal structure of $[Cu_3(\mathbf{XII})_3]^{3+}$ cation: a) side view, b) tetrahedral array resulting from aggregation of four trimers.

Ligand **XIII** reacts with $[Cu(OAc)_2]\cdot H_2O$ or $[Ni(OAc)_2]$ to form the trinuclear circular helicates $[Cu_3(\mathbf{XIII})_3(OAc)_3][PF_6]_3$ and $[Ni_3(\mathbf{XIII})_3(OAc)_3][PF_6]_3$ respectively. In the structurally characterised copper(II) trimeric circular helicate, the copper(II) centre adopts a square-based pyramidal geometry and consequently the structure of the trimer is not markedly different from that of the trimer formed with octahedral nickel(II) (Figure 15). However, in solution copper(II) and nickel(II) are significantly different, with a

substantial dimer component for copper(II), whereas trimers are dominant for nickel(II) [102].

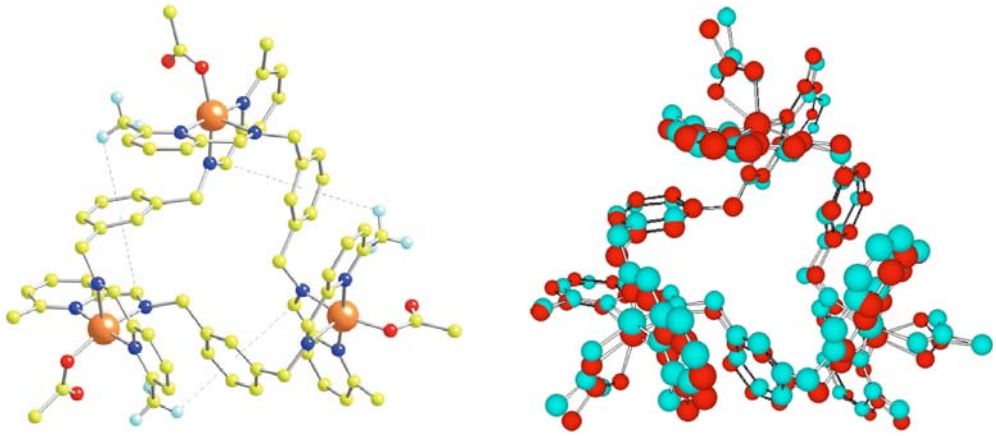

a) b)

Figure 15. a) The structure of the trinuclear circular-helical cation in the complex $[Cu_3(\mathbf{XIII})_3(OAc)_3][PF_6]_3$. b) Overlay of the structures of the trinuclear circular-helical cations in the complexes $[Cu_3(\mathbf{XIII})_3(OAc)_3][PF_6]_3$ (green) and $[Ni_3(\mathbf{XIII})_3(OAc)_3][PF_6]_3$ (red).

2.1 Synthesis and structure of bis-pyridylimine ligands

2.1.1 Ligand syntheses

The ligands $\mathbf{L^1}$–$\mathbf{L^5}$ were synthesized according to the previously reported procedure [84, 103] by condensation of appropriate diamine compounds and 2–pyridinecarboxaldehyde in methanol or acetonitrile. Suitable single X-ray quality crystals of $\mathbf{L^1}$, $\mathbf{L^4}$ and $\mathbf{L^5}$ grow with slow evaporation of their acetonitrile solutions at 4 °C.

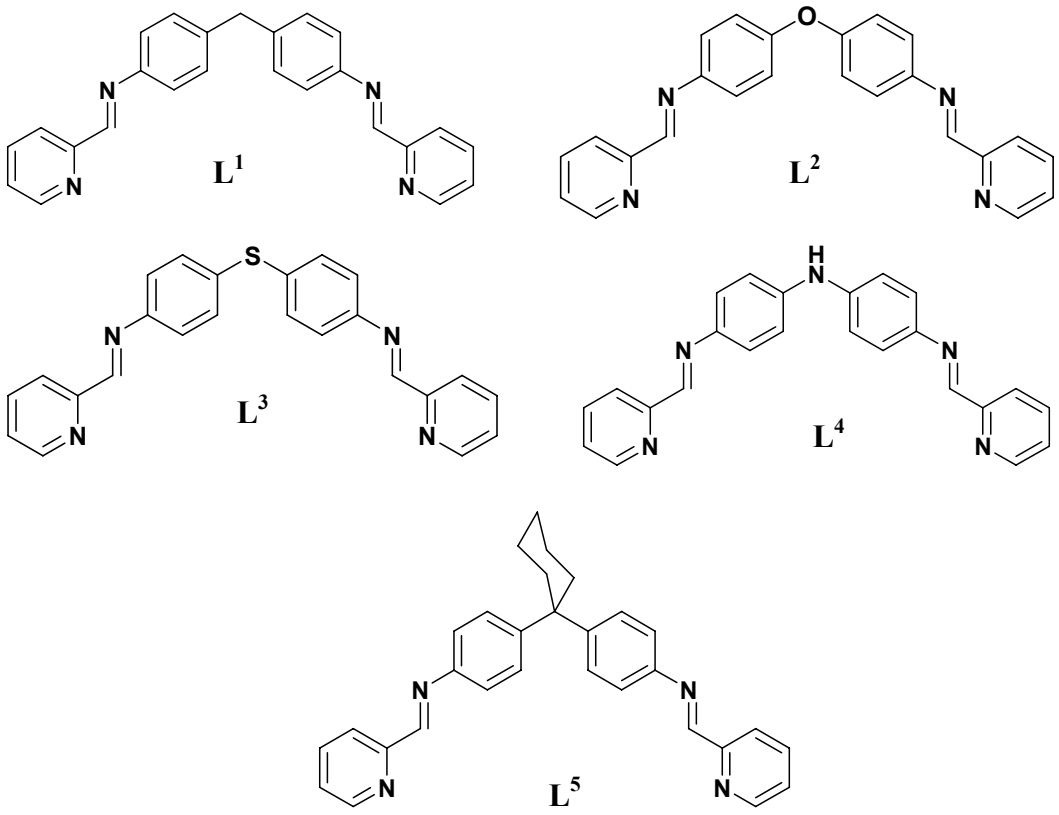

2.1.2 Structures of selected ligands

2.1.2.1 Structure of bis[4-(2-pyridylmethyleneimino)phenyl]methane (L^1)

Ligand L^1 possesses twofold symmetry, with the twofold axis running through the central CH_2 linking element existing between the two bidentate chelating subunits, and exhibits an imine E configuration (Figure 16). The conformations of the two halves of the molecule do not differ too much. The both moieties, involving pyridine ring N1/C2–C6 and phenylene ring C9–C14, are almost flat with a dihedral angle of 15.12(8)° between the rings. The pyridine–imine system is almost planar within the two moieties.

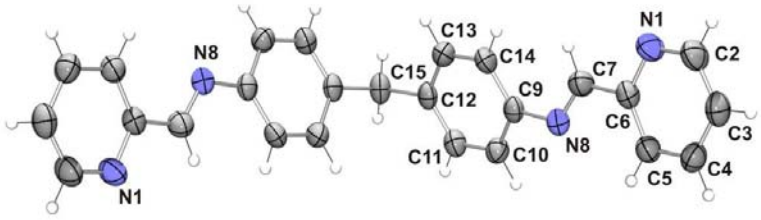

Figure 16. Molecular structure of $\mathbf{L^1}$ showing the numbering scheme and displacement ellipsoids at the 50% probability level.

The torsion angles N1–C6–C7–N8 and C6–C7–N8–C9 are 176.8(2)° and 178.4(1)°, respectively. This is consistent with the presence of a π-conjugated system, only interrupted by the central CH_2 linking element, although bond-length alternation is always observed [the C7-N8 bond distance of 1.269(2) Å is indicative of double-bond character]. These characteristics are in agreement with similar structures [79, 104, 105]. The angle C12–C15–C12 (110.6°) is a bit smaller than the angle C–O–C (119.39°) observed in reported analogous ligand [79]. The crystal packing (Figure 17) does not involve any weak interactions compared to its analogue with O as a central linking element [79].

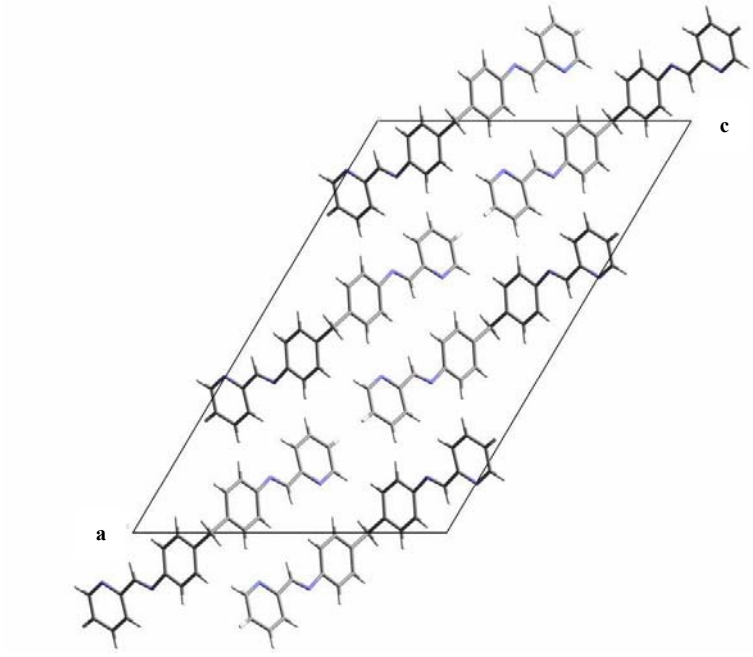

Figure 17. The crystal packing of $\mathbf{L^1}$ along the *b* axis.

2.1.2.2 Structure of bis[4-(2-pyridylmethyleneimino)phenyl]amine (L^4)

Ligand $\mathbf{L^4}$ possesses pseudo-twofold symmetry, with the twofold axis running through the central NH linking element existing between the two bidentate chelating subunits, and exhibits also an imine E configuration (Figure 18). The conformations of the two halves of the molecule differ considerably. One moiety, involving pyridine N29/C24–C28 and phenylene ring C16–C21, is almost flat with a dihedral angle of 13.83(13)° between the aromatic rings. In the second moiety, the pyridine ring N1/C2–C6 and phenylene ring C9–C14 are inclined with respect to one another by 33.02(12)°.

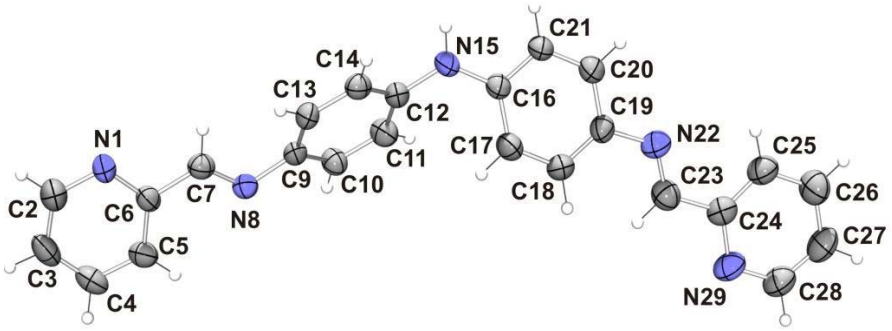

Figure 18. Molecular structure of $\mathbf{L^4}$ showing the numbering scheme and displacement ellipsoids at the 50% probability level.

The pyridine–imine system is almost planar within the two moieties. The torsion angles N1–C6–C7–N8 and C6–C7–N8–C9 are –174.6(2)° and –178.0(2)°, respectively, whereas torsion angles N22–C23–C24–N29 and C19–N22–C23–C24 are 173.7(3)° and –176.9 (2)°, respectively. This is consistent with the presence of a π-conjugated system, only interrupted by the central NH linking element, although bond-length alternation is always observed [the C7-N8 and C23-N22 bond distance of 1.263(4) Å is indicative of double-bond character]. These characteristics are in agreement with similar structures [79, 104, 105]. The angle C12–N15–C16 (126.1°) is larger than the angle C–CH_2–C (110.6°) of the above described structure and the angle C–O–C (119.39°) observed for $\mathbf{L^2}$ [79]. In the crystal packing (Figure 19), the pyridine N1 atoms are involved in weak intermolecular N–H···N interactions with NH central group of the neighbouring molecule. The distance

between the two nitrogen atoms (N1···N15) is 3.04(2) Å. The more planar moieties of symmetry-related molecules are also considerably overlapped. Also, molecules are packed together through weak face-to-face $\pi\cdots\pi$ (*Cg*···*Cg* between 4.13 and 4.29 Å) and edge-to-face interactions with a distance C···*Cg* of ca 3.8 Å. These weak interactions are summarized in Table 1.

Table 1. D–H···*A* interactions in **L**[4].

D – H	*A*	H···*A* [Å]	D···*A* [Å]	D–H···*A* [°]
N15 – H15	N1[i]	2.20	3.04	162
C11 – H11	*Cg*2[ii]	2.84	3.74	157
C21 – H21	*Cg*3[iii]	2.95	3.80	148

Symmetry codes: (i) = -x,-1/2+y,3/2-z ; (ii) = 1−x,1/2+y,3/2−z ; (iii) = x,−1/2−y,1/2+z

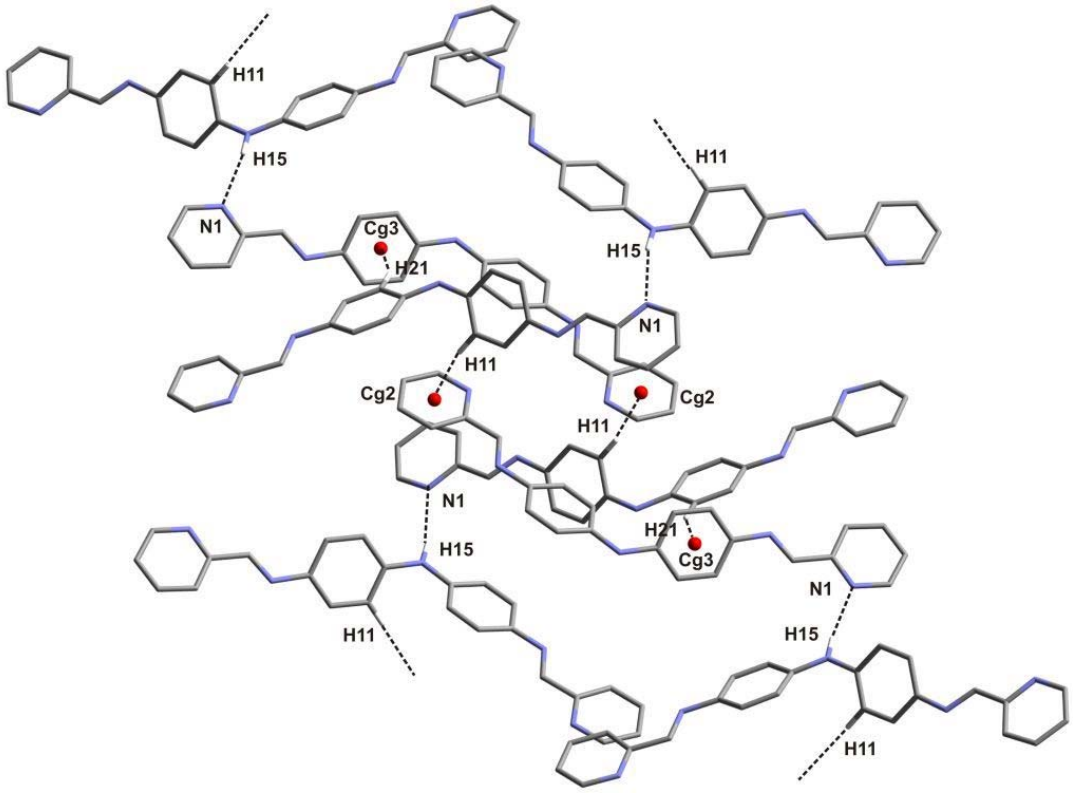

Figure 19. The crystal packing of **L**[4] showing the different weak interactions as dotted lines.

2.1.2.3 Structure of bis[4-(2-pyridylmethyleneimino)phenyl]-1,1-cyclohexane (L^5)

Ligand $\mathbf{L^5}$ possesses one-fold symmetry having an inversion center, with the onefold axis running through the central C_6H_{10} linking element present between the two bidentate chelating subunits, and exhibits an imine E configuration (Figure 20). The conformations of the two halves of the molecule differ considerably from each other and also from the structure analogous ligands $\mathbf{L^1}$, $\mathbf{L^2}$ and $\mathbf{L^4}$. In both moities, pyridine ring and phenylene ring are inclined which contrasts with the structures of the other ligands, where one half of the ligand is inclined and the other half is almost planar. The dihedral angle between the pyridine ring N1/C2−C6 and the neighbouring phenylene ring C9−C14, is 65.72(7)° while in the second moiety, the aromatic units N34/C29−C33 and C21−C25 are inclined with respect to one another by 40.97(8)°.

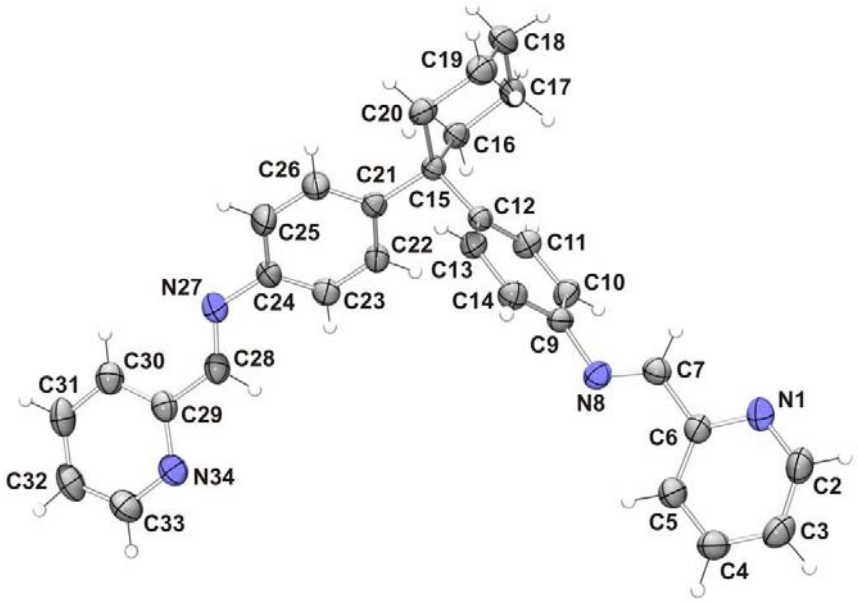

Figure 20. Molecular structure of $\mathbf{L^5}$ showing the numbering scheme and displacement ellipsoids at the 50% probability level.

The pyridine–imine system is almost planar within the two moieties. The torsion angles N1–C6–C7–N8 and C6–C7–N8–C9 are –167.9(2)° and –179.04(13)°, respectively, whereas torsion angles N27–C28–C29–N34 and C24–N27–C28–C29 are –173.4(2)° and 179.4(1)°, respectively. This is consistent with the presence of a π–conjugated system,

only interrupted by the central C_6H_{10} linking element, although bond-length alternation is always observed [the average C=N bond distance is 1.260(1) Å]. These characteristics are in agreement with similar structures [79, 104, 105]. The angle C12–C15–C21 (107.1°) is lower than all other angles around the linking element present between chelating subunits of analogous ligands (Table 2). In the crystal packing (Figure 21) the pyridine N1 atom of one ligand molecule is involved in weak intermolecular C–H···N interactions with an adjacent molecule having a distance C32···N1 of 3.44(1) Å. Additionaly, molecules are stacked together through edge-to-face C–H···π interactions with a distance CH···centroid of ca 2.9 Å. The geometry details of these weak interactions are sumarized in Table 3.

Table 2. Comparison of angles around the linking element present between chelating subunits of **L**[1], **L**[2], **L**[4] and **L**[5] ligands.

Ligand	**L**[1]	**L**[2]	**L**[4]	**L**[5]
Linking elememt present between chelating subunits	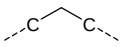	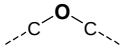	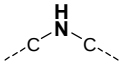	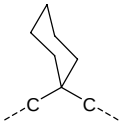
Angles (°)	110.54°	119.39° [79]	126.09°	107.13°

Table 3. C–H···*A* interactions in **L**[5].

C – H	***A***	**H···*A* [Å]**	**C···*A* [Å]**	**C–H···*A* [°]**
C32 – H32	N1[i]	2.50	3.44	172
C4 – H4	*Cg*3[ii]	2.82	3.68	151
C14 – H14	*Cg*5[iii]	2.99	3.91	163
C18 – H18A	*Cg*3[iv]	2.91	3.89	171

Symmetry codes: (i) = −1+x,1+y,1+z ; (ii) = 2−x,− y, 1−z ; (iii) = 1+x,y,z ; (iv) = 1−x, −y, −z

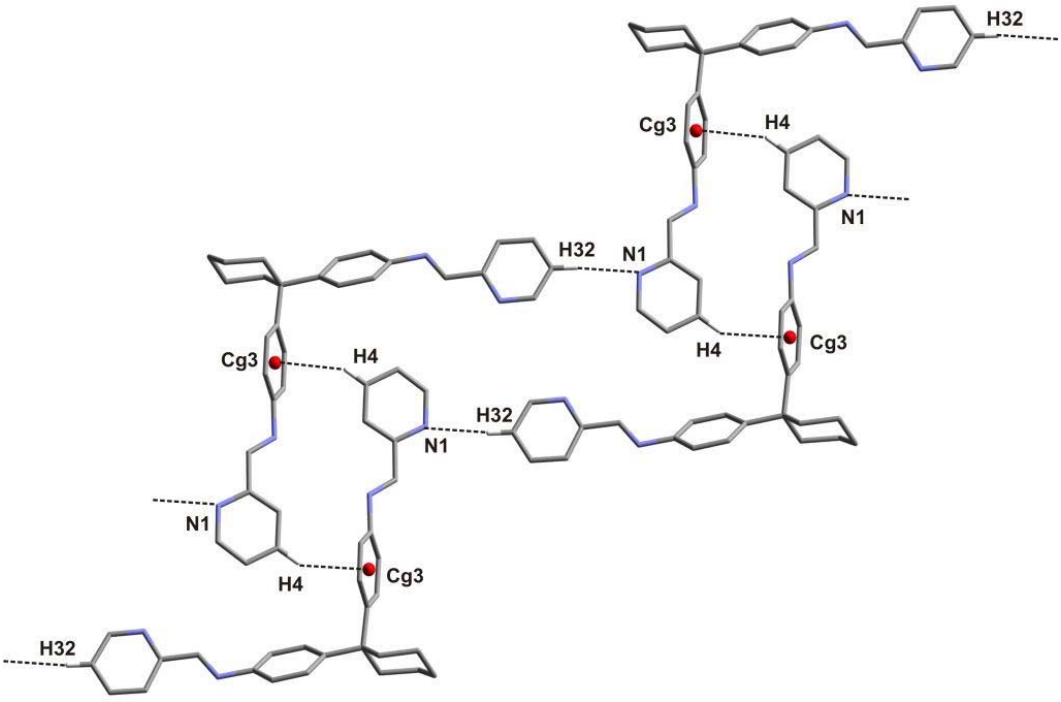

Figure 21. The crystal packing of ($\mathbf{L^5}$) showing the differents weak interactions in dotted lines.

2.2 Synthesis and structure characterization of some transition metal complexes

In the present work, numerous experiments on the complexation properties of bis-pyridylimine ligands towards different transition metal ions such as Ag(I), Cu(II), Hg(II), Mn(II), Ni(II) and Fe(II) were performed.

Solid complexes were prepared by mixing the Schiff base ligands and selected metal salts ($AgClO_4$, $CuSO_4$, $Hg(ClO_4)_2$, $Mn(ClO_4)_2$, $Ni(NO_3)_2$, $NiCl_2$, $FeCl_2$) in an appropriated solvent or solvent mixture using different ligand/metal ratios. Single X-ray crystals were obtained either by slow evaporation of the mother solvent or mostly by slow diffusion of diethylether in the sample mixture. Figure 22 shows the diffusion method which has been used as general procedure to grow single crystals of the complexes.

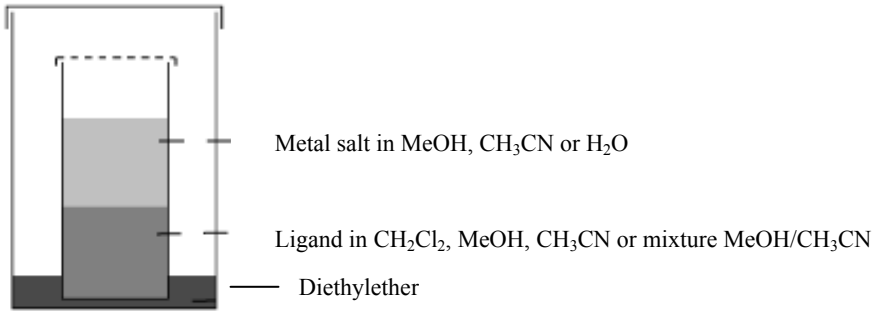

Figure 22. Diffusion method used for the synthesis of crystalline metal complexes.

2.2.1 Ag(I) complexes

The reaction of $AgClO_4$ with the ligands $\mathbf{L^1}$ and $\mathbf{L^2}$ in various solvents led to three complexes **1**, **2** and **3** with different structure topology. The crystal structures of these complexes are discussed below.

2.2.1.1 Complex $\{[AgL^1](ClO_4) \cdot CH_3CN\}_n$ (1)

The self-assembly of $\mathbf{L^1}$ with $AgClO_4$ yielded the complex cation $[Ag\mathbf{L^1}]^+$, as a one-dimensional zigzag coordination polymer. This product crystallizes in the space group *P*21 as determined uniquely by the pattern of systematic absences in the intensity data. The asymmetric unit contains one Ag(I) ion, one independent ligand, one acetonitrile molecule and a perchlorate anion.

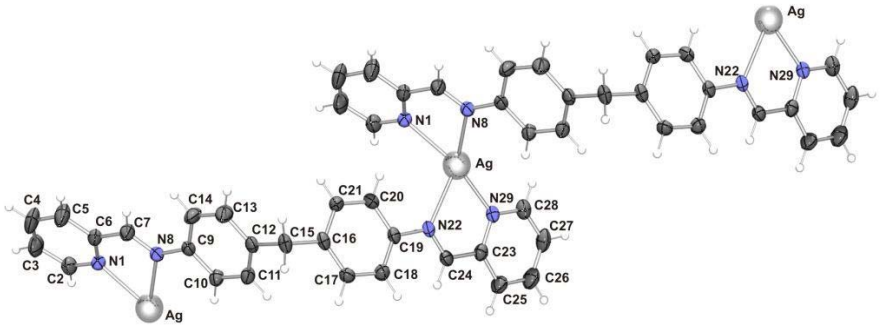

Figure 23. Local coordination environment of Ag(I) in **1**. Atoms are represented as 50% thermal ellipsoids. All anions and solvent molecules are omitted for clarity.

Each Ag(I) ion is bound to two pyridylimine units of two ligand molecules to yield a distorted tetrahedral coordination geometry. A 1D zigzag coordination polymer is generated. An ORTEP diagram of **1** is shown in Figure 23 and pertinent crystallographic data are given in Tables 4 and 5.

Table 4. Selected bond lengths (Å) and angles (°) for **1**.

Atom	Bond lengths (Å)	Atom	Angles (°)
Ag-N_1	2.413(2)	N_1-Ag-N_{29}^{i}	148.64(9)
Ag-N_8	2.301(2)	N_1-Ag-N_{22}^{i}	105.68(8)
Ag-N_{22}^{i}	2.457(2)	N_1-Ag-N_8	72.40(9)
Ag-N_{29}^{i}	2.255(2)	N_8-Ag-N_{22}^{i}	126.36(8)
		N_8-Ag-N_{29}^{i}	134.87(8)
		N_{22}^{i}-Ag-N_{29}^{i}	72.39(9)

Symmetry code: i = 1+x, y, z

Table 5. C–H···*A* interactions in **1.**

C – H	*A*	H···*A* [Å]	C···*A* [Å]	C–H···*A* [°]
C7 – H7	$O3^{i}$	2.42	3.33	160
C14 – H14	$O3^{i}$	2.54	3.48	171
C15 – H15A	$O8^{ii}$	2.37	3.28	153
C20 – H20	$N1^{iii}$	2.60	3.52	163
C24 – H24	$N31^{iii}$	2.62	3.55	164
C25 – H25	$O5^{iv}$	2.34	3.10	137
C27 – H27	$O1^{v}$	2.47	3.32	150
C20 – H20	$Cg4^{iii}$	2.91	3.80	156
C18 – H18	$Cg6^{v}$	3.12	3.83	133
C17 – H17	$Cg7^{v}$	2.97	3.90	168

Symmetry codes: (i) = −x,−1/2+y,1−z ; (ii) = −1+x,−1+y,z ; (iii) = −1+x,y,z ; (iv) = −1+x, −1+y,1+z ; (v) = −1-x,−1/2+y,2−z

The Ag-$N_{pyridyl}$ bond lengths are in the range 2.413(2)-2.255(2) Å, while the Ag-N_{imine} bond distances lie between 2.301(2) and 2.457(2) Å. All these bond lengths are also within the expected range. The chelate bite angles for N_1-Ag-N_8 and N_{22}-Ag-N_{29} are respectively 72.40(9)° and 72.39(9)°. The halves of the ligand are not planar and the torsion angle between the two neighboring phenylene rings is *ca*. 62°. The packing diagram shows that the zigzag chains are interdigitated with weak edge-to-face (CH-π) stacking between adjacent phenyl rings, with a C–H···centroid distance in the range 2.91-3.12 Å. Strong face-to-face π-π interactions also occur between phenyl rings and adjacent pyridine rings [72] There are also π-π stacking interactions between pyridine rings themselves (Figure 24). The interplanar distances are in the range of 3.52–3.70 Å. No silver–anion interactions are present in **1**.

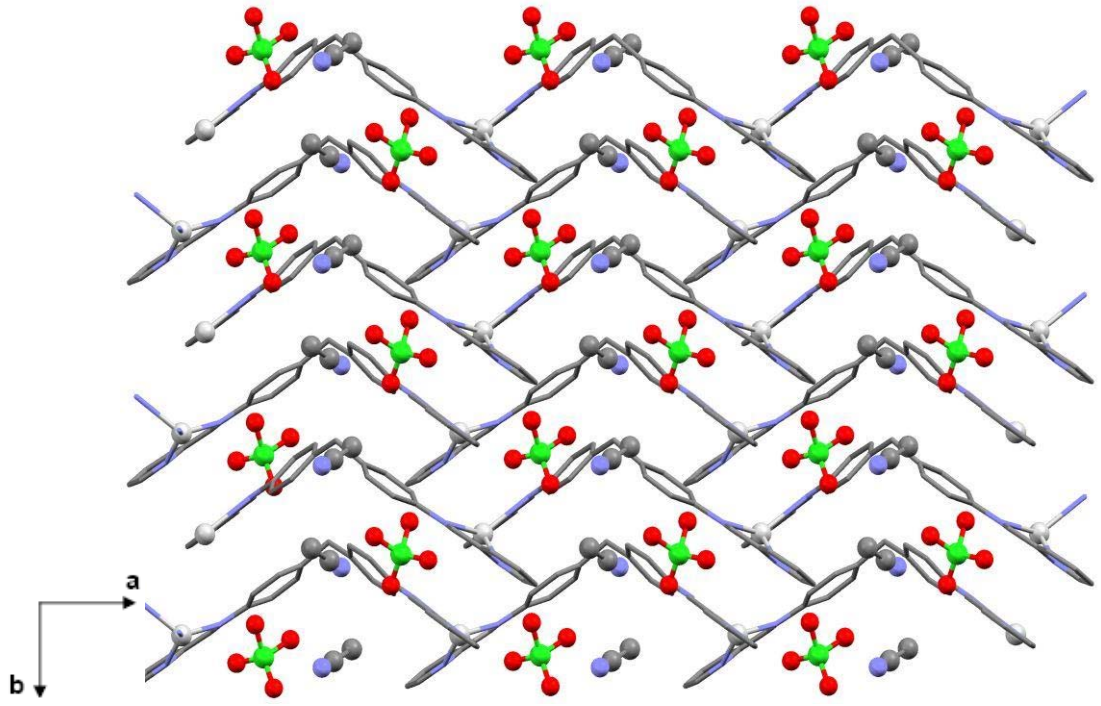

Figure 24. Crystal packing for **1** showing the different π-π, CH-π interactions between the zigzag chains. Perchlorate anions and acetonitrile molecules are stacked in the crystal lattice. Hydrogen atoms are omitted for clarity.

This compound also forms layered structure where the ClO_4^- anions and the CH_3CN molecules are intercalated between the two dimensional cationic layers (Figures 24-26) stabilizing the packing via hydrogen bonds with C-H···O and C-H···N distances in the range 3.10-3.48 Å and 3.52-3.55 Å respectively (Table 5). Individual perchlorate anions interact with the methylene bridge of one schiff base unit and the pyridine rings of an opposite Schiff base via C-H···O hydrogen bonds (Figure 25) to bridge the layers.

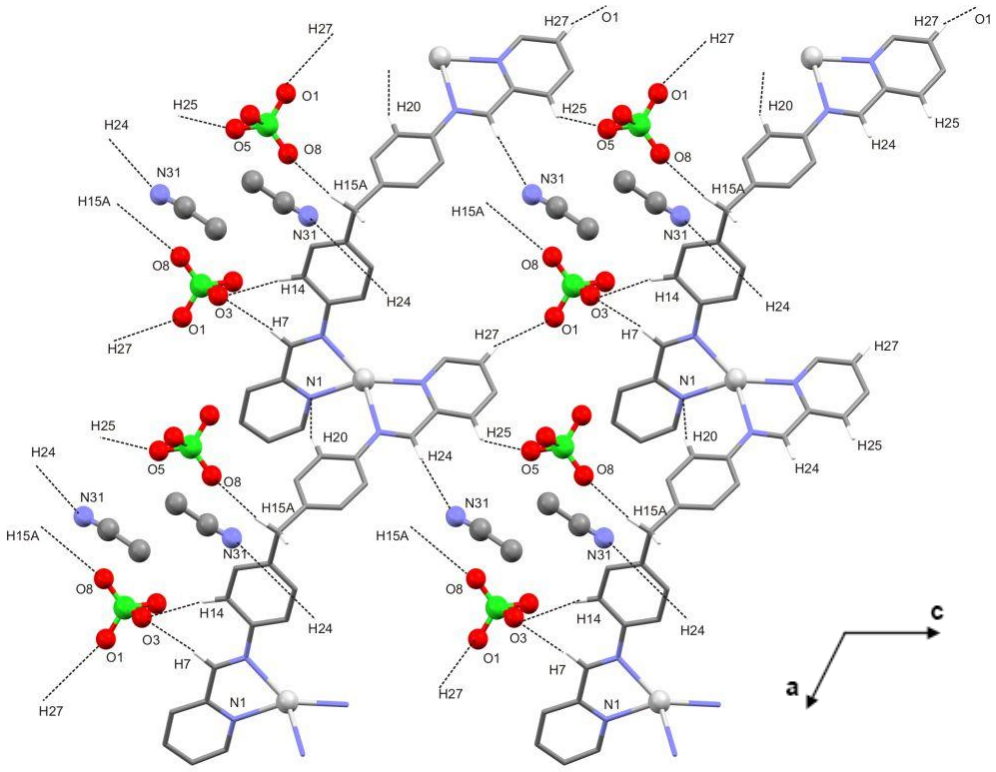

Figure 25. Side view of the structure for **1** showing how the perchlorate anions form a bridge between the cationic polymeric chains. Some hydrogen atoms are omitted for clarity.

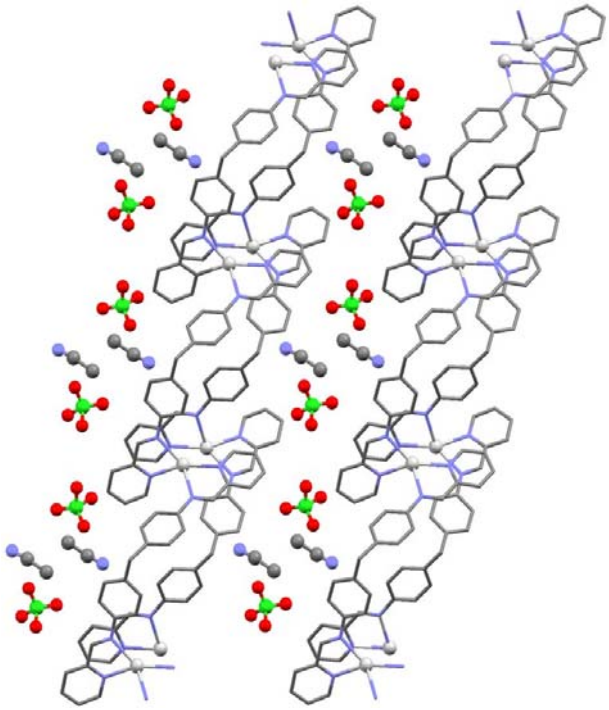

Figure 26. Side view along the *b*-axis of the layered structure of **1** showing the intercalation of the perchlorate anions and solvent (CH_3CN) molecules. Hydrogen atoms are omitted for clarity.

2.2.1.2 Complex $\{[AgL^2]ClO_4 \cdot CH_2Cl_2\}_n$ (2)

The reaction of $\mathbf{L^2}$ with $AgClO_4$ via slow diffusion of diethylether in a mixture of CH_2Cl_2 and CH_3CN at room temperature led to the formation in high yield of a coordination polymer $\{[AgL^2]ClO_4 \cdot CH_2Cl_2\}_n$ (**2**) with a 1D zigzag structure. Similar single-stranded silver polymers have been reported previously. [79] Compound **2** crystallizes in the space group *Pcca* as determined uniquely by the pattern of systematic absences in the intensity data. The asymmetric unit contains one Ag(I) ion, one independent ligand $\mathbf{L^2}$, one dichloromethane molecule and a perchlorate anion. In this complex, each Ag(I) ion is coordinated to two Schiff base ligands via pyridyl and imine nitrogen atoms. Each Schiff base bridges two Ag(I) ions. A distorted tetrahedral configuration occurs around each metal center to yield a 1D zigzag coordination polymer. An ORTEP diagram of **2** is shown in Figure 27, and pertinent crystallographic data are given in Tables 6 and 7. The

Ag-$N_{pyridyl}$ bond lengths are in the range 2.252(3)-2.259(3) Å, while the Ag-N_{imine} bond distances lie in the range 2.373(4)-2.395(3) Å. All these bond lengths are consistent with those reported for other Ag(I) Schiff base complexes. [79, 80, 84, 86, 87, 103, 106, 107] The N_1-Ag-N_8 and N_{25}-Ag-N_{22} bond angles are 72.75(11) and 72.63(11)° respectively. The ligand is twisted around the central O atom.

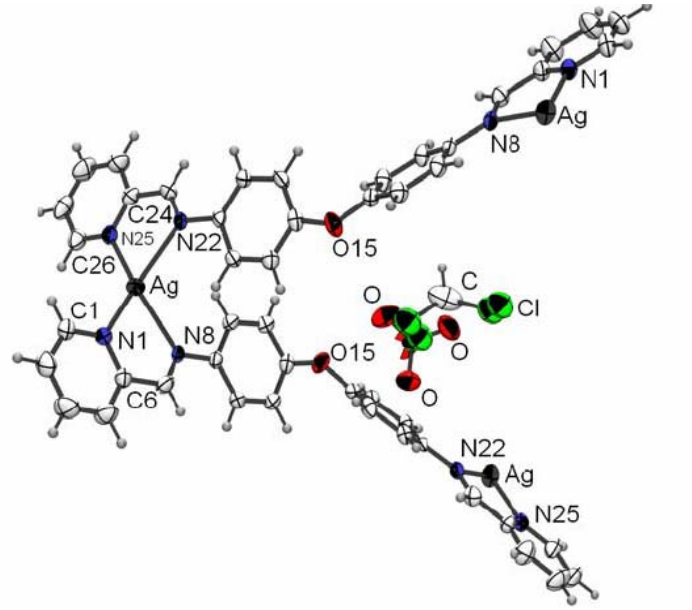

Figure 27. An ORTEP diagram for the asymmetric unit of **2**. Thermal ellipsoids are shown at the 50% probability level.

Table 6. Selected Bond lengths (Å) and angles (°) for **2**.

Atom	Bond lengths (Å)	Atom	Angles (°)
Ag-N_1	2.259(3)	N_1-Ag-N_{25}	134.08(11)
Ag-N_8	2.373(4)	N_1-Ag-N_{22}	139.61(11)
Ag-N_{22}	2.395(3)	N_1-Ag-N_8	72.75(11)
Ag-N_{25}	2.252(3)	N_8-Ag-N_{22}	110.65(10)

Table 7. C–H···*A* interactions in **2**.

C – H	*A*	H···*A* [Å]	C···*A* [Å]	C–H···*A* [°]
C30A-H30A	O4^{vi}	2.47	3.44	168
C30A-H30B	O3^{vii}	2.57	3.33	134
C13 – H13	*Cg*4^{viii}	3.09	3.96	153
C21 – H21	*Cg*5^{ix}	2.82	3.58	138
C26 – H26	*Cg*6^{x}	2.60	3.54	169
C2 – H2	*Cg*7^{xi}	2.96	3.90	173

Symmetry codes: (vi) = x,1/2−y,−1/2+z; (vii) = 1/2−x,1−y,−1/2+z; (viii) = −1/2+x,y,1/2−z; (ix) = 1/2+x,y,1/2−z; (x) = −1/2−x,−1/2+y,z; (xi) = 1/2−x,1/2+y,z

The packing diagram shows that the zigzag chains are linked by face-to-face (π-π) stacking between adjacent phenyl rings with a distance of ca 3.8 Å; also edge-to-face (CH-π) interactions between phenyl rings and adjacent pyridine rings occur with C-H···centroid distances in the range 2.60-2.96 Å (Figure 28). The π-π interactions in **2** are comparatively weak [72]. This compound forms a layered structure where the anions (ClO_4^-) and the solvent molecules (CH_2Cl_2) are sandwiched between cationic sheets (Figure 29 and 30) and interact each other via C-H···O hydrogen bonds with distances in the range 3.33-3.44 Å (Table 7).

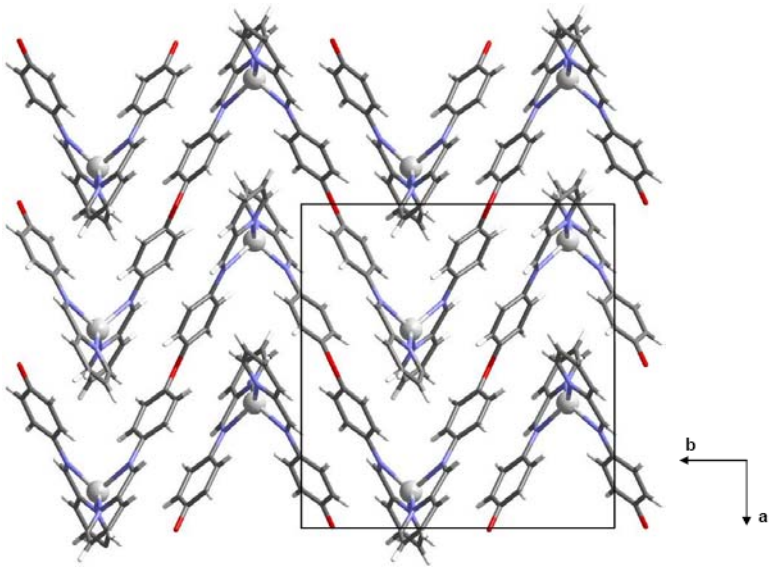

Figure 28. Crystal packing for **2** showing the π-π stacking between zigzag chains. Perchlorate anions and dichloromethane molecules are omitted for clarity.

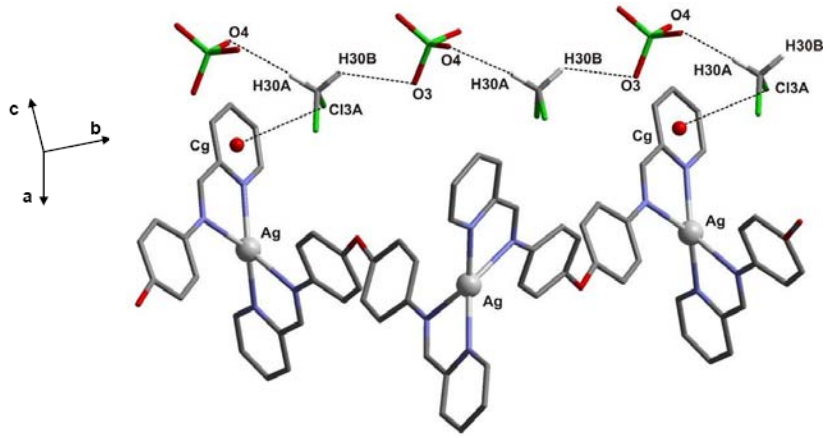

Figure 29. Side view of the structure of **2** showing both the interaction between perchlorate and dichloromethane and between one chlorine atom of CH_2Cl_2 and a pyridine ring. Hydrogen atoms of the ligand are omitted for clarity.

One chlorine atom of CH_2Cl_2 also interacts with a pyridine ring to give a C-Cl···π contact with a distance (Cl···centroid) of around 3.53 Å (Figure 29). The cationic sheets are best described as 2D arrangements involving coordination polymers with tetracoordinated silver centers. The perchlorate anions do not coordinate the Ag(I) centres. A view of this packing behaviour is given in Figures 28 and 30. The previously reported structure [79] posessing $CF_3SO_3^-$ as counter ion shows a similar coordination pattern. The unit cell is a bit larger in this case and the anion is disordered.

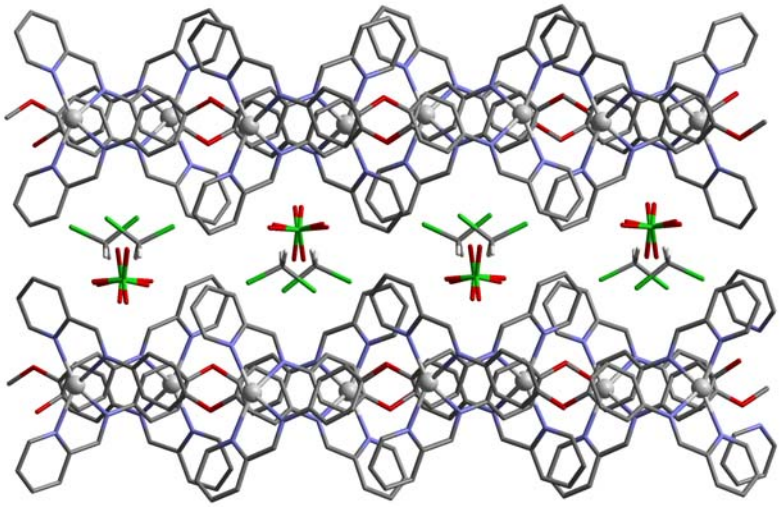

Figure 30. Side view along the *b*-axis of the layered structure of **2** showing the sandwiching of the perchlorate anions and solvent (CH_2Cl_2) molecules. Hydrogen atoms are omitted for clarity.

2.2.1.3 Complex $[Ag_2(L^2)_2](ClO_4)_2$ (3)

Crystals of complex **3** were obtained using a CH_3OH/CH_3CN mixture instead of CH_2Cl_2 in case of **2**. The solid-state structure reveals that **3** may be described as a molecular box, very similar to the complex $[Ag_2(\mathbf{L^2})_2](BF_4)_2$ obtained by Cheng et *al*. [80] Indeed it is clear that the phenyl ether spacer sterically inhibits the two metal binding sites from coordinating to a single metal center. Nevertheless in contrast to the methylene bridge in $\mathbf{L^1}$ the central ether oxygen atom in $\mathbf{L^2}$ will introduce enhanced flexibility into the ligand backbone, as discussed by Hannon et al. [84, 86, 87, 106, 107]. This flexibility allows two possible arrangements for dimeric $[M_2\mathbf{L_2}]^{2+}$ species: a double-helical structure or a non-helical box-like structure.

a)

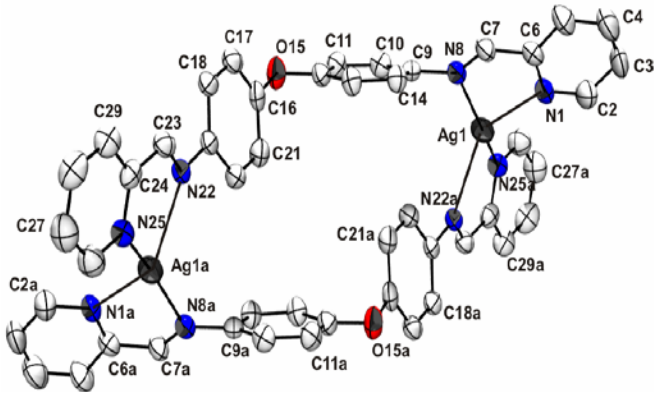

b)

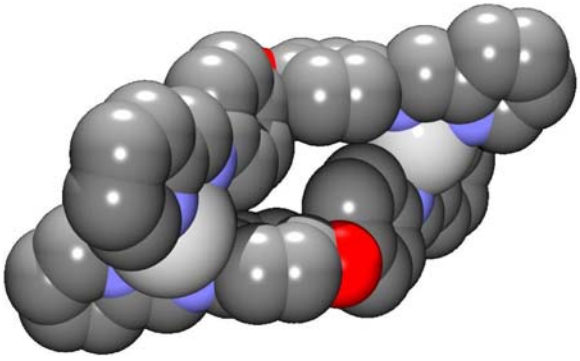

Figure 31. a) ORTEP plot of the box-like $[Ag_2\mathbf{L^2})_2]^{2+}$ cation showing 50% probability displacement ellipsoids. **b)** Space-filling representation. Hydrogen atoms and perchlorate anions are omitted for clarity.

$[Ag_2(\mathbf{L^2})_2](ClO_4)_2$ (**3**) crystallizes in the triclinic system with the space group being *P*–1. The asymmetric unit consists of one dinuclear complex cation and two perchlorate anions. The structure of the dimeric $[Ag_2(\mathbf{L^2})_2]^{2+}$ box is shown in Figure 31 and corresponding crystallographic data are given in Tables 8 and 9.

Table 8. Selected Bond lengths (Å) and angles (°) for **3**.

Atom	Bond lengths (Å)	Atom	Angles (°)
Ag_1-N_1	2.429(4)	N1–Ag1–N22^{i}	132.01(13)
Ag_1-N_8	2.307(4)	N1–Ag1–N25^{i}	115.44(14)
Ag_1-N_{22}	2.425(4)	N_1- Ag_1-N_8	71.01(14)
Ag_1-N_{25}	2.297(4)	N8–Ag(1)–N22^{i}	117.69(13)
		N8–Ag(1)–N25^{i}	162.25(13)
		N22^{i}–Ag(1)–N25^{i}	71.38(13)

Symmetry codes: i = 1−x, 1−y, −z

Table 9. C–H···*A* interactions in **3**.

C – H	*A*	H···*A* [Å]	C···*A* [Å]	C–H···*A* [°]
C3-H3A	O4B^{xii}	2.56	3.43	152
C5-H5A	O2B^{xiii}	2.58	3.13	117
C10-H10A	O3B^{xiv}	2.53	3.47	171
C18-H18A	O4B^{xv}	2.52	3.36	148
C11– H11A	*Cg*5^{xvi}	2.88	3.80	164
C17 – H17A	*Cg*1^{xvii}	2.88	3.80	163
C20 – H20A	Cg6^{xviii}	2.92	3.77	149

Symmetry codes: (xii) = 2−x, 1−y, 1−z, z; (xiii) = 1−x, 1−y, 1−z; (xiv) = x, −1+y, z; (xv) = −1+x, y, z; (xvi) = −1+x, y, z; (xvii) = −1+x, y, z; (xviii) = −1+x, y, z.

The cationic molecular box in **3** is composed of two Ag(I) ions and two Schiff base ligands $\mathbf{L}^2$. Each Schiff base is doubly chelated and bridges two silver ions. One Schiff base passes above the Ag(I)–Ag(I) axis, while the other passes beneath it. Each Ag(I) is coordinated to two pyridyl and two imine nitrogen atoms, generating a distorted tetrahedral geometry. The dihedral angle between the two coordination planes is *ca*. 61°. The Ag–$N_{pyridyl}$ distances are 2.297(4) and 2.429(4) Å and Ag–N_{imine} distances are 2.307(4) and 2.425(4) Å. The bite angles $N_{pyridyl}$–Ag–N_{imine} are 71.01(14)° and 71.38(13)° (Table 8). The structure has opposite phenyl rings parallel to each other, with the torsion angle between two neighboring phenyl rings of one ligand being *ca* 67.7°. The dimensions of the resulting distorted rhombic cavity are approximately 7×7 Å, measured between opposite phenyl rings. This cavity is similar to that in $[Ag_2(\mathbf{L}^2)_2][BF_4]_2 \cdot 1.5CH_3CN$ recently reported [80]. The intermetallic Ag···Ag distance is 12.4 Å.

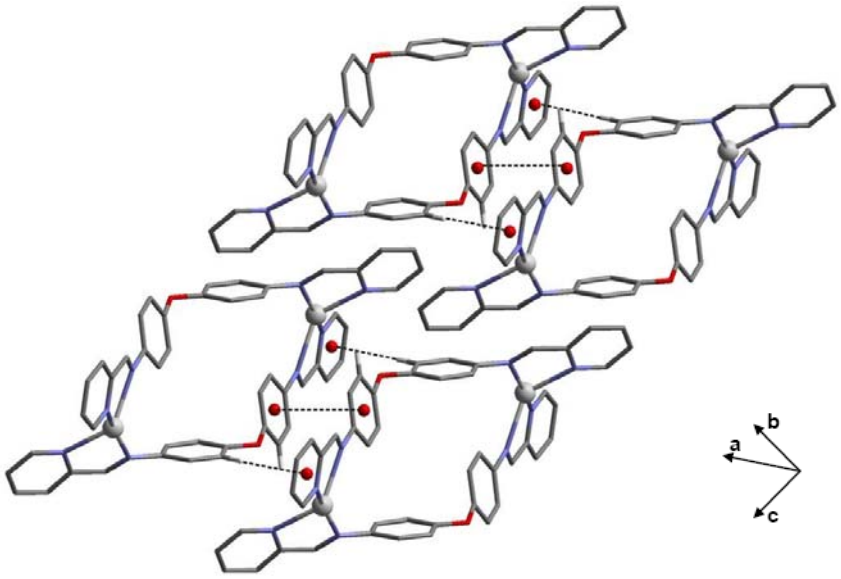

Figure 32. Perspective view of the 2D sheets showing the π–π and CH-π interactions in **3**. Hydrogen atoms and perchlorate anions are omitted for clarity.

Intermolecular face-to-face (π-π) interactions between the phenyl rings with a centroid…centroid distance of 3.57 Å (β = 22°) and edge-to-face (CH-π) interactions between the phenyl rings and pyridine rings with (CH···centroid) distances in the range

2.88-2.99 Å may enhance the stability of the molecular box architecture (Figure 32). Perchlorate anions also play a role in the stabilisation since they serve to bind the molecular boxes throughout the crystal lattice; These anions are not disordered and interact with the phenyl and the pyridine rings respectively (Figures 33 and 34) via C-H···O hydrogen bonds with C···O distances in the range 3.13-3.47 Å (Table 9).

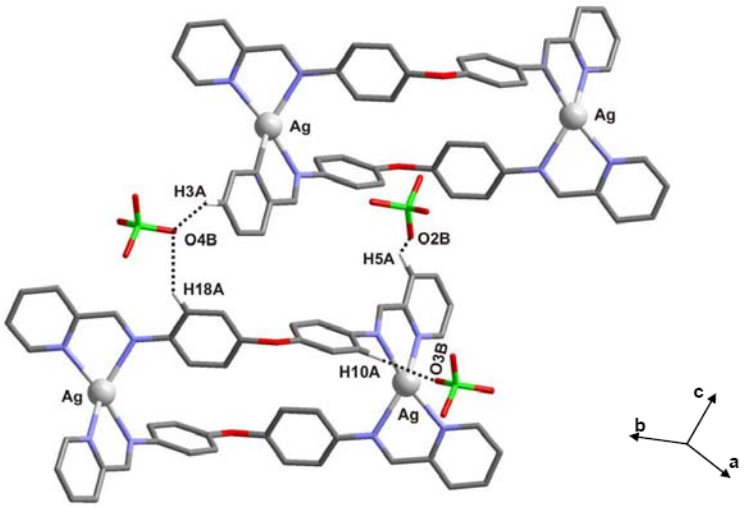

Figure 33. Side view of the structure of **3** showing the interactions between perchlorate and H atoms of adjacent phenyl and pyridine rings. Non-bound hydrogen atoms are omitted for clarity.

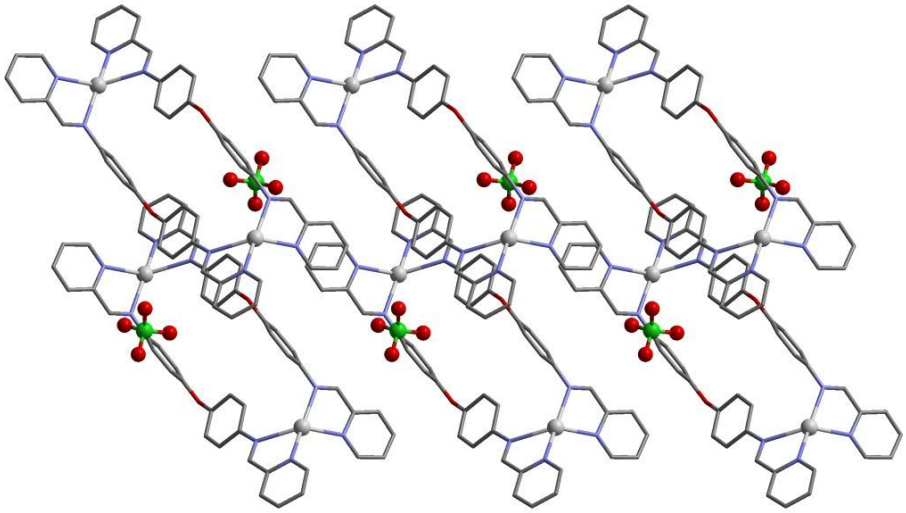

Figure 34. Side view of the structure of **3** along the crystallographic *b*-axis showing the perchlorate interactions. Hydrogen atoms are omitted for clarity.

2.2.2 Cu(II) complexes

2.2.2.1 Complexes $[CuL^1(SO_4)]_6 \cdot 24H_2O$ (4), $[CuL^2(SO_4)]_6 \cdot 24H_2O$ (5) and $[CuL^3(SO_4)]_6 \cdot 24H_2O$ (6)

Reaction of $\mathbf{L^1}$–$\mathbf{L^3}$ with $CuSO_4 \cdot 5H_2O$ in a MeOH/H_2O/MeCN mixture (v/v 2:1:2) gave brown (**6**) and green complexes (**4**, **5**) of uniform composition $[Cu\mathbf{L}(SO_4)]_6 \cdot 24H_2O$ in almost quantitative yields. In each case single crystals suitable for X-ray crystallography were obtained by slow diffusion of diethyl ether into the corresponding reaction mixture. All three complexes crystallize isostructurally with one independent $[CuL(SO_4)]$ fragment in the asymmetric unit yielding essentially superimposable hexanuclear circular helical arrangements (Figure 35a, c) *via* the symmetry operations of space group $R\bar{3}$. The six Cu(II) ions alternately have *Λ*- and *Δ*-configurations leading to overall centrosymmetric *meso*-helicates. Two of the six Cu(II) centres are twisted out of plane allowing a chair-like conformation of the complexes (Figure 35b). The distances of adjacent Cu(II) ions in **4**, **5** and **6** are 12.49, 12.46, and 12.58 Å, respectively, all three being significantly longer than the corresponding distance (11.38 Å) in the triple-helicate species derived from $\mathbf{L^1}$[85]. In the title complexes each Cu(II) has a severely distorted octahedral coordination environment involving interactions with two bidentate pyridylimine strands of different ligands and one bidentate sulfate ion (Figure 35d, e). This binding pattern leads to a neutral hexanuclear complex with three anions located at the top and three at the bottom of the molecule. Selected bond lengths and angles for these complexes are given in Tables 10 and 11. The coordinating sulfate anions clearly play a major role in formation of the hexanuclear *meso*-helicates; on changing the anion from SO_4^{2-} to ClO_4^- or NO_3^- only the cationic, non-cyclic triple helicate $[Cu_2(\mathbf{L^2})_3]^{4+}$ was formed under the same conditions.

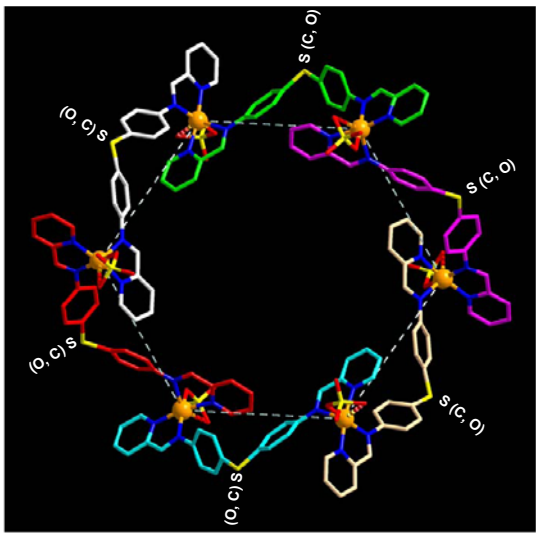

a)

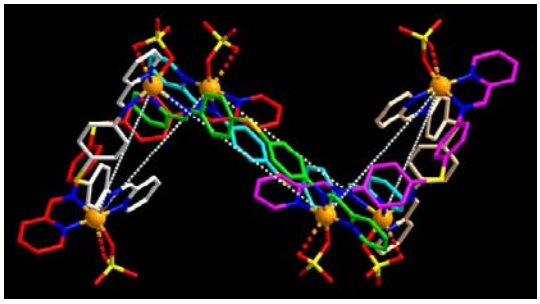

b)

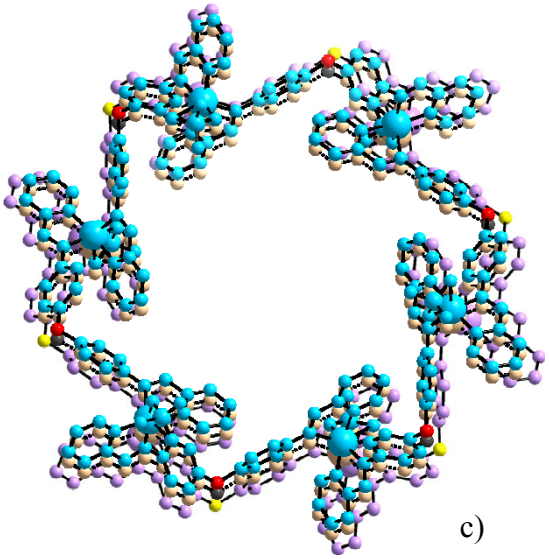

c)

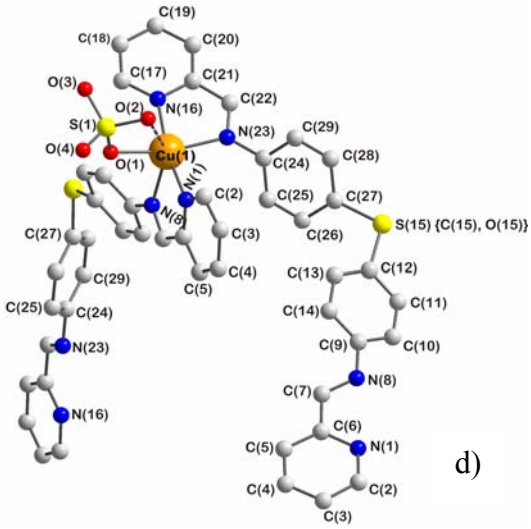

d)

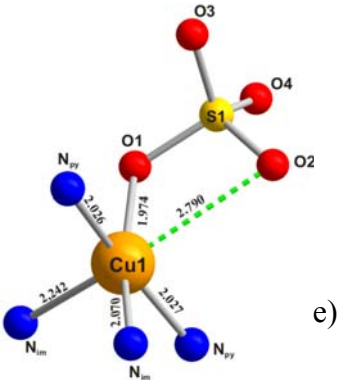

e)

Figure 35. Molecular structure of the circular *meso*-helicates [Cu**L**$(SO_4)]_6$ showing the hexagonal arrangement (a), the chair-like conformation (b), the overlay of the three structures (c) and the binding mode [d and e(in **6**)] of a single Cu(II) ion. The ligands are shown in different colours in (a) and (b); Cu in orange, N in blue, O in red, S in yellow. Helicates are represented in different colours in c) (**4** in light brown, **5** in blue and **6** in violet). H atoms are omitted for clarity.

Table 10. Selected Bond lengths (Å) and angles (°) of the circular *meso*-helicates **4**, **5** and **6**.

atoms	$[Cu\mathbf{L}^{1}(SO_4)]_6 \cdot 24H_2O$ (**4**)	$[Cu\mathbf{L}^{2}(SO_4)]_6 \cdot 24H_2O$ (**5**)	$[Cu\mathbf{L}^{3}(SO_4)]_6 \cdot 24H_2O$ (**6**)
Cu – N1	2.020(3)	2.022(2)	2.027(3)
Cu – N16	2.018(3)	2.017(2)	2.026(3)
Cu – N8	2.246(2)	2.261(2)	2.242(4)
Cu – N23	2.045(2)	2.051(2)	2.070(3)
Cu – O1	1.959(2)	1.963 (2)	1.974(3)
Cu – O2	2.770(2)	2.792(2)	2.790(3)
O1 – Cu – N1	93.91(11)	93.01(7)	93.81(12)
O1 – Cu – N16	92.65(10)	92.83(8)	93.19(12)
O1 – Cu – N8	93.36 (9)	93.27 (8)	90.55(12)
O1 – Cu – N23	163.34(9)	164.14(8)	165.41(13)
N1 – Cu – N16	170.64(10)	171.05(10)	169.63(15)
N1 – Cu – N23	91.96(10)	92.65(8)	91.51(12)
N16 – Cu – N23	79.94(10)	79.99(8)	79.92(12)
N1 – Cu – N8	77.90(11)	77.94(8)	77.71(12)
N8 – Cu – N23	103.12(9)	102.39(8)	103.85(12)
N8 – Cu – N16	108.37(11)	108.49(8)	109.86(13)
O2 – Cu – N1	82.67(8)	81.46(8)	82.56(8)
O2 – Cu – N16	95.21(10)	95.99(10)	94.80(8)
O2 – Cu – N8	144.06(10)	143.20(10)	141.17(8)
O2 – Cu – N23	107.52(10)	108.75(10)	109.82(8)

Table 11. C–H···*A* interactions in **4**, **5** and **6**.

C – H	*A*	H···*A* [Å]	C···*A* [Å]	C–H···*A* [°]
$[Cu\mathbf{L}^{3}(SO_4)]_6 \cdot 24H_2O$ (**6**)				
C2 – H2	O2	2.542(3)	3.143(5)	121
C4 – H4	O3^{i}	2.577(3)	3.468(5)	156
C7 – H7	O3^{ii}	2.430(3)	3.276(5)	148
C25 – H25	O4^{ii}	2.581(3)	3.250(5)	128
C22 – H22	O4^{iii}	2.242(4)	3.164(6)	164
$[Cu\mathbf{L}^{1}(SO_4)]_6 \cdot 24H_2O$ (**4**)				
C17 – H17A	O2	2.487(3)	3.101(4)	122
C18 – H18A	O2^{iv}	2.527(3)	3.192(5)	127
C7 – H7A	O3^{v}	2.208(3)	3.118(4)	160
C19 – H19A	O4 ^{iv}	2.462(4)	3.353(5)	156
C22 – H22A	O4^{vi}	2.411(2)	3.272(4)	151
C15 – H15A	*Cg*4^{vii}	3.165	4.038	148
C15 – H15A	*Cg*7^{vii}	3.312	3.637	101
C15 – H15B	*Cg*7^{vii}	3.188	3.637	109
$[Cu\mathbf{L}^{2}(SO_4)]_6 \cdot 24H_2O$ (**5**)				
C17 – H17	O1	2.599(2)	3.088(3)	112
C2 – H2	O2	2.465(2)	3.072(3)	122
C3 – H3	O2^{i}	2.569(2)	3.213(3)	125
C4 – H4	O3^{i}	2.478(2)	3.390(3)	161
C7 – H7	O3^{viii}	2.452(2)	3.301(3)	149
C22 – H22	O4^{iii}	2.193(2)	3.097(3)	158
C28 – H28	Cg6^{ix}	3.112	3.600	114

Symmetry codes: (i) = 2/3+x-y,1/3+x,1/3-z; (ii) = 4/3-y,2/3+x-y,-1/3+z; (iii) = -1/3+y,1/3-x+y,1/3-z; (iv) = 1+y,1-x+y,-z; (v) = x-y,-1+x,-z; (vi) = 5/3-x+y,4/3-x,1/3+z; (vii) = 5/3-x,1/3-y,1/3-z; (viii) = 4/3-y,2/3+x-y,-1/3+z; (ix) = 1-x,1-y,-z

As expected, the characteristic bond lengths of the complexes vary with the donor atom type and position, and are in agreement with data for structurally related systems: Cu-$N_{pyridyl}$ (2.02 – 2.03 Å), Cu–N_{imine} (2.05 – 2.26 Å) and Cu–$O_{sulfate}$ (1.97; 2.79 Å). Bond lengths are shorter in the equatorial (2×$N_{pyridyl}$, 1×N_{imine}, 1×$O_{sulfate}$) than in the axial positions (1×N_{imine}, 1×$O_{sulfate}$) reflecting the presence of Jahn-Teller distortions. In particular, the axial Cu–$O_{sulfate}$ bonds (2.77 – 2.79 Å) are very weak; each of these oxygen atoms forms one weak hydrogen bond CH···$O_{sulfate}$ (2.47 – 2.54 Å) to a neighbouring pyridyl unit. In addition, the *meso*-helicates incorporate six weak π–π interactions (*Cg2*···*Cg3*: 3.90 – 3.94 Å) between pyridyl rings of one ligand and phenylene spacers of an adjacent ligand. The space-filling model of the *meso*-helicate structure (Figure 36) clearly illustrates the nanometre-scale dimensions of the complex assembly: d_{cavity} ≈ 2.2 nm, width ≈ 2.5 nm and height ≈ 1.7 nm.

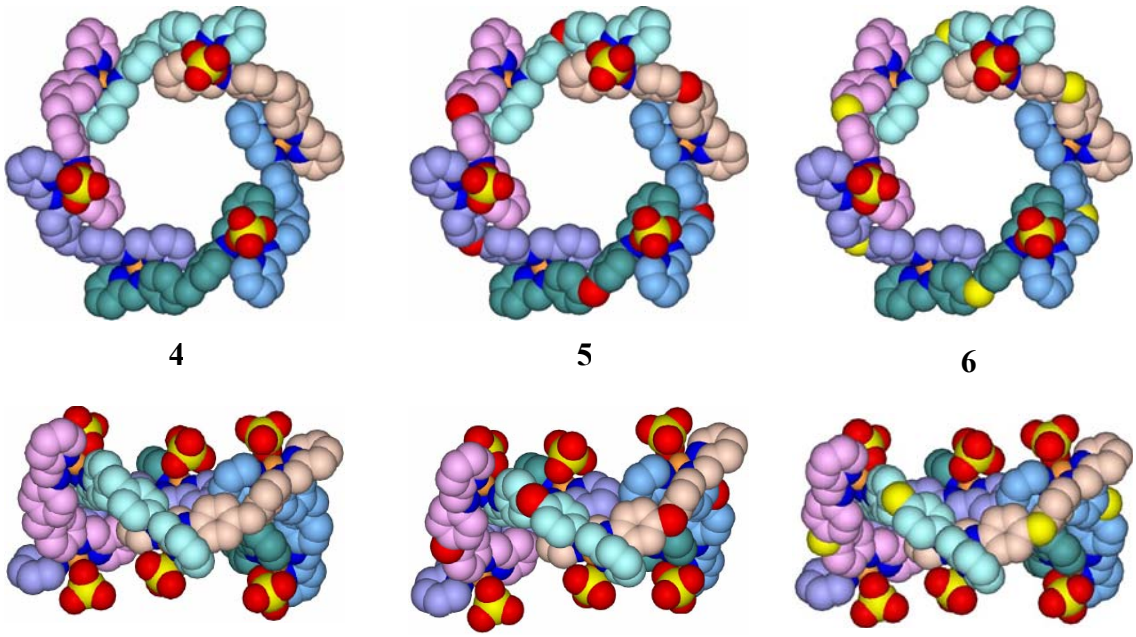

Figure 36. Space-filling representation of the molecular structure of [Cu**L**$(SO_4)]_6$: Top: top view; Bottom: side view. The six ligands are shown in different colours in every helicate; Cu in orange, N in blue, O in red, S in yellow. H atoms are omitted for clarity.

The crystal packing is characterized by a dense supramolecular assembly of puckered hexameric *meso*-helicates with an ABC stacking sequence reflecting the motif of a cubic close packing (Figure 37). Each sulfate ion is surrounded by hydrogen-bonded disordered H_2O molecules which are mainly arranged in two slightly distorted cubic clusters. One of these clusters is linked *via* additional H_2O molecules to SO_4^{2-} by OH···O hydrogen bonds forming a 3D network. If O···O distances up to 3 Å are considered, each SO_4^{2-} is bound to 4 (**4**, **6**) or 5 H_2O (**5**) molecules. The second cluster is loosely hydrogen bonded to the ligands without connection to SO_4^{2-}. Altogether each complex molecule is linked with six neighbouring molecules in the assembly by 24 moderate (2.19 – 2.24 Å) and weak (2.41 – 2.60 Å) CH···O hydrogen bonds involving the sulfate oxygen atoms. Furthermore 12 relatively strong π-π stacking interactions (*Cg1*···*Cg2*: 3.61 – 3.64 Å) between pyridyl rings of neighbouring molecules stabilize the arrangement (Figure 38). The geometrical details of the π-π interactions are listed in Table 12.

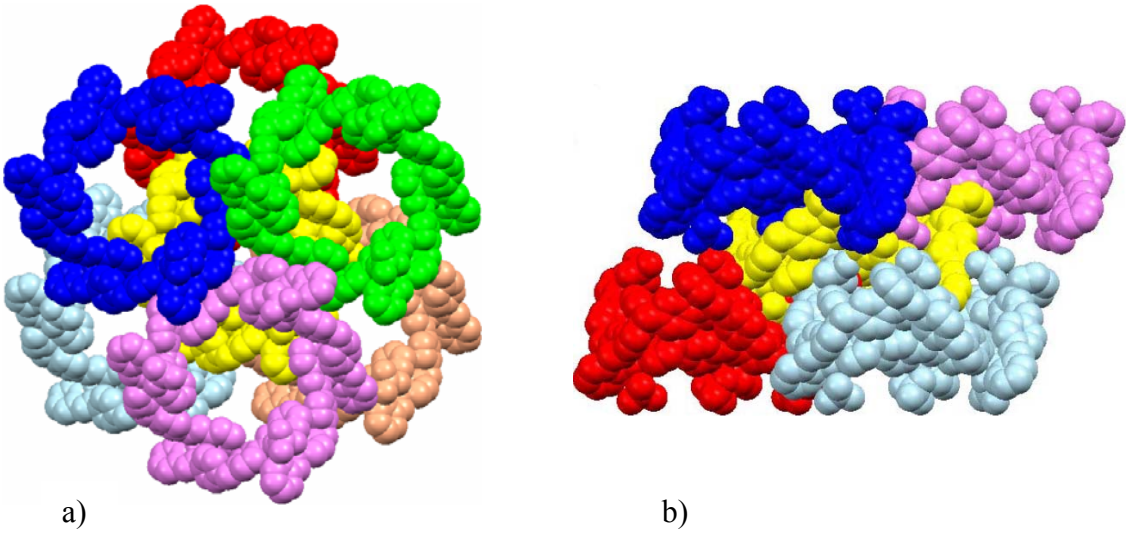

Figure 37. Dense 3D packing of the *meso*-helicates $[Cu\mathbf{L}^2(SO_4)]_6$ driven by hydrogen bonding and π-π stacking: a) top view; b) side view. Each helicate is shown in a different colour. H atoms are omitted for clarity.

Table 12. π–π interactions in **4**, **5** and **6**.

Cg	*Cg*	*Cg*···*Cg* [Å]	*β* [°]	*CgI*···perp [Å]
$[CuL^3(SO_4)]_6 \cdot 24H_2O$ (**6**)				
*Cg*4	*Cg*5^{i}	3.640	25	0.52
*Cg*4	*Cg*7	3.940	18	3.05
$[CuL^1(SO_4)]_6 \cdot 24H_2O$ (**4**)				
*Cg*4	*Cg*5^{ii}	3.613	24	6.64
*Cg*5	*Cg*6	3.899	18	3.16
$[CuL^2(SO_4)]_6 \cdot 24H_2O$ (**5**)				
*Cg*4	*Cg*5^{i}	3.630	25	0.32
*Cg*4	*Cg*7	3.926	19	3.09

Symmetry codes: (i) = 2/3+x-y,1/3+x,1/3-z; (ii) = x-y,-1+x,-z

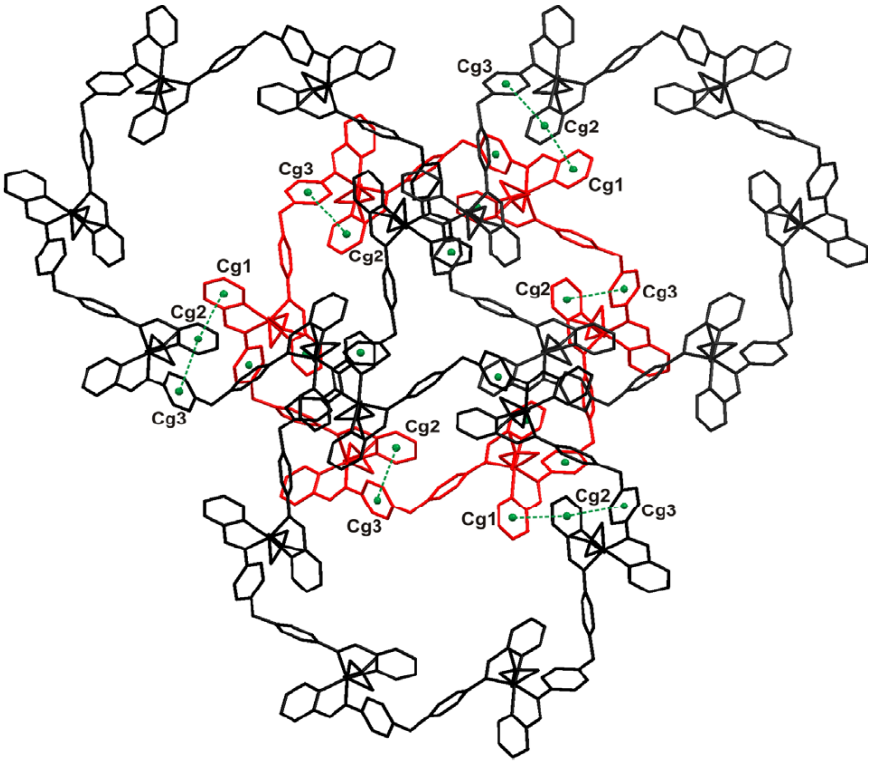

Figure 38. Representation of a part of the self-assembly of $[CuL^1(SO_4)]_6$ showing the π–π stacking interactions. H atoms are omitted for clarity.

2.2.2.2 Complex $[Cu_6(L^2)_3(L^3)_3(SO_4)_6] \cdot 24H_2O$ (7)

Compound (**7**) was prepared similarly as that of **4–6** but using in this case the ligand mixture $\mathbf{L^2}$ and $\mathbf{L^3}$ (in a 1:1 ratio) to react with $CuSO_4 \cdot 5H_2O$ in a MeOH/H_2O/MeCN mixture (v/v 2:1:2). The green–brown crystalline product of (**7**) grows uppon slow diffusion of diethyl ether into the corresponding reaction mixture and the microanalytical data of the complex were consistent with the formulation $[Cu_6(\mathbf{L^2})_3(\mathbf{L^3})_3(SO_4)_6] \cdot 18H_2O$. This crystalline material proved to be suitable for X-ray crystallography and the structure revealed a hexanuclear circular helical arrangements (Figure 39a) almost similar to compounds **4–6** but alternating –O– and –S– bridge. The complexe crystallizes in the space group $R\bar{3}$ with one independent $[Cu(\mathbf{L^2})_{0.5}(\mathbf{L^3})_{0.5}(SO_4)]$ fragment in the asymmetric unit. The six Cu(II) ions alternately have *Λ*- and *Δ*-configurations leading to overall centrosymmetric *meso*-helicates. Two of the six Cu(II) centres are twisted out of plane allowing a chair-like conformation of the complexes (Figure 39b). The distances of adjacent Cu(II) ions are 12.46 Å, and significantly longer than the corresponding distance (11.38 Å) in the triple-helicate species derived from $\mathbf{L^1}$ [117].

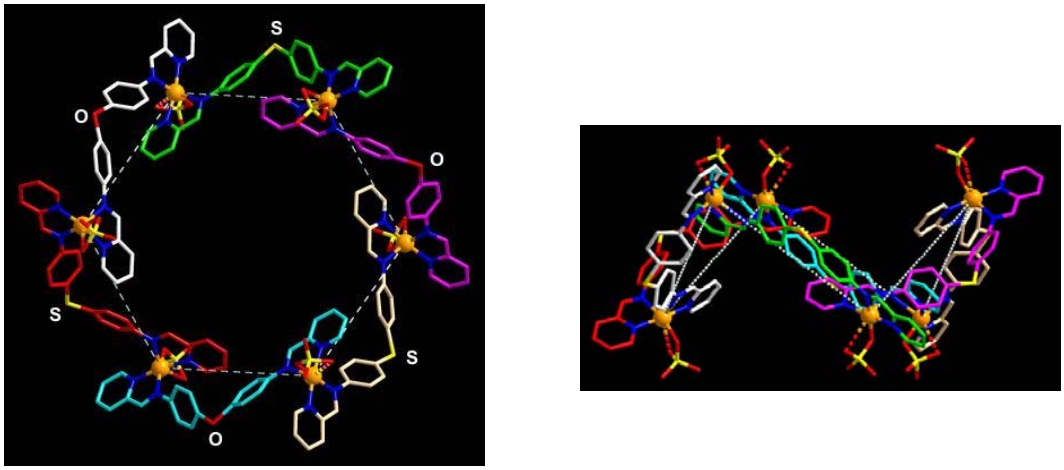

a) b)

Figure 39. Molecular structure of the circular *meso*-helicates $[Cu_6(\mathbf{L^2})_3(\mathbf{L^3})_3(SO_4)_6]$ showing the hexagonal arrangement (a) and the chair-like conformation (b) The ligands are shown in different colours and solvent molecules and H atoms are omitted for clarity.

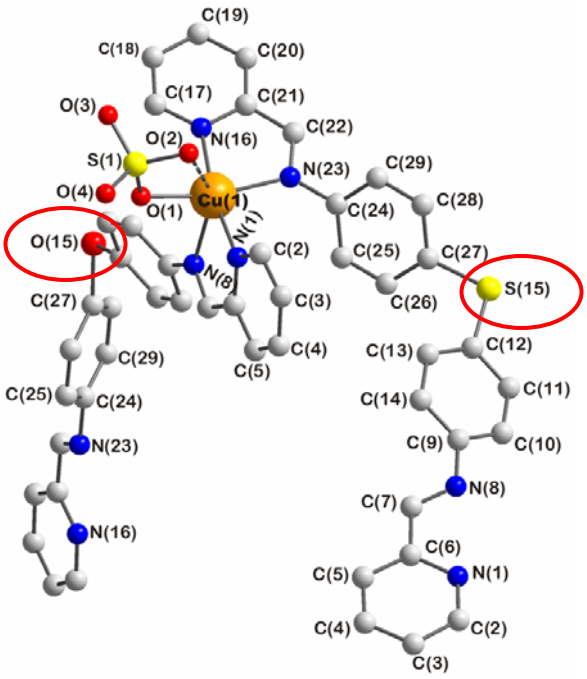

Figure 40. Fragment of molecular structure of the circular *meso*-helicates $[Cu_6(\mathbf{L}^2)_3(\mathbf{L}^3)_3(SO_4)_6]$ showing the binding mode of a single Cu(II) ion. Solvent molecules and H atoms are omitted for clarity.

In the title complexes each Cu(II) has a severely distorted octahedral coordination environment involving interactions with two bidentate pyridylimine strands of different ligands and one bidentate sulfate ion (Figure 40). This binding pattern leads to a neutral hexanuclear complex with three anions located at the top and three at the bottom of the molecule. As expected, the characteristic bond lengths (Table 13) of the complexes vary with the donor atom type and position, and are in agreement with data for structurally related systems: $Cu–N_{pyridyl}$ (2.02 – 2.03 Å), $Cu–N_{imine}$ (2.06 – 2.26 Å) and $Cu–O_{sulfate}$ (1.97; 2.77 Å). Bond lengths are shorter in the equatorial ($2\times N_{pyridyl}$, $1\times N_{imine}$, $1\times O_{sulfate}$) than in the axial positions ($1\times N_{imine}$, $1\times O_{sulfate}$) reflecting the presence of Jahn-Teller distortions. In particular, the axial $Cu–O_{sulfate}$ bonds (2.77 Å) are very weak; each of these oxygen atoms forms one weak hydrogen bond $CH\cdots O_{sulfate}$ (2.48 Å) to a neighbouring pyridyl unit. In addition, the *meso*-helicates incorporate six weak π–π interactions (*centroid*···*centroid*: 3.92 Å) between pyridyl rings of one ligand and phenylene spacers

of an adjacent ligand. The space-filling model of the *meso*-helicate structure is similar to that shown in Figure 36.

The crystal packing is characterized by a dense supramolecular assembly of puckered hexameric *meso*-helicates with an ABC stacking sequence reflecting the motif of a cubic close packing (Figure 37). Each sulfate ion is surrounded by hydrogen-bonded disordered H_2O molecules which are mainly arranged in two slightly distorted cubic clusters. One of these clusters is linked *via* additional H_2O molecules to SO_4^{2-} by OH···O hydrogen bonds forming a 3D network. If O···O distances up to 3 Å are considered, each SO_4^{2-} is bound to 4 H_2O molecules. The second cluster is loosely hydrogen bonded to the ligands without connection to SO_4^{2-}. Altogether each complex molecule is linked with six neighbouring molecules in the assembly by 24 moderate (2.20 Å) and weak (2.48 – 2.60 Å) CH···O hydrogen bonds involving the sulfate oxygen atoms. Furthermore 12 relatively strong π-π stacking interactions (*centroid···centroid*: 3.66 Å) between pyridyl rings of neighbouring molecules stabilize the arrangement (Figure 38). Weak interactions data are summarized in Table 14 and 15.

Table 13. Selected Bond lengths (Å) and angles (°) for **7**.

Cu – N1	2.030(3)	Cu – N23	2.059(4)
Cu – N16	2.023(3)	Cu – O1	1.965(3)
Cu – N8	2.255(4)	Cu – O2	2.766(3)
O1 – Cu – N1	93.16(13)	N1 – Cu – N8	77.66(14)
O1 – Cu – N16	93.09(13)	N8 – Cu – N23	102.40(13)
O1 – Cu – N8	92.20(13)	N8 – Cu – N16	109.45(15)
O1 – Cu – N23	165.21(14)	O2 – Cu – N1	81.59(12)
N1 – Cu – N16	170.33(17)	O2 – Cu – N16	95.48(12)
N1 – Cu – N23	92.28(14)	O2 – Cu – N8	142.72(12)
N16 – Cu – N23	79.93(14)	O2 – Cu – N23	109.09(13)

Table 14. C–H···*A* interactions in **7**.

C– H	*A*	H···*A* [Å]	C···*A* [Å]	C–H···*A* [°]
C2 – H2	O2	2.48	3.075(5)	121
C3 – H3	O2^{i}	2.60	3.203 (6)	122
C4 – H4	O3^{i}	2.56	3.459(6)	158
C7 – H7	O3 ^{ii}	2.49	3.324(5)	146
C22 – H22	O4^{iii}	2.20	3.118(6)	163

Symmetry codes: (i) = 2/3+x-y,1/3+x,1/3-z; (ii) = 4/3-y,2/3+x-y,-1/3+z; (iii) = -1/3+y,1/3-x+y,1/3-z

Table 15. π–π interactions in **7**.

Cg	*Cg*	*Cg*···*Cg* [Å]	*β* [°]	*CgI*···perp [Å]
*Cg*4	*Cg*5^{i}	3.66	25	0.36
*Cg*4	*Cg*7	3.92	19	3.09

Symmetry codes: (i) = 2/3+x-y,1/3+x,1/3-z

2.2.2.3 Thermal analysis of 4, 5 and 6

Thermal properties of compounds **4**-**6** were investigated by DTA/TG methods in a static air atmosphere with heating and cooling rates of 5 °C·min^{-1} (NETZSCH STA 409) (Figure 41–43). Thermogravimetric (TG) curves of **4** and **5** show three steps weight loss while that of **6** shows two steps weight loss under the chosen experimental conditions. In the temperature between 50 and 200 °C the samples weight decrease by 8.9, 8.86 and 9 % in **4**, **5**, and **6** respectively, corresponding to the loss of water molecules. These mass losses are close to the calculated ones {8.88 % (18 moles of water), 8.85 % (18 moles of water) and 9.2 % (19 moles of water)} assuming the chemical formula deduced from elemental analysis. The last steps of weight loss (67.2-79.6 %) occurring in the range 200–500 °C, may correspond to the complete destruction of the network as shown the endothermic peaks in DTA curves at around 450°C.

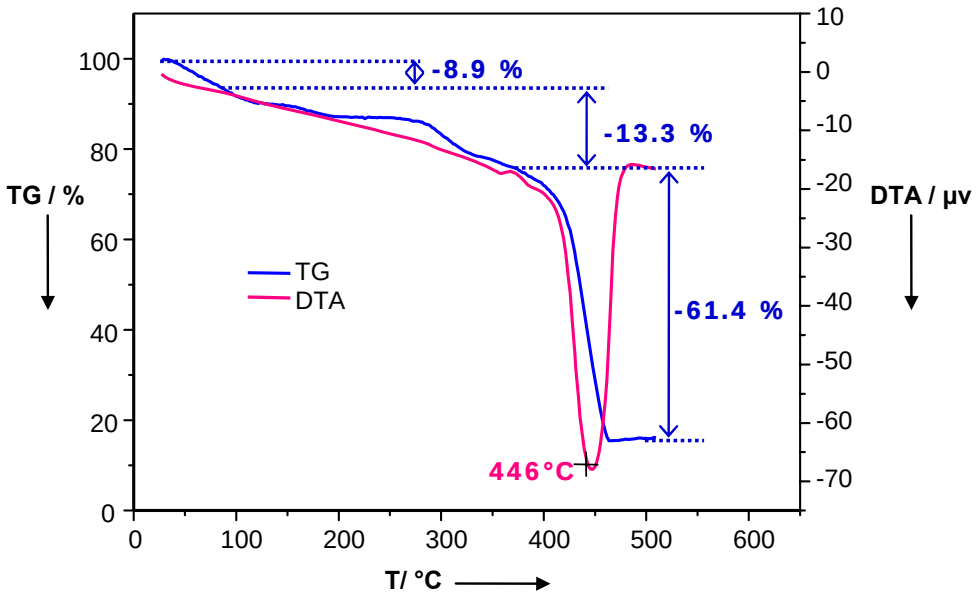

Figure 41. Thermogravimetric measurements (static air, heating rate: 5 °C·min^{-1}) of $[Cu\mathbf{L}^{1}(SO_4)]_6 \cdot 24H_2O$ (**4**) show a weight loss of 8.9 % in the temperature range between 30 and 110 °C (calc.: 8.88 %) corresponding with the loss of 18 moles of H_2O.

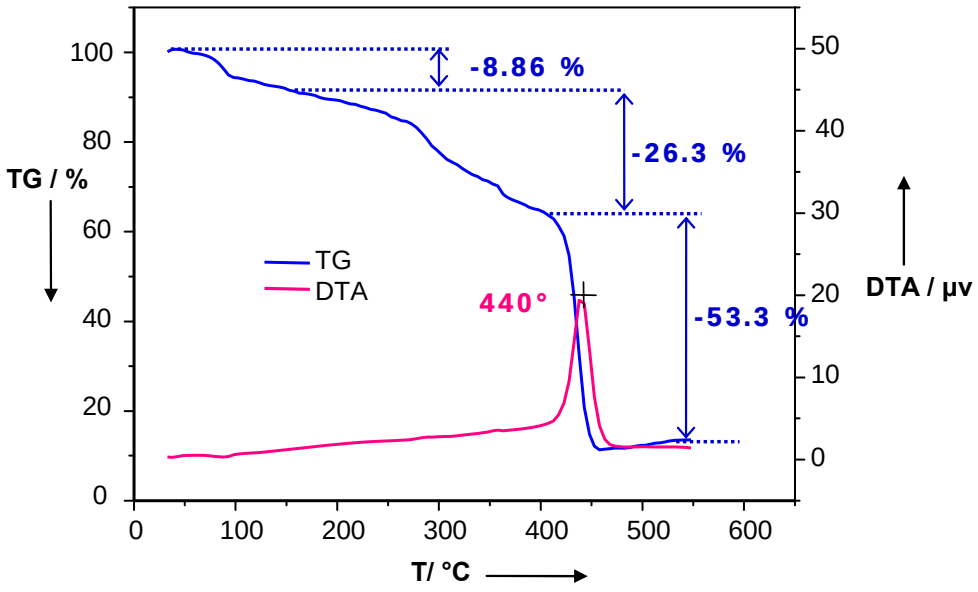

Figure 42. Thermogravimetric measurements (static air, heating rate: 5 °C·min^{-1}) of $[Cu\mathbf{L}^{2}(SO_4)]_6 \cdot 24H_2O$ (**5**) show a weight loss of 8.86 % in the temperature range between 30 and 150 °C (calc.: 8.85 %) corresponding with the loss of 18 moles of H_2O.

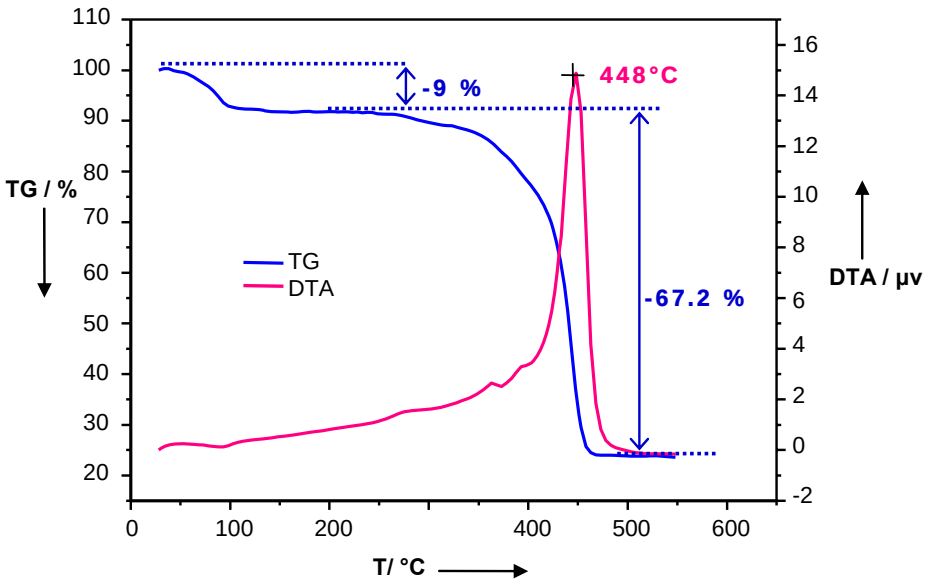

Figure 43. Thermogravimetric measurements (static air, heating rate: 5 °C·min^{-1}) of [Cu**L**^{3}(SO$_4$)]$_6$ · 24H$_2$O (**6**) show a weight loss of 9 % in the temperature range between 30 and 150 °C (calc.: 9.2 %) corresponding with the loss of 19 moles of H$_2$O.

2.2.2.4 Magnetic properties of complex Complex [Cu**L**^{1}(SO$_4$)]$_6$ · 24H$_2$O (4)

The static magnetic susceptibility χ of [Cu(L)SO$_4$]$_6$·nH$_2$O complex has been studied at temperatures T = 2 – 350 K in a magnetic field B = 5 T. The plot of the T-dependence of the inverse susceptibility $\chi^{-1}(T)$ is shown in Figure 44. Almost in the whole temperature range χ^{-1} is linear in T following thus perfectly the Curie-Weiss law $\chi = C/(T+\theta)$. Here C is the Curie constant and θ is the Curie-Weiss temperature. The fit yields C = 2.72 emuK/mole and a small positive value of θ < 0.4 indicating a rather weak antiferromagnetic interaction between the Cu ions. The magnitude of the effective magnetic moment p_{eff} related to $C \sim \chi T$ as $p_{eff} = (3Ck_B/N_A)^{1/2}$ is plotted in the left inset of Figure 44 as a function of temperature. Here k_B is the Boltzmann constant, N_A is the Avogadro number and μ_B is the Bohr magneton. p_{eff} reveals an almost T-independent value (characteristic for paramagnetism) of 1.86 μ_B at T >10 K and decrease of the magnitude at low temperatures which is related to antiferromagnetic interaction between the Cu ions.

The ESR measurements have been performed at a frequency of 9.5 GHz at room temperature. Obtained ESR spectrum plotted in the right inset of Figure 44 shows a single ESR line with an isotropic *g*-factor of 2.13. The magnitude of the effective magnetic moment is related to the *g*-factor as $p_{\text{eff}} = g[S(S+1)]^{1/2}\ \mu_B$, where *S* is the spin of the Cu(II) ion ($3d^9$) equal to 1/2. Thus from the above value of *g*-factor one obtains $p_{\text{eff}} = 1.84\ \mu_B$ which is indeed very close to the estimate from the static susceptibility data.

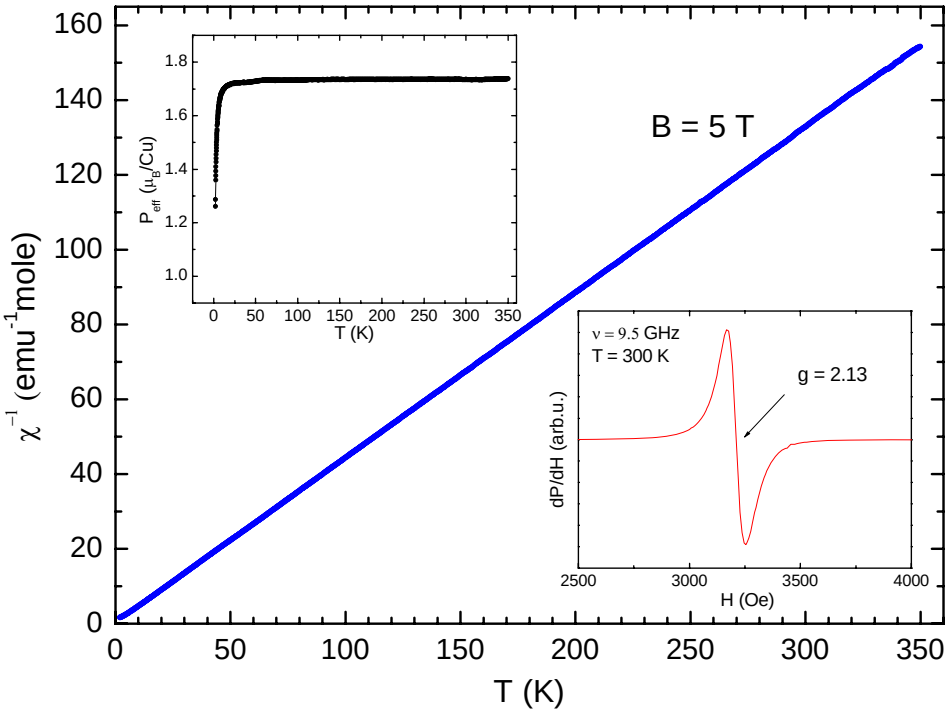

Figure 44. Temperature dependence of the inverse static magnetic susceptibility χ^{-1} of complex $[Cu(L)SO_4]_6 \cdot nH_2O$. A small temperature independent contribution χ_0 arising due to diamagnetism, Van-Vleck paramagnetism and instrumental effects has been subtracted from the raw data. Left inset shows the effective magnetic moment calculated from the χ data (see the text). Right inset – ESR spectrum (field derivative of the absorbed power d*P*(*H*)/d*H*) of a powder sample at room temperature.

2.2.2.5 Laser fluorecence spectroscopy studies of complex formation of Cu(II) with ligands L^1 and L^2

The fluorescence properties of the ligands $\mathbf{L^1}$ and $\mathbf{L^2}$ are summarized in Table 16. The time-resolved fluorescence spectrum of $\mathbf{L^2}$ is shown in Figure 45 as an example.

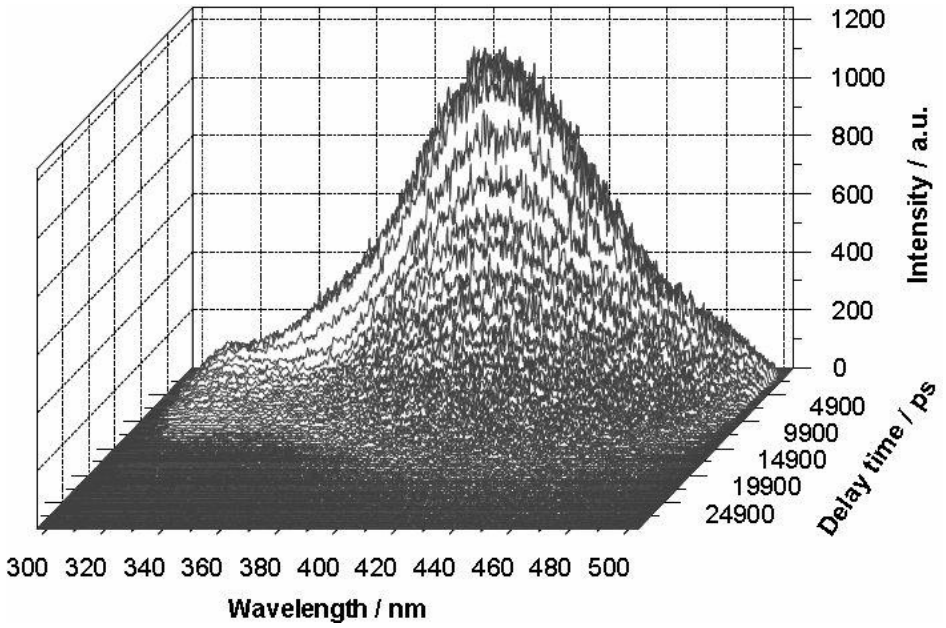

Figure 45. Time-resolved fluorescence spectrum of ligand $\mathbf{L^2}$, $[\mathbf{L^2}] = 1x10^{-5}$ M in CH_3OH.

Table 16. Fluorescence properties of $\mathbf{L^1}$ and $\mathbf{L^2}$.

Ligand	Center of gravity (1) nm	Decay time (1) ps	Center of gravity (2) nm	Decay time (2) ps	Intensity ratio (1)/(2)
$\mathbf{L^1}$	348.5	2010 ± 7	334.7	12795 ± 610	14.2
$\mathbf{L^2}$	403.8	2800 ± 20	410.3	10415 ± 420	10.1

For these two ligands a two-exponential fluorescence decay behaviour was observed in the absence of Cu(II). The component with the shorter fluorescence decay time shows the

higher fluorescence intensity. The maxima of this fluorescence emission are located at ca. 350 and 404 nm for $\mathbf{L^1}$ and $\mathbf{L^2}$, respectively. The fluorescence maxima for the second emitting component were found at ca. 335 and 410 nm for $\mathbf{L^1}$ and $\mathbf{L^2}$, respectively. Addition of copper(II) to the solution of the ligands leads to a slight decrease in fluorescence intensity (static fluorescence quenching) and influences strongly the fluorescence lifetime (Table 17). The formed complexes show also fluorescence properties.

Table 17. Fluorescence lifetimes of the ligands $\mathbf{L^1}$ and $\mathbf{L^2}$ as function of the added Cu(II) concentration (total concentration of ligand $1 \cdot 10^{-5}$ M).

[Cu(II)] / M	$\mathbf{L^1}$		$\mathbf{L^2}$	
0	12795	2010	10415	2800
1.00E–6	11602	1994	10873	2867
2.00E–6	12191	2052	8387	2867
3.00E–6	11921	1976	16922	3162
5.00E–6	10112	1964	8784	2694
1.00E–5	13997	2019	4827	3315
2.00E–5	12109	2023	7018	2020
5.00E–5	5827	1884	4072	395

The fluorescence with the shorter fluorescence lifetime was mainly influenced by the formation of the complexes (see Table 18). At Cu^{II}/ligand ratios of 1:2 the fluorescence of the 335 and 410 nm component disappears. This behaviour is in agreement with the ESI-MS results where 1:2 complexe compositions were the most abundant in solution.

Table 18. Emission maxima for $\mathbf{L^1}$ and $\mathbf{L^2}$ with increasing Cu(II) concentration (total concentration of ligand $1 \cdot 10^{-5}$ M).

[Cu(II)] / M	$\mathbf{L^1}$	$\mathbf{L^2}$
0	334.7	403.8
1.00E–6	336.1	399.7
2.00E–6	330.4	401.2
3.00E–6	325.2	390.6
5.00E–6	320.3	332.4
1.00E–5	325.5	345.1
2.00E–5	315.2	320.5
5.00E–5	310.6	315.2

In addition the fluorescence intensities were used to confirm complex formation. Due to the observation that mainly the fluorescence intensity of the component with the shorter fluorescence lifetime is influenced by the complex formation these data were evaluated for the stability of the complexes. The species concentration can be calculated from the fluorescence intensities of the free ligand. The resulting stability constants are summarized in Table 19.

Table 19. Stability constants of the formed Cu(II) complexes.

Ligand	**Stoichiometry (L:Cu)**	**log *K***	**Solvent**
$\mathbf{L^1}$	2:1	10.43 ± 0.7	CH_3OH
$\mathbf{L^2}$	2:1	11.13 ± 0.4	CH_3OH

2.2.3 Hg(II) complexes

2.2.3.1 Complex $[Hg_2(L^2)_2(ClO_4)_3(H_2O)_2]\ ClO_4 \cdot CH_3CN$ (8)

Reaction of $\mathbf{L^2}$ with $Hg(ClO_4)_2 \cdot H_2O$ in a MeOH/MeCN mixture (v/v 1:1) gave, upon slow diffusion of diethylether, crystalline sample of (**8**) whose microanalyses were consistent with the formation of $[M_nL_n]$ (n = 1, 2,…) species. The IR spectrum of $\mathbf{L^2}$ displays a sharp peak characteristic of the C=N bond at 1625 cm^{-1}, which upon complexation of Hg(II) slightly shifts to higher frequency (*ca*. 1633 cm^{-1}), and is consistent with coordination to the imino nitrogen. ESI mass spectroscopy in CH_3OH/DMSO solution found predominant peaks centred at *m*/*z* 479 and 596, which are consistent with the presence in solution of $[Hg(L^2)_2]^{2+}$ and $[Hg(L^2)_2 + 3\ DMSO]^{2+}$ respectively and the existence of either an achiral molecular box, a dinuclear double helix or polymeric architecture. The atomic numbering scheme and atom connectivity for **8** is shown in Figure 46 and 47. The asymmetric unit of **8** contains two unique Hg ions, two ligands, four ClO_4^- anions, and disordered solvent that has been modelled as a mixture of CH_3CN and H_2O. A racemic mixture of both enantiomers is observed in the unit cell.

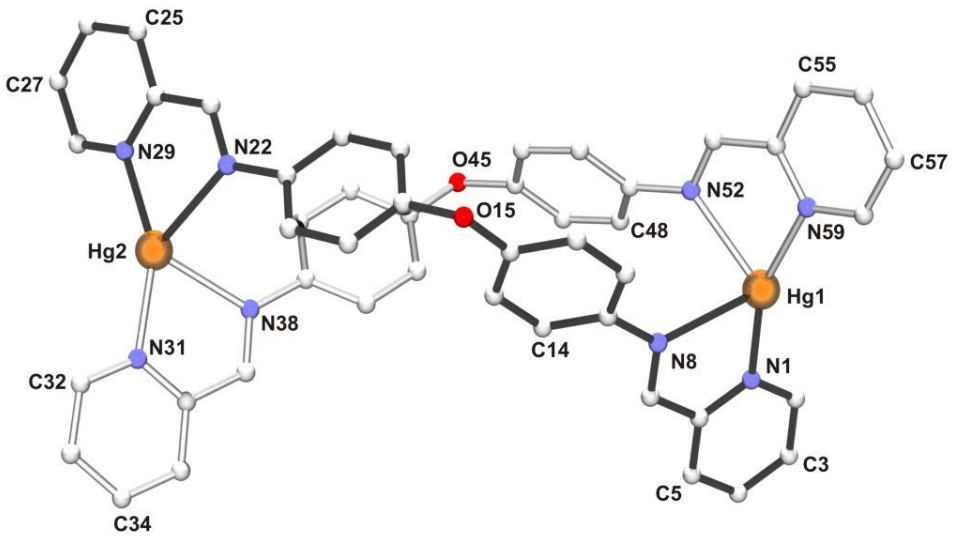

Figure 46. Molecular structure and atomic numbering scheme of **8**. H atoms, perchlorate anions and solvent molecules of crystallisation are removed for clarity.

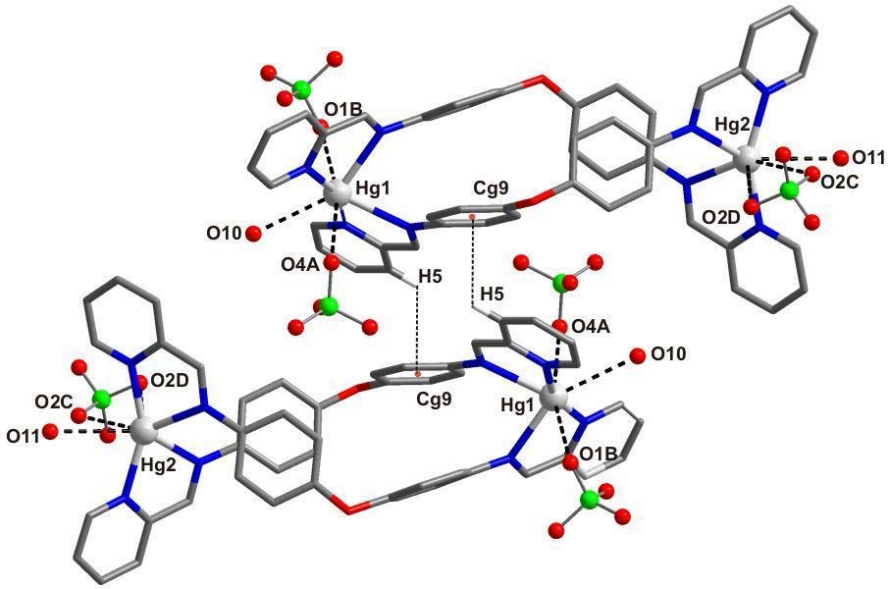

Figure 47. Molecular structure of **8** showing the interaction of the perchlorate anions and water molecules with the Hg(II) centres**.** H atoms and CH_3CN molecules are removed for clarity.

Table 20 Selected Bond lengths (Å) and angles (°) for **8**.

Hg1 – N1	2.162(4)	Hg2 – N22	2.452(5)
Hg1 – N8	2.457(4)	Hg2 – N29	2.193(5)
Hg1 – N52	2.453(4)	Hg2 – N31	2.190(5)
Hg1 – N59	2.182(4)	Hg2 – N38	2.394(5)
N1 – Hg1– N8	72.69(17)	N22 – Hg2 – N29	72.30(17)
N1 – Hg1– N52	124.83(17)	N22 – Hg2 – N31	131.54(17)
N1 – Hg1– N59	159.88(18)	N22 – Hg2 – N38	84.47(15)
N8 – Hg1– N52	80.49(15)	N29 – Hg2 – N31	153.55(18)
N8 – Hg1– N59	123.38(15)	N29 – Hg2 – N38	127.16(17)
N52 – Hg1– N59	73.00(16)	N31 – Hg2 – N38	73.02(17)

Both Hg(II) ions of the helicate have distorted tetrahedral coordination environments if only the chelating iminopyridyl subunits are considered. Bond lengths and angles are all in common ranges (Table 20); the Hg···Hg separation is 12.72 Å. The dihedral angles for

the two arms are 58.5° and 57.5° for Hg1 and Hg2, respectively. Dihedral angles of 0° and 90° would be expected for planar and pseudo-tetrahedral geometries, respectively. Each mercury(II) centre weakly interact with surrounded H_2O molecules and ClO_4^- anions. If Hg···O distances up to 3.1 Å are considered, Hg1 is bound to two ClO_4^- anions and one H_2O molecule while Hg2 is bound to one H_2O and one bidentate ClO_4^-. Considering these weak interactions, each Hg(II) centre will be connected to 7 donor atoms and therefore have a distorted pentagonal bipyramidal coordination geometry (Figure 47). The ligands wrap around the metal centres such that a helical structure is formed with a twist defined by the torsion angles Hg1–N8–N22–Hg2 and Hg1–N52–N38–Hg2 of 145.2° and 147.7°, respectively. The difference in torsion angle for the two binding ligands is probably a consequence of the different intra- and inter-molecular interactions experienced by each ligand. This also gives the helical structure a major and minor groove [86] as exemplified by the distance C5–C35 (11.00 Å) being *ca*. 3 Å shorter than C25–C55A (14.05 Å). The phenyl rings of the diarylether spacer are face-to-face π-stacked (Figure 48) with those on the adjacent ligand strand (distance centroid–centroid *ca* 4.10 Å). These interactions are probably a consequence of the constraints imposed upon the ligands on coordination to the mecury centres. Furthermore, it is also noteworthy that pyridyl and phenyl rings in the different ligand moieties are not co-planar with each other: angles between the mean planes are in the range 31.1°–40.8°. This ligand distortion probably derives from the steric constraints imposed by the geometry disposed Hg(II) centres. The helical complexes pack together through a combination of several intermolecular interactions leading to a 3D arrangement. Firstly, each double-stranded helicate uses four aromatic rings in the connection with other helicates, two from the spacer units and the other two from the pyridyl moieties. Overall, each helicate is connected with six other molecules, through six, face-to-face π···π (3.8–4.1 Å) interactions (Table 22), forming an unusually compact, ordered and stable molecular solid (Figure 48 and 49). Secondly, C–H···π (3.4 Å) interactions occur between the C5 pyridyl proton (H5) *via* a self-complementary C–H···π interaction with one of the phenyl rings from an adjacent molecule Figure 47.

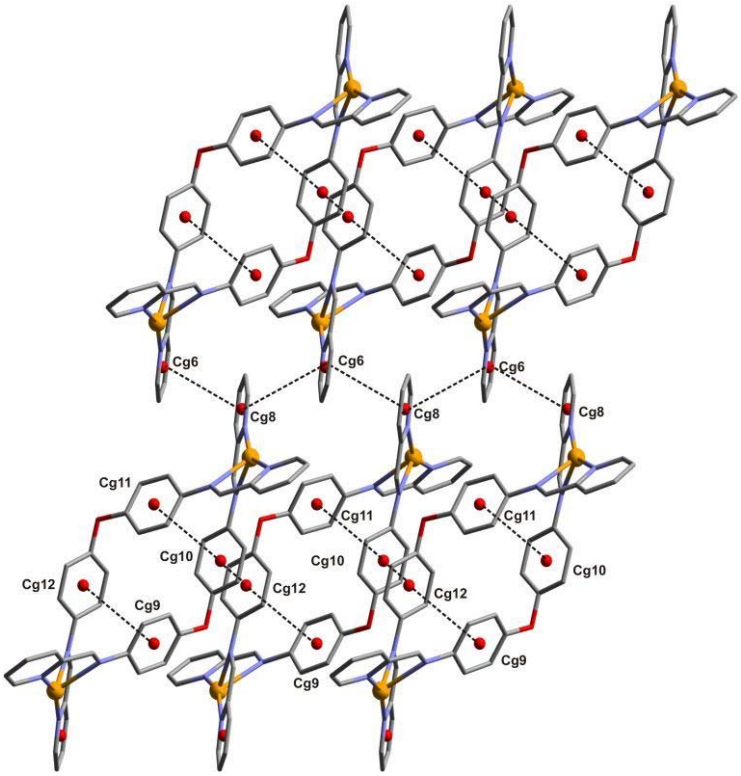

Figure 48. Crystal packing along the *b* axis showing the 3D arrangement of the helicates by π–π stacking interactions in **8**. H-atoms, perchlorate anions and solvent molecules are removed for clarity.

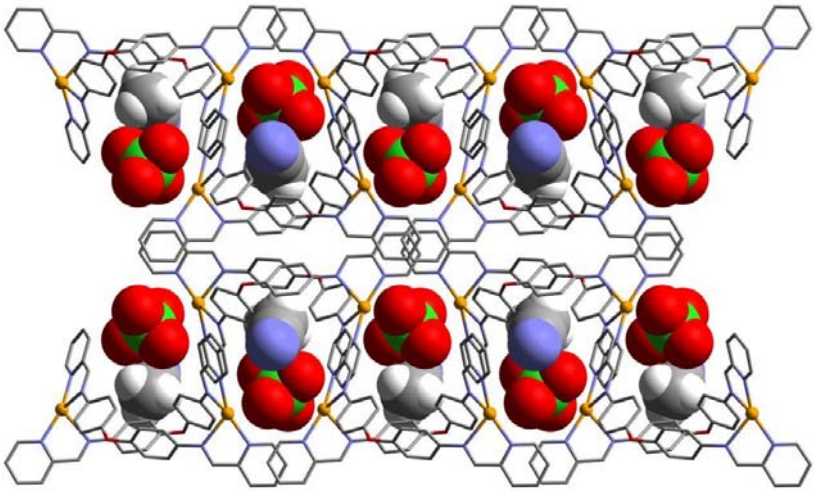

Figure 49. Crystal packing of **8** along the *c* axis showing the inclusion of non-metal bound ClO_4^- ions and CH_3CN molecules. H-atoms, metal-bound ClO_4^- ions and H_2O molecules are removed for clarity.

Thirdly, (C-H···O) hydrogen bond interactions (Figure 50) are observed between helicates and anions; the distances C···O are in the range 2.95-3.60 Å (Table 21). Altogether these interactions lead to a porous-like supramolecular network, in which the CH_3CN solvent molecules are located together with the non-metal bound anions (Figure 49). The distance between the two closest Hg(II) centres of stacked helicates is smaller (6.84– 9.96 Å) than the intramolecular Hg–Hg distance (12.72 Å).

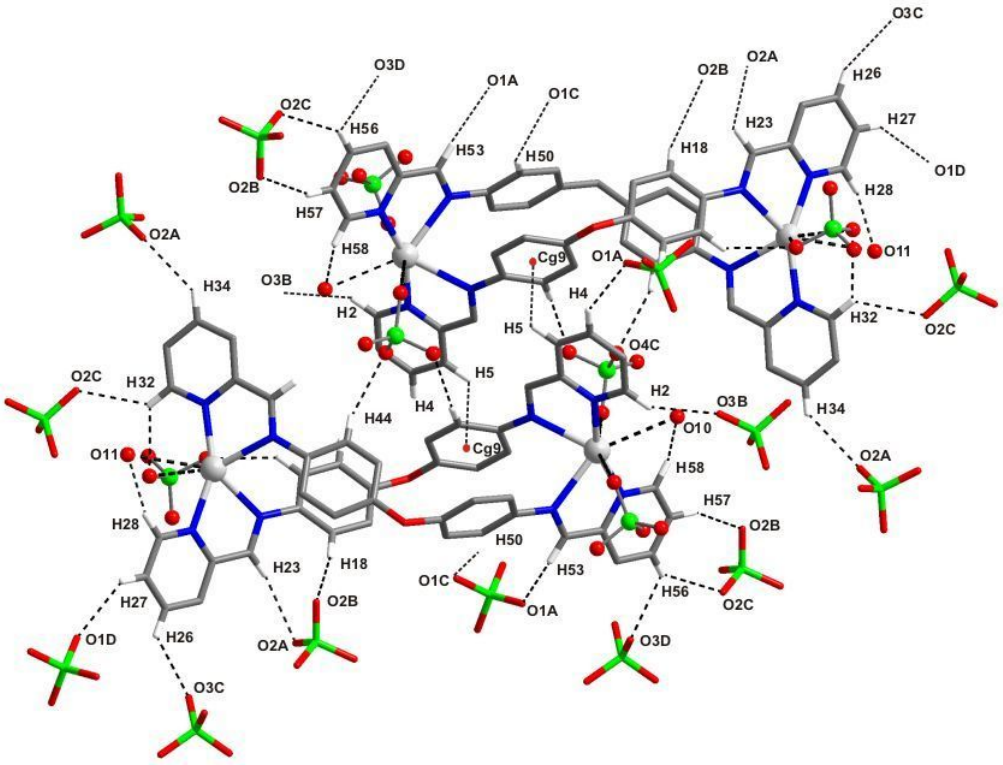

Figure 50. Stereo illustration showing hydrogen bond interactions in **8**.

Table 21. C–H···*A* interactions in **8**.

C – H	*A*	H···*A* [Å]	C···*A* [Å]	C–H···*A* [°]
C2 – H2	O3B^{i}	2.45	3.28	147
C4 – H4	O1A^{ii}	2.42	3.25	145
C14 – H14	O4D^{iii}	2.45	3.60	162
C18– H18	O2B^{iv}	2.52	3.44	162
C20 – H20	O2D^{v}	2.44	3.26	144
C23 – H23	O2A^{iv}	2.57	3.37	142
C23 – H23	O45^{vi}	2.56	3.29	134
C26 – H26	O3C^{iv}	2.50	3.15	126
C27 – H27	O1D^{vii}	2.42	3.11	129
C28 – H28	O11^{viii}	2.21	2.95	134
C32 – H32	O2C^{v}	2.53	3.25	133
C32 – H32	O3A^{v}	2.49	3.17	129
C34– H34	O2A^{ix}	2.55	3.35	142
C44 – H44	O4C^{iii}	2.55	3.46	161
C50 – H50	O1C^{v}	2.60	3.47	153
C53 – H53	O1A^{v}	2.49	3.27	140
C53 – H53	O11^{i}	2.45	3.13	128
C56– H56	O2C^{i}	2.44	3.24	141
C56 – H56	O3D^{i}	2.48	3.14	127
C57 – H57	O2B^{i}	2.57	3.43	151
C58– H58	O10^{x}	2.35	3.07	133
C5 – H5	*Cg*9^{iii}	2.89	3.41	116

Symmetry codes: (i) = x,1/2-y,1/2+z; (ii) = 1-x,-y,1-z; (iii) = 2-x,-y,-z; (iv) = 1+x,y,z; (v) = 1+x,1/2-y,-1/2+z; (vi) = x,1/2-y,-1/2+z; (vii) = 2+x,1/2-y,-1/2+z; (viii) = 2-x,1-y,-z; (ix) = 2-x,-1/2+y,-1/2-z; (x) = 1-x,-1/2+y,1/2-z

Table 22. π–π interactions in **8**.

Cg	*Cg*	*Cg*···*Cg* [Å]	*β* [°]	*CgI*···perp [Å]
*Cg*6	*Cg*8^{i}	3.839	21	3.58
*Cg*6	*Cg*8^{ii}	4.090	31	3.45
*Cg*9	*Cg*12^{iii}	4.076	22	3.45
*Cg*10	*Cg*11^{iii}	4.116	27	3.85
*Cg*10	*Cg*12^{iv}	3.807	22	3.49

Symmetry codes: (i) = 1+x,y,z; (ii) = 1+x,1/2-y,-1/2+z; (iii) = x,y,z; (iv) = x,1/2-y,-1/2+z

2.2.3.2 Complexes $[Hg_2(L^1)_2]$ $(ClO_4)_4$ (9) and $[Hg_2(L^3)_2]$ $(ClO_4)_4$ (10)

Compounds (**9**) and (**10**) were synthesized similarly as in the case of (**8**) by slow diffusion of diethylether in MeOH/MeCN (v/v 1:1) solution containing $\mathbf{L^1}$ or $\mathbf{L^3}$ and $Hg(ClO_4)_2 \cdot H_2O$. Microanalyses of the resultant crystalline products of (**9**) and (**10**) were consistent with the formation of $[M_nL_n]$ (n = 1, 2,…) species. The IR spectrum of $\mathbf{L^1}$ and $\mathbf{L^3}$ displays a sharp peak characteristic of the C=N bond at 1628 cm^{-1} and 1626 cm^{-1}, respectively, which shifts slightly to 1633 cm^{-1} upon complexation of Hg(II). This result is consistent with coordination of the imine nitrogen at the metal center. ESI mass spectroscopic measurements of CH_3OH/DMSO solutions of the complexes point to the presence of $[Hg\mathbf{L}_2]^{2+}$ ion in solution. Unfortunately single crystals of both samples provived for X-ray analyses had poor quality but a preliminary structural determination was possible (Figure 51). The data are in good agreement with the formation of $[Hg_2(\mathbf{L^1})_2]^{2+}$ (**9**) and $[Hg_2(\mathbf{L^3})_2]^{2+}$ (**10**) species having the typical double helicate structure of **8**. In both complexes each mercury(II) centre occupies a pseudo-tetrahedral environment based on two pyridylimine units from two different ligands.

a)

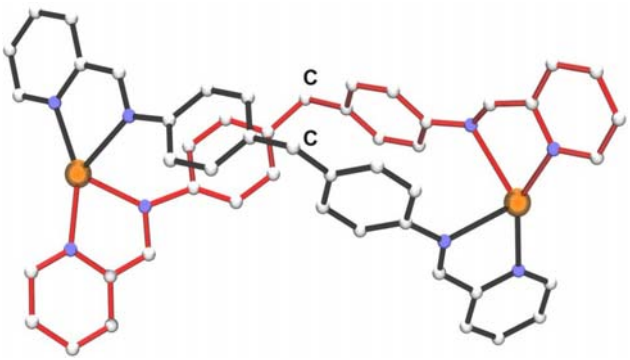

b)

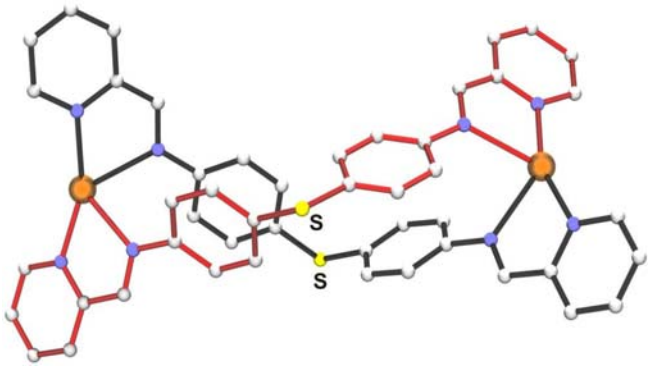

c)

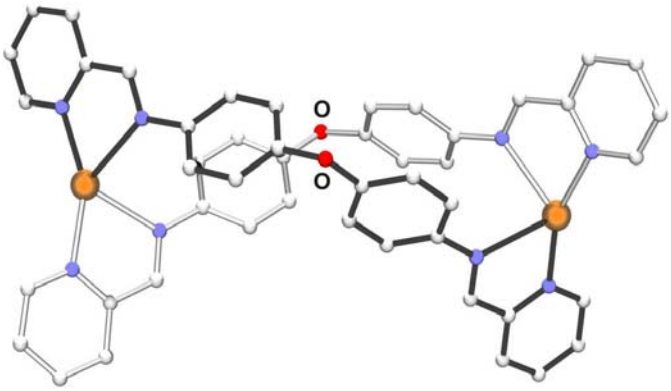

Figure 51. Comparison of the helicates formed between Hg(II) and the ligands $\mathbf{L^1}$-$\mathbf{L^3}$: a) $[Hg_2(\mathbf{L^1})_2]^{2+}$ (**9**), b) $[Hg_2(\mathbf{L^3})_2]^{2+}$ (**10**) and c) $[Hg_2(\mathbf{L^2})_2]^{2+}$ (**8**).

2.2.4 Mn(II), Fe(II) and Ni(II) complexes

2.2.4.1 Complex $[Mn_2(L^1)_3](ClO_4)_4$ (11)

Treatment of an acetonitrile solution of $\mathbf{L^1}$ with $Mn(ClO_4)_2 \cdot 6H_2O$ in methanol in a 3:2 concentration ratio (L:Mn) followed by slow diffusion of diethylether yielded the orange-red crystalline complex **11**. Mass spectrometric analysis (ESI) in solution shows the presence of peaks corresponding to the species $[Mn_2(\mathbf{L^1})_3 + ClO_4]^{3+}$, $[Mn(\mathbf{L^1})_3]^{2+}$ and $[Mn_2(\mathbf{L^1})_3 + (ClO_4)_2]^{2+}$. The molecular structure and atom connectivity of one of the two complex enantiomers formed during synthesis is shown in Figure 52 and confirms the formation of the expected triple-helical structure. Selected bond lengths and angles are listed in Table 23. The asymmetric unit of **11** contains two Mn(II) centres, three ligand molecules and four perchlorate anions.

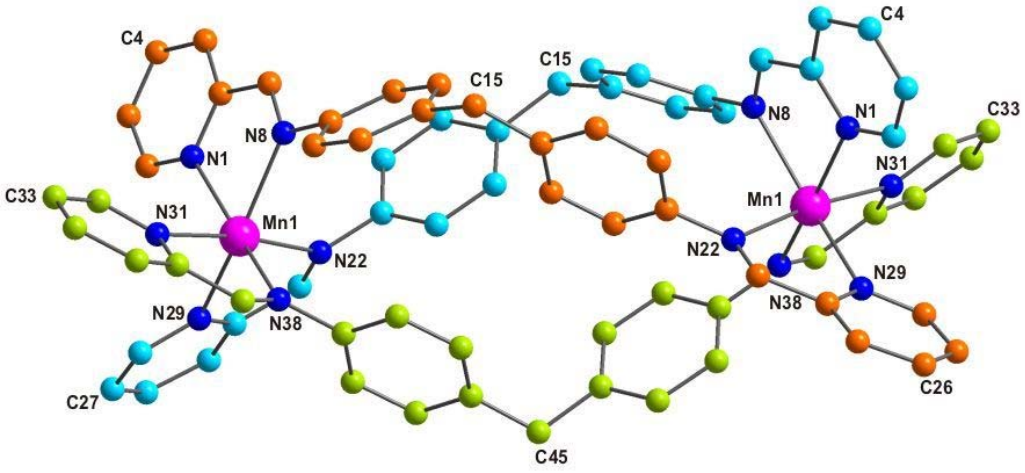

Figure 52. Structure and numbering scheme of the M-enantiomer of helicate **11**. Hydrogen atoms and lattice anions are omitted for clarity.

Table 23. Selected Bond lengths (Å) and angles (°) for **11**.

Mn-N_1	2.287(3)	Mn-N_{29}^{i}	2.249(3)
Mn-N_8	2.269(3)	Mn-N_{31}	2.265(3)
Mn-N_{22}^{i}	2.255(3)	Mn-N_{38}	2.222(3)
N_1-Mn-N_8	73.09(11)	N_{38}-Mn-N_{22}^{i}	102.46(11)
N_{22}^{i} -Mn-N_{29}^{i}	73.76(11)	N_8-Mn-N_{22}^{i}	92.35(11)
N_{31}-Mn-N_{38}	73.89(11)	N_8-Mn-N_{31}	94.16(11)
N_1-Mn-N_{38}	168.59(11)	N_{31}-Mn-N_{29}^{i}	100.79(11)
N_8-Mn-N_{29}^{i}	157.67(11)	N_{38}-Mn-N_{29}^{i}	100.44(11)
N_{31}-Mn-N_{22}^{i}	172.99(11)	N_8-Mn-N_{38}	99.59(11)
N_1-Mn-N_{31}	97.57(11)	N_1-Mn-N_{29}^{i}	88.46(11)
N_1-Mn-N_{22}^{i}	86.80(10)		

Symmetry code: i = -x,y,1/2-z

The Mn···Mn separation is 11.47 Å and the ligands wrap around the two manganese centers forming a triple helicate as defined by the Mn1–N8–N22–Mn1, Mn1–N38–N38–Mn1, and Mn1–N22–N8–Mn1 dihedral angles of 106.5°, 112.3°, and 106.5°, respectively. The ligands coordinate Mn(II) in such a manner that the imine and pyridyl nitrogens occupy opposite faces. This leads to an arrangement where one pyridyl and one imine nitrogen donor atom occupy axial positions, and two pyridyl and two imine nitrogen donor atoms occupy equatorial positions. The Manganese centers are both pseudooctahedral. The bond lengths around Mn(II) vary in dependence on the donor atom type: Mn···N(imine) (2.22-2.27 Å) and Mn···N(pyridyl) (2.25-2.29 Å), and its position: Mn···N(equatorial) (2.22-2.25 Å), and Mn···N(axial) (2.26-2.27 Å). The shorter bond lengths to the imine nitrogen atom are in accord with its stronger basicity compared to the pyridyl nitrogen atoms. There are several intramolecular interactions between the strands within the helicate: two pairs of stronger C–H···π interactions (with distances CH···Cg of 2.73 and 2.99 Å) and two pairs of weaker C-H···π interactions (distances C-H···Cg 3.12

and 3.33 Å). The helicates form a 3D network (Figure 53 and 54) based on the perchlorate anions via (CH···O) hydrogen bonds with distances (C···O) in the range of 3.13-3.47 Å (Table 24) and anion–π interactions [108] indicated by O1B–Cg and O2C–Cg distances of 3.40 (with pyridine ring) and 3.69 Å (with phenylene ring) respectively.

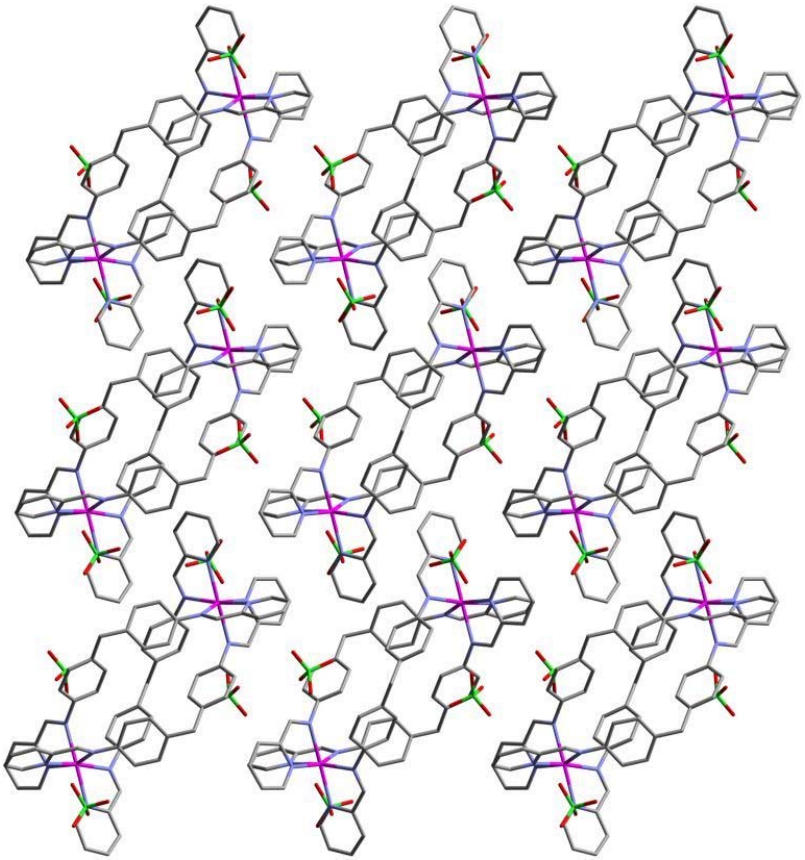

Figure 53. Crystal packing of **11** along the *b* axis. Perchlorate anions are stacked in the crystal lattice. Hydrogen atoms are omitted for clarity.

Table 24. D–X···*A* interactions in **11**.

D– X	*A*	X···*A* [Å]	D···*A* [Å]	D–X···*A* [°]
C11 – H11	O2A^{i}	2.52	3.44	162
C11 – H11	O2B^{i}	2.58	3.40	144
C23 – H23	O1D^{ii}	2.51	3.00	112
C43– H43	O1A^{iii}	2.48	3.35	150
C2 – H2	*Cg*6^{iv}	2.99	3.75	137
C20 – H20	*Cg*10^{iv}	2.73	3.67	171
Cl1 – O1B	*Cg*5^{v}	3.40	4.81	167
Cl2 – O2C	*Cg*6^{iv}	3.69	4.67	128

Symmetry codes: (i) = 1/2-x,-1/2+y,1/2-z; (ii) = 1/2-x,1/2+y,1/2-z; (iii) = -1/2+x,1/2+y,z; (iv) = -x,y,1/2-z; (v) = 1/2-x,1/2-y,-z

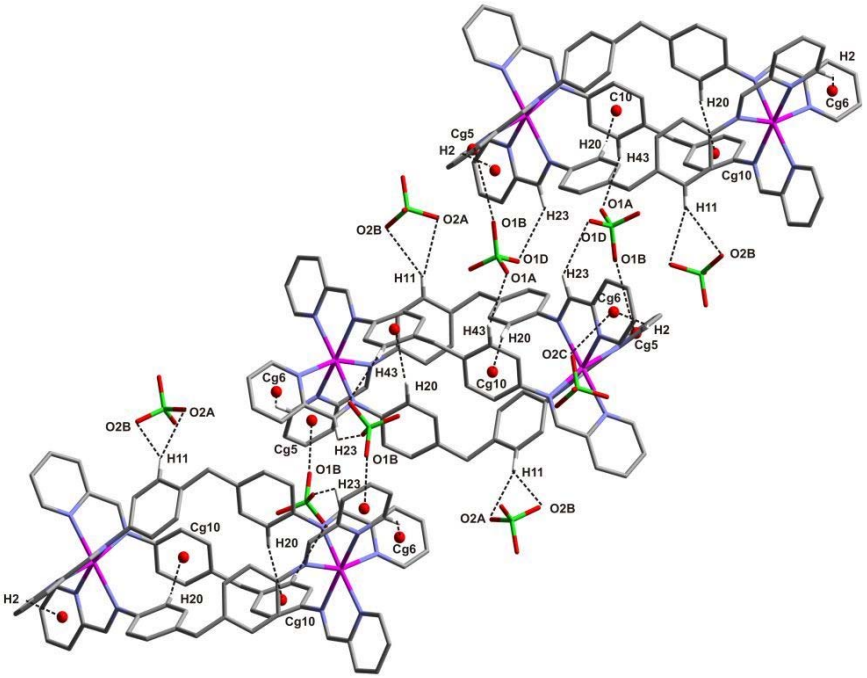

Figure 54. Side view of the structure of **11** showing the different weak interactions. Some hydrogen atoms are omitted for clarity.

2.2.4.2 Complex $[Ni_2(L^2)_3](NO_3)_4 \cdot 2.5H_2O$ (12)

Reaction of acetonitrile solutions of $\mathbf{L^2}$ and $Ni(NO_3)_2 \cdot 6H_2O$ in a 3:2 ligand to metal concentration ratio and followed by slow diffusion of diethylether yielded red single crystals of **12**. Mass spectrometric analysis (ESI) shows the presence of peaks corresponding to $[Ni_2(\mathbf{L^2})_3 + NO_3]^{3+}$, $[Ni_2(\mathbf{L^2})_3 + (NO_3)_2]^{2+}$ and $[Ni_2(\mathbf{L^2})_3 + (NO_3)_3]^{+}$ species. The structure of one of the two complex enantiomers formed during synthesis is shown in Figure 55 and confirms the formation of the expected triple-helical structure.

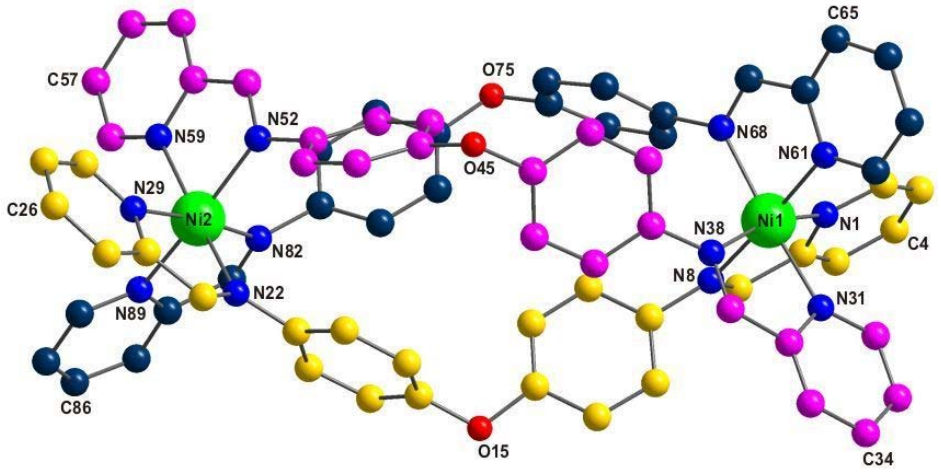

Figure 55. Structure and numbering scheme of the M-enantiomer of **12**. Hydrogen atoms and lattice anions are omitted for clarity.

The asymmetric unit of **12** contains two Ni ions, three ligand molecules and four nitrate anions. Each nickel(II) centre is bound to three pyridylimine units of different ligands to attain a pseudo-octahedral coordination geometry. Coordination to the metal centre forces interannular twisting between the phenylene rings and the pyridylimine units with the logical consequence of formation of a triple-helical array. The dihedral angles between the phenylene and the pyridyl rings in each ligand moiety are in the range 48.73–83.10°. The bond lengths and angles are unremarkable (Table 25) and the two nickel(II) centres are separated by 11.37 Å. The ligand twists through a half-turn around the metal–metal axis leading to a helical pitch of about 22 Å. This lies between the pitches of around 18 Å for William's cobalt triple helicate [109] and 41 Å for Lehn's nickel triple helicate [4].

Table 25. Selected Bond lengths (Å) and angles (°) for **12**.

Ni_1-N_1	2.08(2)	Ni_2-N_{22}	2.13(2)
Ni_1-N_8	2.11(2)	Ni_2-N_{29}	2.05(2)
Ni_1-N_{31}	2.10(2)	Ni_2-N_{52}	2.12(2)
Ni_1-N_{38}	2.11(2)	Ni_2-N_{59}	2.11(2)
Ni_1-N_{61}	2.07(2)	Ni_2-N_{82}	2.10(2)
Ni_1-N_{68}	2.11(2)	Ni_2-N_{89}	2.09(2)
N_1-Ni_1-N_8	78.8(8)	N_{22}-Ni_2-N_{29}	79.2(8)
N_{31}-Ni_1-N_{38}	79.1(8)	N_{52}-Ni_2-N_{59}	78.4(8)
N_{61}-Ni_1-N_{68}	78.6(8)	N_{82}-Ni_2-N_{89}	79.0(8)
N_1-Ni_1-N_{31}	89.6(8)	N_{22}-Ni_2-N_{52}	96.6(8)
N_1-Ni_1-N_{38}	165.4(8)	N_{22}-Ni_2-N_{59}	172.6(8)
N_1-Ni_1-N_{61}	98.1(8)	N_{22}-Ni_2-N_{82}	99.4(8)
N_1-Ni_1-N_{68}	91.7(8)	N_{22}-Ni_2-N_{89}	91.8(8)
N_8-Ni_1-N_{38}	91.5(8)	N_{29}-Ni_2-N_{52}	91.1(8)
N_8-Ni_1-N_{61}	175.1(8)	N_{29}-Ni_2-N_{59}	95.3(8)
N_8-Ni_1-N_{68}	97.5(8)	N_{29}-Ni_2-N_{82}	174.4(9)
N_{31}-Ni_1-N_{61}	95.7(8)	N_{29}-Ni_2-N_{89}	95.7(8)
N_{31}-Ni_1-N_{68}	174.3(8)	N_{52}-Ni_2-N_{82}	94.4(8)
N_{31}-Ni_1-N_{68}	100.5(8)	N_{52}-Ni_2-N_{89}	170.2(8)
N_{38}-Ni_1-N_{61}	92.3(8)	N_{59}-Ni_2-N_{82}	86.6(8)
N_8-Ni_1-N_{31}	88.1(8)	N_{59}-Ni_2-N_{89}	93.8(8)

The twisting of the phenylene units results in a chiral aryl-dominated cavity at the centre of the helicate with (CH···Cg) distances in a range 2.77–2.89 Å, giving a ‘hole’ with some potential to trap small molecules. The helicates form a three-dimensional network

(Figure 56 and 57) via (C-H···O) hydrogen bonds of anions with distances (C···O) in the range 3.07-3.46 Å (Table 26) and nitrate anion–π interactions [108] indicated by O3A···Cg (phenylene), O3B···Cg and O4A···Cg (pyridine) distances of 3.25, 3.82 Å and 3.75 respectively. No face-to-face π- π stacking interactions are observed.

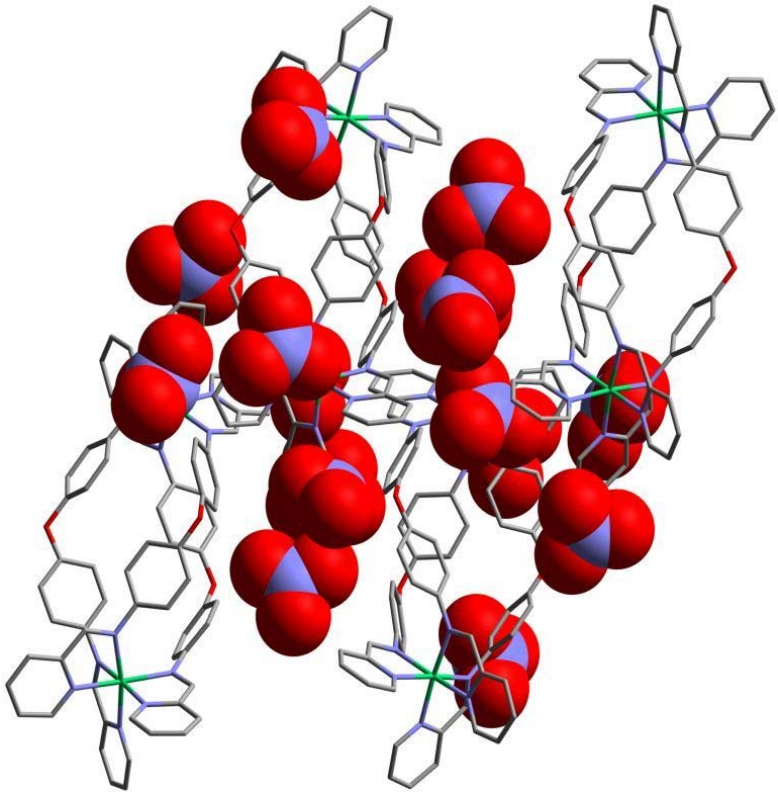

Figure 56. Crystal packing for **12** along the *b* axis. Nitrate anions (as calotte models) are stacked in the crystal lattice. Hydrogen atoms are omitted for clarity.

Table 26. D–X···*A* interactions in **12.**

D– X	***A***	**X···*A* [Å]**	**D···*A* [Å]**	**D–X···*A* [°]**
C7 – H7	O2A^{i}	2.50	3.27	138
C10– H10	O4A	2.39	3.18	139
C27 – H27	O2C^{ii}	2.50	3.12	122
C28– H28	O3A^{iii}	2.51	3.37	151
C32 – H32	N1	2.61	3.10	112
C37 – H37	O3W^{iv}	2.50	3.42	163
C37 – H37	O5B^{iv}	2.58	3.24	126
C41 – H41	O1B^{v}	2.50	3.25	136
C53 – H53	O1C^{vi}	2.41	3.26	148
C65 – H65	O2C^{vi}	2.51	3.23	133
C67 – H67	O5C^{vii}	2.53	3.07	116
C71 – H71	O2C^{i}	2.35	3.21	151
C81 – H81	O3B^{viii}	2.54	3.46	163
C86 – H86	O5A	2.57	3.22	126
C87 – H87	O4B^{iv}	2.45	3.27	145
C87 – H87	O5B^{iii}	2.42	3.32	157
C5 – H5	*Cg*15^{vi}	2.85	3.43	120
C14 – H14	*Cg*17^{ix}	2.77	3.71	168
C32 – H32	*Cg*7^{ix}	2.93	3.67	136
C40 – H40	*Cg*13^{ix}	2.83	3.47	125
C48 – H48	*Cg*18^{ix}	2.89	3.63	136
C78 – H78	*Cg*14^{ix}	2.88	3.81	170
C85 – H85	*Cg*16^{ii}	2.82	3.27	110
N3A – O3A	*Cg*10^{x}	3.25	3.55	95
N3A – O3B	*Cg*11^{ix}	3.82	3.95	89
N4A – O4A	*Cg*9^{ix}	3.77	3.98	91

Symmetry codes: (i) = x,1+y,z; (ii) = 2-x,1/2+y,1/2-z; (iii) = 1+x,y,z; (iv) = 2-x,2-y,1-z; (v) = 1-x,1/2+y,1/2-z; (vi) = 1-x,1-y,-z; (vii) =2-x,-1/2+y,1/2-z; (viii) = 1-x,2-y,-z; (ix) = x,y,z; (x) = -1+x,y,z

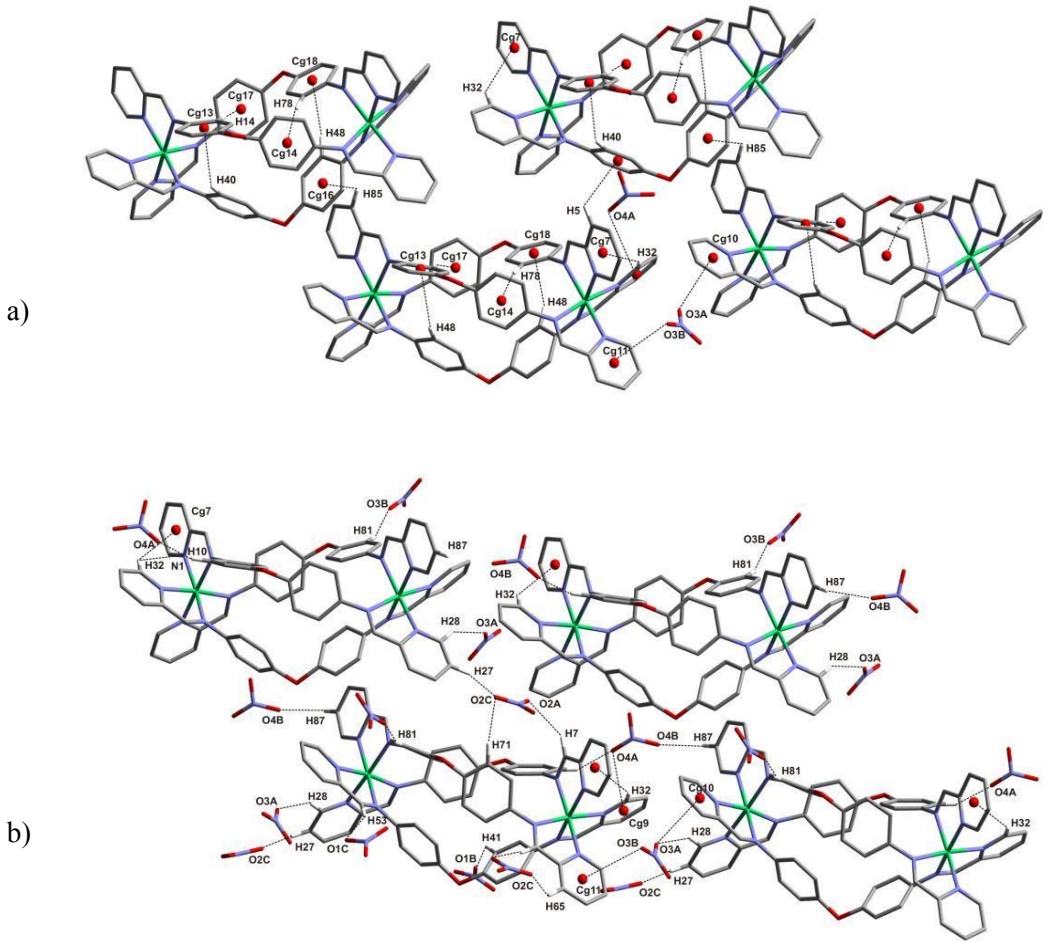

Figure 57. Side view of the structure of **12** showing the different weak interactions. a) CH···π and nitrate···π interactions, b) hydrogen bond interactions. Some hydrogen atoms are omitted for clarity.

2.2.4.3 Complex $[Ni_2(L^5)_3](PF_6)_4 \cdot 0.9H_2O$ (13) and $[Fe_2(L^5)_3](PF_6)_4$ (14)

The reaction of 3 equivalents of $\mathbf{L^5}$ with 2 equivalents of $NiCl_2 \cdot 6H_2O$ or $FeCl_2 \cdot 4H_2O$ in methanol under reflux leads to the formation of orange-red and deep purple solutions, respectively. From these solutions the complexes $[Ni_2(\mathbf{L^5})_3][PF_6]_4$ (**13**) and $[Fe_2(\mathbf{L^5})_3][PF_6]_4$ (**14**) have been isolated after addition of a methanolic solution of $[NH_4][PF_6]$ in high yields (> 80%). Mass spectrometric analysis (ESI) shows the presence of peaks corresponding to $[M_2(\mathbf{L^5})_3 + (PF_6)_3]^+$, $[M_2(\mathbf{L^5})_3 + (PF_6)_2]^{2+}$, $[M_2(\mathbf{L^5})_3 + (PF_6)]^{3+}$ and $[M_2(\mathbf{L^5})_3]^{4+}$. These data are consistent with formation of a dinuclear

$[Ni_2(\mathbf{L}^5)_3]^{4+}$ and $[Fe_2(\mathbf{L}^5)_3]^{4+}$ cations containing each three ligands acting as a dinucleating ligand employing all four nitrogen atoms, and this has been confirmed by X-ray crystallography. Orange crystals of the nickel(II) complex (**13**), suitable for X-ray diffraction were obtained by slow diffusion of diethylether into an acetonitrile solution of the complex while iron complex (**14**) do not give suitable X-ray quality crystals despite multiple attempts.

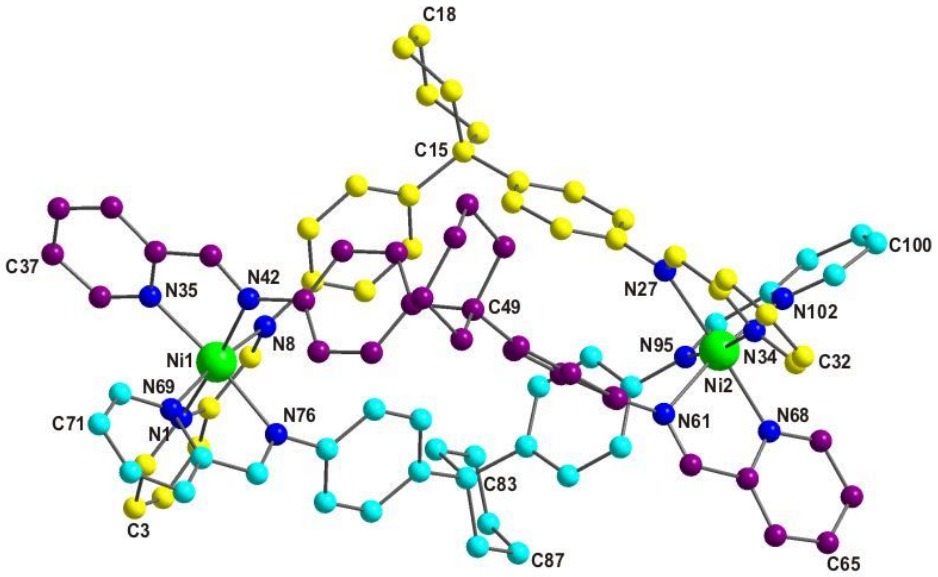

Figure 58. Molecular structures of the nickel complex cation $[Ni_2(\mathbf{L}^5)_3]^{4+}$. Hydrogen atoms, solvent molecules and anions are omitted for clarity and the (M) enantiomer is shown although both enantiomers are present in the structure.

Table 27. Selected Bond lengths (Å) and angles (°) for **13**.

Ni_1-N_1	2.106(7)	Ni_2-N_{27}	2.187(7)
Ni_1-N_8	2.176(7)	Ni_2-N_{34}	2.115(7)
Ni_1-N_{35}	2.045(7)	Ni_2-N_{61}	2.129(7)
Ni_1-N_{42}	2.147(7)	Ni_2-N_{68}	2.088(7)
Ni_1-N_{69}	2.104(7)	Ni_2-N_{95}	2.120(7)
Ni_1-N_{76}	2.081(7)	Ni_2-N_{102}	2.062(7)
N_1-Ni_1-N_8	78.7(3)	N_{27}-Ni_2-N_{34}	78.6(3)

Table 27. continued.

N_{35}-Ni_1-N_{42}	78.8(3)	N_{61}-Ni_2-N_{68}	77.8(3)
N_{69}-Ni_1-N_{76}	77.9(3)	N_{95}-Ni_2-N_{102}	78.8(3)
N_1-Ni_1-N_{35}	96.8(3)	N_{27}-Ni_2-N_{61}	95.1(3)
N_1-Ni_1-N_{42}	175.2(3)	N_{27}-Ni_2-N_{68}	170.2(3)
N_1-Ni_1-N_{69}	94.3(3)	N_{27}-Ni_2-N_{95}	95.8(3)
N_1-Ni_1-N_{76}	85.4(3)	N_{27}-Ni_2-N_{102}	92.9(3)
N_8-Ni_1-N_{35}	93.6(3)	N_{34}-Ni_2-N_{61}	83.4(3)
N_8-Ni_1-N_{42}	99.5(3)	N_{34}-Ni_2-N_{68}	93.8(3)
N_8-Ni_1-N_{69}	171.4(3)	N_{34}-Ni_2-N_{95}	172.2(3)
N_8-Ni_1-N_{76}	96.4(3))	N_{34}-Ni_2-N_{102}	95.8(3)
N_{35}-Ni_1-N_{69}	92.3(3)	N_{61}-Ni_2-N_{95}	102.8(3)
N_{35}-Ni_1-N_{76}	170.1(3)	N_{61}-Ni_2-N_{102}	171.7(3)
N_{42}-Ni_1-N_{69}	87.9(3)	N_{68}-Ni_2-N_{95}	92.3(3)
N_{42}-Ni_1-N_{76}	99.3(3)	N_{68}-Ni_2-N_{102}	94.1(3)

The molecular structure of one of the two complex enantiomers of **13** formed during synthesis is shown in Figure 58 and confirms the formation of the dinuclear triple-helical arrangement. Each Ni(II) centre is bound to three pyridylimine units in the *fac* configuration attaining a *pseudo*-octahedral coordination geometry. Coordination to the metal centre forces interannular twisting between the phenylene ring and pyridylimine unit and the consequence is the formation of a triple-helical array Figure 58, both enantiomers of which are present in the structures. The pyridyl rings are approximately planar with the adjacent imine units (torsion angles in the range of [(–12°) to 1°], and the phenylene rings are twisted with respect to that plane (40–64°). The phenylene rings in the centre of the helicate are not engaged in edge-to-face π- interactions and this behaviour is in constrast to structure related compounds [84, 85, 107]. Intramolecular CH···π (2.9 Å) interactions only occur between the pyridyl proton (C70-H70) *via* a self-complementary C–H···π interaction with one of the adjacent pyridine rings (Figure 60). Bond lengths and angles are all in common ranges (Table 27); the separation between

two nickel(II) centres is 10.98 Å being significantly shorter than the corresponding distance (~11.5 Å) in the structure related compounds [84, 85, 107]. The space-filling model of the present structure (Figure 61) illustrates the nanometer-scale dimensions of the complex assembly: width ~2 nm and height ~1.6 nm. In the complex one proton of one cyclohexane ring is engaged in an edge-to-face CH··· π interaction (distance CH···Cg 2.6 Å) and that supports the helicate assembling into a 3D network (Figure 59, 60). From this process cavities are resulting in which the solvent molecules and anions are located. The PF_6^- anions make short contacts (Figure 60) with ligand protons (PF···HC = 2.3–2.5 Å) and aromatic rings (PF···π = 3.4–3.7 Å) (Table 28). No face-to-face π-stacking interactions are observed.

Table 28. D–X···*A* interactions in **13**.

D– X	***A***	**X···*A* [Å]**	**D···*A* [Å]**	**D–X···*A* [°]**
C4 – H4	F12^{i}	2.54	3.30	138
C16– H16A	F15^{ii}	2.49	3.40	154
C36 – H36	F21^{i}	2.42	3.18	138
C38– H38	F12^{iii}	2.35	3.25	160
C65 – H65	F11^{iv}	2.39	3.14	137
C71 – H71	F36	2.47	3.22	137
C75 – H75	F44	2.51	3.15	125
C91 – H91	F15^{ii}	2.52	3.22	131
C99 – H99	F32^{iv}	2.30	3.04	135
C101 – H101	F46^{v}	2.39	3.13	136
C18 – H18A	*Cg*19^{iv}	2.62	3.52	153
C70 – H70	*Cg*9^{vi}	2.96	3.75	143
P2 – F21	*Cg*7^{i}	3.58	4.74	128
P2 – F26	*Cg*9^{vii}	3.69	4.73	122
P4 – F43	*Cg*11^{vi}	3.47	4.78	138
P4 – F46	*Cg*12^{viii}	3.40	4.94	164

Symmetry codes: (i) = 1-x,1-y,-z; (ii) = 1+x,-1+y,z; (iii) = x,-1+y,z; (iv) = 2-x,-1/2+y,1/2-z; (v) = 1+x,1/2-y,1/2+z; (vi) = x,y,z; (vii) = x,1+y,z; (viii) = 2-x,1/2+y,1/2-z

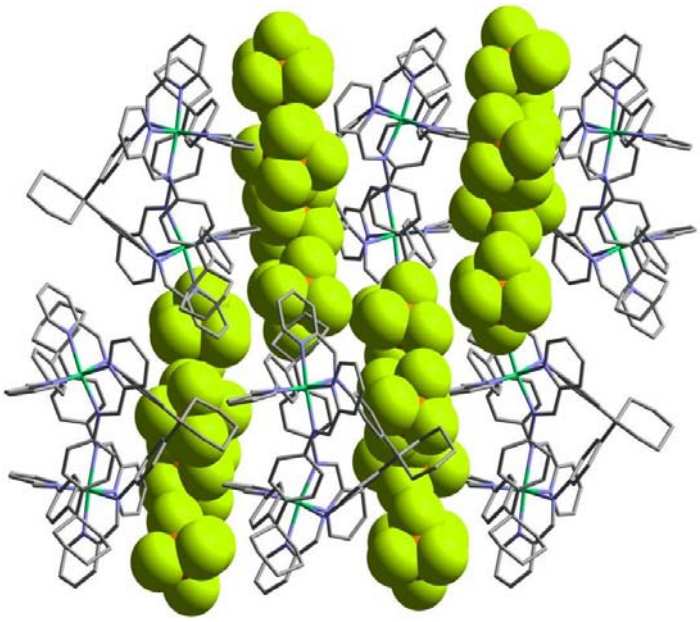

Figure 59. Crystal packing for **13** along the *a* axis. $[PF_6]^-$ anions, shown as space filling models, are stacked in the crystal lattice. Hydrogen atoms and solvent molecules are omitted for clarity.

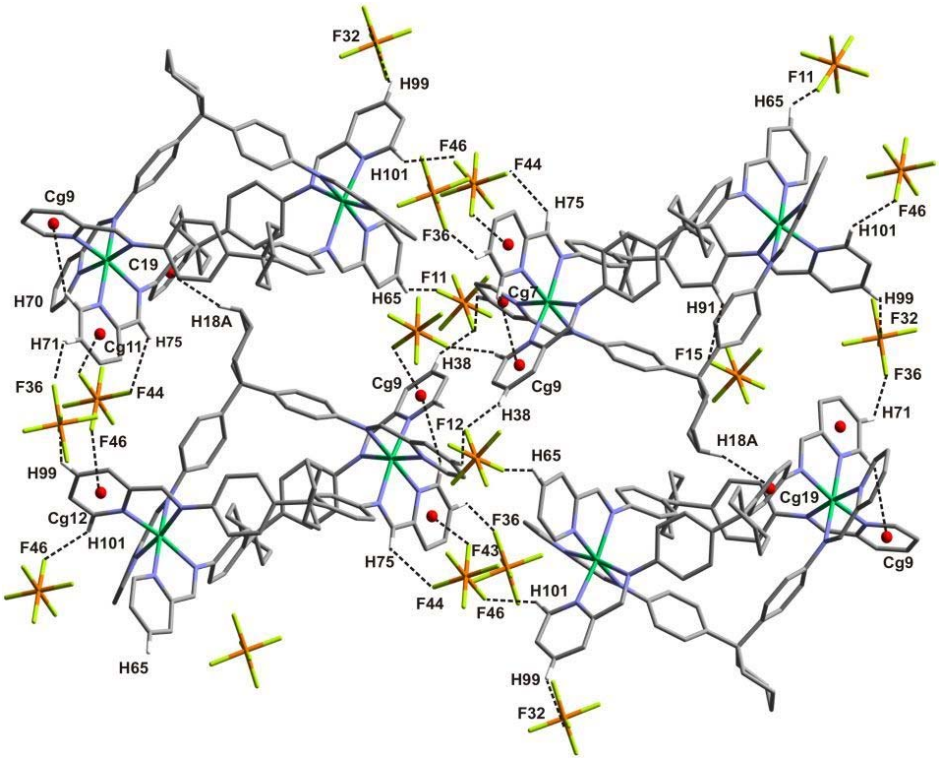

Figure 60. Side view of the structure of **13** showing the different weak interactions. Solvent molecules and some hydrogen atoms are omitted for clarity.

Although this complex **13** and the previously discussed nickel complexes **12** and $[Ni_2(\mathbf{L^1})_3]\cdot(PF_6)_4$ [84] are structurally quite similar, a detailed comparison (Table 29) shows interesting differences, obviously caused by the different linking elements between the two pyridylimine arms. Generally, the coordination to the metal centre forces interannular twisting between the phenylene rings of the linker and both pyridylimine units with the logical consequence of formation of a triple-helical array in these complexes, but the twisting of the phenylene units results weak edge-to-face C–H···π interactions (distances in a range 2.77–2.89 Å) between the aromatic rings of the spacer units of two ligand molecules in **12** and $[Ni_2(\mathbf{L^1})_3]\cdot(PF_6)_4$. In case of **13** only one intramolecular CH···π (2.9 Å) interaction between two pyridine rings is observed. The distance between two nickel(II) centres in **13** (10.98 Å) is significantly shorter than the corresponding distances in **12** (11.37 Å) and $[Ni_2(\mathbf{L^1})_3]\cdot(PF_6)_4$ (11.58 Å). The angles in the linking element between the two bidentate chelating subunits of the ligands in **13** (~109°) are significant smaller than those of the other nickel complexes (~117° in **12** and ~116° in $[Ni_2(\mathbf{L^1})_3]\cdot(PF_6)_4$). The width of all these triple helicates is almost similar (~2 nm) while the height of **13** (~1.6 nm) is a bit larger than that of the others (~1 nm). The space-filling model of the structures of **12** and **13** (Figure 61) illustrates the nanometer-scale dimensions of the complex assemblies. The helicates form a three-dimensional network via weak hydrogen bonds of anions and anion–π interactions. In addition the assembling into a 3D network of **13** is supported by weak edge-to-face CH···π interactions between one proton of the cyclohexane ring and a phenylene ring.

Table 29. Comparison of the C-X-C angles of the linking group and the size of Ni(II) triple helicates.

Complex cation	$[Ni_2(\mathbf{L}^1)_3]^{4+}$ [84]	$[Ni_2(\mathbf{L}^2)_3]^{4+}$ (in **12**)	$[Ni_2(\mathbf{L}^5)_3]^{4+}$ (in **13**)
C-X-C angles of the linking element present between chelating subunits	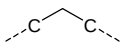 112.83°, 115.98° and 115.98°	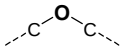 115.02°, 117.50° and 116.85°	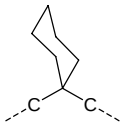 108.73°, 109.97 and 109.10
Ni···Ni distances (Å)	11.58	11.37	10.98
Sizes: width	~ 2 nm	~ 2 nm	~ 2 nm
height	~ 1 nm	~ 1 nm	~ 1.6 nm

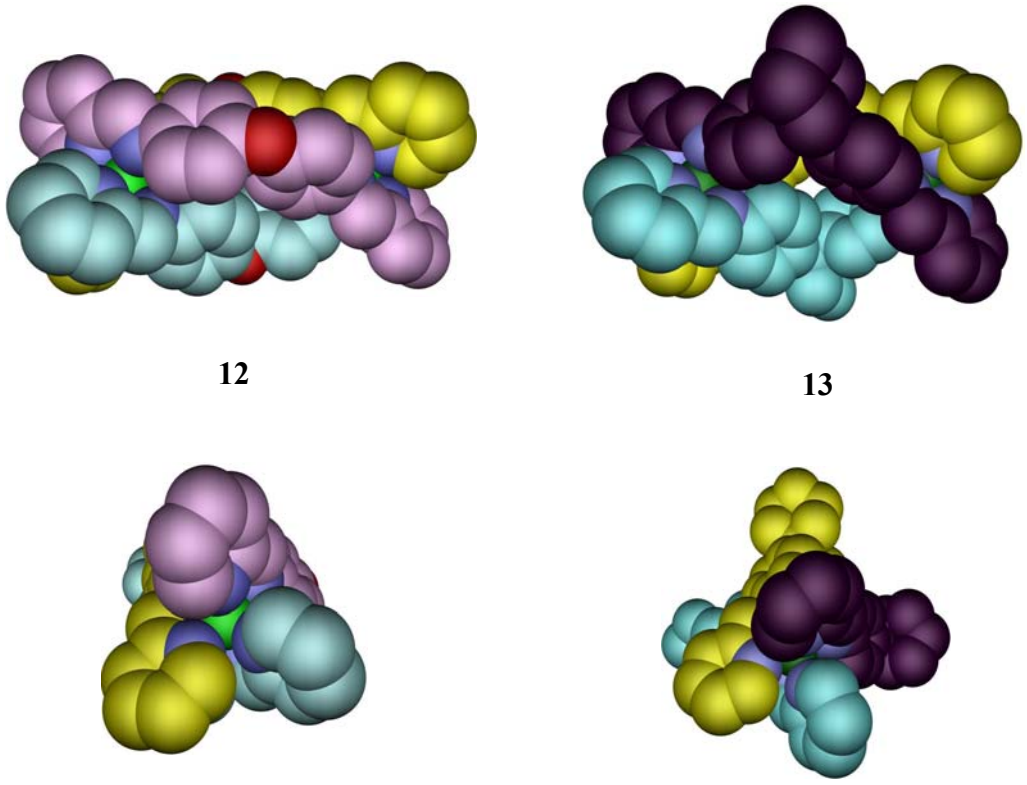

12 **13**

Figure 61. Space-filling representations of the complex cation $[Ni_2(\mathbf{L}^2)_3]^{4+}$ in **12** and $[Ni_2(\mathbf{L}^5)_3]^{4+}$ in **13**, top: side view, bottom: top view. The three ligands **L** are shown in different colours; Ni in green and N in light blue. H atoms are omitted for clarity.

2.3 DNA binding studies of complexes $[Ni_2(L^5)_3](PF_6)_4$ (13) and $[Fe_2(L^5)_3](PF_6)_4$ (14)

The hexafluorophosphate salts $[Fe_2(\mathbf{L}^5)_3][PF_6]_4$ and $[Ni_2(\mathbf{L}^5)_3][PF_6]_4$ are soluble in acetonitrile, ethanol or methanol but not in water. Because DNA binding studies should be performed in aqueous solution the hexafluorophosphate helicates have been transformed into the corresponding chloride salts $[Ni_2(\mathbf{L}^5)_3]Cl_4$ (**13'**) and $[Fe_2(\mathbf{L}^5)_3]Cl_4$ (**14'**) which are better soluble in water.

2.3.1 Thermal stability in absence and presence of DNA

The thermal stability of the compounds was studied by UV-vis absorbance spectroscopy. The compounds **13'** and **14'** were dissolved in aerated tris(hydroxymethyl)methylamine (Tris) buffer (10 mM Tris, 50 mM NaCl, pH = 7.00) at 25 °C. The changes in absorbance were followed at 362 and 577 nm at 90° and 75°C. These temperatures allow the monitoring of the triple helicate decomposition at an accessible time scale. During the treatment both complexes gradually lost their original colours (orange-red for compound **13'** and purple for **14'**) indicating their decomposition. Although the dissociation of Ni(II) and Fe(II) from the triple helicate is reversible, at these low concentrations the overall process appears not to be, possibly due to subsequent hydrolysis of the pyridine carboxaldimine or oxidation of the metal ions.

The effect of salmon testes-DNA on the thermal stability of the triple helicates was also studied by absorbance measurements at 362 and 577 nm for **13'** and **14'** respectively. DNA does not absorb at these wavelengths. The results (Figure 62) indicate that both triple helicates were degraded at rising temperature and that the presence of DNA had no significant stabilising effect on the complex.

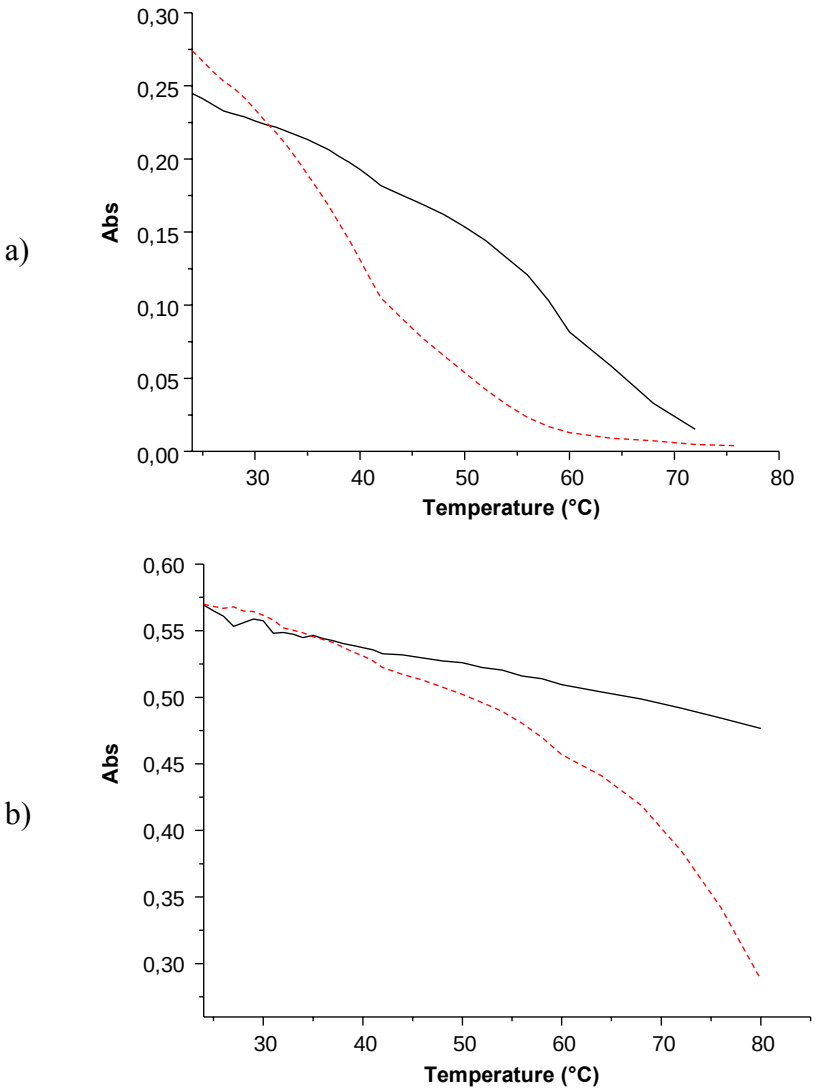

Figure 62. Thermal stabilities of $[Fe_2(\mathbf{L^5})_3]^{4+}$ (a) and $[Ni_2(\mathbf{L^5})_3]^{4+}$ (b) alone (solid) and in the presence of salmon testes-DNA (dash) at 10 : 1 base–triple helicate mixing ratio. Concentration of salmon testes-DNA was 2×10^{-4} M. Absorbance is measured at 577 nm (a) and 362 nm (b). Experiments were carried out in Tris buffer (10 mM Tris, 50 mM NaCl, pH adjusted to 7.00 with HCl) at 1 °C min^{-1} temperature gradient.

2.3.2 UV-vis absorption spectroscopy study

UV-vis absorbance spectra of $[Ni_2(\mathbf{L^5})_3]^{4+}$ and $[Fe_2(\mathbf{L^5})_3]^{4+}$ with and without DNA were collected at room temperature (Figure 63). The absorbance observed around 330 nm is

due to in-ligand transitions, while the bands around 362 nm and 577 nm are characteristic of nickel(II) and iron(II) metal → ligand charge transfer (MLCT) respectively.

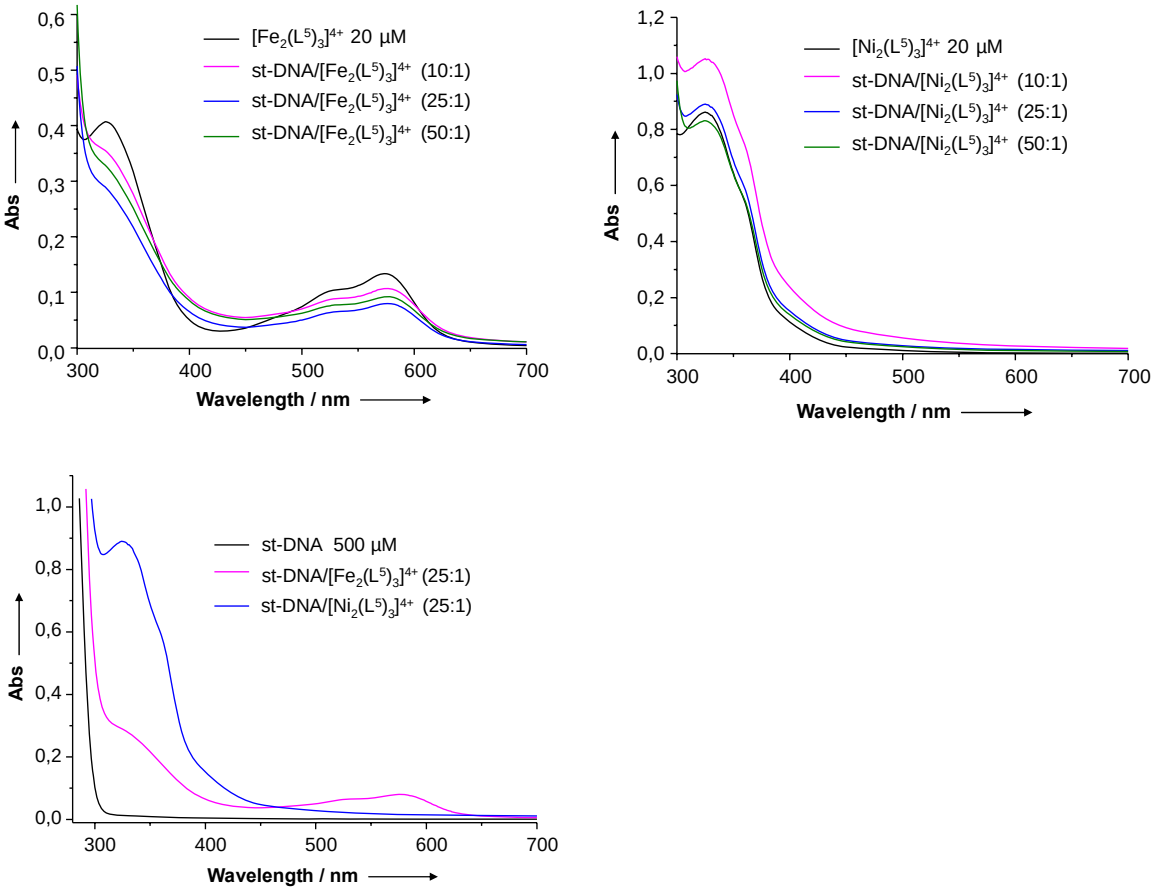

Figure 63. UV-vis spectra of $[Fe_2(\mathbf{L^5})_3]^{4+}$ and $[Ni_2(\mathbf{L^5})_3]^{4+}$ with st-DNA. Titrations were carried out in 10 mM Tris buffer and 50 mM NaCl, pH = 6.00 at constant 500 µM concentration of DNA.

The MLCT bands are unperturbed on binding indicating that in each case the integrity of the triple helicate is retained on addition to DNA. The MLCT bands in these complexes are similar to structure related compounds [84, 91] implying that those transitions are localized at the ends of the triple helicate not much perturbed by the linking element (–CH_2–, –O–, –S– and –C_6H_{10}–) present between the two bidentate chelating subunits in the ligands, while the in-ligand bands are as expected more sensitive to the electronic properties of the spacer.

2.3.3 Circular dichroism spectroscopy study

Circular dichroism (CD, the difference in absorption of left and right circularly polarized light) is sensitive only to the asymmetry or chirality of a system [110] Therefore, CD was also used to probe binding of the triple helicates to the DNA (Figure 64). The CD of DNA has a characteristic pattern from 220 nm to 300 nm, and no signal from 300 nm to 750 nm. Originally the triple helicates exist as a racemic mixture and give no CD signal. Observation of a circular dichroism signal at wavelengths higher than 300 nm, thus indicates that the triple helicates interact with the chiral DNA molecule. Titration of the racemic iron(II) complex into salmon testes-DNA (300 μM st-DNA; 20 mM NaCl; 1 mM sodium cacodylate) led to a strong induced MLCT CD (ICD) signal indicating DNA binding (Figure 64) while that of nickel(II) complex don't show any effect. The induced CD spectrum show that $[Fe_2(\mathbf{L^5})_3]^{4+}$ is interacting with the DNA in a single binding mode, which is consistent with major groove binding. Since the triple helicate is a racemate, we cannot determine to what extent the ICD could be due to a diastereomeric interaction of the M and P enantiomers with the DNA, or to what extent it could be due to a chiral perturbation, common to both enantiomers. But the comparison of the present CD spectrum (Figure 64) with that of the structure related $[Fe_2(\mathbf{L^1})_3]^{4+}$ complex [92, 94-96] (Figure 65), allows to conclude at a preliminary stage that the M enantiomer of $[Fe_2(\mathbf{L^5})_3]^{4+}$ have a stronger effect than the P enantiomer because of the close similarity with the M enantiomer spectrum of the iron ($\mathbf{L^1}$) complex . The DNA-region of the CD spectrum is not perturbed significantly at low complex loadings suggesting that the DNA geometry is not significantly perturbed. As DNA CD is dominated by local interactions of the bases [110] this implies that any structural perturbations induced by the complex do not displace the ligands significantly from their nearest neighbor relative orientations. The shape of the CD signal below 300 nm confirms that the DNA retains its B-configuration throughout the titration.

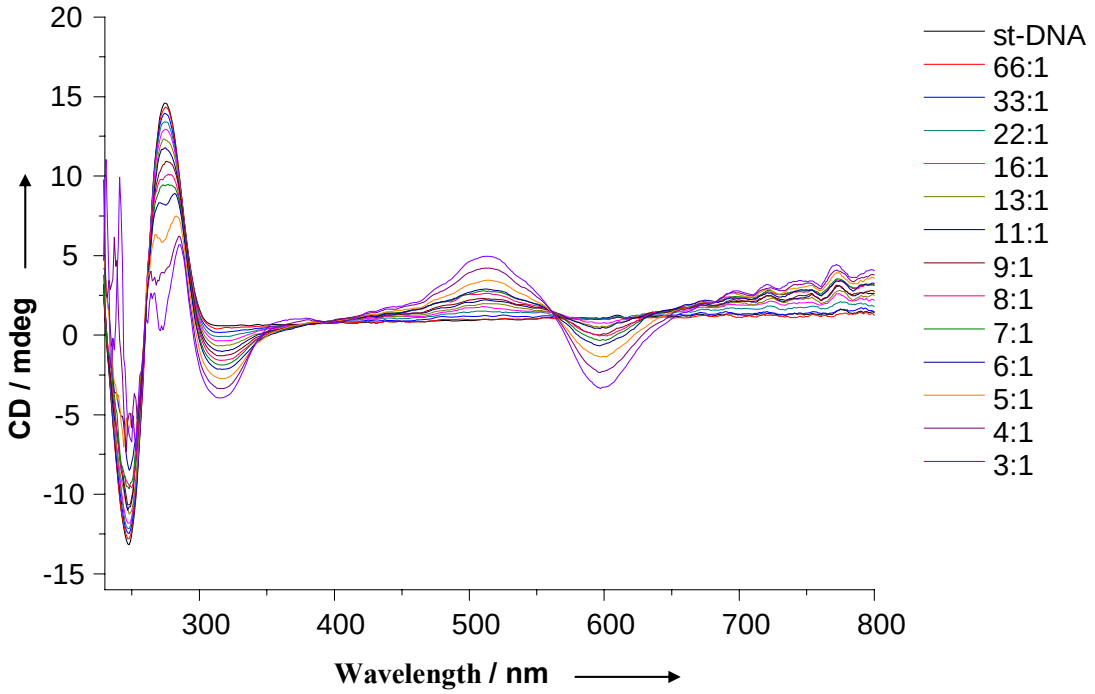

Figure 64. CD spectra of $[Fe_2(\mathbf{L}^5)_3]^{4+}$ with salmon testes-DNA. Mixing ratios DNA base–triple helicate are indicated on the figure. Titrations were carried out in 20 mM NaCl and 1 mM sodium cacodylic buffer at constant 300 μM concentration of the DNA.

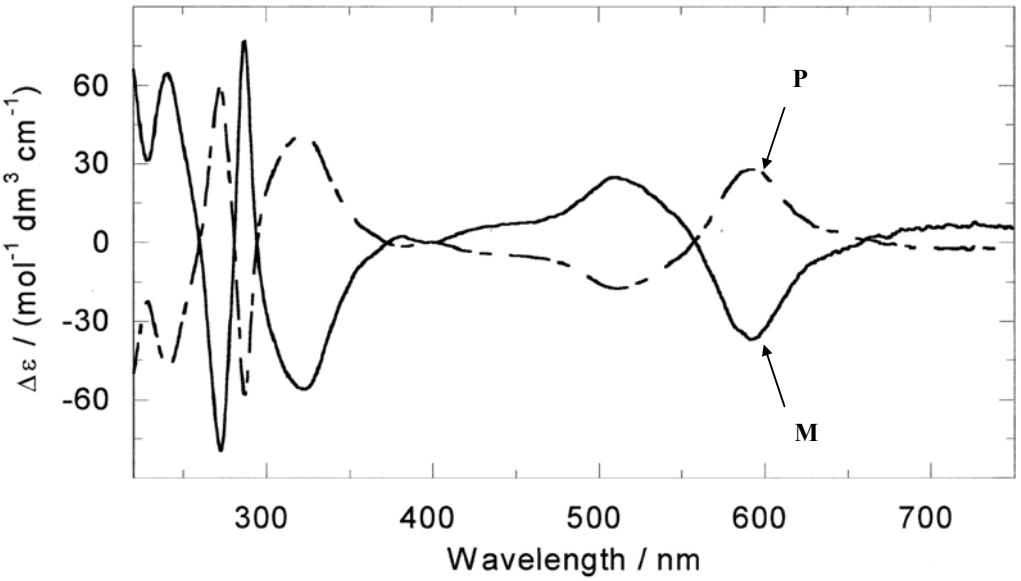

Figure 65. CD spectra of the enantiomers M-$[Fe_2(\mathbf{L}^1)_3]^{4+}$ (solid line) and P-$[Fe_2(\mathbf{L}^1{}_3]^{4+}$ (dashed line) [94].

2.3.4 Reactivity with cancer cell lines

To explore the potential anticancer activity of the new Fe(II) triple helicate **14**', its cytotoxicity on human lung cancer A549 cells was evaluated and compared with that of cisplatin and the previously reported Fe(II) helicate $[Fe_2(\mathbf{L^1})_3]^{4+}$ [84]. The study of the cell viability at various concentrations of these compounds was investigated and the results are reported in Figure 66. All compounds show cytotoxic activity against these cells, but a significant difference is observed between both iron(II) triple helicates. At 25 μM complex concentration, almost all cells died when reacting with **14**' while only 20% died in the presence of $[Fe_2(\mathbf{L^1})_3]^{4+}$. Indeed the activity is quite striking in view of the noncovalent nature of its interaction with DNA. The difference in activity of these iron(II) triple helicates can be caused by the structural differences of the complexes which lead to binding mode changes (see Table 29).

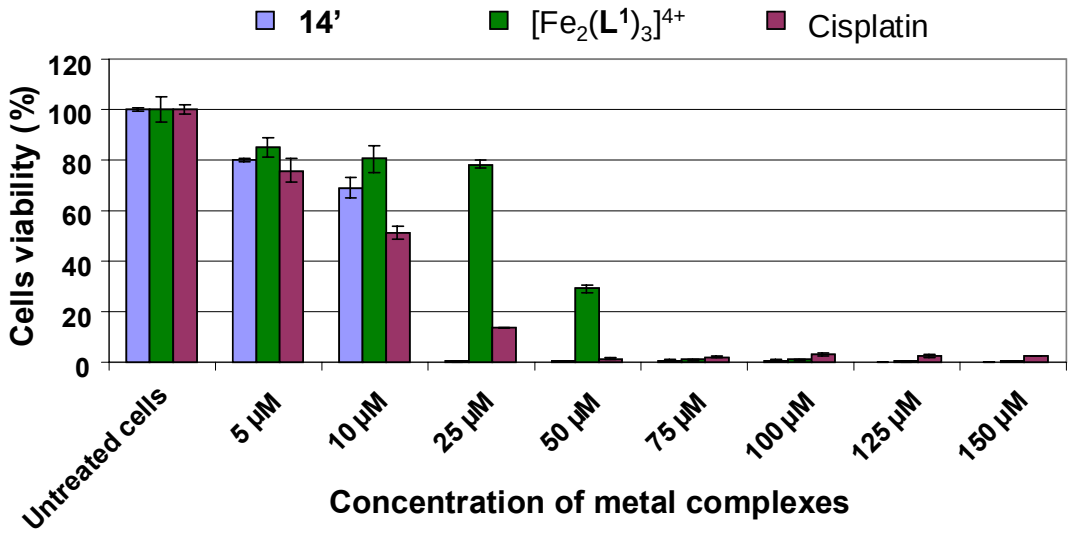

Figure 66. Results of cell viability tests in dependence on complex concentration.

Although the precise molecular basis of the cellular effects and toxicity of the iron triple helicates **14'** and $[Fe_2(\mathbf{L^1})_3]^{4+}$ remains to be fully elucidated, it is clear from the studies that their activities and actions are markedly different from that of cisplatin. On the basis of its known noncovalent DNA binding mode, one possible mechanism for the iron triple helicates is that these are able to bind to and stall DNA replication forks (a three-way

junction structure) [92, 94, 97]. Further research on DNA-binding, mechanism of action, biological studies and potential application of these and other triple helicate complexes are still in progress to understand the activity of these agents more in detail.

3 The bis(2-hydroxyaryl) imine ligand approach

The coordination chemistry of uranium has been the target of increasing attention recently arising from several practical concerns [111-113]. The major interests are the reduction of nuclear waste generated as spent reactor fuel [114] together with the selective extraction of uranium and other metal ions from seawater, groundwater, soil, human beings and waste remediation from actinide decorporation [115-120] as the risk of uranium contamination or poisoning has risen considerably as a consequence of the expanding use of depleted uranium. Uranium and other actinides are major contributors to the long-term radioactivity of nuclear wastes. The separation of actinides from the lanthanides is most difficult due to their similar oxidation state and ionic radii [121]. The coordination chemistry of the linear UO_2^{2+} ion is dominated by between four to six donor atoms all occupying equatorial positions resulting in octahedral, pentagonal bipyramidal or hexagonal bipyramidal coordination, respectively, for U(VI). Typical hard Lewis bases such as F^- or O-donors like phenolate O are good ligands for the hard UO_2^{2+} ion [117, 119, 122]. However, the Lewis basicity of uranyl oxo ligands are generally quite weak and they very rarely produce, for example, dinuclear complex units by forming an oxo bridge between the U(VI) ions [123]. For the specific purpose of uranyl extraction, many kinds of ligand systems have been used including organic phosphorus oxides [124], crown ethers, azacrowns and calixarenes [125, 126], polyhydroxyaryl compounds [117, 119, 127], hydroxamic acids [128], and Schiff base ligands [129-131]. It seems in many cases though, that these ligands are either too rigid or too flexible for optimal complexation as they form uranyl salts or polymeric arrays with weak interactions [115, 126, 132-135]. The introduction of soft heteroatoms, as imine or pyridyl nitrogen, in the ligand system could be used as a tool for more selective and effective binding and extraction. Therefore hydroxy-containing molecules possessing N- and O-donor groups, where N is present as imine, would be good candidates for selective coordination of uranyl ions as they are versatile ligands for various metal ion complexation and contain multidentate mixed aza- and oxo-cores and a flexible backbone. Several Schiff base ligands were previously used for uranyl complexation [129-131, 136-143].

Bandoli et al. reported in 1973 the crystal structure of an uranyl complex obtained from the reaction between $UO_2Cl_2 \cdot 3H_2O$ or $UO_2(NO_3)_2 \cdot 6H_2O$ with stoichiometric amounts of *N,N'*-ethylenebis(salicylideneimine) (H_2salen) [137]. In this structure (Figure 67) the geometry around the UO_2^{2+} ion is closest to pentagonal bipyramidal with uranium atom being bind to the imine nitrogen and deprotonated oxygen atoms of the ligand and to the methanol oxygen atom in the fifth equatorial site.

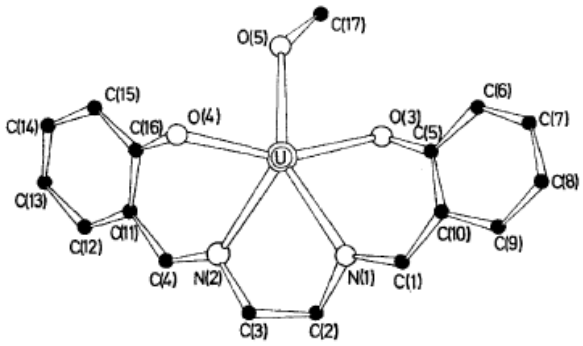

Figure 67. Structure of the complex $[UO_2(salen)(CH_3OH)]$ [137].

Study made by Evans et al. involved the synthesis of a range of solvent adducts of uranyl nitrate with both *N,N'*-ethylenebis(salicylideneimine) (H_2salen) and *N,N'*-propylenebis(salicylideneimine) (H_2salpn) ligands, and illustrated how the solvent used in the synthesis of these complexes can influence the morphology of the resulting crystal structures [141]. The geometry immediately surrounding the uranyl cation is quite similar in all cases, with only slight differences observed in the lengths and angles of the uranyl bonds. These subtle differences, however, are sufficient to drastically alter the packing of each crystal and produce a unique lattice. Two of these structures are presented in Figure 68.

a)

b)

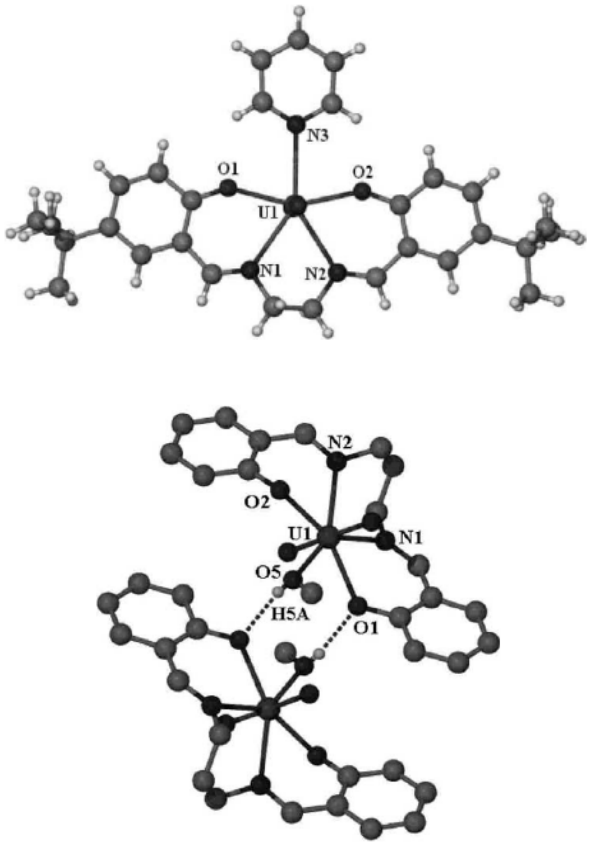

Figure 68. X-ray crystal structure a) of the monomeric [UO_2(*t*-butylsalen)(py)] and b) of the hydrogen-bonded dimer [UO_2(salpn)(CH_3OH)]$_2$ [141].

Ikeda and coworkers have utilized H_2salophen (**XIV**) to investigate the molecular structures of the corresponding uranyl complexes, [UO_2(salophen)(DMF)] and [UO_2(salophen)(DMSO)] (Figure 69), and that without any unidentate solvent molecule (**S**) (Figure 70) [138]. As a result, the uranyl−salophen complex without **S** was identified as the dimeric compound, [UO_2(salophen)]$_2$, in which the [UO_2(salophen)] fragments are held together by the coordination from one of the oxygen atoms in the phenoxides in salophen to the fifth equatorial coordination site of the other [UO_2(salophen)] (Figure 70). Furthermore, it was demonstrated by UV-vis absorption spectroscopy that the complex [UO_2(salophen)]$_2$ keeps its dimeric structure even in solutions of noncoordinating solvents such as CH_2Cl_2 and $CHCl_3$ and is equilibrated with [UO_2(salophen)**S**] upon addition of free **S**. The equilibrium constants and the formation enthalpy and entropy of

the equilibrium between $[UO_2(salophen)\mathbf{S}]$ and $[UO_2(salophen)]_2$ were evaluated from UV-vis and ^1H NMR spectral changes. These thermodynamic parameters suggest differences in the coordination abilities of **S** to $[UO_2(salophen)]$ (DMF < DMSO) and solvent effects on the formation of $[UO_2(salophen)]_2$ (CH_2Cl_2 < $CHCl_3$).

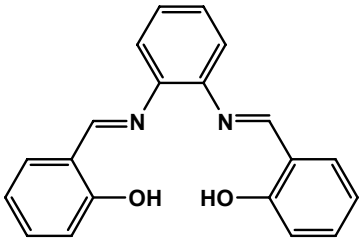

XIV

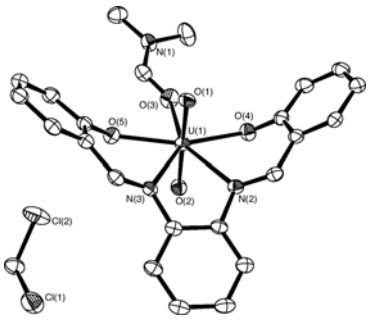

$[UO_2(salophen)(DMF)]\cdot CH_2Cl_2$

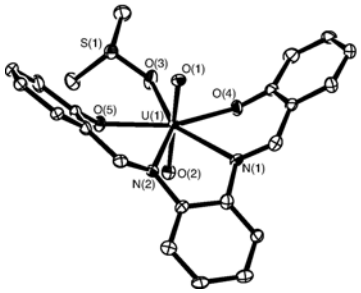

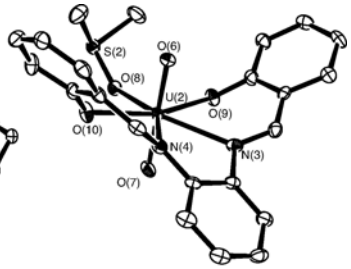

$[UO_2(salophen)(DMSO)]$

Figure 69. View of the H_2salophen structure (**XIV**), the asymmetric units of $[UO_2(salophen)(DMF)]\cdot CH_2Cl_2$ and $[UO_2(salophen)(DMSO)]$ [138].

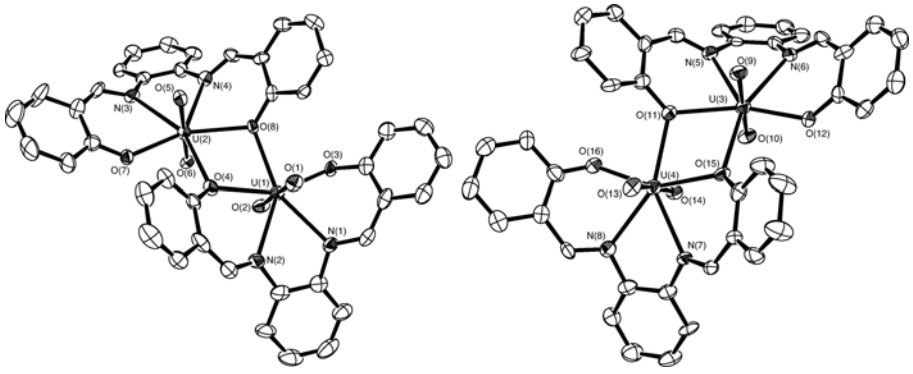

Figure 70. Views of the racemic $[UO_2(salophen)]_2$ dimers [138].

Novel asymmetric Schiff base ligands and their uranyl complexes have been synthesized and characterized by Gorden et al. [131]. The structures of the complexes are similar with pentagonal bipyramidal geometry around the uranyl cation (Figure 71). The uranyl center is coordinated to all the available functional groups of the ligand. Unlike most of the reported uranyl complexes, a ligating solvent molecule to complete uranyl coordination is not observed in these complexes. Weak intermolecular interactions involving solvent molecules, as well as uranyl oxygen atoms, yield a one-dimensional network. Two-phase extraction studies of uranyl ions from aqueous media at different pH conditions employing **XVI** indicates better efficiency at higher pH (99%, pH 5) (Figure 72).

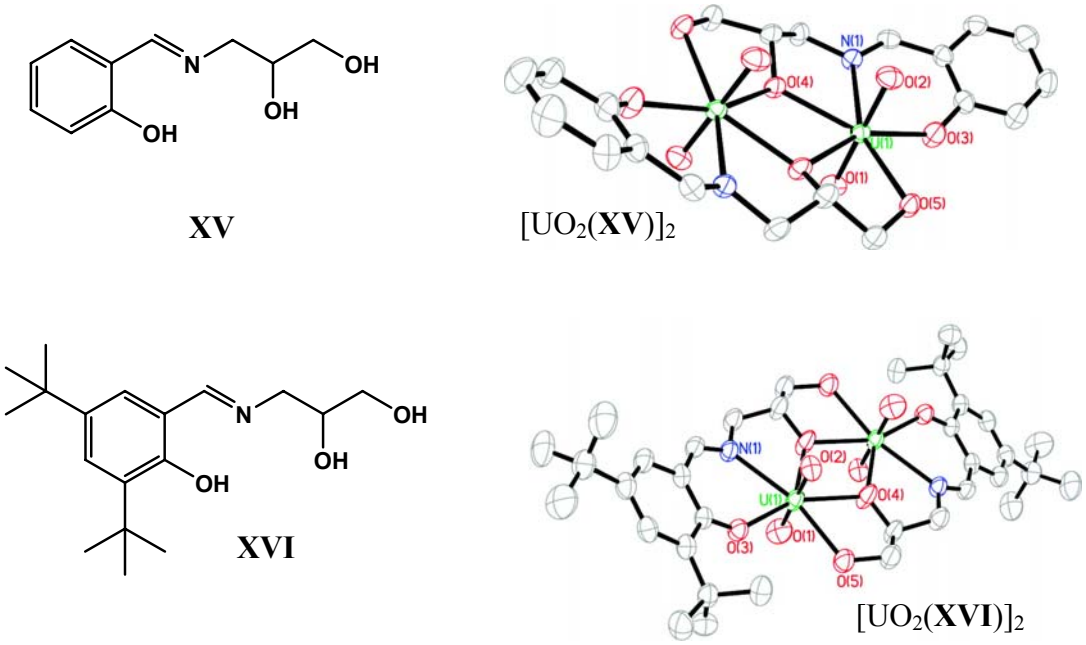

Figure 71. Structures of the ligands **XV** and **XVI** and their corresponding uranyl complexes [131].

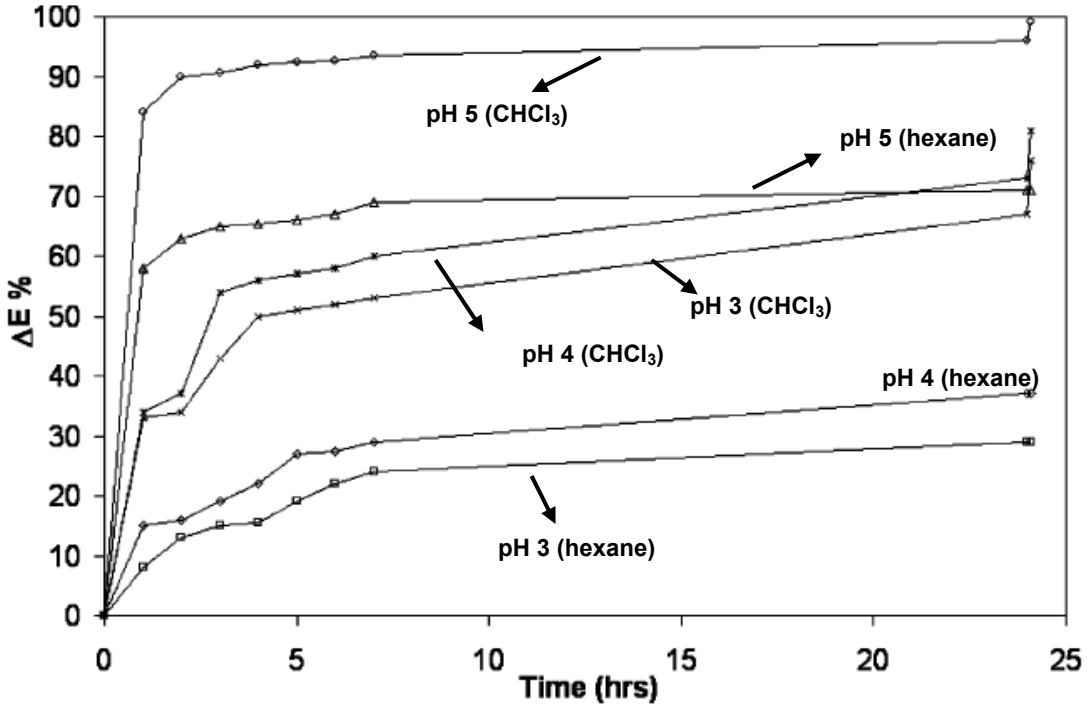

Figure 72. Graph of percent extraction of UO_2^{2+} (4×10^{-3} M) vs time at pH 3−5 in $CHCl_3$ and hexane containing **XVI** (8×10^{-3} M) [hexane: pH 3 (□), 4 (◇), 5 (△); $CHCl_3$: pH 3 (×), 4 (*), 5 (o)] [131].

In principle the general coordination motif of neutral uranyl Schiff base complexes involve the ligand bound in a tetradentate fashion along the equatorial axis of the uranyl ion and a solvent molecule occupying the fifth coordination site in the equatorial position [137, 138]. Till now, no uranyl Schiff base complexes with occupied sixth coordinate site are reported.

3.1 Ligands synthesis

The Schiff base ligands were synthesized by heating amine and the respective aldehyde in absolute ethanol or methanol at reflux temperature. The reduction of $\mathbf{L^8}$ and $\mathbf{L^{10}}$ by KBH_4 on heating gave $\mathbf{L^9}$ and $\mathbf{L^{11}}$ respectively. The yellow Schiff base ligands $\mathbf{L^6}$-$\mathbf{L^8}$, $\mathbf{L^{10}}$, $\mathbf{L^{12}}$, $\mathbf{L^{13}}$ were obtained as solids and the amine ligands $\mathbf{L^9}$ and $\mathbf{L^{11}}$ as brown yellow oil in

quantitative yields. Schiff base ligands were washed with cold methanol and dried to obtain pure compounds. Crude $\mathbf{L^9}$ and $\mathbf{L^{11}}$ were dissolved in $CHCl_3$, washed with distilled water, and the organic solvent was dried with anhydrous $MgSO_4$ and subsequently removed to obtain pure compound. The ligands are stable in air, and soluble in a range of solvents.

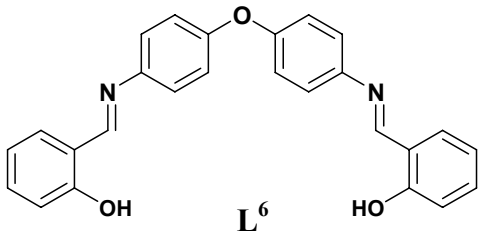

$\mathbf{L^6}$

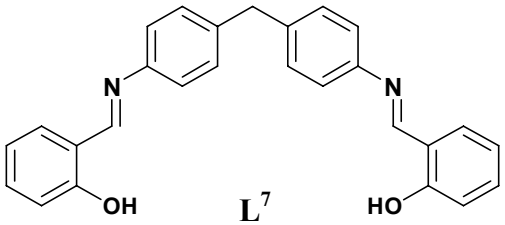

$\mathbf{L^7}$

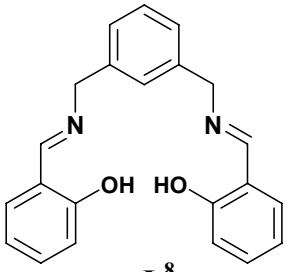

$\mathbf{L^8}$

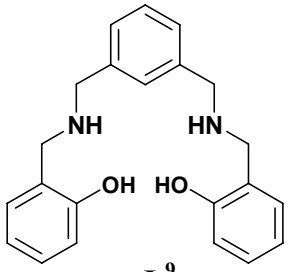

$\mathbf{L^9}$

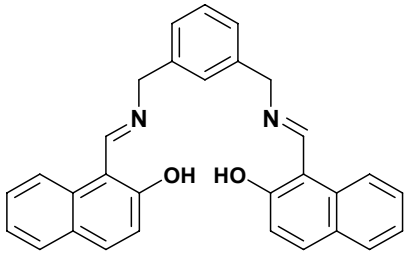

$\mathbf{L^{10}}$

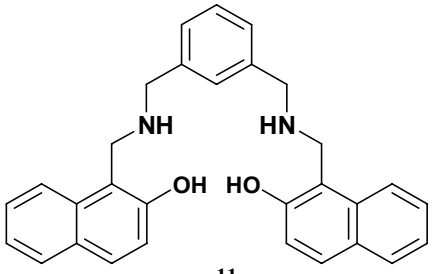

$\mathbf{L^{11}}$

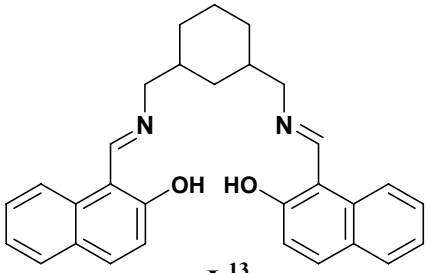

$\mathbf{L^{13}}$

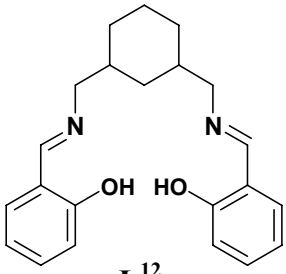

$\mathbf{L^{12}}$

3.2 Characterization of U(VI) complexes

The uranyl complexes have been obtained in high yields (65-94%) by combining the appropriate Schiff base with $UO_2(NO_3)_2 \cdot 6H_2O$ in absolute methanol as orange-red precipitate (**15-20**). Similar reactions of $\mathbf{L^8}$ with metal ions such as Cu^{2+} and Pd^{2+} typically yield binuclear metal complexes [144] while that of $\mathbf{L^6}$ and $\mathbf{L^7}$ with Cu^{2+}, Co^{2+} and Zn^{2+} afforded binuclear double helicate structures [107, 145, 146]. The orange-red colored crystals of **15**, **17**, **18** and **20** suitable for X-ray diffraction studies were obtained by slow diffusion of diethylether into methanol/acetonitrile solution of $UO_2(NO_3)_2$ and the corresponding ligand.

3.2.1 Complex $\{[UO_2(L^6)(NO_3)_2]\}_n$ (15) and $\{[UO_2(L^7)(NO_3)_2]\}_n$ (16)

The assembly of $\mathbf{L^6}$ with $UO_2(NO_3)_2$ in methanol led to the formation of a coordination polymer $\{[UO_2(\mathbf{L^6})(NO_3)_2]\}_n$ (**15**) with 1D zigzag structure in high yield. The compound was characterized by spectroscopic methods and its structure was deduced from single-crystal X-ray diffraction analysis. Microanalytical data are consistent with a formulation $[UO_2(\mathbf{L^6})(NO_3)_2]$ and the ESI-MS indicates the following ion signals in solution: *m/z* 677, $[UO_2(\mathbf{L^6}) - H]^+$; 740, $[UO_2(\mathbf{L^6})(NO_3)]^+$; 1085, $[UO_2(\mathbf{L^6})_2 - H]^+$ corresponding to a mononuclear complex which is in agreement with its polymeric nature. Compound **16** was synthesized in the same way as in the case of **15** using the ligand $\mathbf{L^7}$ which differs to $\mathbf{L^6}$ by the linking element ($\mathbf{L^6}$: –O–; $\mathbf{L^7}$: $–CH_2–$) between the two bidentate chelating subunits. Unfortunately, despite multiple attempts it was not possible to obtain suitable single crystals of **16** for X-ray diffraction studies. Nevertheless the microanalytical and the ESI-MS data (*m/z* 675, $[UO_2(\mathbf{L^7}) - H]^+$; 738, $[UO_2(\mathbf{L^7})(NO_3)]^+$; 1081, $[UO_2(\mathbf{L^7})_2 - H]^+$) for **16** indicate a similar complex structure as for **15**. ^1H NMR spectra of both compounds show no significant shift of the imine proton CH=N for the free ligands and the metal complexes indicating no involvement of the lone pair of this nitrogen atom in metal binding. A slight upfield shift of about 0.45 ppm for the proton of the hydroxyl group [147] of both complexes when compared to those of corresponding "free" ligand points to the coordination of the phenolic oxygen atom with the metal center. Similarly, in the IR spectra of the two complexes (Figure 73, 74), a strong peak around 1640 cm^{-1} (free

ligands 1620 cm^{-1}) indicates a strong interaction of the imine nitrogen with the hydrogen of the hydroxyl group as this can also be proved by the appearance of the new peak at around 2427 cm^{-1} in the spectra of the complexes, indicating the ν CH=N···H vibration. Coordination through the phenolic hydroxyl unit is shown by the shift in the C-O band for uranyl complexes (1385 cm^{-1}) compared to the free ligands (1350 cm^{-1}) [148]. A broad peak around 3400 cm^{-1} is indicative of presence of hydroxyl group. The strong bands at 920 cm^{-1} due to the asymmetric and symmetric UO_2 stretching are characteristic of linear uranyl ion in the complex [142, 149]. Selected vibrating mode band positions are summarized in Table 30. The solid-state structure of compound **15** was solved from single crystal X-ray diffraction data. The complex crystallise in space group *C*2/c(\a0\g)0s. The asymmetric unit contains one UO_2^{2+} ion, one ligand molecule and two nitrate anions.

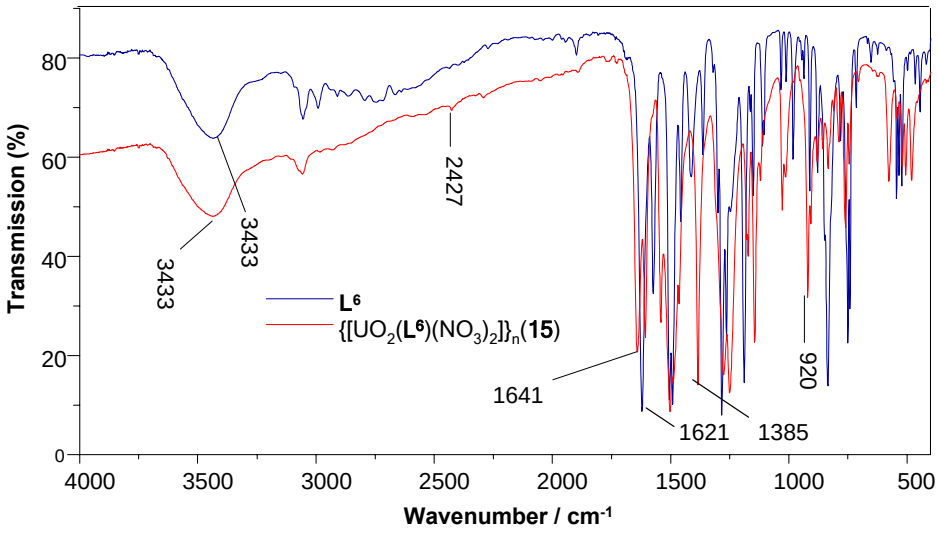

Figure 73. IR-spectrum of $\mathbf{L^6}$ and $\{[UO_2(\mathbf{L^6})(NO_3)_2]\}_n$ (**15**) in the range of 4000-400 cm^{-1}.

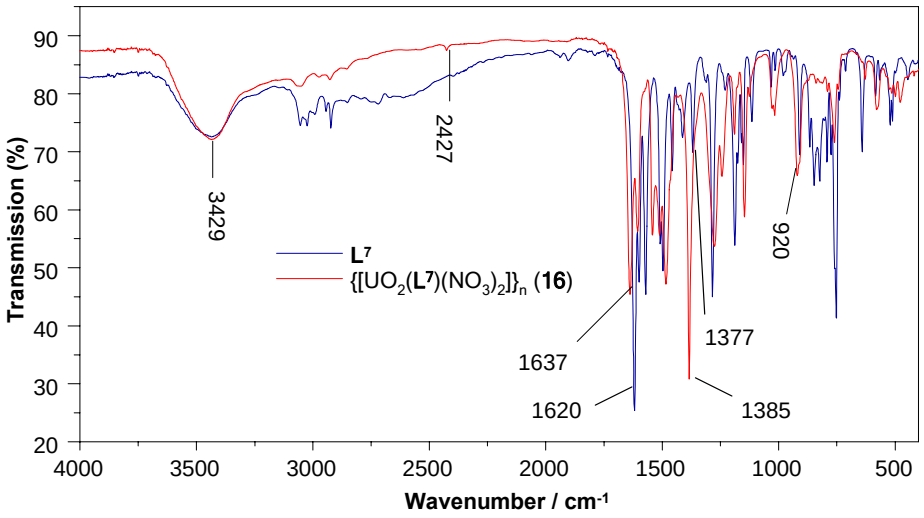

Figure 74. IR-spectrum of $\mathbf{L^7}$ and $\{[UO_2(\mathbf{L^7})(NO_3)_2]\}_n$ (**16**) in the range of 4000-400 cm^{-1}.

Table 30. IR spectroscopic data of compounds **15-20**.

Vibration frequency $\tilde{\nu}$ (cm^{-1})	Intensity†, Band form‡	Assignment [150]
3433−3428	m, br	O−H stretch
3158−2853	w, sr	C−H stretch
2427	w, sr	N−H stretch
1654−1637	s, sp	C=N stretch
1385	vs, sp	O−H deformation and C−O stretch
921	s, sp	U=O stretch

† vs = very strong, s = strong, m = medium, w = weak
‡ br = broad, sp = sharp, sr = shoulder

The structure of the complex is shown in Figure 75; selected bond lengths and angles are given in Table 31, 32. Each UO_2^{2+} is coordinated by two Schiff bases via phenolic OH functions and further two bidendate nitrate anions. One Schiff base is coordinated to two U(VI) atoms leading to a 1D coordination polymer. No solvent is incorporated into the coordination sphere of the uranyl cation.

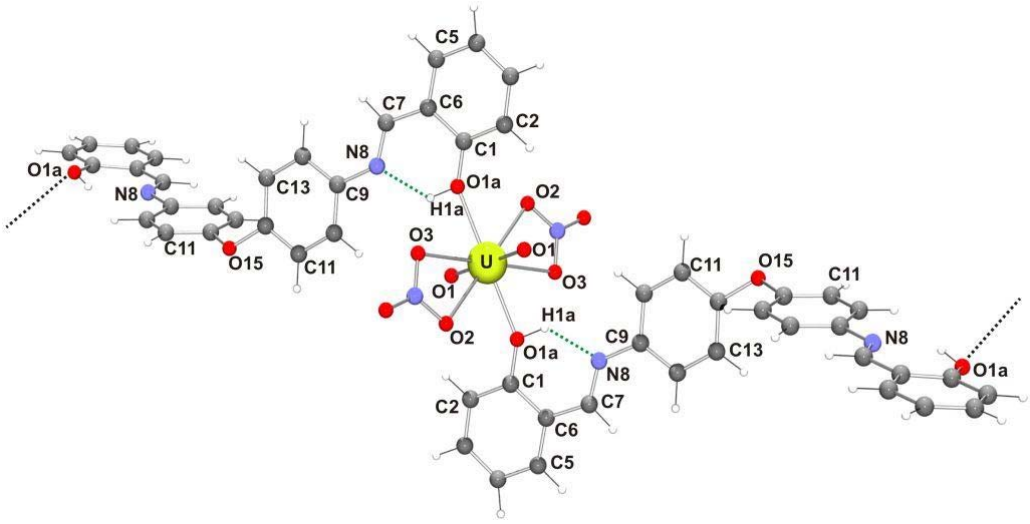

Figure 75. Local coordination environment of UO_2^{2+} in **15**. Atoms are represented as 50% thermal ellipsoids.

Table 31. Selected Bond lengths (Å) and angles (°) for **15**.

U-O(1)	1.761(1)	U-O(1a)	2.322(1)
U-O(2)	2.515(1)	U-O(3)	2.533(1)
O(1)-U-O(1)	180.00	O(1a)-U-O(1a)	180.00
O(1)-U-O(1a)	180.00	O(2)-U-O(3)	49.704(9)

Table 32. C–H···*A* interactions in **15**.

C– H	***A***	**H···*A* [Å]**	**C···*A* [Å]**	**C–H···*A* [°]**
O(1a)–H(1a)	N(8)	1.90	2.58	130

The U-OH distances (2.322 Å) are symmetric and typical for structure related complexes [131, 138, 140, 141, 151]. The two nitrate anions bonds bidentately with U-O distances between 2.515 and 2.533 Å to the UO_2 unit and occupy the four additional coordination

sites around the uranyl center. It is interesting to note that the imine nitrogen atoms do not bind the UO_2^{2+} ion but form strong hydrogen bonds to the OH group with N···H bond distances of about 1.90 Å. The approximate coordination sphere around the U(VI) ion is distorted hexagonal-bipyramidal with axial O=U=O moiety and six oxygen atoms in equatorial position. The U=O distances and O=U=O angles in **15** (av. 1.76 Å; 180°) are in agreement with distances and angles reported for similar uranyl compounds [131, 138, 140, 152]. In **15** a one-dimensional chain of a 'chair' like conformation is observed (Figure 76) as the second 2-hydroxyarylimine arm of the adjacent ligand are present on the opposite site of the coordination plane. Such a distortion can be due to the high separation distance between the two phenolic binding sites of the corresponding ligand compared to the ligands $\mathbf{L^8}$-$\mathbf{L^{13}}$ and the polymeric nature of the complex. Figures 77 show the packing diagram of **15**.

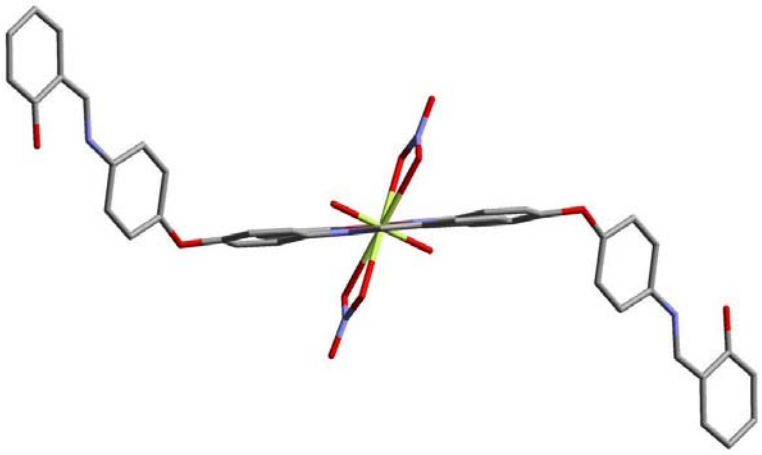

Figure 76. Chair-like ligand arrangement around UO_2^{2+} in the complex **15**.

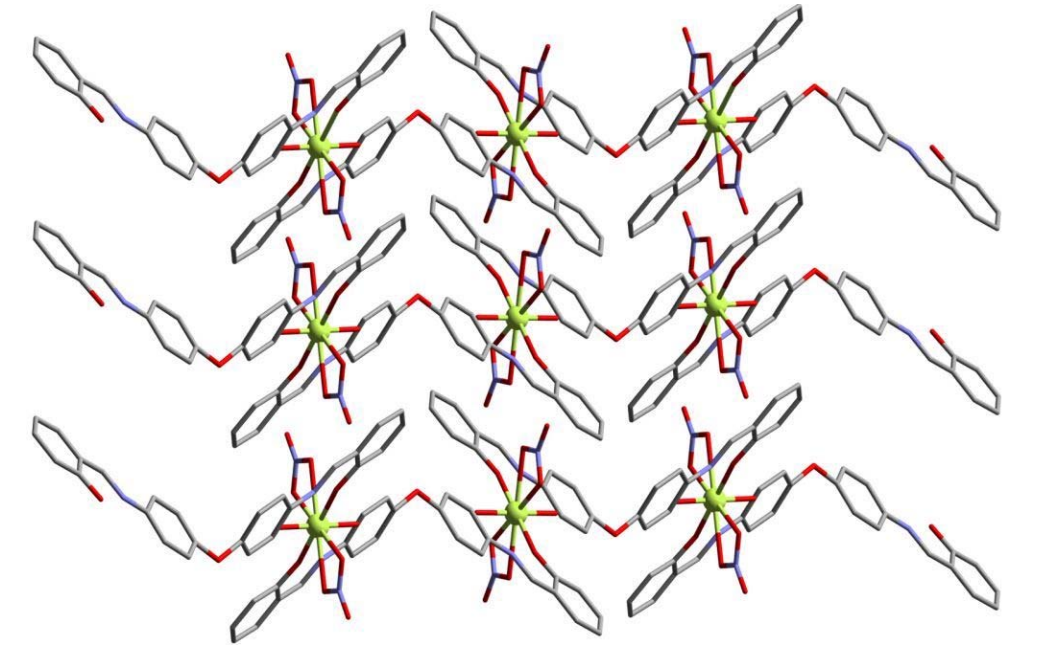

a)

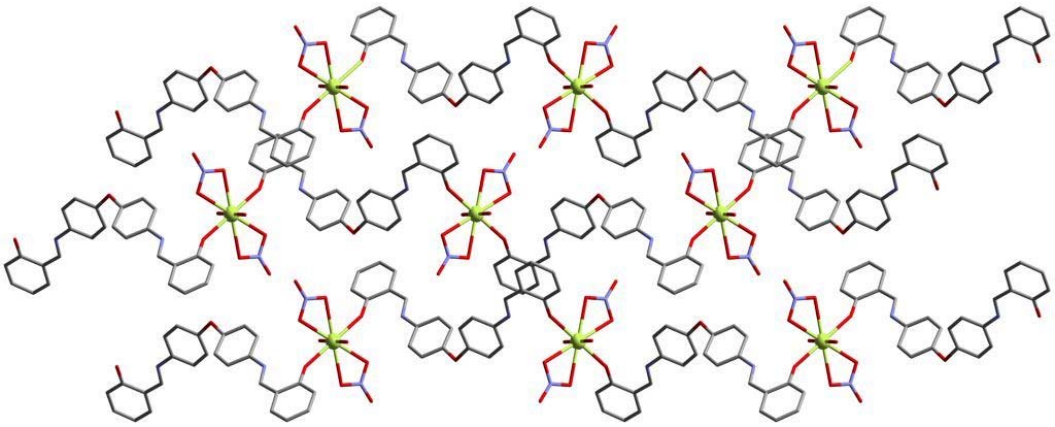

b)

Figure 77. Crystal packing for $\{[UO_2(\mathbf{L}^6)(NO_3)_2]\}_n$ (**15**): a) along the *a* axis**;** b) along the *c* axis.

3.2.2 Complexes $[UO_2(L^8)(NO_3)_2]$ (17), $[UO_2(L^{10})(NO_3)_2]$ (18), $[UO_2(L^{12})(NO_3)_2]$ (19) and $[UO_2(L^{13})(NO_3)_2]$ (20)

Complexes **17-20** were synthesized as describe above. These compounds were characterized by spectroscopic methods and their molecular structures were determined by single-crystal X-ray diffraction analyses. Microanalytical and ESI-MS data are consistent with the formulation $[UO_2(\mathbf{L})(NO_3)_2]$. In ^{1}H NMR spectra, no significant shift is observed for the imine proton (CH=N) between the free ligands and the corresponding metal complexes, again indicating no interaction of the lone pairs on nitrogen with the metal center. A slight upfield shift of about 0.45 ppm of conjugated hydroxyl group through an aromatic ring with the azomethine linkage [147] in all these complexes when compared to those of corresponding "free" ligand can be due to the coordination of the phenolic oxygen with metal center. Similarly, in their IR spectra (Figure 78–81), a strong peak around 1645 cm^{-1} (free ligands 1630 cm^{-1}) indicates a strong interaction of the imine nitrogen with the hydrogen of the hydroxyl group as this can also be proved by the appearance of the new peak at around 2427 cm^{-1}, indicating the (ν CH=N···H) vibration. Coordination through the phenolic hydroxyl unit is shown by the shift in the C-O band for uranyl complexes (1385 cm^{-1}) compared to the free ligands (1350 cm^{-1}) [148].

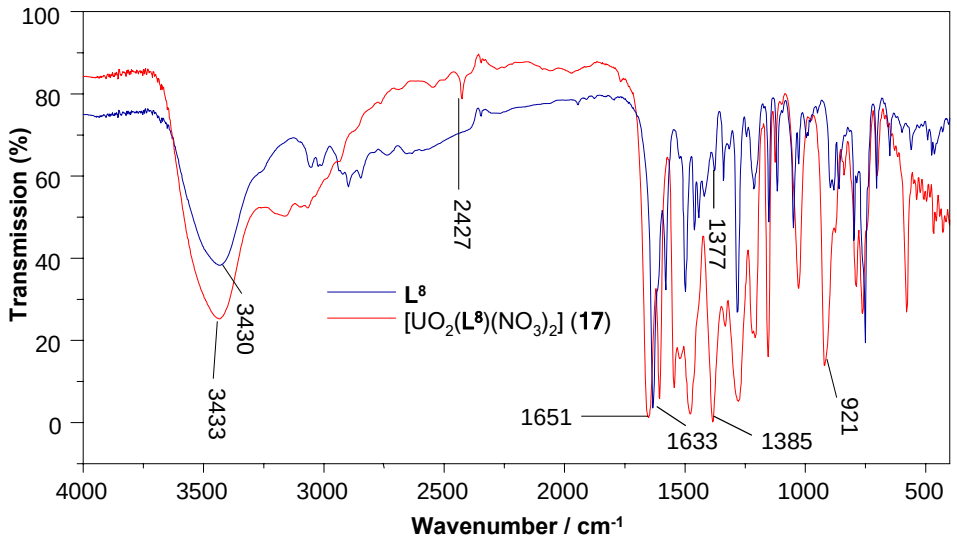

Figure 78. IR-spectrum of $\mathbf{L}^8$ and $[UO_2(\mathbf{L}^8)(NO_3)_2]$ (**17**) in the range of 4000-400 cm^{-1}.

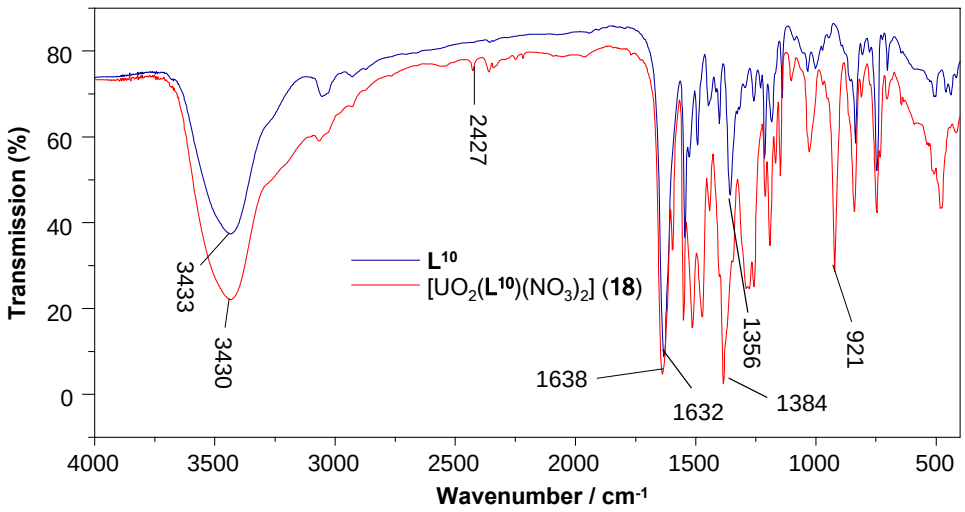

Figure 79. IR-spectrum of $\mathbf{L}^{10}$ and $[UO_2(\mathbf{L}^{10})(NO_3)_2]$ (**18**) in the range of 4000-400 cm^{-1}.

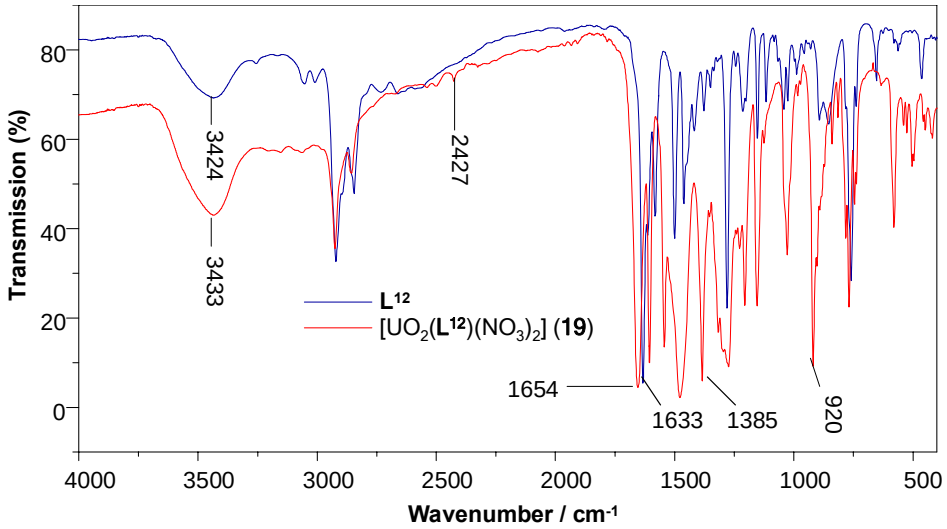

Figure 80. IR-spectrum of $\mathbf{L}^{12}$ and $[UO_2(\mathbf{L}^{12})(NO_3)_2]$ (**19**) in the range of 4000-400 cm^{-1}.

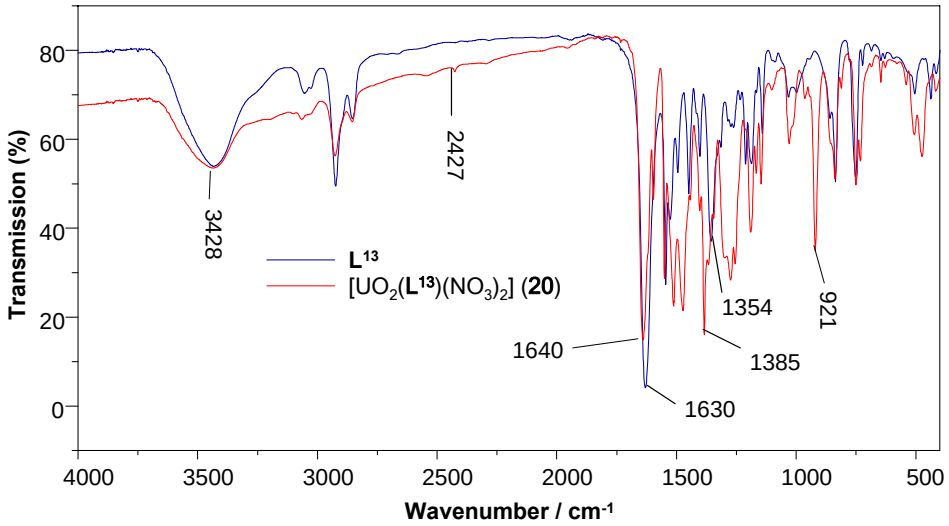

Figure 81. IR-spectrum of $\mathbf{L^{13}}$ and $[UO_2(\mathbf{L^{13}})(NO_3)_2]$ (**20**) in the range of 4000-400 cm^{-1}.

A broad peak around 3400 cm^{-1} is indicative of presence of hydroxyl group. The strong bands at 920 cm^{-1} due to the asymmetric and symmetric UO_2 stretching are characteristic of linear uranyl ion in the complexes [142, 149]. Selected vibrating mode band positions are summarized in Table 30. The electronic spectra of the ligands $\mathbf{L^8}$, $\mathbf{L^{10}}$, $\mathbf{L^{12}}$, $\mathbf{L^{13}}$ and their complexes in acetonitrile at nearly neutral pH are shown in Figure 82. A slightly shift of the characteristic bands in the spectra of these compounds compared to those of the free ligands signify the formation of the uranyl complexes. At extreme pH condition, a significant change is observed with the absence of characteristic peak due may be to the complex hydrolysis [140]. The absorption bands for the ligands around 300 nm are due to the π-π* transition of the imine group [148]. The modification of the bands in the complexes is due to the LMCT (5f ← oxygen 2p). The solid-state structures of compounds **17, 18** and **20** were solved from single crystal X-ray diffraction data and confirmed by DFT calculation. Compounds **17** and **20** crystallise in space group *P*–1 while **20** crystallise in space group *C*2/*c* but all these complexes possess similar asymmetric units which contains one UO_2^{2+} ion, one ligand molecule and two nitrate anions.

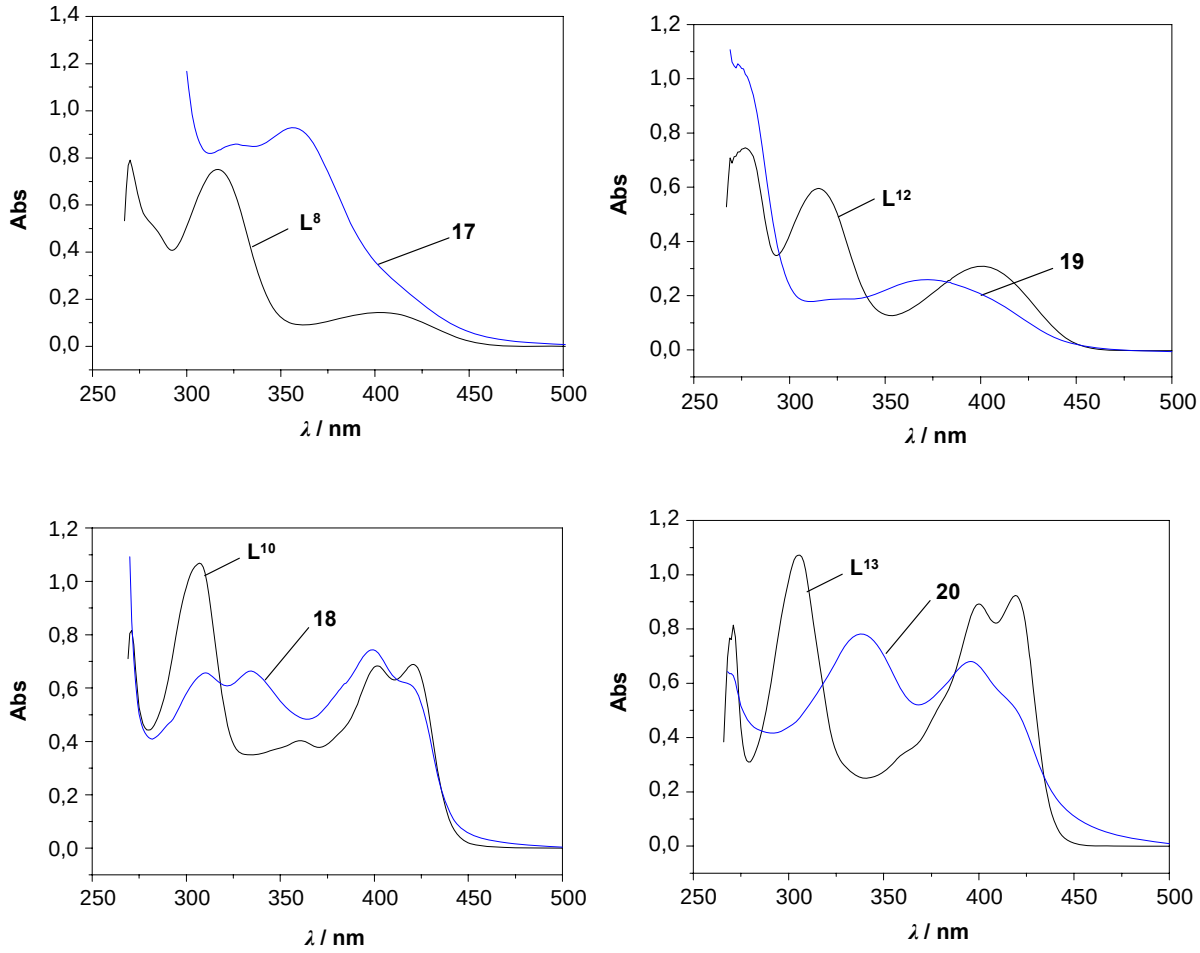

Figure 82. Absorption spectra of ligands $\mathbf{L^8}$, $\mathbf{L^{10}}$, $\mathbf{L^{12}}$, $\mathbf{L^{13}}$ and their uranyl complexes **17**–**20** ($5 \cdot 10^{-5}$ M) in MeCN, pH = 5.5.

The structures of these complexes are shown in Figure 83–85 and selected bond lengths and angles are given in Table 33. The UO_2^{2+} ion is coordinated by the phenolic OH functions of the ligands and two nitrate ions. No solvent is incorporated into the coordination sphere of the uranyl cation. Similar coordination has been observed in $[UO_2(NO_3)_2(salpn)]$, (salpn = *N,N'*-propylenebis(salicylidenimine)) [141]. The U-OH distances in **17** (2.311 and 2.324 Å), **18** (2.345 and 2.358 Å) and **20** (2.335 and 2.385 Å) are asymmetric and typical for structure related complexes [131, 138, 140, 141, 151]. The two nitrate anions bonds bidentately to the UO_2 unit and occupy the four additional coordination sites around the uranyl center.

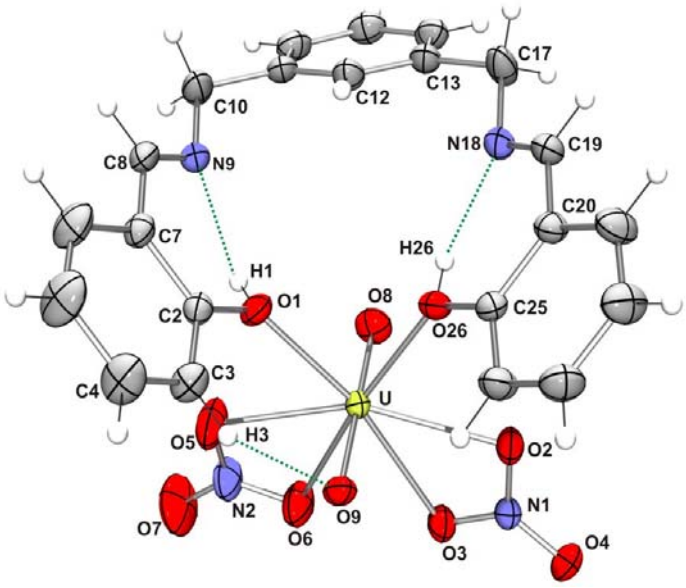

Figure 83. An ORTEP diagram for the asymmetric unit of **17**. Thermal ellipsoids are shown at the 30% probability level.

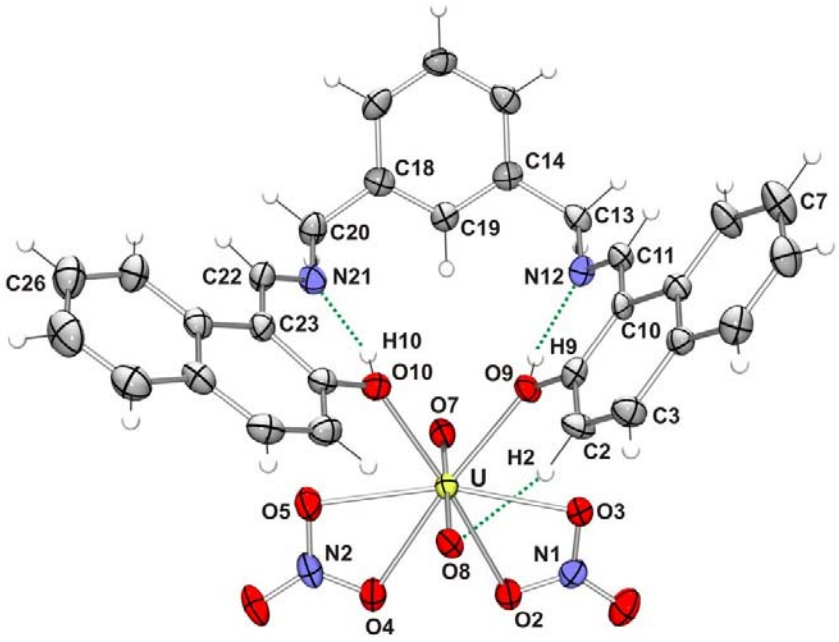

Figure 84. An ORTEP diagram for the asymmetric unit of **18**. Thermal ellipsoids are shown at the 30% probability level.

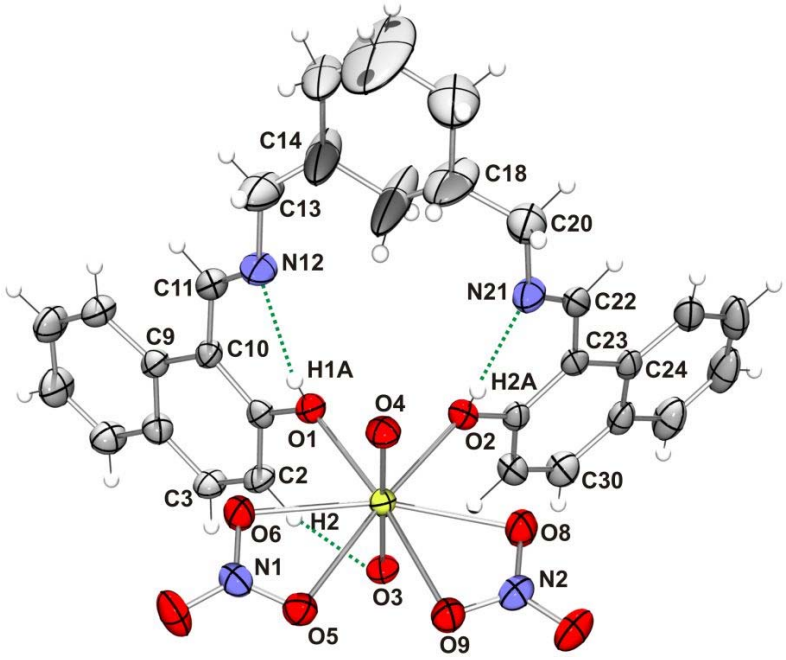

Figure 85. An ORTEP diagram for the asymmetric unit of **20**. Thermal ellipsoids are shown at the 50% probability level.

Table 33. Selected Bond lengths [Å] and angles [°].

$[UO_2(\mathbf{L}^{8})(NO_3)_2]$ (**17**)

U-O(8)	1.760(2)	U-O(1)	2.324(1)
U-O(9)	1.763(2)	U-O(26)	2.311(2)
U-O(2)	2.519(2)	U-O(5)	2.579(3)
U-O(3)	2.575(2)	U-O(6)	2.596(3)
O(8)-U-O(9)	178.09(11)	O(1)-U-O(26)	75.49(9)
O(1)-U-O(8)	90.19(9)	O(26)-U-O(8)	85.91(10)
O(1)-U-O(9)	90.64(8)	O(26)-U-O(9)	95.96(8)
O(2)-U-O(3)	49.25(7)	O(5)-U-O(6)	48.02(11)

$[UO_2(\mathbf{L}^{10})(NO_3)_2]$ (**18**)

U-O(7)	1.750(3)	U-O(10)	2.358(3)
U-O(8)	1.739(4)	U-O(9)	2.345(3)

Table 33. continued.

U-O(2)	2.504(3)	U-O(4)	2.519(4)
U-O(3)	2.544(3)	U-O(5)	2.547(4)
O(7)-U-O(8)	178.63(17)	O(9)-U-O(10)	71.27(12)
O(10)-U-O(7)	88.69(13)	O(9)-U-O(7)	86.77(14)
O(10)-U-O(8)	91.74(13)	O(9)-U-O(8)	94.60(15)
O(2)-U-O(3)	50.32(11)	O(4)-U-O(5)	50.3(11)
$[UO_2(\mathbf{L}^{13})(NO_3)_2]$ (**20**)			
U-O(3)	1.765(3)	U-O(2)	2.335(2)
U-O(4)	1.763(3)	U-O(1)	2.385(3)
U-O(5)	2.570(3)	U-O(8)	2.509(3)
U-O(6)	2.546(3)	U-O(9)	2.534(3)
O(3)-U-O(4)	179.34(13)	O(1)-U-O(2)	71.63(9)
O(2)-U-O(3)	93.34(11)	O(1)-U-O(3)	92.30(12)
O(2)-U-O(4)	86.73(14)	O(1)-U-O(4)	88.34(12)
O(5)-U-O(6)	49.48(9)	O(8)-U-O(9)	50.16(11)

Table 34. D–H···A interactions in **17**, **18** and **20**.

D – H	***A***	**H···*A* [Å]**	**D···*A* [Å]**	**D–H···*A* [°]**
$[UO_2(\mathbf{L}^{8})(NO_3)_2]$ (**17**)				
O(1)–H(1)	N(9)	1.98	2.62	134
O(26)–H(26)	N(18)	1.94	2.67	149
C(3)–H(3)	O(9)	2.45	3.20	138
C(8)–H(8)	$O(5)^{i}$	2.48	3.29	145
C(19)–H(19)	$O(2)^{ii}$	2.56	3.25	132
C(23)–H(23)	$O(3)^{iii}$	2.60	3.38	142
C(10)–H(10B)	$Cg(1)^{i}$	2.61	3.54	162
C(17)–H(17A)	$Cg(3)^{ii}$	2.86	3.74	152
C(22)–H(22)	$Cg(1)^{iv}$	3.05	3.84	143

Table 34. continued.

$[UO_2(\mathbf{L}^{10})(NO_3)_2]$ (**18**)				
O(10)–H(10)	N(21)	1.81	2.57	150
O(9)–H(9)	N(12)	1.85	2.60	149
C(2)–H(2)	O(8)	2.51	3.30	141
C(11)–H(11)	$O(3)^{v}$	2.35	3.17	144
C(13)–H(13B)	$O(3)^{v}$	2.58	3.45	146
C(22)–H(22)	$O(6)^{vi}$	2.46	3.39	168
C(25)–H(25)	$O(6)^{vi}$	2.54	3.48	171
C(6)–H(6)	$Cg(3)^{vii}$	2.71	3.55	148
C(13)–H(13A)	$Cg(1)^{v}$	2.70	3.40	127
C(20)–H(20B)	$Cg(5)^{vi}$	2.92	3.80	148
$[UO_2(\mathbf{L}^{13})(NO_3)_2]$ (**20**)				
O(1)–H(1A)	N(12)	1.99	2.60	128
O(2)–H(2A)	N(21)	1.88	2.58	139
C(2)–H(2)	O(3)	2.45	3.23	140
C(11)–H(11)	$O(6)^{v}$	2.59	3.45	150
C(20)–H(20A)	$O(8)^{viii}$	2.60	3.40	138
C(13)–H(13B)	$Cg(1)^{v}$	2.83	3.68	145
C(13)–H(13B)	$Cg(2)^{v}$	2.96	3.90	160

Symmetry codes: (i) = −x,1−y,1−z; (ii) = 1−x,−y,2−z ; (iii) = −x,1−y,2−z; (iv) = −x,−y,2−z; (v) = −x,1−y,−z; (vi) = 1/2−x,−1/2+y,1/2−z; (vii) = −x,y,1/2−z; (viii) = 1−x, 2−y,1−z

The nitrate oxygen atoms are at the range distance of 2.519-2.596 Å (**17**), 2.504-2.547 Å (**18**) and 2.509-2.570 Å (**20**) from the U atom. The imine nitrogen atoms do not form a bond with the U(VI) ion but acts as a base accepting a phenolic proton via a strong hydrogen bond interaction with N···H bond distances of about (1.98 and 1.94 Å), (1.81 and 1.85 Å) and (1.88 and 1.99 Å) in **17**, **18** and **20** respectively and increasing the distortion of the geometry around the uranyl moiety. The neutral form of the ligand allows the nitrate anions to remain coordinated to the uranyl cation without disturbing the charge balance. The approximate coordination spheres around the U(VI) ion are distorted hexagonal-bipyrimidal with axial O=U=O moiety and six oxygen atoms in equatorial

position. However, the plane of the six coordinated oxygen atoms resembles a four-coordination plane if the nitrate group is taken as a single donor as the oxygen atoms of the nitrate ions and the uranium ions (O-U-O) only form very small angles (48.0 and 49.3°) (**17**), (50.3°) (**18**) and (49.5 and 50.2°) (**20**). The U=O distances and O=U=O angles in **17** (av. 1.76(2) Å; 178°), **18** (av. 1.75(4) Å; 179°) and **20** (av. 1.76(3) Å; 179°) are typical of the corresponding distances and angles reported for similar uranyl compounds [131, 138, 140, 152]. The terminal aryl groups are present in these complexes on one side of the plane with a 'boat' like appearance (Figure 86). Such a conformation has been reported for various mononuclear uranyl Schiff base complexes and attributed to the strong interaction of the ligand with the uranyl metal, which forces the ligand to conform to the coordination geometry of the metal [138, 153].

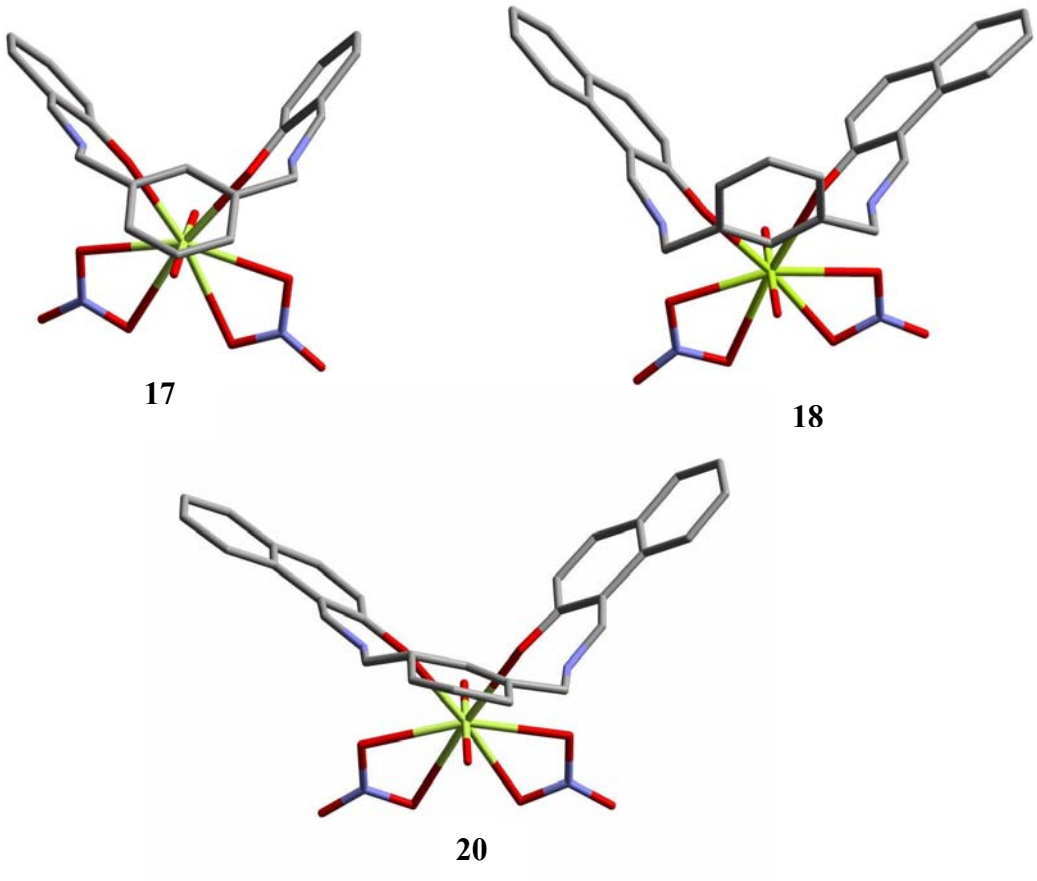

Figure 86. Distortion of the structures observed in the backbone of **17, 18** and **20**.

Extensive weak interactions are observed in **17**, **18** and **20** as some nitrate oxygen atoms bridge adjacent molecules in their extended structures through hydrogen bond interactions in a range of 2.48-2.60 Å (**17**), 2.35-2.58 Å (**18**) and 2.59-2.60 Å (**20**) (Table 34). Also, weak intramolecular hydrogen bond interactions are observed between one of the uranyl oxygen and one hydrogen atom (adjacent to the binding OH group); the distances C–H···O=U (C···O) are 3.20 Å, 3.30 Å and 3.23 Å in **17**, **18** and **20** respectively. Similar interactions have been described in hydrated oxides of U(VI) where the uranyl oxygen are weakly associated with the water molecules present in the inter layer [154]. In **17**, **18** and **20,** molecules are stacked together via relatively strong π-π {3.64 Å (**17**), 3.76-3.79 Å (**18**), 3.61-3.79 Å (**20**) and CH-π {2.61-3.05 Å (**17**), 2.70-2.92 Å (**18**), 2.83-2.96 Å (**20**)} interactions (Figure 87–90). The geometrical details of the π-π interactions are listed in Table 35.

Table 35. π–π interactions in **17**, **18** and **20**.

Cg	***Cg***	***Cg*···*Cg* [Å]**	***β* [°]**	***CgI*···perp [Å]**
$[UO_2(\mathbf{L}^{8})(NO_3)_2]$ (**17**)				
*Cg*3	*Cg*3^{i}	3.644	9	3.60
$[UO_2(\mathbf{L}^{10})(NO_3)_2]$ (**18**)				
*Cg*1	*Cg*1^{ii}	3.757	22	3.48
*Cg*1	*Cg*2^{ii}	3.790	25	3.49
$[UO_2(\mathbf{L}^{13})(NO_3)_2]$ (**20**)				
*Cg*2	*Cg*2^{iii}	3.794	22	3.53
*Cg*4	*Cg*5^{iv}	3.926	18	3.42

Symmetry codes: (i) = 2-x, 2-y, -z; (ii) = -x, y,1/2-z; (iii) = -x, -y, -z; (iv) = 1-x, 1-y, 1-z

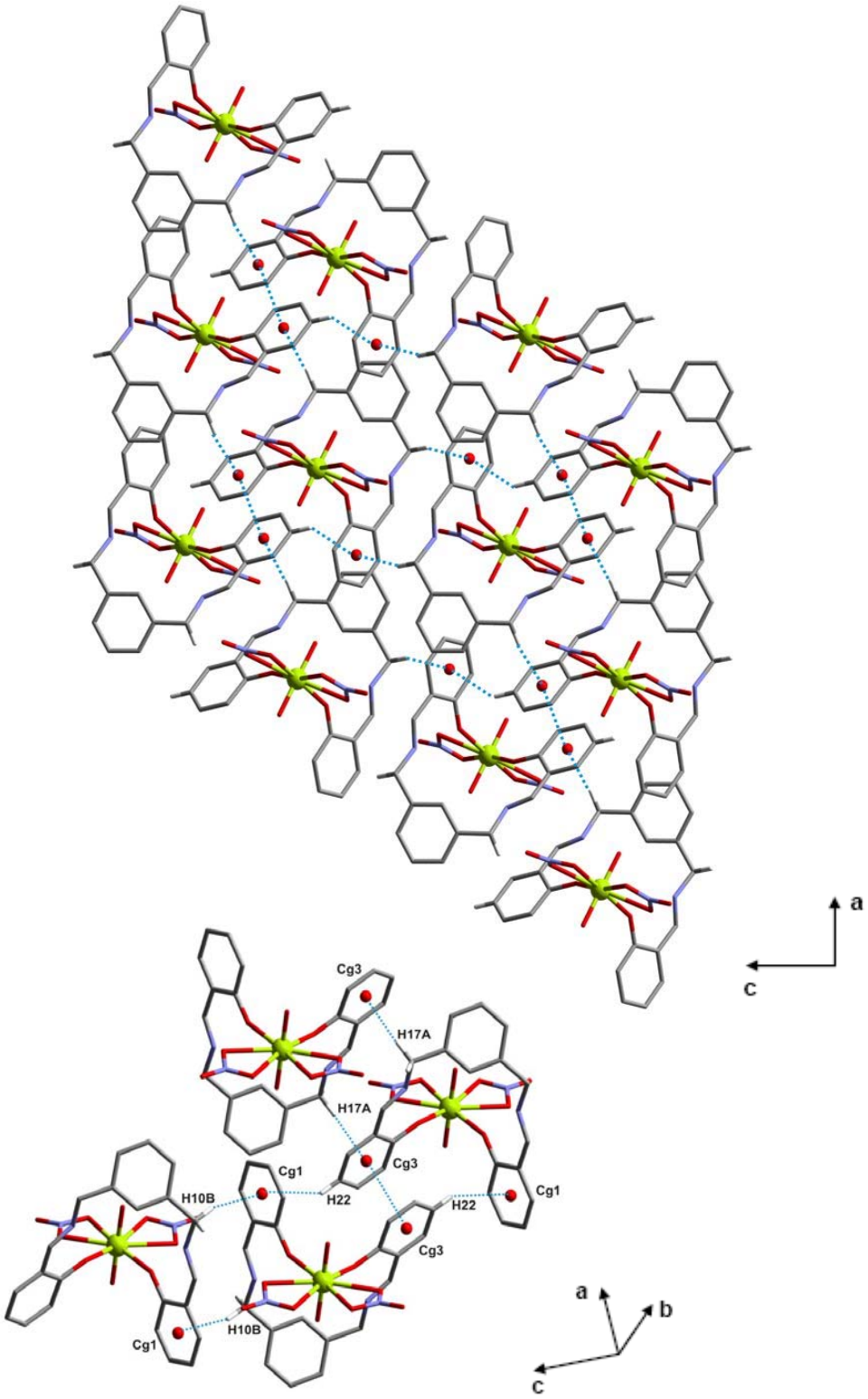

Figure 87. Crystal packing for **17** showing the different π-π and CH-π interactions.

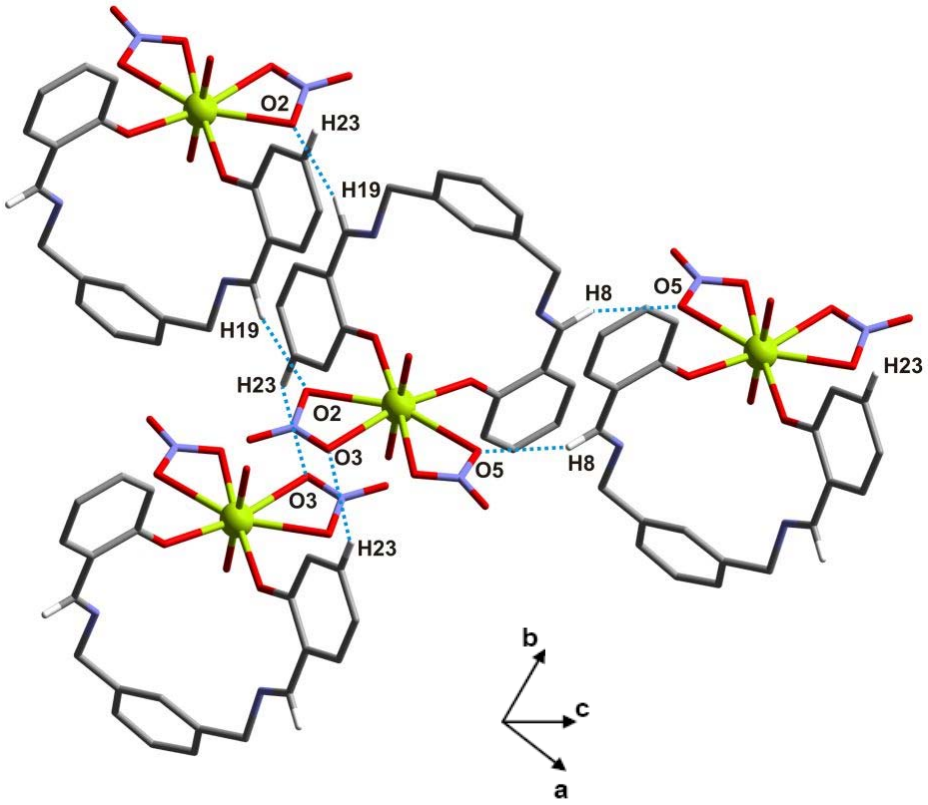

Figure 88. Crystal packing for **17** showing the hydrogen bond interactions.

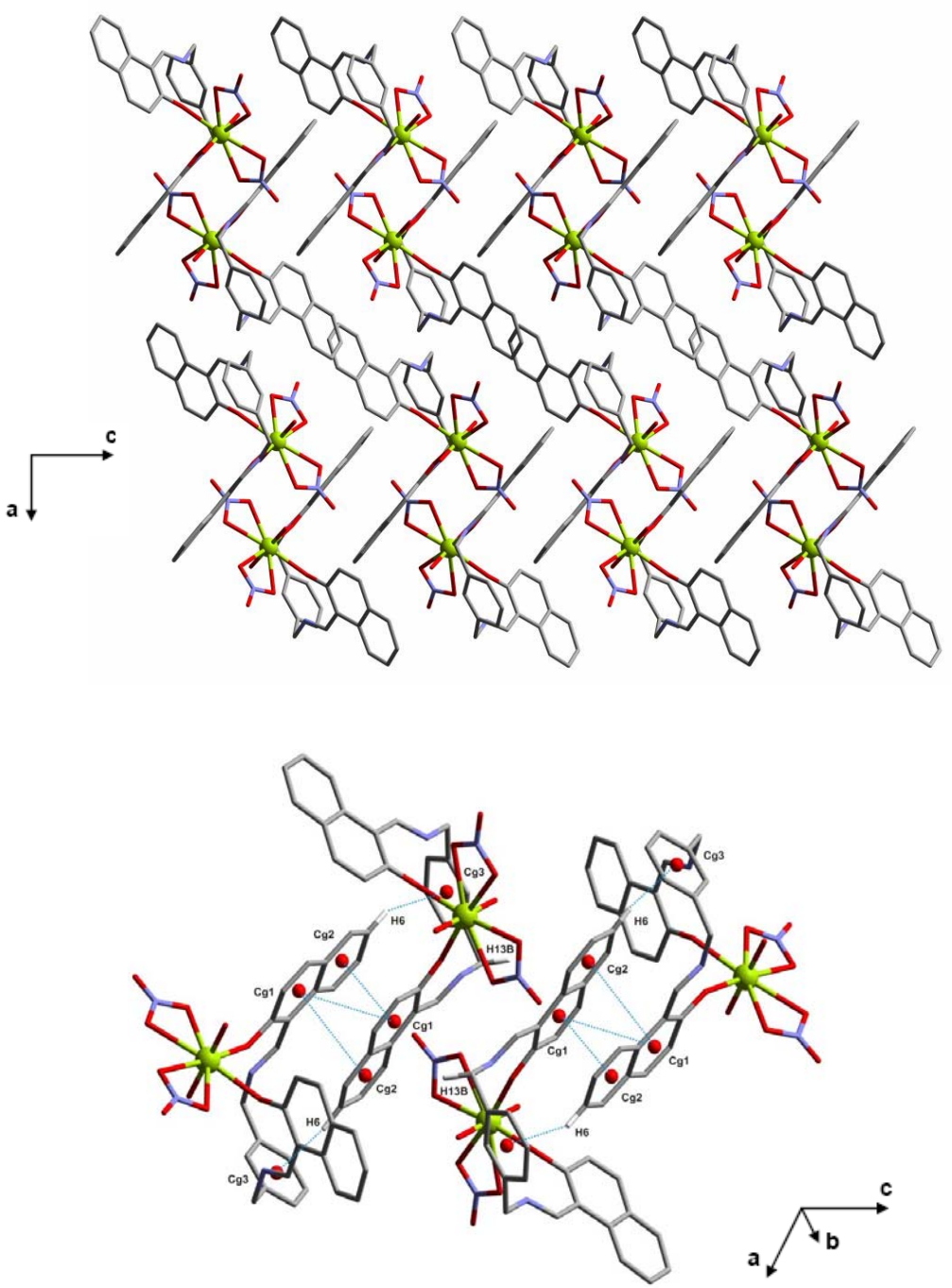

Figure 89. Crystal packing for **18** showing the different π-π and CH-π interactions.

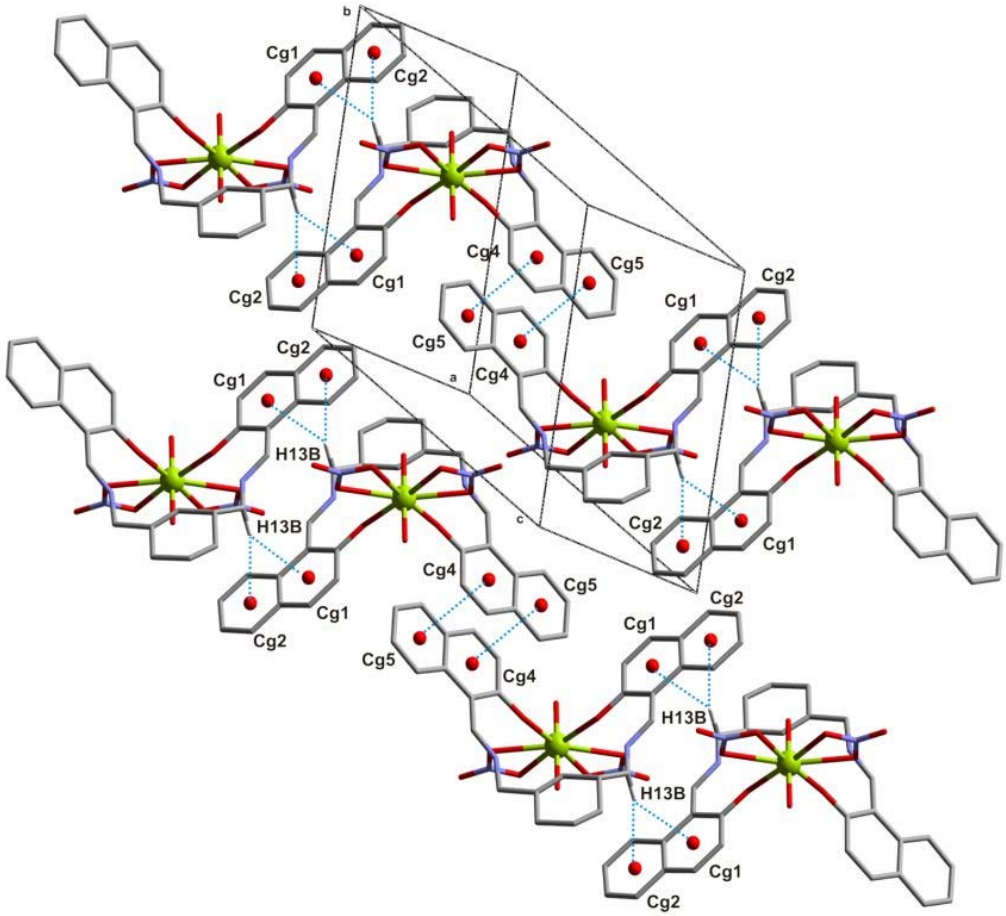

Figure 90. Crystal packing for **20** showing the different π-π, and CH-π interactions.

3.2.3 DFT calculation

In addition to the structural studies of the $UO_2(NO_3)_2$ complex with ligand **L**^{8} (= complex **17**) some DFT calculations have been performed in methanol as solvent. The goal was to model the structure of a possible complex between UO_2^{2+} and the deprotonated ligand **L**^{8} and to compare these results with the structure and the relative Gibbs energy of the corresponding complex with the neutral ligand **L**^{8}. The calculated structures **M1**-**M4** are given in Figure 91.

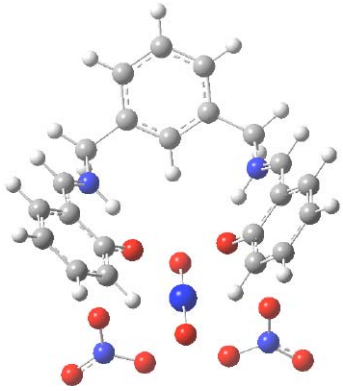

M1

more stable by 101.5 kJ/mol

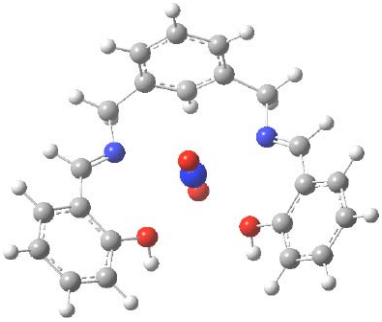

M2

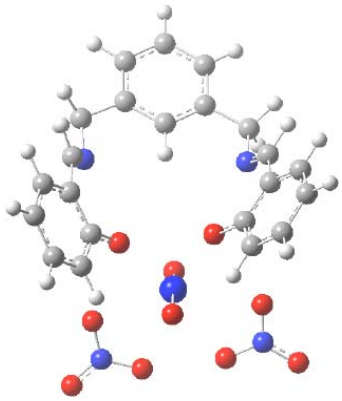

M3

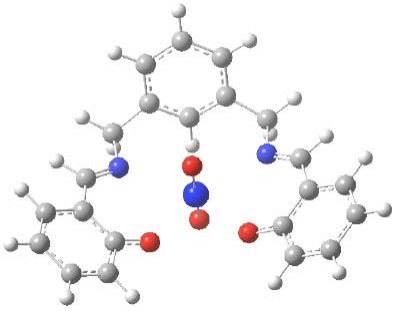

M4

more stable by 172.2 kJ/mol

Figure 91. Calculated structures of the uranyl complexes with the neutral (**M1**, **M2**) and the deprotonated ligand **L**^{8} **(M3, M4)** optimized in CH_3OH at the B3LYP level.

The studies show that in case of the neutral ligand the complex **M1**, $[UO_2(\mathbf{L}^8)(NO_3)_2]$, with an analogous coordination pattern as the crystalline complex **17** is more stable than **M2** fixing the uranyl species in the pseudoring of $\mathbf{L}^8$ by binding through the imine nitrogen atoms and the oxygen donors of the OH function. The relative Gibbs energy difference between both forms is 184.4 kJ/mol. **M3** and **M4** are modelled uranyl complex structures with the twofold negatively charged deprotonated ligand $\mathbf{L}^8$. In this case a neutral chelate complex can be formed and additional nitrate anions do not stabilize the structure. Therefore the formation of the complex **M4** with the formula $[UO_2(\mathbf{L}^8\text{-}2H^+)]$ is favoured with 172.2 kJ/mol. Table 36 shows bond lengths and angles for the complexes **M1**-**M4** calculated by DFT. These results are in good agreement with the crystallographic data discussed above.

Table 36. Bond lengths [Å] and angles [°] of calculated UO_2^{2+} complexes with the neutral and the deprotonated ligand $\mathbf{L}^8$.

	$\mathbf{L}^8$ (neutral)		$\mathbf{L}^8$ (deprotonated)	
	M1	**M2**	**M3**	**M4**
U-O_{ax}	1.776, 1.782	1.755, 1.757	1.791, 1.792	1.787, 1.792
U-O_{nit}	2.611, 2.615	--	2.666, 2.742	--
	2.613, 2.615		2.763, 2.764	
U-O	2.322, 2.324	2.434, 2.434	2.212, 2.237	2.215, 2.217
U-N	--	2.542, 2.544	--	2.641, 2.646
O-H	1.856, 1.860	0.991, 0.991	--	--
N-H	1.021, 1.022	--	--	--

According to the Mulliken population analysis, uranium in **M1** and **M2** has nearly the same net population in all of *s*, *p*, *d*, and *f* orbitals. They are *s* 4.23 (4.22), *p* 11.98 (11.93), *d* 11.86 (11.81), and *f* 2.52 (2.49) for **M1** (**M2**). However, a further detailed analysis of the data reveals that the *f* population has breakdown of $5f_\sigma$ 0.38 (1.03), $5f_\pi$ 1.01 (1.11),

$5f_\delta$ 0.81(0.12), and $5f_\phi$ 0.32 (0.22) for **M1** (**M2**). There are much larger contribution from $5f_\sigma$ and $5f_\delta$ in **M2** and **M1**, respectively. Among the MOs near the HOMO (highest occupied MO) in **M2**, the $5f_\sigma$ contribute mainly to the HOMO-10 (tenth orbital below the HOMO). This MO has anti-bonding character with respect to the UO_2^{2+} unit (as shown in Figure 92) and does not contribute to the uranium-ligand binding. The $5f_\delta$ in **M1**, on the other hand, also contribute little to chemical bond because of its non-bonding nature. From the above Mulliken population analysis, we see no decisive reason why **M1** is favoured over **M2**. Therefore we further analyzed the MOs of **M1** and **M2**. Among a set of MOs near the HOMO in **M1,** HOMO-1 contribute largely to the π bond between U and oxygen of OH, and HOMO-8 and HOMO-9 contribute to the π bond between U and nitrate ligands (Figure 93). On the contrary, among the twenty MOs between HOMO and HOMO-20 in **M2**, none of these MOs contributes to the U to ligand oxygen π bond. U(VI) at the ligand periphery like in **M1** have a stronger uranium to ligand interaction and therefore that is the more stable form of the complex.

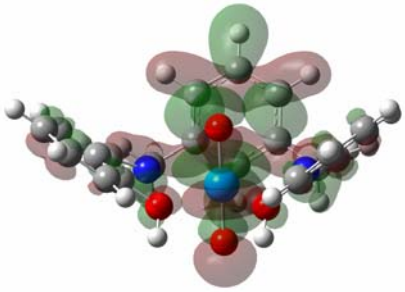

Figure 92. The molecular orbital HOMO-10 in **M2**. The isovalue of the plot is 0.02 a.u.

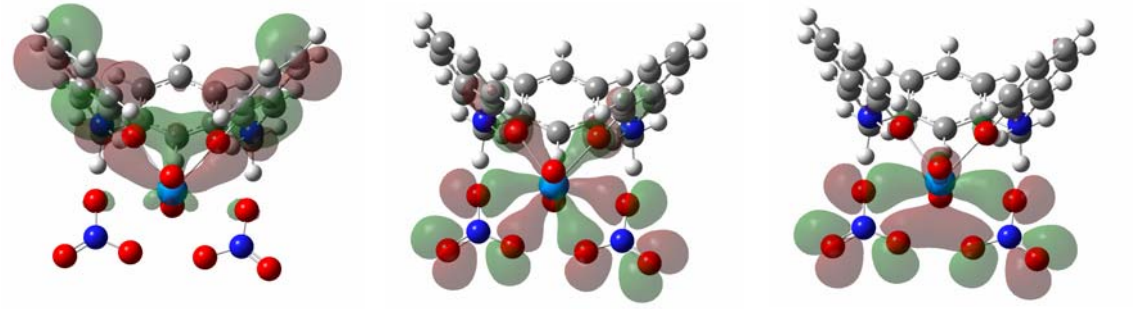

Figure 93. The molecular orbitals near the HOMO in **M1**. From left to right, HOMO-1, HOMO-8, and HOMO-9. The isovalue of the plot is 0.02 a.u.

3.3 Liquid-liquid extraction studies of Eu^{3+} and UO_2^{2+} with selected ligands

Liquid-liquid extraction was used to characterize the phase transfer properties of the ligands towards Eu(III) and U(VI) using the extraction system $Eu(NO_3)_3$ or $UO_2(NO_3)_2$–$NaNO_3$-buffer–H_2O/ ligand–$CHCl_3$.

This technique plays an important role in analytical chemistry, in separation and purification processes as well as in the hydrometallurgical metal winning from primary and secondary resources [155-157]. In addition, the liquid-liquid extraction can also be used for characterization of complex formation in solution [158-161]. However, there is a significant difference between the complex formation equilibrium in the homogeneous single-phase and the extraction equilibrium in the complicated heterogeneous two-phase system [162]. In that case the quantitative analysis becomes difficult because additional processes in both phases possess a decisive influence on the equilibrium [163-165].

The extraction of a metal ion with a neutral ligand can be described according to the following simplified scheme (Figure 94).

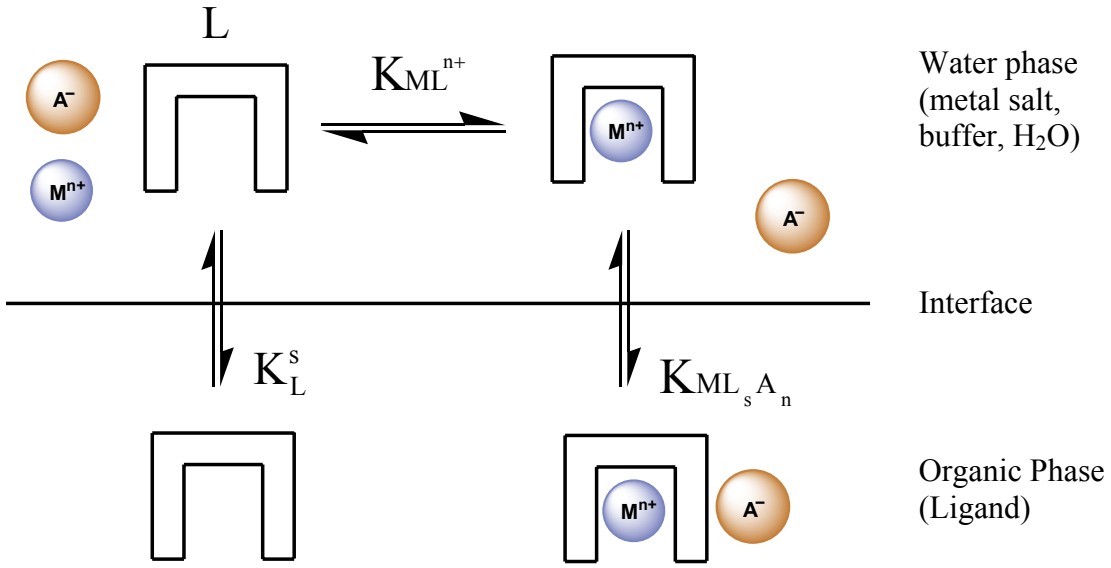

Figure 94. Schematic representation of cation extraction by neutral ligands.

Generally, the extraction equilibrium is expressed according to the equations (1) and (2)

$$M^{n+}_{(w)} + n \cdot A^-_{(w)} + s \cdot L_{(org)} \underset{}{\overset{K_{ex}}{\rightleftharpoons}} (ML_sA_n)_{(org)} \quad (1)$$

$$K_{ex} = \frac{[ML_sA_n]_{(org)}}{[M^{n+}]_{(w)}[L]^s_{(org)}[A^-]^n_{(w)}} \quad (2)$$

To minimize the influence of changes of the activity coefficients on the equilibrium constant K_{ex} [Eq. (2)], it is necessary to work at a nearly constant ionic strength in both phases. Therefore a large excess of the counter ion and of the organic ligand was used for the experiments.

As shown in Figure 94, the extraction equilibrium can be divided into three individual equilibria: the distribution of the free ligand with K_L [Eq. (3)], the complexation in the aqueous phase with $K_{ML_s^{n+}}$ [Eq. (4)], and the distribution of the extracted complex with K_{MLsAn} [Eq. (5)].

$$K_L = \frac{[L]_{(org)}}{[L]_{(w)}} \quad (3)$$

$$K_{ML_s^{n+}} = \frac{[ML_s^{n+}]_{(w)}}{[M^{n+}]_{(w)}[L]^s_{(w)}} \quad (4)$$

$$K_{ML_sA_n} = \frac{[ML_sA_n]_{(org)}}{[ML_s^{n+}]_{(w)}[A^-]^n_{(w)}} \quad (5)$$

The dissociation of the metal complex (ML_sA_n) in the organic phase with low polar solvents can be neglected. Then the extraction equilibrium constant K_{ex} [Eq. (6)] can be described also by these three individual equilibrium constants:

$$K_{ex} = \frac{K_{ML_s^{n+}} \cdot K_{ML_sA_n}}{K_L^s} \tag{6}$$

The characterization of the phase transfer of a metal ion M^{n+} is experimentally accessible through the distribution ratio D_M [Eq. (7)] or the percentage extraction E [%] [Eq. (8)], also known as extraction yield or degree of extraction.

$$D_M = \frac{[ML_sA_n]_{(org)}}{[M^{n+}]_{(w)}} \tag{7}$$

$$E[\%] = \frac{D_M}{\left(D_M + \frac{V_{(w)}}{V_{(org)}}\right)} \cdot 100 \tag{8}$$

Considering that there are no other extraction species and that the activity coefficients are approximately constant, equations (9) and (10) can be deduced from (2) and (7).

$$D_M = K_{ex} \cdot [A^-]_{(w)}^n \cdot [L]_{(org)}^s \tag{9}$$

$$\lg D_M = \lg K_{ex} + n \cdot \lg[A^-]_{(w)} + s \cdot \lg[L]_{(org)} \tag{10}$$

Using the equation (10) the coefficients (s) and (n) can be determined from plots of corresponding experimental data in lg D_M - lg $[L]_{(org)}$ or lg D_M - lg $[A^-]$ diagrams. These stoichiometric coefficients give the number of ligand molecules and anions bound in the extracted complex.

The Figures 95 and 96 give an overview of the extractabilities of UO_2^{2+} and Eu^{3+} for all the ligands studied at comparable experimental conditions. It is clearly shown that the ligands possess a remarkable selectivity for U(VI) over Eu(III). Especially the amine ligands **L**[9] and **L**[11] allow a high extraction of UO_2^{2+} (Figure 95, 96). The time for achieving the extraction equilibrium is above 1 h (Figure 96). The significant lower extractabilities for the Schiff bases are obviously caused by the weaker basicity of the imine nitrogen donors and the resulting lower complex stability of the UO_2^{2+} complexes.

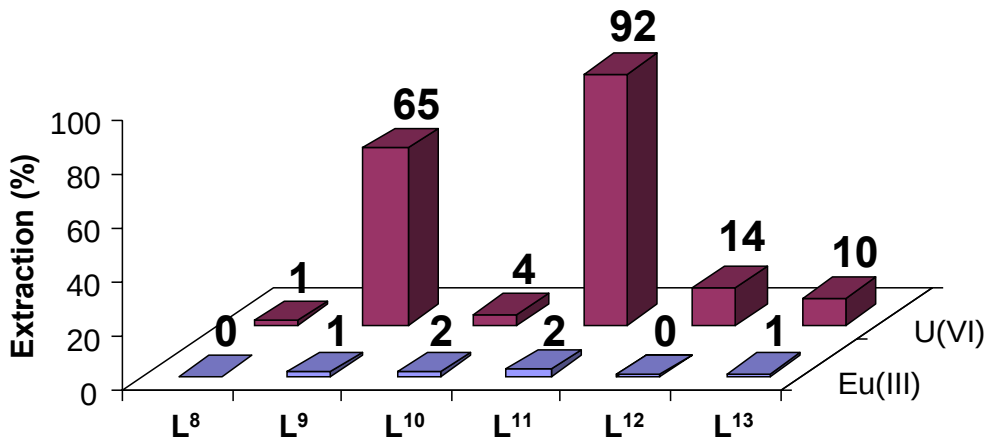

Figure 95. Percentage of metal ion extraction by **L**[8]**–L**[13]. [L] = 1 x 10^{-2} M in $CHCl_3$, [U(VI)] = [Eu(III)] = 1 x 10^{-4} M, [$NaNO_3$] = 5 x 10^{-3} M, pH = 5.2 (HEPES/HNO_3 buffer), shaking time 60 min, T = 23 ± 1°C.

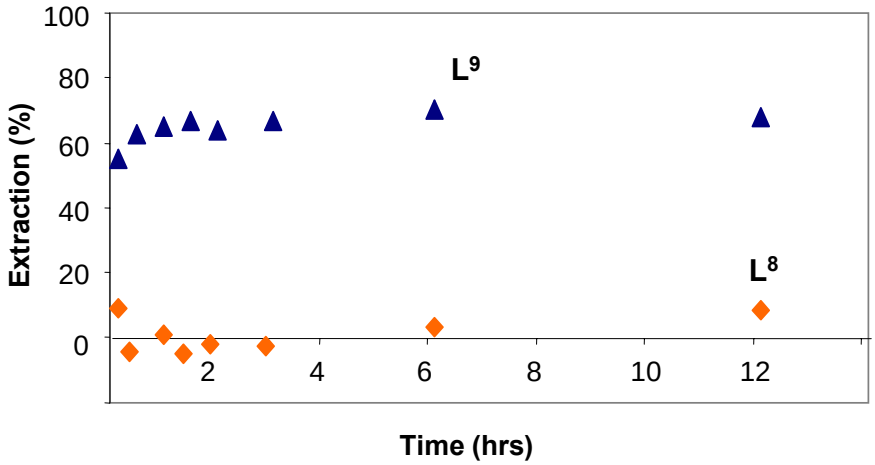

Figure 96. Time dependence of U(VI) extraction with **L**[8] and **L**[9]. [L] = 1 x 10^{-2} M in $CHCl_3$; [U(VI)] = 1 x 10^{-4} M, [$NaNO_3$] = 5 x 10^{-3} M, pH = 5.2 (HEPES/HNO_3 buffer), T = 23 ± 1°C, t = 10–720 min.

Results of studies on the extraction of U(VI) with **L**[8] and **L**[9] in dependence on the pH are presented in Figure 97. It is clearly shown that the extraction yields for both ligands significantly rise with increasing pH. The maximum extraction is reached between pH 7 and 8. This trend is in agreement with a changing protonation state of the ligands in dependence on the pH, which is obviously caused by both the deprotonation of the OH (**L**[8] and **L**[9]) and amine (**L**[9]) functions.

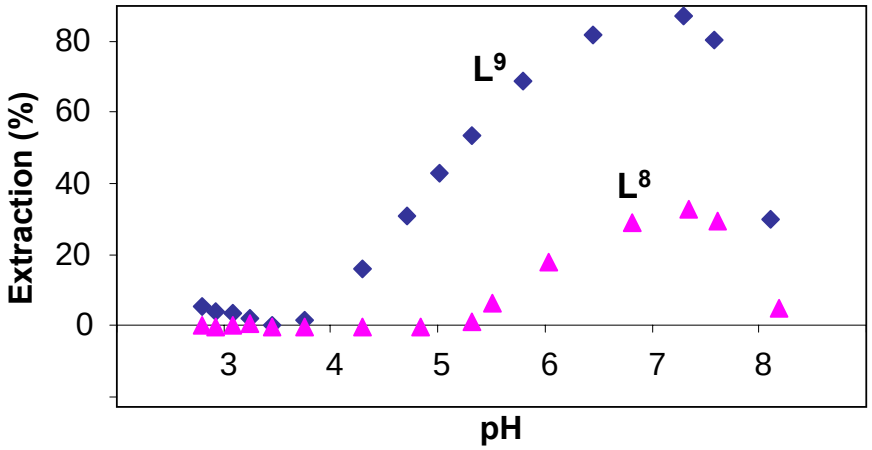

Figure 97. Extraction of U(VI) with **L**[8] and **L**[9] as a function of pH. [L] = 1 x 10^{-2} M in $CHCl_3$, [U(VI)] = 1 x 10^{-4} M, [$NaNO_3$] = 5 x 10^{-3} M, pH = 2–6 (HEPES/HNO_3 buffer), pH = 6–9 (HEPES/NaOH buffer), shaking time 60 min, T = 23 ± 1°C.

4 The tripodal imine and amine ligand approach

Tripodal multifunctional N-donor ligand systems have been proved to form stable lanthanide (Ln) and actinide (An) complexes and become a promising ligand system for effective separation of An(III) over Ln(III) [166-173].

Tripodal heptadentate amine ligands with hydroxyl groups (**XVII**) (Figure 98) react with a series of lanthanide (Ln) nitrates to yield two different types of complex structures (type A and B in Figure 98) [166]. Type A dinuclear complexes are obtained in the presence of a base (hydroxide or acetate), while type B complexes are obtained from the reaction of lanthanide nitrate with one equivalent of the ligand. Type C structures are formed from the structure analogous Schiff bases. There are two ways to prevent the dimerization in case of type B: one is the introduction of bulky groups at 3-position of the aromatic rings and the other is the increase of the length of the three "chelating arms".

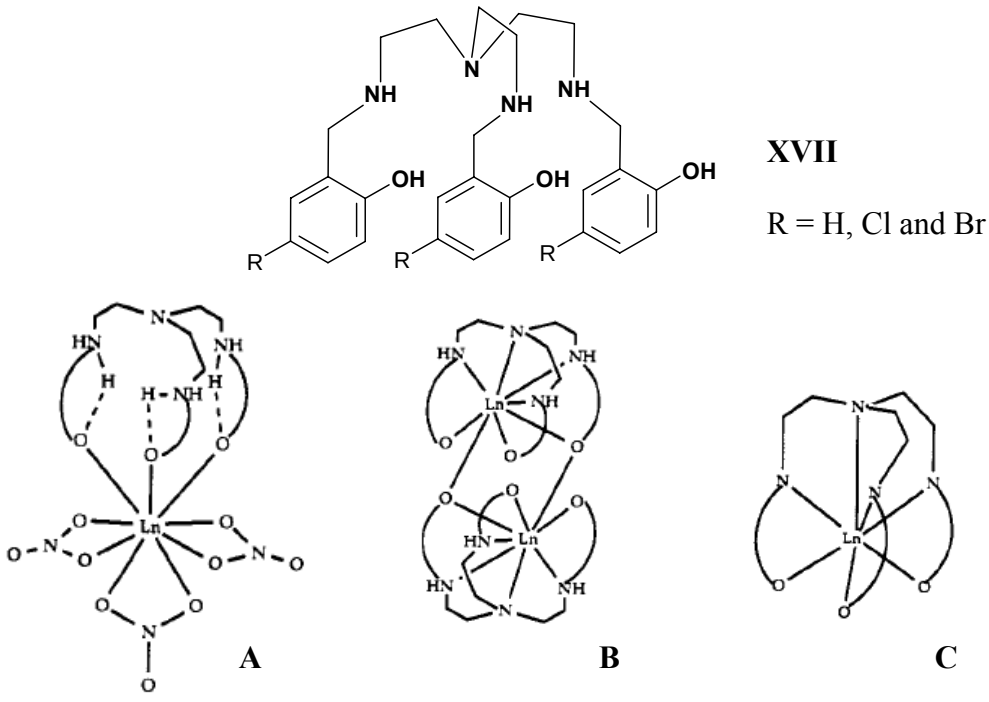

Figure 98. Structures of tripodal heptadentate amine ligands **XVII** and their corresponding complex types A and B with Ln(III). For comparison the complex type C is given showing the typical structure of relating Schiff base complexes with Ln(III) [166].

Reaction of *N,N,N',N'*-tetrakis(2-methylpyridyl)-ethylenediamine ligand (TPEN) (Figure 99) with lanthanide (Ln) metal ions such as La(III), Nd(III), Eu(III), Tb(III) and Y(III) in a water/ethanol mixture lead to isostructural compounds $[Ln(TPEN)(NO_3)_2]NO_3 \cdot 3H_2O$ [167]. The crystal structures of these complexes show that the metal ions are ten-fold coordinated, with six nitrogen donors from the TPEN ligand and four oxygen atoms from two nitrate anions (Figure 99).

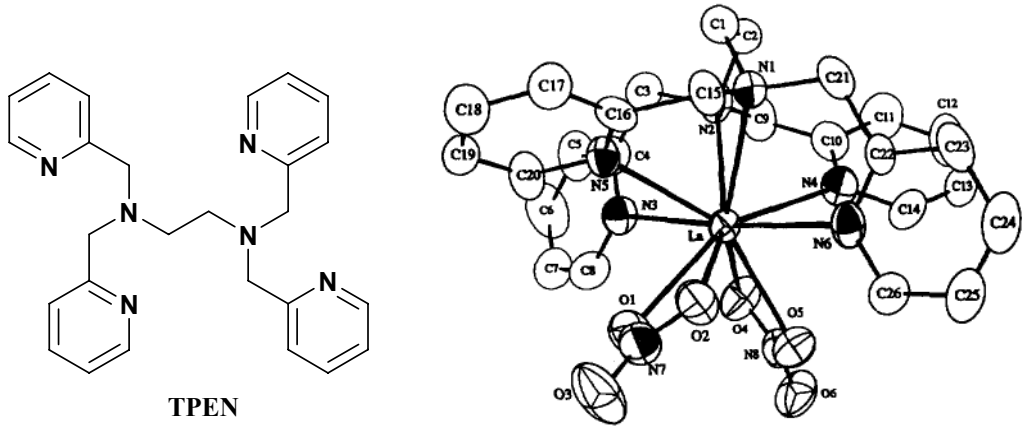

Figure 99. Structure of TPEN and its corresponding 1:1complex with La(III) [167].

Wietzke et al. reported the synthesis and the molecular structure of the first U(III) complex with the heptadentate tripodal aromatic amine tris[(2,2'-bipyridin-6-yl)methyl]amine (tbpa), $[U(tbpa)(I)_2]I \cdot py$, and those of the related lanthanum(III) complex $[La(tbpa)(H_2O)(ClO_4)](ClO_4)_2 \cdot 2CHCl_3 \cdot MeOH$ [168]. The replacement of the iodide ion and of the four "thf" ligands of the starting complex $[UI_3(thf)_4]$ by the heptadentate tbpa results in an increased reactivity towards oxygen and water. The crystal structure of this U(III) complex consists of complex cation-anion pairs and one pyridine molecule connected by hydrogen bonding to three different cations and one anion. The U(III) achieves a coordination number of 9 with tbpa and two iodide anions leading to a capped square antiprismatic coordination geometry while the La(III) has a coordination number of 10 with tbpa, one water molecule and a bidentate perchlorate anion as ligands (Figure 100).

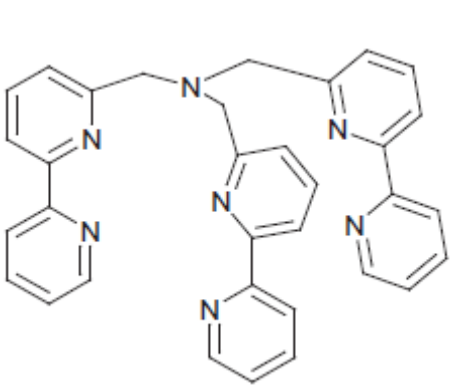

tbpa

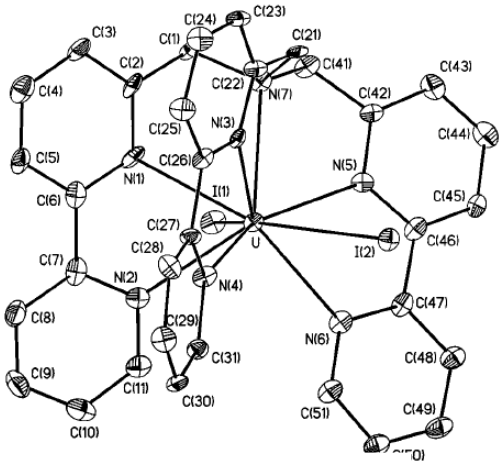

$[U(tbpa)(I)_2]I \cdot py$

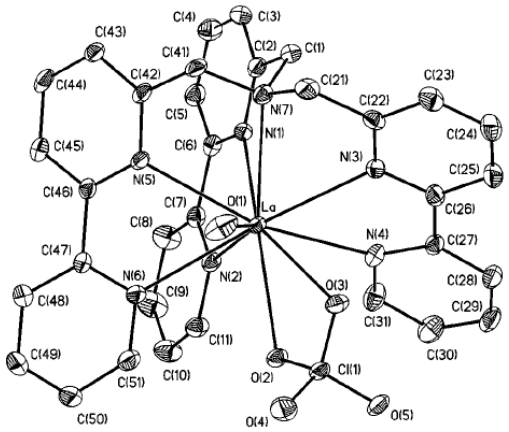

$[La(tbpa)(H_2O)(ClO_4)](ClO_4)_2 \cdot 2CHCl_3 \cdot CH_3OH$

Figure 100. Structure of tbpa and its corresponding U(III) and La(III) complexes [168].

The complexation of Ln(III) by the tripodal ligands tris[(2-pyridyl)methyl]amine (tpa) and tris[(2-pyrazinyl)methyl]amine (tpza) (Figure 101) has been investigated by Wietzke et al [169]. The crystallographic studies show that both ligands, tpa and tpza, form 1:1 complexes in which the tripodal amine acts as a tetradentate ligand. For the tpa complexes the remaining coordination sites are occupied by chloride ions to give sevenfold coordination (Eu, Tb, Lu) (Figure 101) or by chloride ions and a methanol molecule to give eightfold coordination(Nd). In $[Nd(tpza)(H_2O)_3(CH_3CN)_3](ClO_4)_3 \cdot 3H_2O$ (Figure 101) the remaining coordination sites are occupied by water and acetonitrile molecules to give tenfold coordination while the perchlorate ions remain non-

coordinated. The tpza complexes, isolated from acetonitrile solution, dissociate completely in methanol, while the complexes of the more basic tpa can be isolated from methanol; they exist in water in equilibrium with the free ligand. Solvent extraction studies of lanthanides(III) and actinides(III) from nitric acid solutions show that the ligand tpza is, in contrast to tpa, a selective extractant for An(III) ions (Table 37). Considering their structural analogy, this difference could be explained in terms of the electronic differences between the two ligands resulting in a stronger affinity of tpza to An(III) ions.

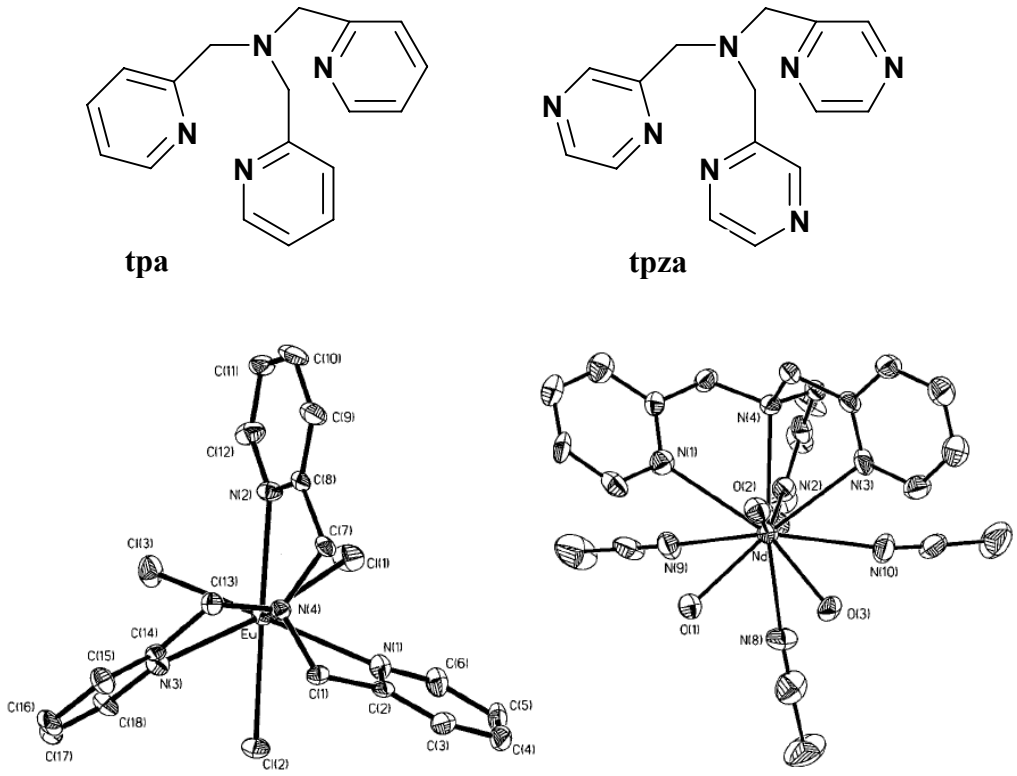

Figure 101. Structures of tpa and tpza ligand and their complexes $[Eu(tpa)Cl_3]$ and $[Nd(tpza)(H_2O)_3(CH_3CN)_3]^{3+}$ [169].

Table 37. Distribution ratios D_M and separation factors SF for Am^{3+} and Eu^{3+} extraction with tpa and tpza ligands [169].

ligand	c (L) (mol/l)	c(HNO_3) (mol/l)	$D_{Am(III)}$ [a]	$D_{Eu(III)}$	$SF_{Am/Eu}$ [b]
tpa	0.001	0.012	0.25	0.13	1.9
	0.001	0.014	0.22	0.12	1.8
	0.001	0.015	0.22	0.13	1.6
tpza	0.02	0.009	4.60	0.43	10.8
	0.02	0.06	0.004	0.0004	10.0
	0.001	0.011	0.46	0.13	3.5
	0.001	0.013	0.44	0.16	2.7

[a]The distribution ratio D_M for a metallic cation M is defined as the ratio of the concentration of the metallic species in organic phase (1 M TPH) over the concentration in aqueous phase. The error of the measure of D_M was estimated to be 5%.[b] The separation factor $SF_{M1/M2}$ for two metal cations M_1 and M_2 is defined as the ratio of their distribution ratios. The error of the measure of SF was estimated to be 10%

Selective separation of Am(III) from Ln(III) with a synergistic extraction system, *N,N,N',N'*-tetrakis(2-methylpyridyl)-ethylenediamine (TPEN) in presence of lipophilic carboxylic acids with 1-octanol as organic solvent, have been done by Watanabe et al. [170]. They found that this extraction system allows not only the selective separation of Am(III) from Ln(III) but also the utilization of the more applicable and acceptable organic solvent 1-octanol. In the case of n-decanoic acid, the separation factor for the pair Am(III)/Eu(III) is about 84 at pH 4.3 (Figure 102). This result confirms the possibility to separate efficiently Am(III) from lighter Ln(III) under such conditions. In the case of n-octanoic acid the separation factor even increases and reaches about 123.

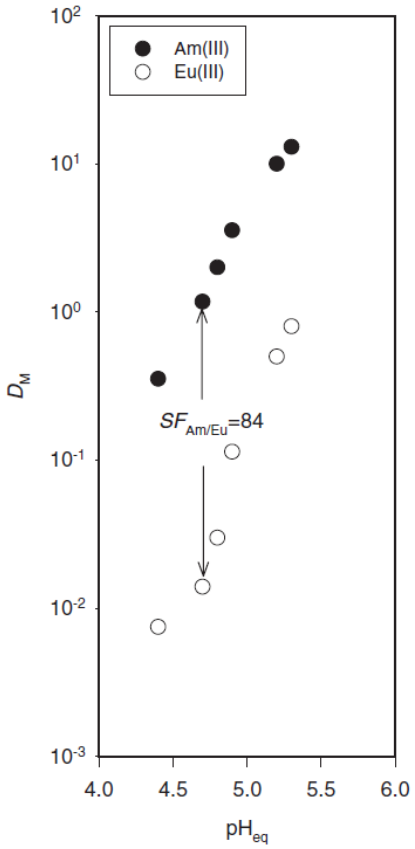

Figure 102. The dependence of the distribution ratios D_M on the equilibrium pH for Am(III) and Eu(III) using the synergistic extraction system TPEN/n-decanoic acid [170].

A further possibility to solve the problem of Ln(III)/An(III) separation is the use of chiral tripodal amine ligands as extractants. One example is shown in Figure 103 using the chiral tris(pyridylmethyl)amines (R)-1, (R,R)-2, and (R,S)-2 [172, 173]. This separation system is characterized by a remarkably high selectivity towards An(III) over Ln(III) driven by the chiral ligands and hydrophobic counter anions. To assess the effects of the ligand structure on the separation factors of An(III), combinations of the tripodal ligands with three different counter anions, picric acid (Pic), n-decanoic acid (Dec), and 2-bromodecanoic acid (Br-Dec), have been investigated. Table 38 shows the results. A combination of the chiral ligands and 2-bromodecanoic acid gave an enhanced extraction performance with pronounced selectivity for Am(III) in comparison with Eu(III).

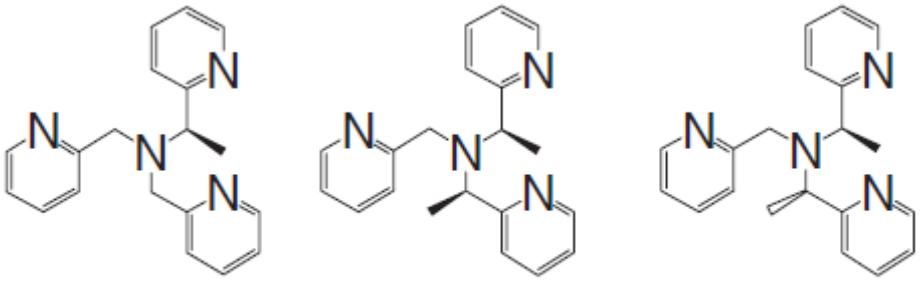

Figure 103. Structures of chiral tripodal amine ligands studied in view of an An(III)/Ln(III) separation [172, 173].

Table 38. Distribution ratios for the Am(III) and Eu(III) extraction with chiral ligands in presence of various counter anions[a] [173].

Counter anion	Ligand	pH	Distribution ratio	
			Am(III)	Eu(III)
Pic	(*R*)-**1**	4.73	1.86	0.23
	(*R*,*R*)-**2**	4.73	0.077	0.0068
	(*R*,*S*)-**2**	4.71	0.0048	0.00037
Dec	(*R*)-**1**	4.70	0.12	0.011
	(*R*,*R*)-**2**	4.70	0.019	0.0011
	(*R*,*S*)-**2**	4.74	0.044	0.0018
Br-Dec	(*R*)-**1**	4.76	52.3	5.42
	(*R*,*R*)-**2**	4.78	14.2	0.67
	(*R*,*S*)-**2**	4.76	26.8	0.95

[a] 1.0×10^{-2} M of ligand, 1.0×10^{-2} M of picric acid, 1.0×10^{-2} M of decanoic acid, 1.0×10^{-2} M of 2-bromodecanoic acid in nitrobenzene and $I = 1.0 \times 10^{-1}$ M $NaNO_3$.

4.1 Ligand syntheses

4.1.1 Synthesis of tripodal imine and amine ligands (L^{14}-L^{20})

Ligands $\mathbf{L^{14}}$-$\mathbf{L^{20}}$ have been synthesized according to the published method of Naiini *et al*. [174] in a two step reaction procedure. First the preparation of the Schiff base by refluxing tris(2-aminoethyl)amine and the respective aldehyde or ketone in absolute ethanol or methanol and the second step was the reduction of the corresponding Schiff bases with KBH_4. The Schiff base ligands were obtained as yellow solids and no further purification was necessary, their amines ($\mathbf{L^{14}}$-$\mathbf{L^{18}}$, $\mathbf{L^{20}}$) were brown yellow oils isolated in high yields. The crude products were dissolved in CH_2Cl_2, washed with distilled water, and the organic solvent was dried with anhydrous $MgSO_4$ and subsequently removed to obtain pure compounds. The ligands are stable in air, and soluble in a range of solvents.

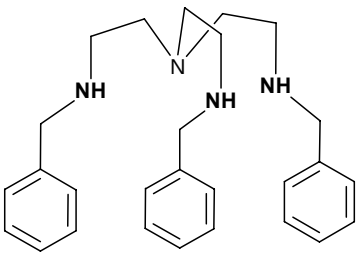

$\mathbf{L^{14}}$

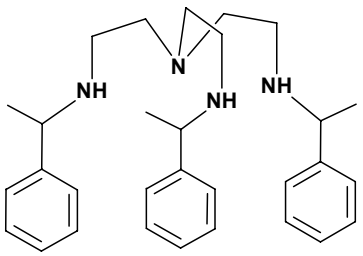

$\mathbf{L^{15}}$

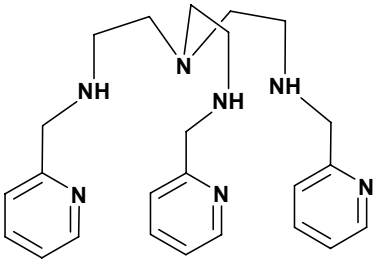

$\mathbf{L^{16}}$

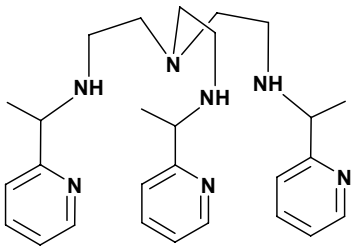

$\mathbf{L^{17}}$

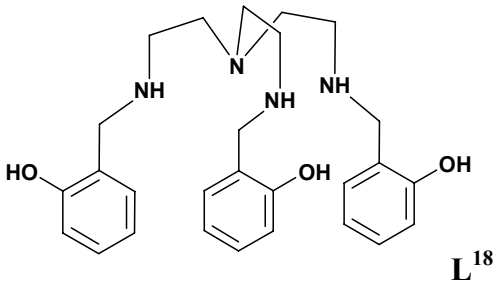

$\mathbf{L^{18}}$

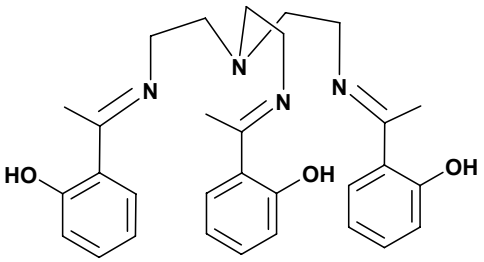

L^{19}

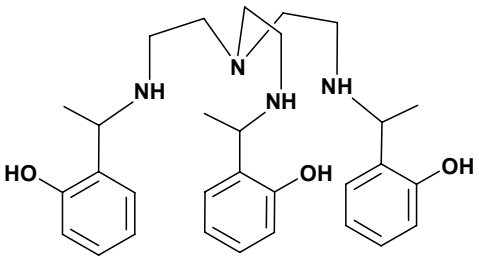

L^{20}

4.1.2 Synthesis of di(2-picolyl)amine ligands (L^{21}-L^{23})

Ligands L^{21}-L^{23} were prepared by *N*-alkylation of 2,2'-dipicolylamine with *m*-xylylenedibromide (L^{21}), 2,6-di(chloromethyl)pyridine (L^{22}) and 2,4,6-trichloro-[1,3,5]triazine (L^{23}). Solutions containing *m*-xylylenedibromide, 2,6-di(chloromethyl)pyridine or 2,4,6-trichloro-[1,3,5]triazine and di-2-picolylamine were refluxed in acetone and concentrated to give brown products which were dissolved in water and extracted with chloroform. The organic layer was dried over $MgSO_4$ and the solvent removed under reduced pressure to give brown oily substances.

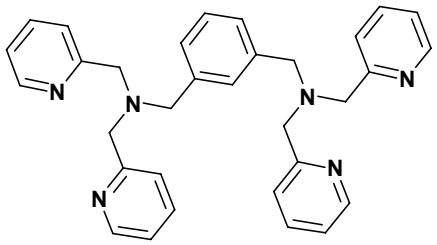

L^{21}

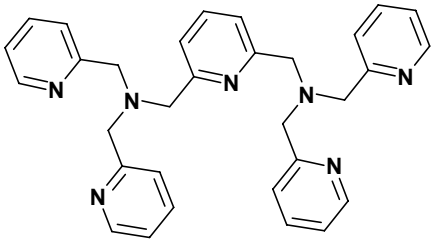

L^{22}

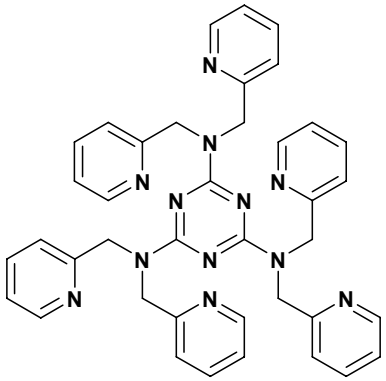

L^{23}

4.2 Synthesis and characterization of U(VI), Nd(III), Eu(III) and Yb(III) complexes

4.2.1 U(VI) Complexes with L^{21}, L^{22}

Reaction of $\mathbf{L^{21}}$ or $\mathbf{L^{22}}$ with $UO_2(NO_3)_2{\cdot}6H_2O$ in a MeOH/MeCN mixture (v/v 1:1) gave brown-orange solutions of complexes **21** and **22**. Crystallization was not successful despite multiple attempts. The ESI mass spectroscopy was used to characterize the solution complexes. ESI spectra show the presence of signals corresponding to $[UO_2(\mathbf{L^{21}})(NO_3)]^+$ and $[UO_2(\mathbf{L^{21}})(NO_3) + MeOH]^+$ at m/z = 833 and 864 for **21** and $[UO_2(\mathbf{L^{22}})(NO_3) + MeOH]^+$ at m/z = 865 for **22** respectively (Figure 104). These data are consistent with the formation of complexes with a 1:1 metal to ligand ratio. The experimental and theoretical isotopic distribution patterns are identical in both cases (Figure 104).

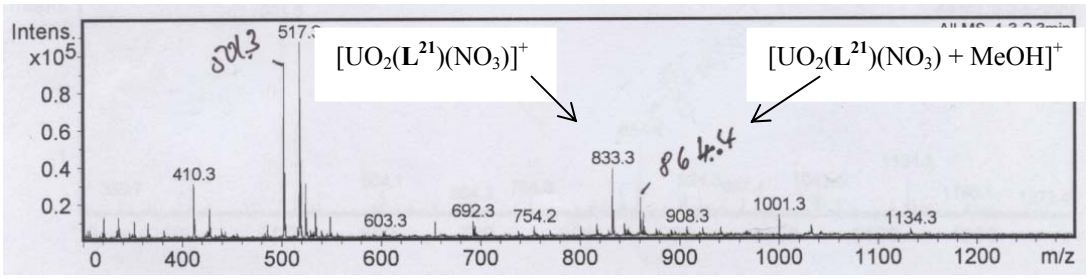

a)

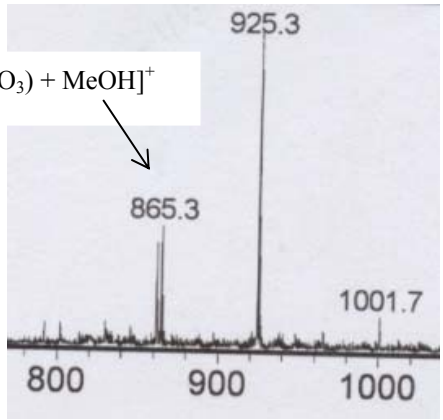

b)

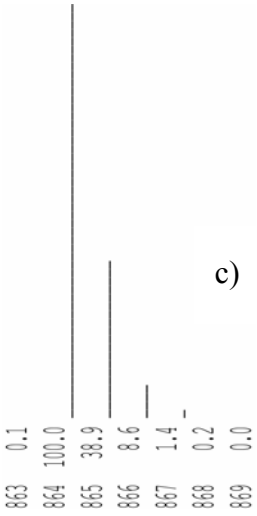

c)

Figure 104. ESI–MS spectra showing the different isotopic patterns in **21** (a) and **22** (b). Theoretical model of $[UO_2(\mathbf{L^{22}})(NO_3) + MeOH]^+$ is shown in (c).

4.2.2 Nd(III), Eu(III) and Yb(III) complexes

Reaction of $Eu(NO_3)_3{\cdot}5H_2O$ or $Nd(NO_3)_3{\cdot}H_2O$ in acetonitrile with ligand $\mathbf{L^{21}}$ in dichloromethane and slow diffusion of diethylether afforded yellow precipitates of $[Eu(\mathbf{L^{21}})(NO_3)_3]$ (**23**) and $[Nd(\mathbf{L^{21}})(NO_3)_3]$ (**24**) complexes in high yields. X-ray quality crystals of these complexes have not been obtained. The ESI mass spectroscopy was used to characterize these complexes. The ESI spectra (Figure 105, 106) show the presence of signals corresponding to $[Eu(\mathbf{L^{21}})(NO_3)_2]^+$ and $[Eu(\mathbf{L^{21}})(NO_3)_3 + H]^+$ at m/z = 777 and 840, respectively, for **23** and $[Nd(\mathbf{L^{21}})(NO_3)_2]^+$ and $[Nd(\mathbf{L^{21}})(NO_3)_3 + H]^+$ at m/z = 766 and 829, respectively, for **24**. As expected, again these data are consistent with the formation of complexes with a 1:1 metal to ligand ratio. The experimental and theoretical isotopic distribution patterns are identical in both cases (Figure 105, 106).

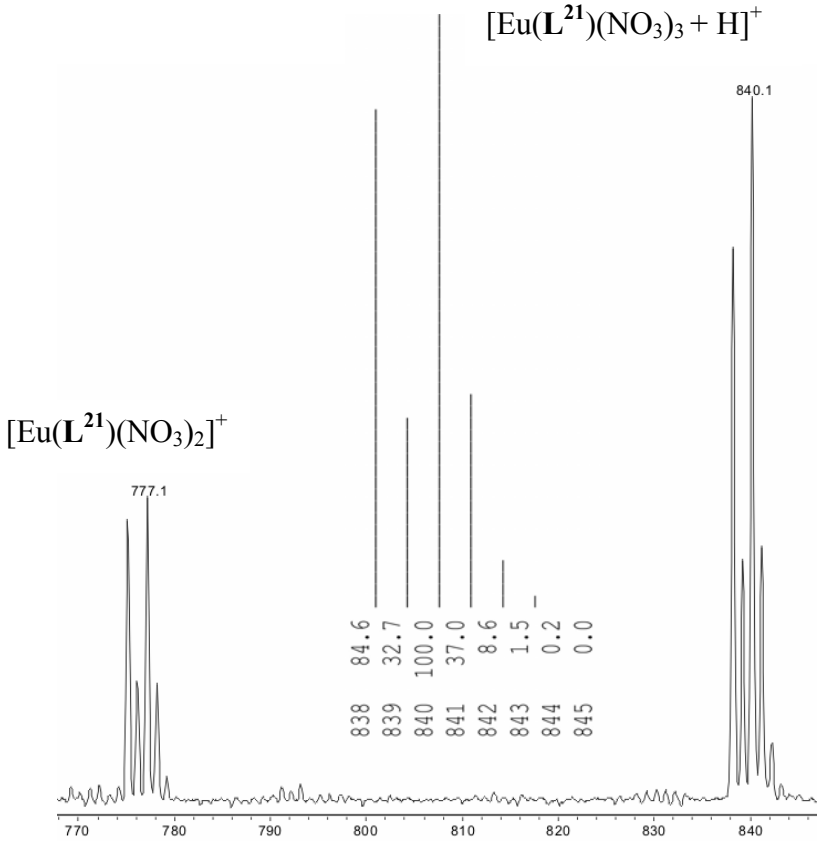

Figure 105. ESI–MS spectrum of **23** and theoretical model of $[Eu(\mathbf{L^{21}})(NO_3)_3 + H]^+$.

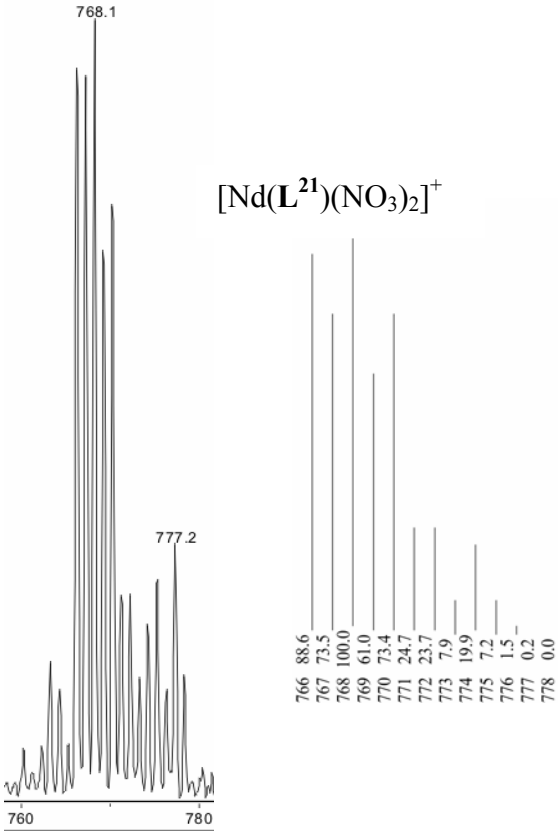

Figure 106. ESI–MS spectrum of **24** and theoretical model of $[Nd(\mathbf{L}^{21})(NO_3)_2]^+$.

The Eu(III) and Yb(III) nitrate complexes of $\mathbf{L}^{23}$ were synthesized by stirring one equivalent of $\mathbf{L}^{23}$ with one equivalent of metal salt in MeCN for 30 min. The white crystalline products $[Eu(\mathbf{L}^{23})(NO_3)_3]$ (**25**) and $[Yb(\mathbf{L}^{23})(NO_3)_3]$ (**26**) were isolated by slow evaporation of the initial reaction mixture at room temperature. Unfortunately crystals were not useful for X-ray analysis. Microanalytical data for these compounds were consistent with a formulation of $[M_n(\mathbf{L}^{23})_n(NO_3)_{3n}]$ and the ESI mass spectroscopy was additionally used to characterize the complexes. Analysis of methanolic solutions of the complexes show the presence of the species $[Eu(\mathbf{L}^{23})_2(NO_3)]^{2+}$ and $[Eu(\mathbf{L}^{23})(NO_3)_2]^+$ at m/z = 780 and 949 respectively for **25** and $[Yb(\mathbf{L}^{23})(NO_3)_2]^+$ at m/z = 970 for **26** (Figure 107). These data point at the formation of 1:1 and 1:2 (Metal:Ligand) complexes for $\mathbf{L}^{23}$ with Eu(III) and a 1:1 complex for for $\mathbf{L}^{23}$ with Yb(III)**.** The experimental and theoretical isotopic distribution patterns are identical in both cases (Figure 107).

$[Eu(\mathbf{L}^{23})(NO_3)_2]^+$ $[Yb(\mathbf{L}^{23})(NO_3)_2]^+$

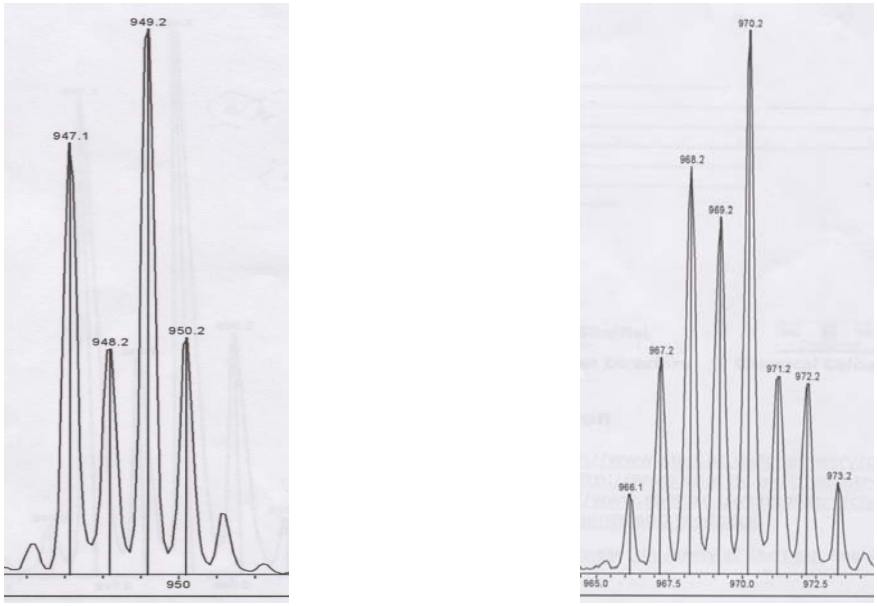

Figure 107. ESI–MS spectra of $[Eu(\mathbf{L}^{23})(NO_3)_3]$ (**25**) and $[Yb(\mathbf{L}^{23})(NO_3)_3]$ (**26**) and theoretical model of $[Eu(\mathbf{L}^{23})(NO_3)_2]^+$ and $[Yb(\mathbf{L}^{23})(NO_3)_2]^+$.

4.3 Liquid-liquid extraction studies of Eu(III) and U(VI) with selected ligands

Liquid-liquid extraction was used to characterize the phase transfer properties of the tripodal ligands $\mathbf{L}^{14}$–$\mathbf{L}^{23}$ towards Eu(III) and U(VI). The studies were perfomed using the extraction system $Eu(NO_3)_3$ or $UO_2(NO_3)_2$–buffer–H_2O/ ligand–(co-ligand)–$CHCl_3$ with the aim of search for structure-binding and structure-extraction relationships.

The time required to reach the extraction equilibrium was determined for selected ligands (Figure 108). This study shows that the extraction of Eu(III) practically was not influenced by the shaking time while the necessary time for the U(VI) extraction was quite different in dependence on the ligand type used. Especially the sterically hindered tripodal systems $\mathbf{L}^{17}$ and $\mathbf{L}^{19}$ need a longer time to achieve the equilibrium.

a)

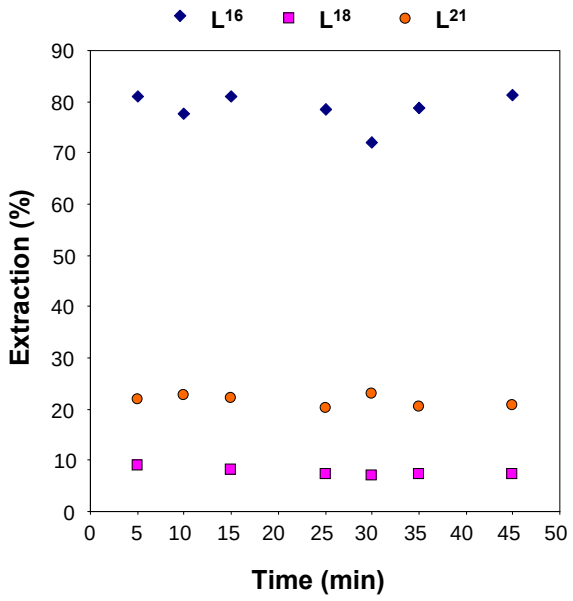

b)

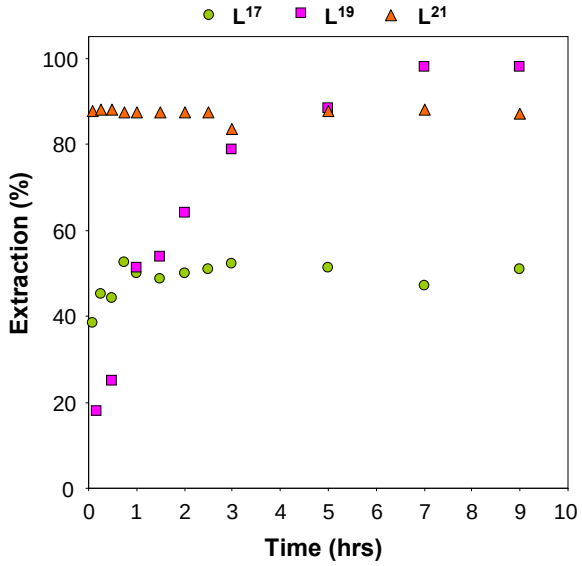

Figure 108. Time dependence of Eu(III) (a) and U(VI) (b) extraction with selected ligands. [**L**] = $1 \cdot 10^{-2}$ M in $CHCl_3$; [Eu(III)] = [U(VI)]= $1 \cdot 10^{-4}$ M, [$NaNO_3$] = $5 \cdot 10^{-3}$ M, pH = 5.2 (HEPES/HNO_3 buffer), T = 23 ± 1°C, t = 5–45min (a), 10min–9h (b). Octanoic acid ($1 \cdot 10^{-2}$ M) was added in the case of Eu(III).

The results of the extraction experiments both in the absence and presence of octanoic acid (RCOOH) as co-ligand are illustrated in Figure 109. At pH 5.4 in the absence of octanoic acid, the ligand series show almost no Eu(III) extraction efficiency. Only the $\mathbf{L}^{22}$ gives 9% Eu(III) extraction in opposition extraction yields between 31 to 97% for U(VI) were observed for $\mathbf{L}^{14}$–$\mathbf{L}^{23}$.

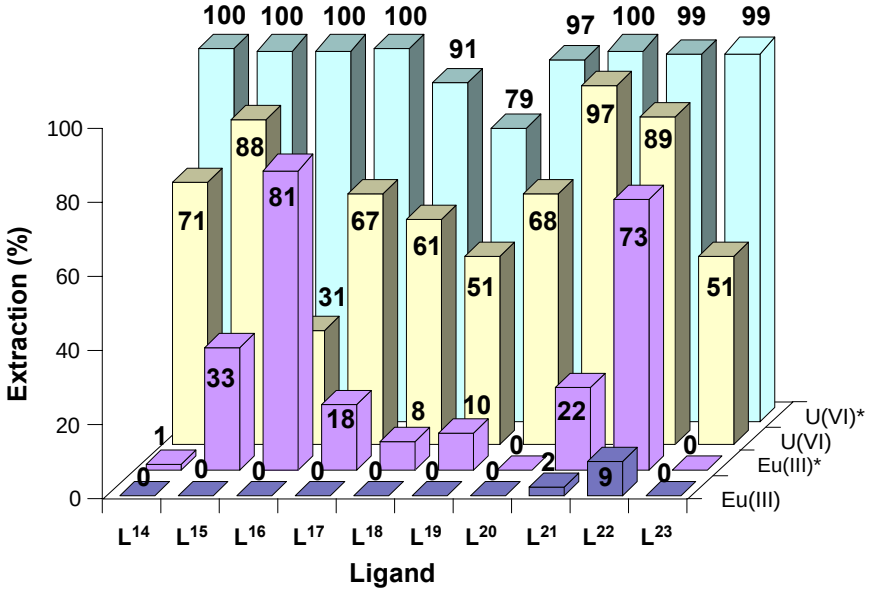

Figure 109. Percentage of metal ion extracted by $\mathbf{L}^{14}$–$\mathbf{L}^{23}$ without and with addition of octanoic acid (*). $[Eu(NO_3)_3] = [UO_2(NO_3)_2] = 1 \cdot 10^{-4}$ M, $[NaNO_3] = 5 \cdot 10^{-3}$ M, pH 5.4 (MES/NaOH buffer); [**L**] = $1 \cdot 10^{-2}$ M, (*) [Octanoic acid] = $1 \cdot 10^{-2}$ M in $CHCl_3$; shaking time 1 h; $T = 23 \pm 1$ °C.

In a second run of experiments, octanoic acid (1×10^{-2} M) was added to the organic phase under otherwise identical experimental conditions to those used above; the extraction behaviour for each of the ligands is also summarised in Figure 109. With the addition of one equivalent (relative to **L**) of octanoic acid the extraction of Eu(III) is markedly increased in almost all cases (e.g. from 0 to 81% in the case of $\mathbf{L}^{16}$ and from 9 to 73% in the case of $\mathbf{L}^{22}$); the U(VI) extraction get >90% in most cases. The ligands $\mathbf{L}^{20}$ and $\mathbf{L}^{23}$ do not show any Eu(III) extraction both in the absence and presence of octanoic acid. This study has shown that the distribution ratios of U(VI) were significant higher than the corresponding data of Eu(III). This tendency reflects the fact that all these ligands favour U(VI) over Eu(III) extraction. Parallel 'control' experiments (involving

the absence of the ligand but at the same concentration of octanoic acid) were performed; under these conditions the metal extraction was negligible ≤ 1% for both cations. Therefore one important conclusion of this study is that a pronounced synergistic effect is characteristic for nearly all examples.

Uranyl complex form on extraction with $\mathbf{L^{18}}$ was characterized by ESI mass spectroscopy. The spectrum revealed the presence of peaks (Figure 110) corresponding to $[UO_2(\mathbf{L^{18}}) - 3H]^-$ and $[UO_2(\mathbf{L^{18}})(NO_3) - 2H]^-$ at m/z = 731 and 794 respectively. These data point at the formation of 1:1 (Metal/Ligand) complexes.

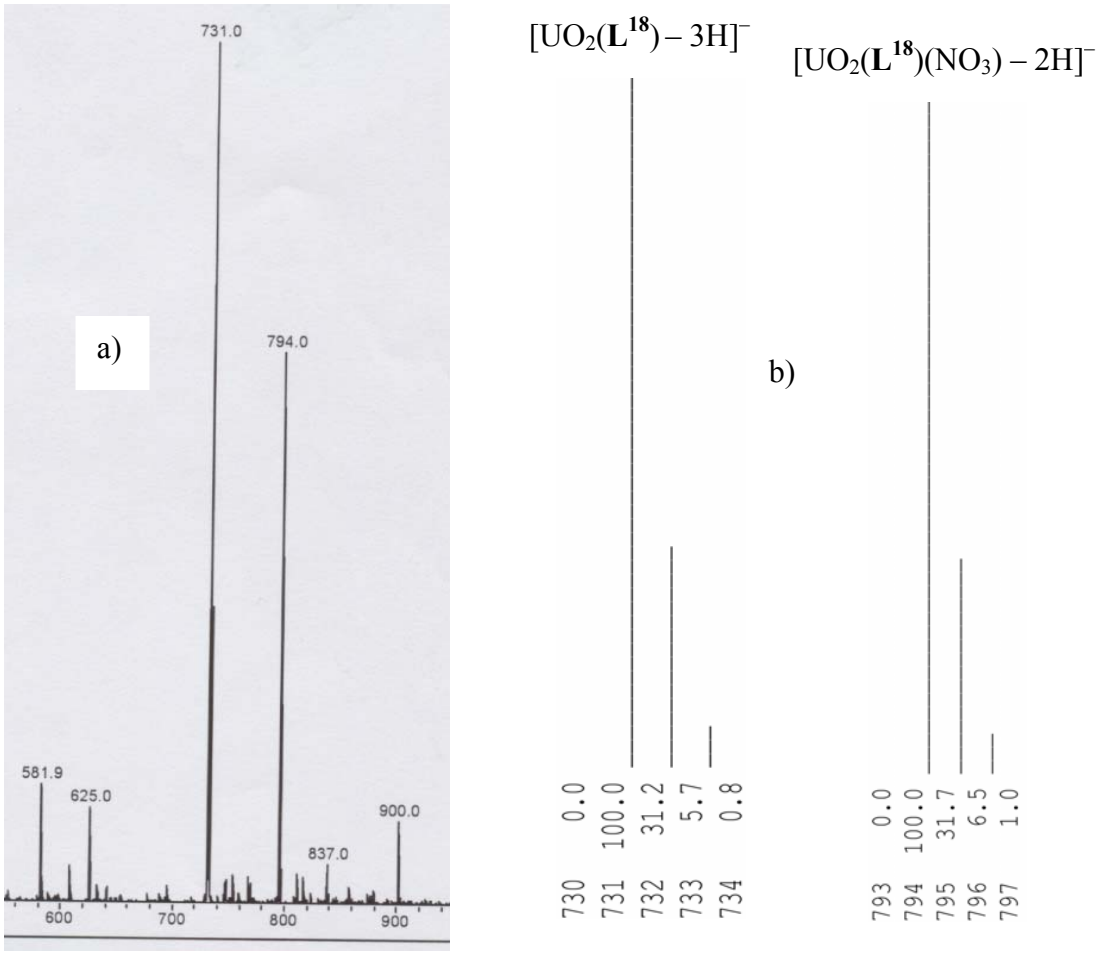

Figure 110. ESI–MS spectra showing the abundant isotopic patterns of the U(VI) complex formed on extraction by $\mathbf{L^{18}}$**:** a) experimental, b) theoretical.

Additional experiments were made to check the influence of the counter anion on Eu(III) extraction with $\mathbf{L}^{15}$, $\mathbf{L}^{16}$ and $\mathbf{L}^{21}$ testing nitrate, picrate, carboxylate and related mixtures. Figure 111 shows an overview of the extraction percentage for the ligands studied. It is noted that in the absence of octanoic acid no Eu(III) extraction was observed. In contrast to that the presence of octanoic acid has a pronounced synergistic effect on the extraction. Especially in case of $\mathbf{L}^{16}$ but also for $\mathbf{L}^{15}$ the Eu(III) extraction power strongly increase.

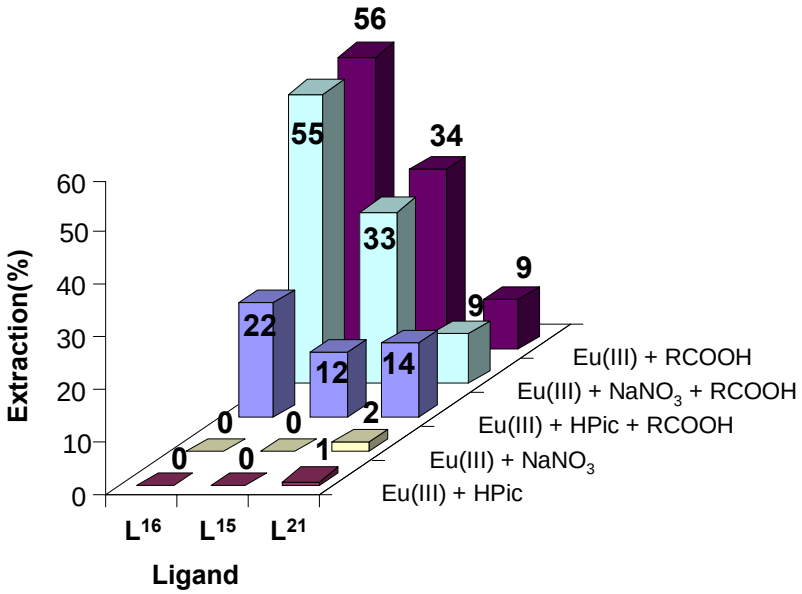

Figure 111. Extraction of Eu(III). $[Eu(NO_3)_3] = 1 \times 10^{-4}$ M, $[NaNO_3] = [HPic] = 5 \times 10^{-3}$ M, pH 5.4 (MES/NaOH buffer); [**L**] = 1×10^{-2} M, [RCOOH] = [Octanoic acid] = 1×10^{-2} M in $CHCl_3$; shaking time 1 h; $T = 23 \pm 1$ °C.

In a further set of experiments the stoichiometries of the extracted species were analysed by undertaking the extraction of Eu(III) (at 1×10^{-4} M) under variation of the ligand concentrations (5×10^{-3} to 2.5×10^{-2} M) in the presence of a fixed concentration of octanoic acid (1×10^{-2} M).

For each of the selected ligand log D_M was plotted against log c_L. The results at pH 5.4 show that linear relationships occur (Figure 112); the slopes range between 0.6 and 2.8 (Table 39) pointing to the formation of 1:1, 1:2 and 1:3 (metal:ligand) species with varying ratios during extraction.

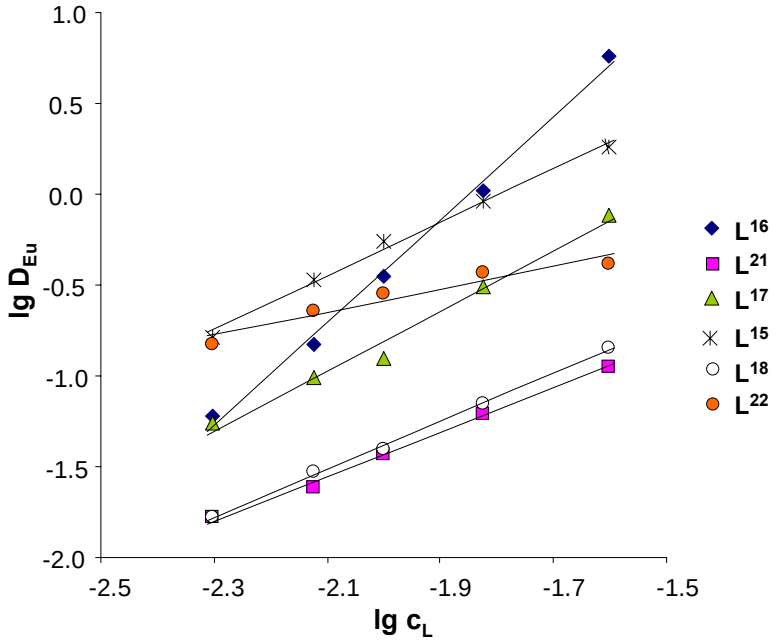

Figure 112. Extraction of Eu(III) as a function of ligand concentration. [Eu(III)] = 1 x 10^{-4} M, [$NaNO_3$] = 5 x 10^{-3} M, pH 5.4 (MES/NaOH buffer); [Ligand] = 5 x 10^{-3} M···2.5 x 10^{-2} M in $CHCl_3$; T = 23 ± 1 °C.

An investigation of the above type has been carried out to probe the influence of octanoic acid on the extraction. The octanoic acid concentration was varied over the range 5 × 10^{-3} to 2.5 × 10^{-2} M while the other concentrations were held constant. The results also show linear relationships (Figure 113). In this case the ratios Eu(III) : octanoic acid also vary from 1:1 to 1:3 (Table 39). This suggests that, under the conditions employed, the species extracted contain a different number of octanoic acid molecules coordinated per Eu(III) metal centre. This fact is obviously caused by the different structure and the resulting steric demand of the chelating ligand molecules used.

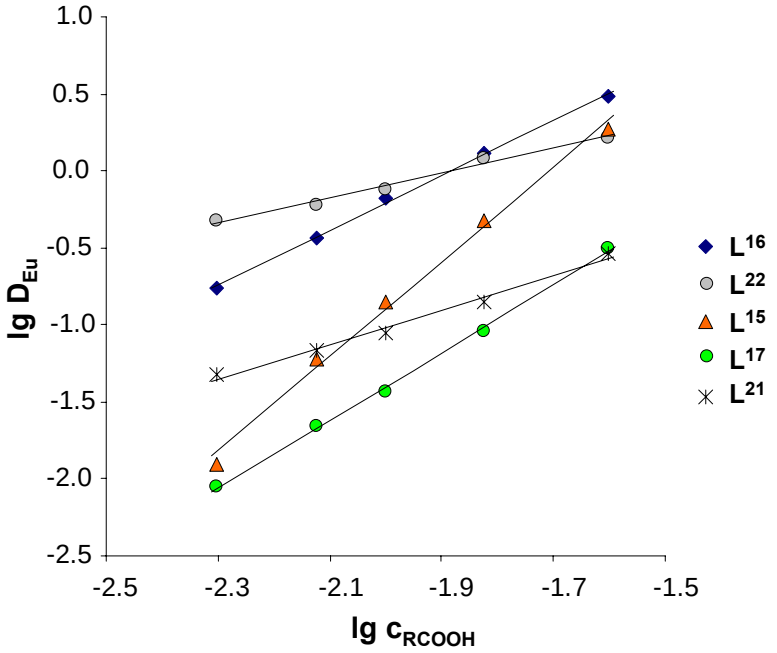

Figure 113. Extraction of of Eu(III) as a function of co-ligand concentration. [Eu(III)] = 1 x 10^{-4} M, [$NaNO_3$] = 5 x 10^{-3} M, pH 5.4 (MES/NaOH buffer); [RCOOH] = 5 x 10^{-3} M …2.5 x 10^{-2} M in $CHCl_3$; T = 23 ± 1 °C; RCOOH = octanoic acid.

Table 39. Slopes of the plots obtained for Eu(III) extraction using selected ligands with and without addition of octanoic acid in dependence of ligand and co-ligand concentration (results based on Figure 112 and 113).

Ligand	Slopes at varied ligand concentration	Slopes at varied co-ligand (octanoic acid) concentration
L^{15}	1.5	3.1
L^{16}	2.8	1.8
L^{17}	1.7	2.2
L^{18}	1.3	—
L^{21}	1.2	1.1
L^{22}	0.6	0.8

Further information about the extraction equilibrium was obtained in view of the pH influence on the extraction of Eu(III) and U(VI) by selected ligands. The results of these

studies are presented in Figure 114. With increasing pH, the extractabilities of these ligands increase. The maximum extraction is reached between pH 6.5 and 7.0 for Eu(III) and between pH 4.5 and 5.5 for U(VI). This trend is in agreement with the changing protonation state of the ligands, which is influencing both the lipophilicity of the compound and the availability of the donor functions.

a)

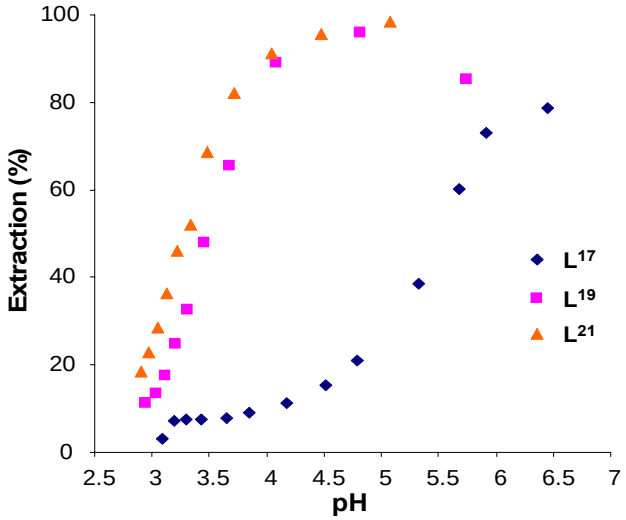

b)

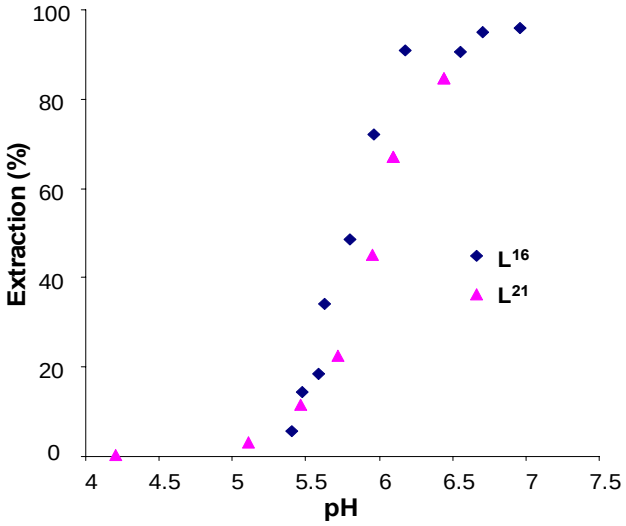

Figure 114. Extraction of a) U(VI) and b) Eu(III) with selected ligands as a function of pH. [**L**] = 1 x 10^{-2} in $CHCl_3$; [U(VI)] = [Eu(III)] = 1 x 10^{-4} M, [$NaNO_3$] = 5 x 10^{-3} M, pH = 2 − 6 (HEPES/HNO_3 buffer), pH = 6 − 9 (HEPES/NaOH buffer), T = 23 ± 1°C.

5 Conclusions

It was the intention of this work to use self-assembly processes to construct supramolecular architectures based on metal-ligand interactions. The structures formed strongly depend on the used metal ion, the ligand type, the chosen counter ion and solvent as well as on the experimental conditions. The focus of the studies was the design of multifunctional N-donor ligands and the characterization of their complexing and structural properties. This work was divided into three distinct main parts: The bis(2-pyridylimine), the bis(2-hydroxyaryl) imine and the tripodal imine / amine ligand approach.

In the first part a series of bis(2-pyridylimine) derivatives having different linking elements (Figure 115) were employed as building blocks for novel supramolecular architectures. Reaction of individual *d*-block metal salts with these ligands has led to the isolation of coordination polymers, $\{[Ag\mathbf{L^1}](ClO_4)\cdot CH_3CN\}_n$ **1** and $\{[Ag\mathbf{L^2}]ClO_4\cdot CH_2Cl_2\}_n$ **2**, a metallamacrocycle, $([Ag_2(\mathbf{L^2})_2](ClO_4)_2$ **3**, double-stranded helicates, $[Hg_2(\mathbf{L^2})_2(ClO_4)_3(H_2O)_2]ClO_4\cdot CH_3CN$ **8**, $[Hg_2(\mathbf{L^1})_2](ClO_4)_4$ **9** and $[Hg_2(\mathbf{L^3})_2](ClO_4)_4$ **10**, triple-stranded helicates, $[Mn_2(\mathbf{L^1})_3](ClO_4)_4$ **11**, $[Ni_2(\mathbf{L^2})_3](NO_3)_4\cdot 2.5H_2O$ **12**, $[Ni_2(\mathbf{L^5})_3](PF_6)_4\cdot 0.9H_2O$ **13** and $[Fe_2(\mathbf{L^5})_3](PF_6)_4$ **14**, as well as of circular *meso*-helicates [175], $[Cu\mathbf{L^1}(SO_4)]_6\cdot 24H_2O$ **4**, $[Cu\mathbf{L^2}(SO_4)]_6\cdot 24H_2O$ **5**, $[Cu\mathbf{L^3}(SO_4)]_6\cdot 24H_2O$ **6** and $[Cu_6(\mathbf{L^2})_3(\mathbf{L^3})_3(SO_4)_6]\cdot 24H_2O$ **7** (Figure 115).

The X-ray structure analyses of the bis(2-pyridylimine) ligands $\mathbf{L^1}$, $\mathbf{L^4}$ and $\mathbf{L^5}$ have been performed. Although these ligands exhibit an imine E configuration the conformations of the two halves of the molecule differ considerably from one ligand to the other. So the angles of the linking elements existing between the two bidentate chelating subunits vary in the order: $\mathbf{L^4} > \mathbf{L^2} > \mathbf{L^1} > \mathbf{L^5}$. The ligand molecules $\mathbf{L^2}$, $\mathbf{L^4}$ and $\mathbf{L^5}$ are packed in the crystal through weak hydrogen bonds and edge-to-face CH-π interactions while in $\mathbf{L^1}$ no weak interactions are observed.

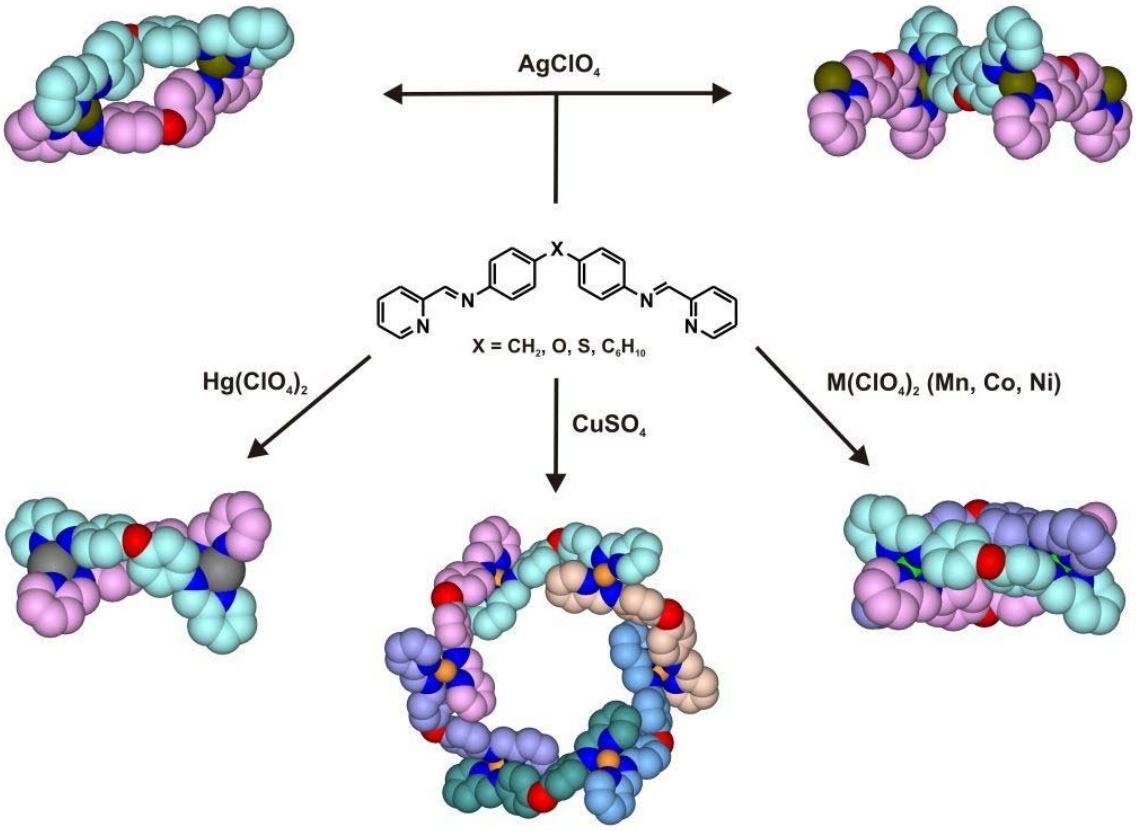

Figure 115. Overview of structurally characterized metal complexes with bis-(2-pyridylimine) ligands.

$\{[Ag\mathbf{L}^1](ClO_4)\cdot CH_3CN\}_n$ **1**, $\{[Ag\mathbf{L}^2]ClO_4\cdot CH_2Cl_2\}_n$ **2**, $[Ag_2(\mathbf{L}^2)_2](ClO_4)_2$ **3**

The self-assembly of Ag(I) with the ligands $\mathbf{L}^1$ and $\mathbf{L}^2$ leads to the formation of two coordination polymers **1** and **2** and one discrete molecular box **3**. The nature of the spacer in the Schiff base ligands, the noncovalent weak interactions, such as face-to-face π-π and edge-to-face CH-π interactions, are all important factors influencing the architecture of the final products. In **1** and **2**, the anions and the solvent molecules are bridging the chelate units to form coordination networks. In case of **3** the change of the solvent from CH_2Cl_2 to CH_3OH results a quite different structure compared to **2**.

$[Cu\mathbf{L}^{1}(SO_4)]_6 \cdot 24H_2O$ **4**, $[Cu\mathbf{L}^{2}(SO_4)]_6 \cdot 24H_2O$ **5**, $[Cu\mathbf{L}^{3}(SO_4)]_6 \cdot 24H_2O$ **6** and $[Cu_6(\mathbf{L}^{2})_3(\mathbf{L}^{3})_3(SO_4)_6] \cdot 24H_2O$ **7**

The unusual hexanuclear *meso*-helicates **4**, **5**, **6** and **7** are, to the best of our knowledge, first examples of nanometer-scaled neutral circular helicates fully self-assembled around Cu(II) under the influence of H-bonding and π-π stacking interactions. Topological control of the assembly process is clearly associated with the bidentate coordination of the sulfate anion which directs the formation of a double- rather than a triple-stranded helicate around the octahedrally coordinated Cu(II). Surprisingly, the variation of the linker function in the ligands $\mathbf{L}^{1}$-$\mathbf{L}^{3}$, which significantly changes the linking angle of the pyridylimine strands, has only a little influence of the resulting structure. Also the use of a mixture of ligands $\mathbf{L}^{2}$ and $\mathbf{L}^{3}$ does not influence the *meso*-helicate topology; the result is the symmetrically mixed *meso*-helicate **7**.

$[Hg_2(\mathbf{L}^{2})_2(ClO_4)_3(H_2O)_2]\ ClO_4 \cdot CH_3CN$ **8**, $[Hg_2(\mathbf{L}^{1})_2]\ (ClO_4)_4$ **9** and $[Hg_2(\mathbf{L}^{3})_2]\ (ClO_4)_4$ **10**

The ligands $\mathbf{L}^{1}$–$\mathbf{L}^{3}$ react with $Hg(ClO_4)_2$ to yield the dinuclear double-stranded helicates **8**, **9** and **10** where each Hg(II) centre occupies a pseudo-tetrahedral environment based on two pyridylimine units from two different ligands. In **8** each Hg(II) centre weakly interact with H_2O molecules and ClO_4^- anions. Considering these weak interactions, each Hg(II) centre will be coordinated by 7 donor atoms and resulting in a distorted pentagonal bipyramidal coordination geometry. The phenylene rings of the diarylether spacer show face-to-face π-π stacking with the adjacent ligand strand. These interactions are probably a consequence of the constraints imposed upon the ligands if they are coordinated to the mecury centre. All helical complexes are packed in the crystal through a combination of several weak intra- and intermolecular interactions leading to a 3D arrangement.

$[Mn_2(\mathbf{L^1})_3](ClO_4)_4$ **11**, $[Ni_2(\mathbf{L^2})_3](NO_3)_4{\cdot}2.5H_2O$ **12**, $[Ni_2(\mathbf{L^5})_3](PF_6)_4{\cdot}0.9H_2O$ **13** and $[Fe_2(\mathbf{L^5})_3](PF_6)_4$ **14**

The reactions of $\mathbf{L^1}$ with $Mn(ClO_4)_2$, $\mathbf{L^2}$ with $Ni(NO_3)_2$ and $\mathbf{L^5}$ with $NiCl_2$ or $FeCl_2$ yielded in each case the dinuclear triple-stranded helicates **11-14** where both metal centres have a pseudooctahedral coordination geometry based on three pyridylimine units from three different ligands. Coordination to the metal centre forces interannular twisting between the phenylene rings of the linkers and the pyridylimine units with the logical consequence of a triple-helical array formation. The twisting of the phenylene units results weak edge-to-face C–H···π interactions between the aromatic spacers for **11** and **12** but not for **13**. Only one intramolecular CH···π interactions between two pyridine rings is observed in **13**. The distance between two nickel(II) centres in **13** (10.98 Å) is significantly shorter than the corresponding metal···metal distance in **11** (11.47 Å) and **12** (11.37 Å). The angle of the linking element present between the two bidentate chelating subunits of the ligands in **13** (~109°) is smaller than that of the other metal complexes (~116° in **11** and ~117° in **12**). The width of all these triple helicates is almost similar (~2 nm) while the height of **13** (~1.6 nm) is a bit larger than that of the others (~1 nm). The helicates form a three-dimensional network via weak H-bonds of the anions and additional anion–π interactions. The self-assembly into the 3D network of **13** is furthermore supported by weak edge-to-face CH···π interactions including the cyclohexane ring.

The new iron(II) triple helicate **14** in its chloride form binds strongly to DNA as shown by CD spectroscopy. The induced CD spectrum gives some evidence that $[Fe_2(\mathbf{L^5})_3]^{4+}$ interacts with the DNA in a single binding mode, which is consistent with major groove binding.

The cytotoxicity of the new iron(II) triple helicate **14'** was evaluated on human lung cancer A549 cells and compared with that of cisplatin and that of the previously reported iron(II) triple helicate $[Fe_2(\mathbf{L^1})_3]^{4+}$ [84]. The first results show some distinguishing features for **14'** obviously caused by the existing structural differences of the complexes.

In the second part of the thesis, novel uranyl complexes of the bis(2-hydroxyaryl) imine ligands $\mathbf{L^6}$–$\mathbf{L^8}$, $\mathbf{L^{10}}$, $\mathbf{L^{12}}$ and $\mathbf{L^{13}}$ have been synthesized and characterized. With $\mathbf{L^6}$ and $\mathbf{L^7}$ 1D coordination polymers, $\{[UO_2(\mathbf{L^6})(NO_3)_2]\}_n$ **15** and $\{[UO_2(\mathbf{L^7})(NO_3)_2]\}_n$ **16**, are formed while those with the other ligands afforded mononuclear structures, $[UO_2(\mathbf{L^8})(NO_3)_2]$ **17**, $[UO_2(\mathbf{L^{10}})(NO_3)_2]$ **18**, $[UO_2(\mathbf{L^{12}})(NO_3)_2]$ **19** and $[UO_2(\mathbf{L^{13}})(NO_3)_2]$ **20**. In all complexes a distorted hexagonal bipyramidal coordination geometry around the uranyl centre is observed. The imine nitrogen atoms of the ligands do not bind to the metal centre but interact strongly with the hydroxy group via H-bonding. DFT calculations made with $\mathbf{L^1}$ are in good agreement with the X-ray crystal structure data. Liquid-liquid extraction studies involving ligands $\mathbf{L^8}$-$\mathbf{L^{13}}$ and Eu(III) or U(VI) indicate remarkably high selectivity for U(VI) over Eu(III) at weak acidic pH conditions. We believe that the study made opens up new possibilities for uranyl ion extraction which could be interesting in view of the treatment of nuclear waste.

In the third part of the thesis, a series of multifunctional tripodal ligands with different N-donor centres ($\mathbf{L^{14}}$–$\mathbf{L^{23}}$) were used for U(VI) and lanthanide, Nd(III), Eu(III) and Yb(III), binding and extraction. Reaction of these metal ions with selected tripodal ligands afforded complexes which were characterized by ESI mass spectroscopy. The complex composition was found to be 1:1 in all cases.

The extraction behaviour of the tripodal ligands towards Eu(III) and U(VI) was studied both in the absence and presence of octanoic acid as co-ligand using the extraction system $Eu(NO_3)_3$ or $UO_2(NO_3)_2$–buffer–H_2O/ ligand–$CHCl_3$. These separation systems show a remarkably high selectivity for U(VI) over Eu(III). It is interesting to note that the addition of the octanoic acid to the extraction system leads to high synergistic effects. A series of Eu(III) extraction experiments were done to clarify the composition of the extracted complexes. The results clearly point to the formation of various species with changing composition.

6 Experimental

6.1 Analytic methods

^{1}H and ^{13}C NMR Spectroscopy

The ^{1}H and ^{13}C NMR were carried out in the Organic Chemistry Department at the Technical University of Dresden. They were recorded on Bruker Avance DRX-500 spectrometer operated at 500 MHz and 126 MHz respectively with DMSO-*d*6 and $CHCl_3$-*d*1 as solvents with tetramethylsilane as the reference. The following abbreviations were used to indicate the multiplicity of the signals: s = Singulet, d = Doublet, dd = double Doublet, t = Triplet, q = Quartet, m = Multiplet.

Mass Spectrometry

The electrospray ionization mass spectrometry (ESI-MS) analyses were also carried out in the Organic Chemistry Department at the Technical University of Dresden. The measurements were performed on a Bruker ESQUIRE mass spectrometer coupled together with a Hewlett & Packard HPLC system. Methanol was used as mobile phase and if necessary, 0.5 mmol / l of ammonium acetate were added to the sample solutions. The ionization was carried out by the electron spray method (ESI). The following abbreviations were used to assignment the m / z values:

[M]	= Molecular mass of the compound
$[M + H]^+$-ion	= Molecular mass of the compound in the positive ion spectrum
$[M - H]^-$-ion	= Molecular mass of the compound in the negative ion spectrum
$[L + \text{metal ion} + \text{anion}]^+$-ion	= Molecular mass of the complex species with ligand L

Elemental Analyses

Elemental analysis of compounds **8** and **10** were carried out at the Max Planck Institute for Chemical Physics of Solids Dresden. C, H, N and O contents of these samples are determined by the carrier-gas-hot-extraction- and combustion-method using the following analyzer instruments: LECO TCH 600, LECO RH 400, LECO TC 436 DR/5 and LECO C-200 CHLH. The determination of the Cl amount succeeds via oxidative combustion connected with ion chromatography (CIC) on AQF-100, GA-100, WS-100 (Mitsubishi Chemical, a[1] envirotech) combustion unit and ICS-1000 (Dionex) ion chromatograph. The Hg amounts are quantitatively analyzed by ICP-OES technique using the spectrometer Varian VISTA. The analyses of all other samples were carried out on a Carlo Erba (EA 1108) Analyser in the Organic Chemistry Department at the Technical University of Dresden.

Differential Thermal Analyses (DTA) and Thermogravimetric Analyses

Thermal analyses (DTA/TG) of **4-6** samples were carried out in the Inorganic Chemistry Department at the Technical University of Dresden using the NETZSCH STA 409 thermal analysis instrument. Samples for analysis were introduced to the aluminium oxide tube (empty tube takes as reference). The measurements were made on static air in the temperature range of 30-600 °C with 5 $°C \cdot min^{-1}$ heating rate and analyzed by applying the program from NETZSCH (Proteus 4.0 beta, NETZSCH-Gerätebau). Weight changes in TG curves and temperature difference in DTA curves gives information on reactions and decompositions.

IR Spectroscopy

The IR data were recorded as KBr pellets on a BioRad Excalibur FTS 3000-Spectrometer in the range 400-4000 cm^{-1} in the Inorganic Chemistry Department at the Technical University of Dresden. The IR spectra were used to obtain either structure information or “finger prints”.

UV-Vis Spectroscopy

All UV data were collected using a Perkin Elmer type Lambda 25 double canal-spectrophotometer in the range 200-1000 nm.

CD Spectroscopy

Circular dichroism spectra were collected in 1 cm path length cuvettes (280–850 nm) path length cuvettes using a Jasco J-810 spectropolarimeter. Spectroscopic titrations were performed in which CD and UV-vis absorbances spectra were collected. Titrations were carried out at constant concentrations of DNA (300 μM), NaCl (20 mM) and sodium cacodylate buffer (1 mM). The DNA–metal complex ratio was decreased during the titration series by incrementing the concentration of metal complex in the cuvette from 0–37.5 μM. Titrations were performed so as the concentration of DNA, NaCl and buffer in the cuvette remained unaltered.

Time-Resolved Laser-Induced Fluorescence Spectroscopy (TRLFS)

Fluorescence measurements were carried out by use of a spectrometer system described elsewhere [176]. The ligands $\mathbf{L^1}$ and $\mathbf{L^2}$ were dissolved in CH_3OH. The total concentration of the ligand was $1 \cdot 10^{-5}$ mol·dm^{-3}. The fluorescence of solutions with increasing concentration of added $CuSO_4$ were measured. The ligand to Cu(II) ratio was varied from 10:1 to 1:5. The fluorescence of the non-complexed ligand was excited by 130 fs laserpulses at 266 nm. The repetition rate of the laser system was 1 kHz. The emitted fluorescence was focussed into a 270 mm spectrograph (Acton Research) and the spectrum was measured by an intensified CCD (charged coupled device) camera (LaVision). The gate of the camera system was set to be 120 ps and the observed wavelength range was set from 300 nm to 510 nm. The range for time-resolved measurements was limited from 0 to 30000 ps with steps of 100 ps.

6.2 Chemicals

All reagents and solvents were purchased from commercial sources and used without further purification. Dry methanol was prepared by distillation and stored over 3-4 Å molecular sieves.

6.3 Synthesis

6.3.1 Ligands synthesis

In general the analytical control of the reaction progress was made by thin layer chromatography (TLC) using TL-silica gel 60 F 254 aluminium foil from Merck. The detection wavelength for UV-active substances was 254 nm. If necessary the quantitative separation of the reaction products was carried out by column chromatography on silica gel SG60 (0.063-0.200 mm) (Merck) with defined eluent volume ratios.

Bis[4-(2-pyridylmethyleneimino)phenyl]methane (**L**^{1})

L^{1} was synthesized according to the published method of Hannon *et al*. [84]. 4,4'-Methylenedianiline (1 g, 5.04 mmol) and pyridine-2-carbaldehyde (1.25g, 11.67 mmol) were mixed in dry methanol (25 ml) and refluxed for 2 h. The ligand precipitates from the reaction mixture as pale yellow solid (1.68 g), isolated by filtration and dried under vacuum. Crystals of **L**^{1} are shown in Figure 116.

Figure 116. Crystal photograph of **L**^{1}

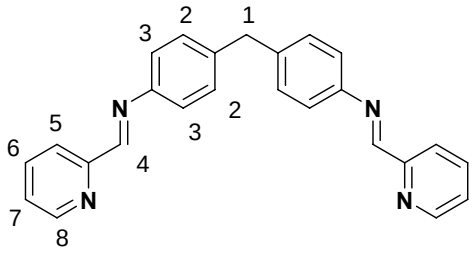

Yield	1.68 g, 88%
$C_{25}H_{20}N_4$	376.45 g.mol^{-1}
Calc.[%]	C 79.76, H 5.35, N 14.88
Found [%]	C 79.82, H 5.29, N 14.93
ESI-MS (MeOH)	m/z = 377 [$\mathbf{L^1}$ + H]$^+$

^{1}H-NMR (500 MHz, $(CD_3)_2$−SO, 25 °C, TMS): δ [ppm] = 8.72 (d, *J* = 4.8 Hz, 2H, H8), 8.60 (s, 2H, H4), 8.15 (d, *J* = 7.9 Hz, 2H, H5), 7.95 (t, *J* = 7.7, 8.7 Hz, 2H, H6), 7.52 (dd, *J* = 6.0, 7.2 Hz, 2H, H7), 7.33 (dd, *J* = 8.5 Hz, 8H, H2,3), 4.02 (s, 2H, H1)

IR Spectroscopy data

Vibration frequency ṽ (cm^{-1})	Intensity†, band form‡	Assignment [150]
3433	s, br	C−H_{ph} stretch
3054−3984	w, sr	C−H_{py} stretch
2923	w, sr	C−H_{im} stretch
2853	w, sr	C−H_{ali} stretch
1628	m, sp	C=N_{im} stretch
1504−1435	m, sp	C−C_{arom} stretch
1204−1015	w, sr	C−N_{py} stretch

† vs = very strong, s = strong, m = medium, w = weak
‡ br = broad, sp = sharp, sr = shoulder

Bis[4-(2-pyridylmethyleneimino)phenyl]ether ($\mathbf{L^2}$)

$\mathbf{L^2}$ was synthesized in the same way as in the case of $\mathbf{L^1}$ by refluxing a methanolic solution of bis(4-aminophenyl)ether (1 g, 5 mmol) and pyridine-2-carbaldehyde (1.5g, 14 mmol). The green solid obtained (1.72 g) was filtered off and dried under vacuum.

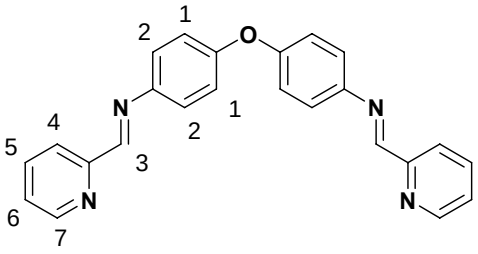

Yield	1.72 g, 91%
$C_{24}H_{18}N_4O$	378.43 g.mol^{-1}
Calc.[%]	C 76.17, H 4.76, N 14.81
Found [%]	C 76.19, H 4.83, N 14.87
ESI-MS (MeOH)	m/z = 379 [**L²** + H]$^+$, 411 [**L²** + MeOH + H]$^+$, 433 [**L²** + MeOH + Na]$^+$

^{1}H-NMR (500 MHz, $(CD_3)_2$−SO, 25 °C, TMS): δ [ppm] = 8.72 (d, *J* = 4.7, 2H, H7), 8.60 (s, 2H, H3), 8.16 (d, *J* = 7.9 Hz, 2H, H4), 7.96 (ddd, *J* = 1.5, 1.4, 1.5 Hz, 2H, H5), 7.53 (dd, *J* = 5.6, 5.9 Hz, 2H, H6), 7.44 (ddd, *J* = 3.3, 6.7, 3.3 Hz, 4H, H2), 7.12 (ddd, *J* = 3.3, 6.7, 3.3 Hz, 4H, H1)

IR Spectroscopy data

Vibration frequency ṽ (cm^{-1})	Intensity[†], band form[‡]	Assignment [150]
3430	m, br	C−H_{ph} stretch
3047−2980	w, sr	C−H_{py} stretch
2925−2874	w, sr	C−H_{im} stretch
1625	m, sp	C=N_{im} stretch
1495−1434	s, sp	C−C_{arom} stretch
1240−1198	s, sp	C−O stretch
1163−1008	w, sp	C−N_{py} stretch

[†] vs = very strong, s = strong, m = medium, w = weak

[‡] br = broad, sp = sharp, sr = shoulder

Bis[4-(2-pyridylmethyleneimino)sulfide(**L**^{3})

L^{3} was synthesized with a slightly modification of the previously reported method. [91] 4,4'-Diaminodiphenylsulfide (1 g, 4.62 mmol) was dissolved in acetonitrile (30 ml) and stirred under a nitrogen atmosphere. A solution of 2-pyridinecarboxyaldehyde (0.99 g, 9.24 mmol) in acetonitrile was added dropwise and the mixture was refluxed for 5 h. The brown solution was then concentrated by rotary evaporation to produce a brown solid which was filtered off and dried under vacuum.

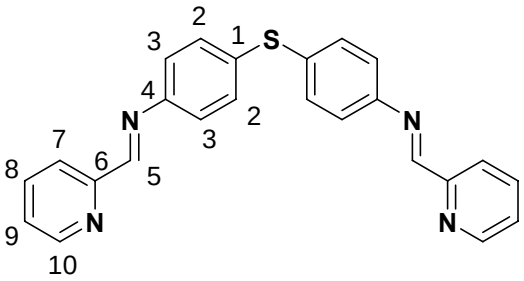

Yield	1.62 g, 89%
$C_{24}H_{18}N_4S$	394.49 g.mol^{-1}
Calc.[%]	C 73.07, H 4.60, N 14.20, S 8.13
Found [%]	C 72.49, H 4.73, N 14.10, S 7.68
ESI-MS (MeOH)	m/z = 395 [**L**^{3} + H]$^{+}$, 427 [**L**^{3} + MeOH + H]$^{+}$

^{1}H-NMR (500 MHz, $CDCl_3$, 25 °C, TMS): δ [ppm] = 8.71 (d, *J* = 4.3, 0.9 Hz, 2H, H10), 8.60 (s, 2H, H5), 8.18 (d, *J* = 7.9 Hz, 2H, H7), 7.81 (t, *J* = 1.6 Hz, 2H, H8), 7.40 (dd, *J* = 1.9, 2.0 Hz, 2H, H9), 7.35 (m, 4H, H3), 7.24 (d, *J* = 3.0 Hz, 4H, H2)

^{13}C-NMR (500 MHz, $CDCl_3$, 25 °C, TMS): δ [ppm] = 193 (C6), 161 (C5), 154 (C4), 150 (C10), 137 (C8), 134 (C1), 132 (C3), 128 (C9), 125 (C7), 122 (C2)

IR Spectroscopy data

Vibration frequency $\tilde{\nu}$ (cm^{-1})	Intensity[†], band form[‡]	Assignment [150]
3430	m, br	C−H_{ph} stretch
3053−2982	w, sr	C−H_{py} stretch
2926−2856	w, sr	C−H_{im} stretch
1626	s, sp	C=N_{im} stretch
1484−1435	s, sp	C−C_{arom} stretch
1203−1170	m, sp	C−S stretch
1146−994	m, sp	C−N_{py} stretch

[†] vs = very strong, s = strong, m = medium, w = weak
[‡] br = broad, sp = sharp, sr = shoulder

Bis[4-(2-pyridylmethyleneimino)phenyl]amine (**L^4**)

To a stirred solution of pyridine-2-carbaldehyde (0.72 g, 6.73 mmol) in 30 ml acetonitrile was slowly add an acetonitrile solution containing 4,4′-diaminodiphenylamine sulphate (1 g, 3.36 mmol) and triethylamine (0.5 ml). The resulting deep brown-yellow solution was refluxed for 2 hours, cooled to room temperature and kept in the refrigerator over night. Brown-yellow crystals (Figure 117) which were growing during that time were collected by filtration, washed with acetonitrile (3 times 10 ml) and diethyl ether (2 times 20 ml) and recrystalized from dry methanol. The resulting solid was collected and dried under vacuum.

Figure 117. Crystal photograph of **L^4**

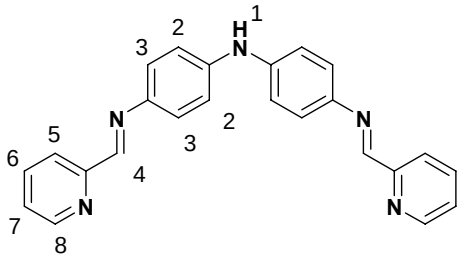

Yield	0.92 g, 72%
$C_{24}H_{19}N_5$	377.44 g.mol^{-1}
Calc.[%]	C 76.37, H 5.07, N 18.55
Found [%]	C 76.34, H 5.00, N 18.59
ESI-MS (MeOH)	m/z = 378 [**L**^{4} + H]$^+$, 410 [**L**^{4} + MeOH + H]$^+$

^{1}H-NMR (500MHz, $(CD_3)_2$−SO, 25 °C, TMS): δ [ppm] = 8.70 (d, *J* = 4.9, 2H, H8), 8.65 (s, 2H, H4), 8.64 (s, 1H, H1), 8.15 (d, *J* = 7.9 Hz, 2H, H5), 7.93 (dd, *J* = 1.3, 7.8 Hz, 2H, H6), 7.49 (ddd, *J* = 1.06, 4.9, 4.8 Hz, 2H, H7), 7.40 (d, *J* = 8.7 Hz, 4H, H3), 7.18 (d, *J* = 8.8 Hz, 4H, H2)

Bis[4-(2-pyridylmethyleneimino)phenyl]-1,1-cyclohexane (**L**^{5})

L^5 was synthesized by refluxing an acetonitrile solution containing 1,1-bis(4-aminophenyl)cyclohexane (1 g, 3.75 mmol) and pyridine-2-carbaldehyde (0.80 g, 7.51 mmol) for 4 hours. The resulting yellow solution was then cooled to room temperature and kept in the refrigerator over night. Pale yellow crystals (Figure 118) of **L**^{5} growed during that time. The obtained solid was separated by filtration and dried under vacuum.

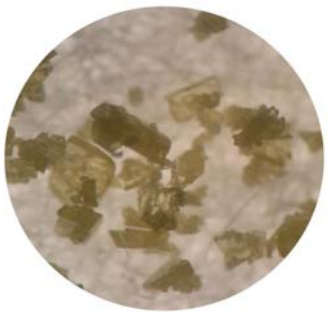

Figure 118. Crystal photograph of **L**^{5}

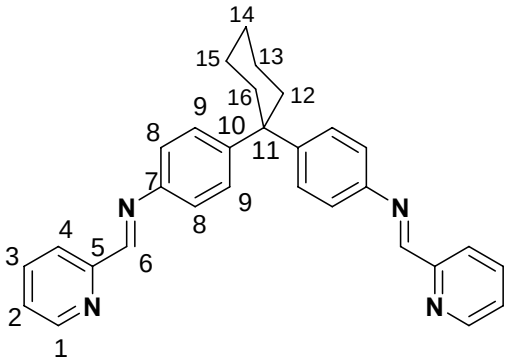

Yield	0.91 g, 55%
$C_{30}H_{28}N_4$	444.57 g.mol^{-1}
Calc.[%]	C 81.05, H 6.35, N 12.60
Found [%]	C 81.23, H 6.33, N 12.73
ESI-MS (MeOH)	m/z = 445 [**L**^{5} + H]$^{+}$, 467 [**L**^{5} + Na]$^{+}$, 499 [**L**^{5} + MeOH + Na]$^{+}$
UV/Vis (MeCN)	331 (ε = 23720) nm, 281 (ε = 27600) nm

^{1}H-NMR (500 MHz, $(CD_3)_2$−SO, 25 °C, TMS): δ [ppm] = 8.70 (d, *J* = 3.2, 2H, H1), 8.59 (s, 2H, H6), 8.14 (d, *J* = 7.9 Hz, 2H, H4), 7.93 (ddd, *J* = 1.7, 5.9, 4.5 Hz, 2H, H2), 7.52 (dddd, *J* = 1.1, 4.8, 2.7 Hz, 2H, H3), 7.41 (d, *J* = 8.6 Hz, 4H, H8), 7.29 (d, *J* = 8.6 Hz, 4H, H9), 2.32 (m, 4H, H12,16), 1.5 (m, 6H, H13,14,15)

^{13}C-NMR (500 MHz, $(CD_3)_2$−SO, 25 °C, TMS): δ [ppm] = 160 (C1), 154 (C5), 150 (C6), 148 (C7), 138 (C10), 137 (C2), 128 (C8), 126 (C3), 122 (C9), 121 (C4), 45 (C11), 36 (C12, C16), 26 (C13, C15), 23 (C14)

IR Spectroscopy data

Vibration frequency $\tilde{\nu}$ (cm^{-1})	Intensity[†], band form[‡]	Assignment [150]
3434	m, br	C−H_{ph} stretch
3053−2987	w, sr	C−H_{py} stretch
2936	s, sp	C−H_{im} stretch
2861	m, sp	C−H_{ali} stretch
1627	s, sp	C=N_{im} stretch
1500−1437	s, sp	C−C_{arom} stretch
1151−1014	w, sp	C−N_{py} stretch

[†] vs = very strong, s = strong, m = medium, w = weak
[‡] br = broad, sp = sharp, sr = shoulder

4,4'-Bis(2-hydroxybenzylideneamino)diphenyl ether (**L**^{6})

L^{6} was synthesized according to the published method of Yoshida *et al*. [106]. Ethanolic solution of bis(4-aminophenyl)ether (1 g, 5 mmol) and salicylaldehyde (1.22 g, 10 mmol) was heated at 80°C for 3 hours to yield yellow precipitate which was filtered off, washed with ethanol, and dried under vacuum.

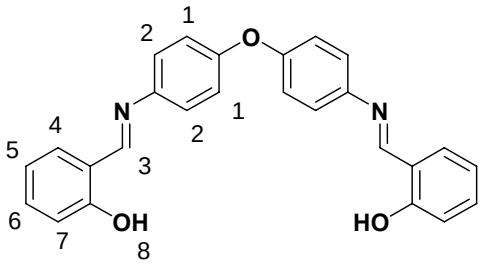

Yield	2 g, 98 %
$C_{26}H_{20}N_2O_3$	408.45 $g.mol^{-1}$
Calc.[%]	C 76.45, H 4.94, N 6.86
Found [%]	C 76.29, H 5.05, N 6.93
ESI-MS (MeOH)	m/z = 409 [**L**^{6} + H]$^{+}$

^{1}H-NMR (500 MHz, $(CD_3)_2$−SO, 25 °C, TMS): δ [ppm] = 13.10 (s, 2H, H8), 8.98 (s, 2H, H3), 7.65 (dd, *J* = 7.7 Hz, 2H, H7), 7.50 (ddd, *J* = 5.4, 6.7 Hz, 4H, H2), 7.41 (t, *J* = 7.9 Hz, 2H, H6), 7.14 (ddd, *J* = 11.9, 8.2, 7.5 Hz, 4H, H1), 6.98 (m, 4H, H4,5)

IR Spectroscopy data

Vibration frequency ṽ (cm^{-1})	Intensity†, band form‡	Assignment [150]
3432	m, br	O−H stretch
3055−2717	w, sr	C−H stretch
1620	s, sp	C=N stretch
1575−1458	s, sp	C−C_{arom} stretch
1413−1363	m, sp	O−H deformation and C−O stretch

† vs = very strong, s = strong, m = medium, w = weak
‡ br = broad, sp = sharp, sr = shoulder

4,4'-Bis(2-hydroxybenzylideneamino)diphenyl methane (**L**^{7})

L^7 was synthesized similarly to that of **L**^{6}. The condensation of bis(4-aminophenyl)methane (1 g, 5 mmol) and salicylaldehyde (1.23 g, 10 mmol) yielded fluorescence pale yellow powder of **L**^{7}.

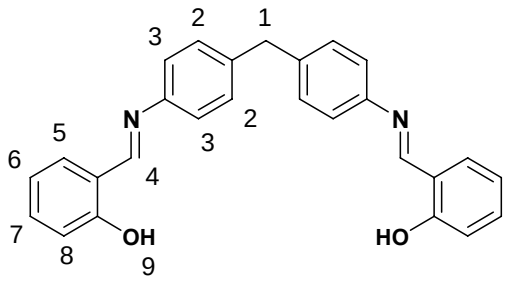

Yield	1.97 g, 96%
$C_{27}H_{22}N_2O_2$	406.48 g.mol^{-1}
Calc.[%]	C 79.78, H 5.46, N 6.89
Found [%]	C 79.20, H 5.47, N 6.91
ESI-MS (MeOH)	m/z = 407 [**L**^{7} + H]$^+$

^{1}H-NMR (500 MHz, $(CD_3)_2$−SO, 25 °C, TMS): δ [ppm] = 13.16 (s, 2H, H9), 8.95 (s, 2H, H4), 7.63 (dd, *J* = 8.7 Hz, 2H, H8), 7.38 (m, 10H, H2,3,7), 6.97 (m, 4H, H5,6), 4.02 (s, 2H, H1)

IR Spectroscopy data

Vibration frequency ṽ (cm^{-1})	Intensity†, band form‡	Assignment [150]
3430	m, br	O−H stretch
3054−2718	w, sr	C−H stretch
1619	s, sp	C=N stretch
1571−1496	m, sp	C−C_{arom} stretch
1412−1285	m, sp	O−H deformation and C−O stretch

† vs = very strong, s = strong, m = medium, w = weak
‡ br = broad, sp = sharp, sr = shoulder

α,α'-Bis(salicylimino)-*m*-xylene (**L^8**)

Methanolic solution of m-xylylenediamine (0.56 g, 4.10 mmol) and salicylaldehyde (1 g, 8.2 mmol) was refluxed for 3 hours to yield yellow precipitate of **L^8** which was filtered off, washed with methanol, and dried under vacuum.

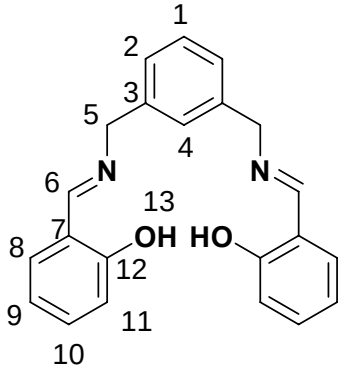

Yield	1.35 g, 96%
$C_{22}H_{20}N_2O_2$	344.41 g.mol^{-1}
Calc.[%]	C 76.72, H 5.85, N 8.13
Found [%]	C 76.78, H 5.94, N 8.20

ESI-MS (MeOH) m/z = 345 $[\mathbf{L}^{8} + H]^{+}$, 689 $[2\mathbf{L}^{8} + H]^{+}$

^{1}H-NMR (500 MHz, $(CD_3)_2$−SO, 25 °C, TMS): δ [ppm] = 13.42 (s, 2H, H13), 8.72 (s, 2H, H6), 7.48 (dd, *J* = 8.6, 8.7 Hz, 2H, H2), 7.38 (t, *J* = 7.7, 7.5 Hz, 1H, H1), 7.35 (s, 1H, H4), 7.33 and 6.91 (t, *J* = 11.9, 8.2, 7.5 Hz, 4H, H9,10), 7.27 (d, *J* = 7.6 Hz, 2H, H11), 6.87 (d, *J* = 8.2 Hz, 2H, H8), 4.82 (s, 4H, H5)

^{13}C-NMR (500 MHz, $CDCl_3$, 25 °C, TMS): δ [ppm] = 160 (C6), 161 (C12), 139 (C3), 132 (C2), 131 (C9), 129 (C4), 127 (C1), 126 (C11), 119 (C7), 118 (C10), 117 (C8), 63 (C5)

IR Spectroscopy data

Vibration frequency $\tilde{\nu}$ (cm^{-1})	Intensity[†], band form[‡]	Assignment [150]
3433	m, br	O−H stretch
3054−2733	w, sr	C−H stretch
1633	s, sp	C=N stretch
1580−1498	m, sp	C−C_{arom} stretch
1420−1282	m, sp	O−H deformation and C−O stretch

[†] vs = very strong, s = strong, m = medium, w = weak
[‡] br = broad, sp = sharp, sr = shoulder

α,α'-Bis(salicylamino)-*m*-xylene ($\mathbf{L}^{9}$)

Reduction of $\mathbf{L}^{8}$ by KBH_4 (0.44 g, 8.2 mmol) gave $\mathbf{L}^{9}$ in an oily visquous form.

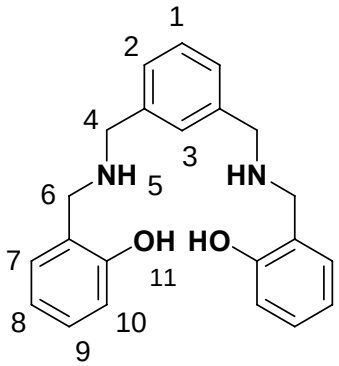

Yield	1.50 g, 70%
$C_{22}H_{24}N_2O_2$	348.44 g.mol^{-1}
Calc.[%]	C 75.83, H 6.94, N 8.04
Found [%]	C 75.90, H 6.98, N 8.15
ESI-MS (MeOH)	m/z = 349 [$\mathbf{L}^9$ + H]$^+$, 697 [2$\mathbf{L}^9$ + H]$^+$

^{1}H-NMR (500 MHz, $CDCl_3$, 25 °C, TMS): δ [ppm] = 7.32 (t, *J* = 7.3 Hz, 1H, H1), 7.24 (s, 2H, H11), 7.23 (s, 1H, H3), 7.22 (d, *J* = 7.5 Hz, 2H, H10), 7.16 (t, *J* = 1.6, 1.1 Hz, 2H, H8), 6.97 (d, *J* = 1.1 Hz 2H, H7), 6.84 (d, *J* = 0.9 Hz, 2H, H2), 6.77 (t, *J* = 1.1, 1.0 Hz, 2H, H9), 5.28 (s, 2H, H5), 4.00 (s, 4H, H6), 3.80 (s, 4H, H4)

α,α''-Bis(2-hydroxy-1-naphthalimino)-*m*-xylene ($\mathbf{L}^{10}$)

$\mathbf{L}^{10}$ was synthesized using the same procedure as in the case of $\mathbf{L}^8$ by refluxing a methanolic solution of m-xylylenediamine (0.59 g, 4.36 mmol) and 2-hydroxy-1-naphthaldehyde (1.5 g, 8.71 mmol) for 3 hours. The yellow solid obtained was filtered off, washed with methanol, and dried under vacuum.

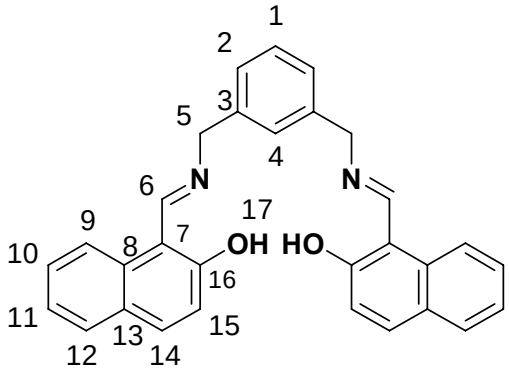

Yield	1.86 g, 97%
$C_{30}H_{24}N_2O_2$	444.52 g.mol^{-1}
Calc.[%]	C 81.06, H 5.44, N 6.30
Found [%]	C 80.78, H 5.53, N 6.38

ESI-MS (MeOH) m/z = 445 [$\mathbf{L}^{10}$ + H]$^+$, 889 [2$\mathbf{L}^{10}$ + H]$^+$

^{1}H-NMR (500 MHz, $(CD_3)_2$−SO, 25 °C, TMS): δ [ppm] = 14.38 (s, 2H, H17), 9.30 (d, *J* = 9.4 Hz, 2H, H6), 8.10 (d, *J* = 8.4 Hz, 2H, H2), 7.74 and 7.65 (d, *J* = 9.3, 7.9 Hz, 4H, H12,14), 7.47 (s, 1H, H4), 7.40−7.46 (m, 3H, H1,11), 7.38 (d, *J* = 8.1 Hz, 2H, H15), 7.20 (t, 2H, H10), 6.72 (d, *J* = 9.3 Hz, 2H, H9), 4.9 (d, *J* = 4.7 Hz, 4H, H5)

^{13}C-NMR (500 MHz, $CDCl_3$, 25 °C, TMS): δ [ppm] = 174 (C16), 159 (C6), 138 (C3), 137 (C14), 133 (C8), 130 (C4), 129 (C2), 128 (C15), 127 (C9), 126 (C1, C7), 124 (C12), 123 (C10), 118 (C11), 107 (C13), 58 (C5)

IR Spectroscopy data

Vibration frequency ṽ (cm^{-1})	Intensity†, band form‡	Assignment [150]
3434	m, br	O−H stretch
3054−2870	w, sr	C−H stretch
1632	s, sp	C=N stretch
1544−1492	w, sp	C−C_{arom} stretch
1446−1258	m, sp	O−H deformation and C−O stretch

† vs = very strong, s = strong, m = medium, w = weak
‡ br = broad, sp = sharp, sr = shoulder

α,α''-Bis(2-hydroxy-1-naphthalamino)-*m*-xylene ($\mathbf{L}^{11}$)
Reduction of $\mathbf{L}^{10}$ by KBH_4 (0.47 g, 8.75 mmol) gave oily substance of $\mathbf{L}^{11}$.

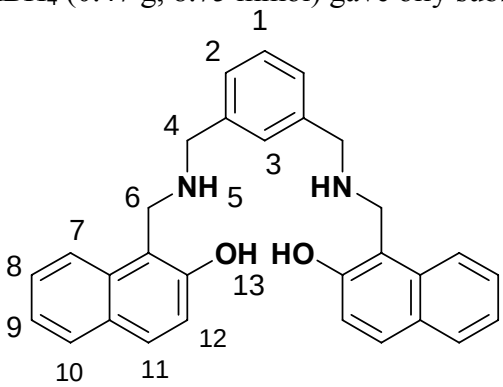

Yield	1.65 g, 85%
$C_{27}H_{22}N_2O_2$	448.56 g.mol^{-1}
Calc.[%]	C 80.33, H 6.29, N 6.25
Found [%]	C 80.10, H 6.37, N 6.31
ESI-MS (MeOH)	m/z = 449 [$\mathbf{L}^{11}$ + H]$^+$

^{1}H-NMR (500 MHz, $(CD_3)_2$−SO, 25 °C, TMS): δ [ppm] = 7.62 (t, *J* = 8.3 Hz, 1H, H1), 7.54 (s, 2H, H13), 7.53 (s, 1H, H3), 7.51 (d, *J* = 6.5 Hz, 2H, H12), 7.46 (d, *J* = 7.5 Hz, 2H, H11), 7.32 (t, *J* = 1.3 Hz 2H, H9), 7.23 (d, *J* = 0.9 Hz, 2H, H7), 7.20 (t, *J* = 1.8 Hz, 2H, H8), 7.12 (d, *J* = 6.2 Hz, 2H, H10), 5.28 (s, 2H, H5), 4.72 (s, 4H, H6), 3.9 (s, 4H, H4)

α,α"-Bis(salicyliminomethyl)-1,3-cyclohexane ($\mathbf{L}^{12}$)

Methanolic solution containing 1,3-bis(aminomethyl)cyclohexane (0.87 g, 6.14 mmol) and salicylaldehyde (1.5 g, 12.28 mmol) was refluxed for 5 hours to yield yellow precipitate of $\mathbf{L}^{12}$ which was filtered off, washed with methanol, and dried under vacuum.

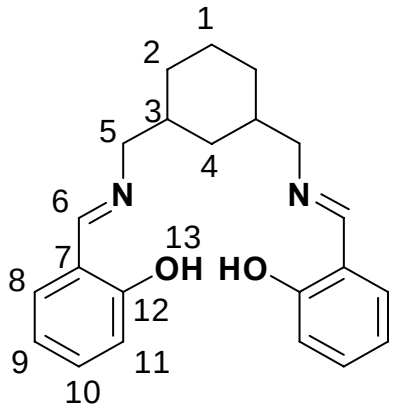

Yield	1.95 g, 91%
$C_{22}H_{26}N_2O_2$	350.45 g.mol^{-1}
Calc.[%]	C 75.40, H 7.48, N 7.99
Found [%]	C 75.18, H 7.52, N 7.98

ESI-MS (MeOH) m/z = 351 $[\mathbf{L}^{12} + H]^+$

^{1}H-NMR (500 MHz, $(CD_3)_2$−SO, 25 °C, TMS): δ [ppm] = 13.68 (s, 2H, H13), 8.49 (d, *J* = 5.7, 2H, H6), 7.42 (dd, *J* = 7.7, 7.6 Hz, 2H, H11), 7.28 (ddd, *J* = 7.3, 6.8, 6.2 Hz, 2H, H9), 6.85 (m, 4H, H8,10), 3.52 (d, *J* = 6.9, Hz, 4H, H5), 3.47 (m, 2H, H1), 0.89 and 1.7 (m, 8H, H2,3,4)

^{13}C-NMR (500 MHz, $CDCl_3$, 25 °C, TMS): δ [ppm] = 165 (C6), 161 (C12), 132 (C11), 131 (C8), 119 (C7), 118 (C10), 117 (C9), 66 (C5), 39 (C3), 36 (C4), 33 (C1), 31 (C12)

IR Spectroscopy data

Vibration frequency $\tilde{\nu}$ (cm^{-1})	Intensity†, band form‡	Assignment [150]
3434	m, br	O−H stretch
3054−2731	m, sp	C−H stretch
1633	s, sp	C=N stretch
1583−1463	m, sp	C−C_{arom} stretch
1419−1279	m, sp	O−H deformation and C−O stretch

† vs = very strong, s = strong, m = medium, w = weak

‡ br = broad, sp = sharp, sr = shoulder

α,α'-Bis(2-hydroxy-1-naphthaliminomethyl)-1,3-cyclohexane (**L**^{13})

To a stirred solution of 1,3-bis(aminomethyl)cyclohexane (0.62 g, 4.36 mmol) in 30 ml dry methanol was slowly add a methanolic solution containing 2-hydroxy-1-naphthaldehyde (1.5 g, 8.71 mmol). The resulting yellow solution was refluxed for 5 hours and cooled to room temperature to yield yellow solid of **L**^{13}.

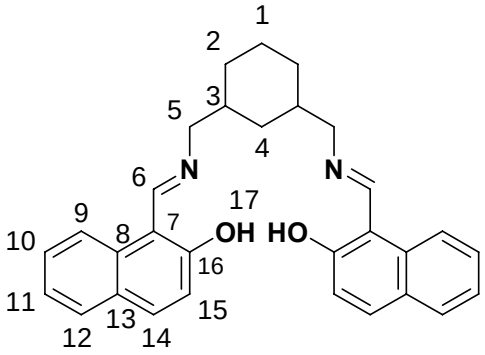

Yield	1.86 g, 95%
$C_{30}H_{30}N_2O_2$	450.57 g.mol^{-1}
Calc.[%]	C 79.97, H 6.71, N 6.22
Found [%]	C 80.05, H 7.18, N 6.25
ESI-MS (MeOH)	m/z = 451 [$\mathbf{L}^{13}$ + H]$^+$

^{1}H-NMR (500 MHz, $(CD_3)_2$−SO, 25 °C, TMS): δ [ppm] = 14.21 (s, 2H, H17), 9.10 (t, *J* = 10.6 Hz, 2H, H9), 8.05 (dd, *J* = 3.6 Hz, 2H, H15), 7.70 (dd, *J* = 3.9 Hz, 2H, H14), 7.61 (d, *J* = 7.9, 2H, H6), 7.39 (t, *J* = 7.1 Hz, 2H, H11), 7.17 (t, *J* = 7.4Hz, 2H, H10), 6.70 (dd, *J* = 5.1 Hz, 2H, H12), 3.64 (d, *J* = 7.9 Hz, 4H, H5), 3.52 (t, 2H, H4), 1.8 (m, 2H, H3), 1.75 (m, 4H, H2), 0.95 (m, 2H, H1)

^{13}C-NMR (500 MHz, $(CD_3)_2$−SO, 25 °C, TMS): δ [ppm] = 178 (C16), 159 (C6), 137 (C15), 134 (C7), 129 (C14), 128 (C12), 126 (C9), 125 (C8), 122 (C11), 118 (C10), 106 (C13), 57 (C5), 38 (C3), 33 (C4), 30 (C2), 28 (C1)

IR Spectroscopy data

Vibration frequency ṽ (cm^{-1})	Intensity†, band form‡	Assignment [150]
3431	m, br	O−H stretch
3054−2852	m, sr	C−H stretch
1630	s, sp	C=N stretch
1544−1449	w, sp	C−C_{arom} stretch
1402−1260	w, sp	O−H deformation and C−O stretch

† vs = very strong, s = strong, m = medium, w = weak
‡ br = broad, sp = sharp, sr = shoulder

Tris(2-benzylaminoethyl)amine ($\mathbf{L}^{14}$)

$\mathbf{L}^{14}$ was synthesized according to the published method of Naiini *et al*. [174]. Benzaldehyde (4.36 g, 41 mmol) was added dropwise to a solution of 2 g (13.68 mmol) of tris(2-aminoethyl)amine in 20 ml of dry methanol. The yellow solution was stirred for

2 h at 80 °C and cooled in an icebath. To this solution was added portionwise 2.21 g (41 mmol) of KBH_4 and the mixture stirred for additional 2 h at room temperature. The reaction mixture was then diluted with 50 ml of water and extracted with 3 × 25 ml of ether. The organic layers were extracted with 2 × 100 ml of 1 N HC1. The HCl layers were washed with 2 × 50 ml of ether, made basic with solid K_2CO_3 to pH > 10, and extracted with 3 × 50 ml of ether. The ether layers were dried over $MgSO_4$ and concentrated in vacuum to give the product as pale yellow oil.

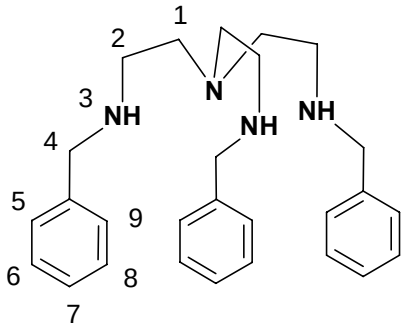

Yield	1.9 g, 70%
$C_{27}H_{36}N_4$	416.6 g.mol^{-1}
ESI-MS (MeOH)	m/z = 417 [$\mathbf{L}^{14}$ + H]$^+$

^{1}H-NMR (500 MHz, $CDCl_3$, 25 °C, TMS): δ [ppm] = 7.32-7.21 (m, 15H, H5-H9), 3.74 (s, 6H, H4), 2.67 (t, 6H, H2), 2.58 (t, 6H, H1), 1.81 (s, 3H, H3)

The spectral properties of $\mathbf{L}^{14}$ correspond to those reported by Naiini [174].

Tris{2-[1-(phenyl)ethyl]aminoethyl}amine ($\mathbf{L}^{15}$)

$\mathbf{L}^{15}$ was synthesized using the same procedure as in the case of $\mathbf{L}^{14}$ to give pale yellow oil. Starting material were acetophenone (3.70 g, 30.77 mmol), tris(2-aminoethyl)amine (1.50 g, 10.26 mmol) and KBH_4 (1.66 g, 30.77 mmol).

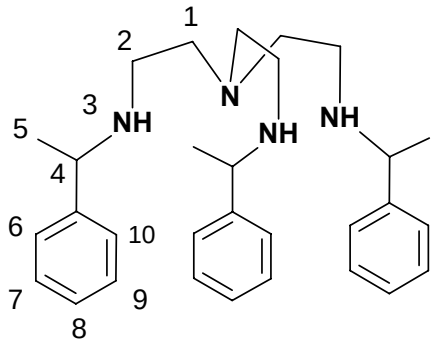

Yield	2.33 g, 50%
$C_{30}H_{42}N_4$	458.68 g.mol^{-1}
ESI-MS (MeOH)	m/z = 459 [**L**^{15} + H]$^+$

^{1}H-NMR (500 MHz, $CDCl_3$, 25 °C, TMS): δ [ppm] = 7.37-7.19 (m, 15H, H6-H10), 3.70 (q, 3H, H4), 2.60 (t, 6H, H2), 2.50 (t, 6H, H1), 2.15 (s, 3H, H3), 1.21 (d, 9H, H5)

Tris[2-(2-pyridylmethyl)aminoethyl]amine (**L**^{16})

To a stirred solution of tris(2-aminoethyl)amine (1.59 g, 10.89 mmol) in 30 ml of dry methanol was added 2-pyridinecarboxaldehyde (3.5 g, 32.68 mmol). To this solution was added in portions 1.76 g (32.68 mmol) of KBH_4 and the mixture was refluxed for 12 h under atmospheric pressure. The filtrate and washings were collected, evaporated, extracted with dichloromethane and concentrated under vacuum, yielding 2 g of yellow brown oil.

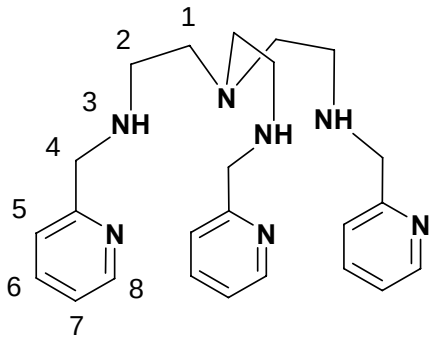

Yield	2 g, 43.76%
$C_{24}H_{33}N_7$	419.57 g.mol^{-1}
ESI-MS (MeOH)	m/z = 420 [**L**^{16} + H]$^+$

^{1}H-NMR (500 MHz, $CDCl_3$, 25 °C, TMS): δ [ppm] = 8.46 (d, 3H, H8), 7.56 (t, 3H, H6), 7.28 (d, 3H, H5), 7.1 (dd, 3H, H7), 3.90 (s, 6H, H4), 2.75 (t, 6H, H2), 2.65 (t, 6H, H1), 2.60 (s, 3H, H3)

Tris{2-[1-(2-pyridyl)ethyl]aminoethyl}amine (**L**^{17})

L^{17} was synthesized the same way as the previous ligand **L**^{16} with 2-acetylpyridyl (3.72 g, 30.77 mmol), tris(2-aminoethyl)amine (1.50 g, 10.26 mmol) and KBH_4 (1.66 g, 30.77 mmol) as starting materials.

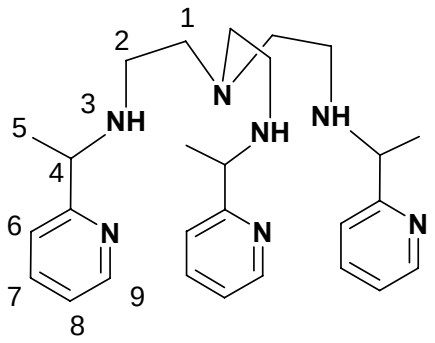

Yield	33.26 g, 68.92%
$C_{27}H_{39}N_7$	461.65 g.mol^{-1}
ESI-MS (MeOH)	m/z = 462 [**L**^{17} + H]$^+$

^{1}H-NMR (500 MHz, $CDCl_3$, 25 °C, TMS): δ [ppm] = 8.53 (d, 3H, H9), 7.64 (t, 3H, H7), 7.38 (d, 3H, H6), 7.17 (t, 3H, H8), 3.90 (q, 3H, H4), 2.57 (t, 6H, H2), 2.46 (t, 6H, H1), 1.35 (d, 9H, H5)

Tris[2-(2-hydroxylbenzyl)aminoethyl]amine (**L**^{18})

Tris(2-aminoethyl)amine (1 g, 6.84 mmol) and salicylaldehyde (2.51 g, 20.52 mmol) were dissolved in dry methanol (20 ml) and vigorously stirred at room temperature (r.t.) and refluxed for 2 h. An orange-yellow precipitate of tris–imine derivative was formed on cooling, filtered off, washed out with methanol, and dried in vacuo. The resulting solid was then added to a solution of 1.11 g (20.51 mmol) of KBH_4 in methanol and the reaction was let to stir overnight at r.t. The reaction mixture was then diluted with water, extracted with dichloromethane, dry with $MgSO_4$ and evaporated to yield orange-yellow viscous oil.

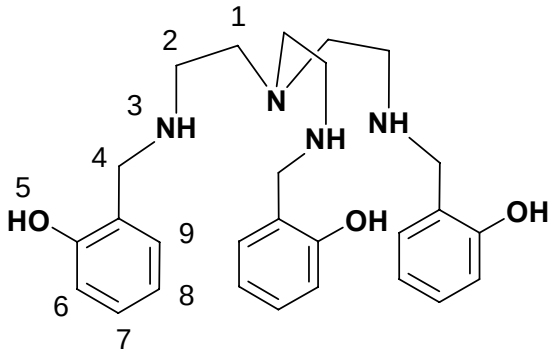

Yield	1.8 g, 66%
$C_{27}H_{36}N_4O_3$	464.6 g.mol^{-1}
ESI-MS (MeOH)	m/z = 465 [**L**^{18} + H]$^+$

^{1}H-NMR (500 MHz, $CDCl_3$, 25 °C, TMS): δ [ppm] = 7.13 (t, 3H, H8), 6.95 (d, 3H, H6), 6.75 (m, 6H, H7,9), 5.29 (s, 3H, H5), 3.97 (s, 6H, H4), 2.7 (t, 6H, H2), 2.57 (t, 6H, H1)

Tris{2-[1-(2-hydroxylphenyl)ethyl]iminoethyl}amine (**L**^{19})

L^{19} was synthesized the same way as in the case of ligand **L**^{18} until the Schiff-base step using 2-hydroxyacetophenone (4.19 g, 30.77 mmol) and tris(2-aminoethyl)amine (1.5 g, 10.26 mmol).

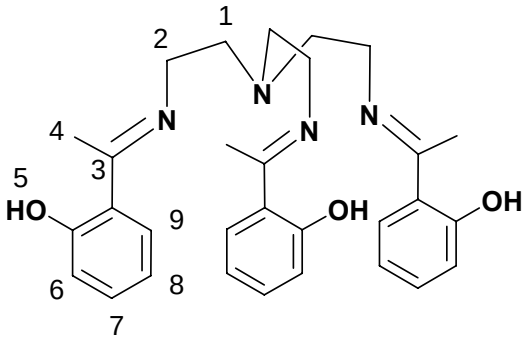

Yield	5 g, 97%
$C_{30}H_{36}N_4O_3$	500.63 g.mol^{-1}
ESI-MS (MeOH)	m/z = 451 [$\mathbf{L}^{19}$ + H]$^+$

^{1}H-NMR (500 MHz, $CDCl_3$, 25 °C, TMS): δ [ppm] = 16.58 (s, 3H, H5), 7.26 (d, 3H, H6), 7.21 (t, 3H, H8), 6.84 (d, 3H, H9), 6.61 (t, 3H, H7), 3.65 (t, 6H, H2), 3.00 (t, 6H, H1), 2.21 (s, 9H, H4)

Tris{2-[1-(2-hydroxylphenyl)ethyl]aminoethyl}amine ($\mathbf{L}^{20}$)

Reduction of $\mathbf{L}^{19}$ with KBH_4 (1.65 g, 30.77 mmol) gave $\mathbf{L}^{20}$**.**

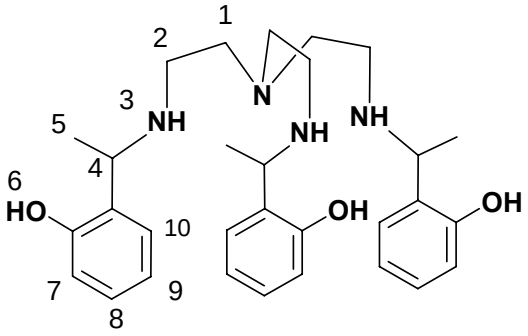

Yield	4.41 g, 84%
$C_{30}H_{30}N_2O_2$	506.68 g.mol^{-1}
ESI-MS (MeOH)	m/z = 507 [$\mathbf{L}^{20}$ + H]$^+$

^{1}H-NMR (500 MHz, $CDCl_3$, 25 °C, TMS): δ [ppm] = 7.15 (t, 3H, H9), 6.96 (t, 3H, H7), 6.75 (m, 6H, H8,10), 5.28 (s, 3H, H6), 3.90 (m, 3H, H4), 2.71 (t, 6H, H2), 2.6 (t, 6H, H1), 1.45 (d, 9H, H5)

N,N,N',N'-Tetrakis(2-pyridylmethyl)-*m*-xylylenediamine (**L^{21}**)

L^{21} was prepared by *N*-alkylation of 2,2'-dipicolylamine with *m*-xylylenedibromide. In 20 ml acetone solution containing *m*-xylylenedibromide (0.67 g, 2.51 mmol) and K_2CO_3 (1.18 g, 8.56 mmol) was slowly added an acetone solution of di-2-picolylamine (1.07 g, 5.35 mmol). The resulting mixture was refluxed for 80 hours and concentrated to give a brown substance which was dissolved in water and extracted from chloroform. The organic layer was dried over $MgSO_4$ and concentrated in vacuum to give the product as brown oil.

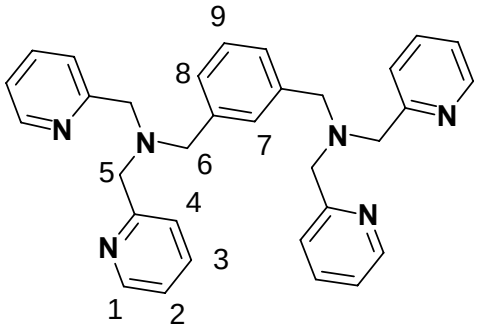

Yield	1.18 g, 94%
$C_{32}H_{32}N_6$	500.64 g.mol^{-1}
ESI-MS (MeOH)	m/z = 501 [**L^{21}** + H]$^+$

^{1}H-NMR (500 MHz, $(CD_3)_2$–SO, 25 °C, TMS): δ [ppm] = 8.48 (d, 4H, H1), 7.73 (t, 4H, H3), 7.59 (s, 1H, H7), 7.57 (d, 4H, H4), 7.25 (m, 7H, H2,8,9), 3.70 (s, 8H, H5), 3.61 (s, 4H, H6)

N,N,N',N'-Tetrakis(2-pyridylmethyl)-2,6-bis(aminomethyl)pyridine (**L**^{22})

L^{22} was similarly to that of **L**^{22} using 2,6-bis(chloromethyl)pyridine (0.36 g, 2.04 mmol), K_2CO_3 (0.75 g, 5.43 mmol) and di-2-picolylamine (0.81 g, 4.08 mmol) to yielded pale brown-yellow oil.

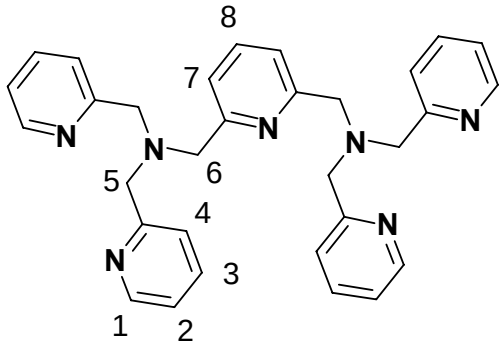

Yield	0.92 g, 90%
$C_{31}H_{31}N_7$	501.62 g.mol^{-1}
ESI-MS (MeOH)	m/z = 502 [**L**^{22} + H]$^+$

^{1}H-NMR (500 MHz, $(CD_3)_2$−SO, 25 °C, TMS): δ [ppm] = 8.50 (d, 4H, H1), 7.62 (m, 9H, H3,4,8), 7.43 (d, 2H, H7), 7.11 (t, 4H, H2), 3.87 (s, 8H, H5), 3.84 (s, 4H, H6)

N,N,N',N',N'',N''-Hexa(2-picolyl)-1,3,5-triazin-2,4,6-triamine (**L**^{23})

L^{23} was synthesized according to the published method of de Hoog *et al*. [177]. 2,4,6-Trichloro-[1,3,5]triazine (0.86 g, 4.65 mmol) was dissolved in tetrahydrofurane (20 mL). Three equivalents of *N*-ethyldiisopropylamine (DIPEA) (1.80 g, 13.95 mmol) were added and the two-necked round-bottomed flask was cooled to 0°C. Di-2-picolylamine (3.24 g, 16.26 mmol) was added portionwise. After the completion of the addition, the clear reaction mixture was warmed to room temperature and then heated under reflux for 24 h. The slightly yellow precipitate was isolated on a glass filter and washed with methanol (3×20 ml) to remove *N*-ethyldiisopropylamine hydrochloride.

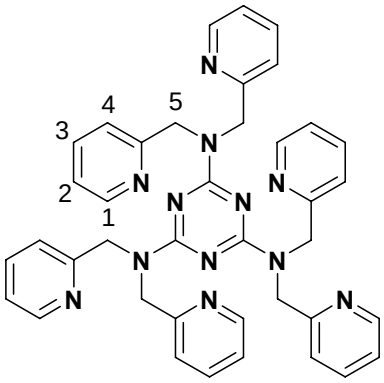

Yield	2.88 g, 92%
$C_{39}H_{36}N_{12}$	672.78 g.mol^{-1}
ESI-MS (MeOH)	m/z = 674 [$\mathbf{L}^{23}$ + H]$^+$

^{1}H-NMR (500 MHz, $(CD_3)_2$–SO, 25 °C, TMS): δ [ppm] = 8.42 (d, 6H, H1), 7.52 (t, 6H, H3), 7.17 (t, 6H, H2), 7.00 (d, 6H, H4), 4.79 (s, 12H, H5)

6.3.2 Complex synthesis

{[Ag($\mathbf{L}^1$)](ClO$_4$)·CH$_3$CN}$_n$ (**1**)

Silver perchlorate (11.0 mg, 0.053 mmol) in acetonitrile (1mL) was added to $\mathbf{L}^1$ (20.0 mg, 0.053 mmol) in dichloromethane (1 mL). Yellow needles (Figure 119) of the title compound were obtained by slow diffusion of diethylether vapour into the resulting solution in the dark over 2 days. The crystals were collected, washed with ether, and dried under vacuum.

Figure 119. Crystals photograph of **1**.

Yield	17 mg, 55%
$[Ag(C_{25}H_{20}N_4)]ClO_4$	583.77 g.mol^{-1}
Calc.[%]	C 51.44, H 3.45, N 9.60
Found [%]	C 51.29, H 3.23, N 9.59
ESI-MS (MeOH)	m/z = 1067 $[Ag_2\mathbf{L_2} + ClO_4]^+$; 690 $[Ag_2\mathbf{L} + ClO_4]^+$; 861 $[Ag\mathbf{L_2}]^+$; 485 $[Ag_2\mathbf{L_2}]^{2+}$

$\{[Ag(\mathbf{L}^2)]ClO_4 \cdot CH_2Cl_2\}_n$ (**2**)

Silver perchlorate (11.0 mg, 0.05 mmol) in acetonitrile (1mL) was added to L^2 (20.0 mg, 0.05 mmol) in dichloromethane (1 mL). Pale yellow needles of the title compound were obtained by slow diffusion of diethylether vapour into the resulting solution in the dark over 3 days. The crystals were collected, washed with ether, and dried under vacuum.

Yield	27 mg, 87%
$[Ag(C_{24}H_{18}N_4O)]ClO_4$	585.74 g.mol^{-1}
Calc.[%]	C 49.21, H 3.10, N 9.57
Found [%]	C 48.68, H 2.53, N 9.38
ESI-MS (MeOH)	m/z = 863 $[Ag\mathbf{L_2}]^+$; 485 $[Ag_2\mathbf{L_2}]^{2+}$

$[Ag_2(\mathbf{L}^2)_2](ClO_4)_2$ (**3**)

Silver perchlorate (11.0 mg, 0.05 mmol) in acetonitrile (1mL) was added to L^2 (20.0 mg, 0.05 mmol) in a mixture of methanol/acetonitrile (1:1) (1 mL). Yellow-green needles (Figure 120) of the title compound were obtained by slow diffusion of diethylether vapour into the resulting solution in the dark over 3 days. The crystals were collected, washed with ether, and dried under vacuum.

Figure 120. Crystals photograph of **3**.

Yield	19 mg, 61%
$[Ag_2(C_{24}H_{18}N_4O)_2](ClO_4)_2$	1171.49 g.mol^{-1}
Calc.[%]	C 49.21, H 3.10, N 9.57
Found [%]	C 48.89, H 2.80, N 9.51
ESI-MS (MeOH)	m/z = 1167 $[Ag_2\mathbf{L_2} + (ClO_4)_2 - H]^-$, 610 $[Ag\mathbf{L}OAC + 2MeOH + H]^+$, 485 $[Ag_2\mathbf{L_2}]^{2+}$

$[Cu\mathbf{L}^{\mathbf{1}}(SO_4)]_6 \cdot 24H_2O$ (**4**)

Copper(II) sulfate pentahydrate (6.63 mg, 0.027 mmol) in methanol /water (2:1) (1.5 ml) was slowly layered on the top of a acetonitrile solution (1 ml) containing ligand $\mathbf{L}^{\mathbf{1}}$ (15.0 mg, 0.04 mmol). Green block-like crystals (Figure 121) of the title compound were obtained by slow diffusion of diethylether into the resulting solution after 3 days. The crystals were collected, washed with ether, and dried under vacuum. Elemental analysis indicated the stoichiometric formula of $[Cu(\mathbf{L}^{\mathbf{1}})SO_4]_6 \cdot 18H_2O$.

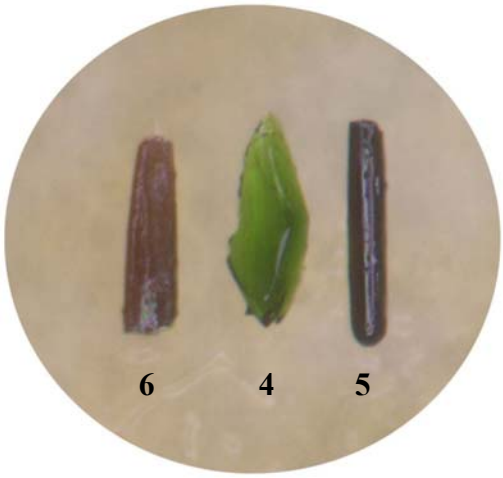

Figure 121. Crystals photograph of **4–6**.

Yield	22 mg, 93%
$C_{150}H_{156}Cu_6N_{24}O_{42}S_6$	3540.65 g.mol^{-1}

Calc.[%]	C 50.88, H 4.44, N 9.49, S 5.43
Found [%]	C 51.50, H 4.41, N 9.66, S 5.30
ESI-MS (MeOH)	m/z = 439 $[Cu(\mathbf{L^1})_2 + 2MeOH]^{2+}$, 536 $\{[Cu\mathbf{L^1}(SO_4)] + H\}$
UV/Vis (MeCN)	401 (ε = 912), 327 (ε = 2160), 300 (ε = 5324) nm

IR Spectroscopy data

Vibration frequency $\tilde{\nu}$ (cm^{-1})	Intensity†, band form‡	Assignment [150]
3429	s, br	$C-H_{ph}$ stretch
3063−3028	w, sr	$C-H_{py}$ stretch
2927−2902	w, sr	$C-H_{im}$ stretch
2855	w, sr	$C-H_{ali}$ stretch
1630	m, sp	$C=N_{im}$ stretch
1503−1445	m, sp	$C-C_{arom}$ stretch
1130−1020	s, sp	$C-N_{py}$ stretch

† vs = very strong, s = strong, m = medium, w = weak
‡ br = broad, sp = sharp, sr = shoulder

$[Cu\mathbf{L^2}(SO_4)]_6 \cdot 24H_2O$ (**5**)

The same procedure was used as for the preparation of (**4**). The complex (dark green needles) (Figure 121) was obtained after 2 months. Elemental analysis indicated the stoichiometric formula of $[Cu(\mathbf{L^2})SO_4]_6 \cdot 18H_2O$.

Yield	20 mg, 85%
$C_{144}H_{144}Cu_6N_{24}O_{48}S_6$	3552.48 $g.mol^{-1}$
Calc.[%]	48.69, H 4.09, N 9.46, S 5.42
Found [%]	C 48.22, H 4.28, N 9.04, S 5.57
ESI-MS (MeOH)	m/z = 441 $[Cu(\mathbf{L^2})_2 + 2MeOH]^{2+}$, 538 $\{[Cu\mathbf{L^2}(SO_4)] + H\}$
UV/Vis (MeCN)	425 (ε = 4397), 336 (ε = 4615), 309 (ε = 7003) nm

IR Spectroscopy data

Vibration frequency $\tilde{\nu}$ (cm^{-1})	Intensity[†], band form[‡]	Assignment [150]
3435	m, br	C−H_{ph} stretch
3064−3035	w, sr	C−H_{py} stretch
2929	w, sr	C−H_{im} stretch
1629	m, sp	C=N_{im} stretch
1495−1436	s, sp	C−C_{arom} stretch
1243−1200	s, sp	C−O stretch
1129−1026	m, sp	C−N_{py} stretch

[†] vs = very strong, s = strong, m = medium, w = weak
[‡] br = broad, sp = sharp, sr = shoulder

$[Cu\mathbf{L}^{3}(SO_4)]_6 \cdot 24H_2O$ (**6**)

The same procedure was used as for the preparation of (**4**). The complex (dark brown needles) (Figure 121) was obtained after 3 weeks. Elemental analysis indicated the stoichiometric formula of $[Cu\mathbf{L}^{3}(SO_4)]_6 \cdot 22H_2O$.

Yield	21 mg, 89%
$C_{144}H_{152}Cu_6N_{24}O_{46}S_{12}$	3720.94 $g.mol^{-1}$
Calc.[%]	C 46.48, H 4.12, N 9.03, S 10.34
Found [%]	C 46.51, H 4.36, N 9.04, S 9.94
ESI-MS (MeOH)	m/z = 457 $[Cu(\mathbf{L}^{3})_2 + 2MeOH]^{2+}$, 554 $\{[Cu\mathbf{L}^{3}(SO_4)] + H\}$
UV/Vis (MeCN)	418 (ε = 4734), 325 (ε = 5213), 309 (ε = 8530) nm

IR Spectroscopy data

Vibration frequency $\tilde{\nu}$ (cm^{-1})	Intensity[†], band form[‡]	Assignment [150]
3429	m, br	C−H_{ph} stretch
3058−2982	w, sr	C−H_{py} stretch
2924−2905	w, sr	C−H_{im} stretch
1625	s, sp	C=N_{im} stretch
1484−1434	s, sp	C−C_{arom} stretch
1204−1171	m, sp	C−S stretch
1087−1010	m, sp	C−N_{py} stretch

[†] vs = very strong, s = strong, m = medium, w = weak
[‡] br = broad, sp = sharp, sr = shoulder

$[Cu_6(\mathbf{L^2})_3(\mathbf{L^3})_3(SO_4)_6] \cdot 24H_2O$ (**7**)

Copper(II) sulfate pentahydrate (6.60 mg, 0.026 mmol) in methanol /water (2:1) (1.5 ml) was slowly layered on the top of a acetonitrile solution (1 ml) containing the mixture of ligand $\mathbf{L^2}$ (7.5 mg, 0.02 mmol) and $\mathbf{L^3}$ (7.5 mg, 0.019 mmol). Brown green needles of the title compound were obtained by slow diffusion of diethylether into the resulting solution after 2 weeks. The crystals were collected, washed with ether, and dried under vacuum. Elemental analysis indicated the stoichiometric formula of $[Cu_6(\mathbf{L^2})_3(\mathbf{L^3})_3(SO_4)_6] \cdot 18H_2O$.

Yield	22 mg, 92%
$C_{144}H_{144}Cu_6N_{24}O_{45}S_9$	3600.68 $g.mol^{-1}$
Calc.[%]	C 48.03, H 4.03, N 9.34, S 8.01
Found [%]	C 48.01, H 3.49, N 9.27, S 7.57
ESI-MS (MeOH)	m/z = 932 $[Cu(\mathbf{L^2})(\mathbf{L^3})(SO_4) + H]^+$

IR Spectroscopy data

Vibration frequency $\tilde{\nu}$ (cm^{-1})	Intensity†, band form‡	Assignment [150]
3429	m, br	C−H_{ph} stretch
3074−3015	w, sr	C−H_{py} stretch
2928	w, sr	C−H_{im} stretch
1626	m, sp	C=N_{im} stretch
1494−1435	s, sp	C−C_{arom} stretch
1243−1198	s, sp	C−O and C−S stretch
1122−1025	m, sp	C−N_{py} stretch

† vs = very strong, s = strong, m = medium, w = weak
‡ br = broad, sp = sharp, sr = shoulder

$[Hg_2(\mathbf{L^2})_2(ClO_4)_3(H_2O)_2]ClO_4{\cdot}CH_3CN$ (**8**)

Mercury(II) perchlorate monohydrate (16.55 mg, 0.04 mmol) in acetonitrile (1 ml) was layered on the top of a methanolic solution (1 ml) containing ligand $\mathbf{L^2}$ (15.0 mg, 0.04 mmol). Brown-yellow crystals (Figure 122) of the title compound were formed by slow diffusion of diethylether into the resulting solution after 3 days. The crystals were collected, washed with cold methanol and dried under vacuum. Elemental analysis indicated the stoichiometric formula of $[Hg_2(\mathbf{L^2})_2](ClO_4)_4{\cdot}H_2O$.

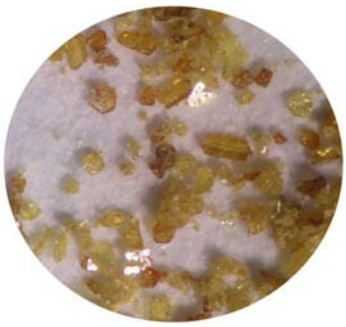

Figure 122. Crystals photograph of **8**.

Yield	26 mg, 83%
$C_{48}H_{38}Cl_4Hg_2N_8O_{19}$	1573.85 $g.mol^{-1}$
Calc.[%]	Hg 25.49, Cl 9.01, C 36.63, H 2.43, N 7.12, O 19.31

Found [%]	Hg 26.90, Cl 8.40, C 36.10, H 2.50, N 7.20, O 19.10
ESI-MS (MeOH/DMSO)	m/z = 479 $[Hg(\mathbf{L^2})_2]^{2+}$, 596 $[Hg(\mathbf{L^2})_2 + 3(DMSO)]^{2+}$

IR Spectroscopy data

Vibration frequency ṽ (cm^{-1})	Intensity†, band form‡	Assignment [150]
3436	m, br	C−H_{ph} stretch
3104−3036	w, sr	C−H_{py} stretch
2925	w, sr	C−H_{im} stretch
1637	m, sp	C=N_{im} stretch
1495−1449	s, sp	C−C_{arom} stretch
1243−1195	s, sp	C−O stretch
1105	s, sp	C−N_{py} stretch

† vs = very strong, s = strong, m = medium, w = weak
‡ br = broad, sp = sharp, sr = shoulder

$[Hg_2(\mathbf{L^1})_2]$ $(ClO_4)_4$ (**9**)

Mercury(II) perchlorate monohydrate (16.55 mg, 0.04 mmol) in acetonitrile (1 ml) was layered on the top of a methanolic solution (1 ml) containing ligand $\mathbf{L^1}$ (15.0 mg, 0.04 mmol). Light-yellow crystals (Figure 123) of the title compound were formed by slow diffusion of diethylether into the resulting solution after 3 days. The crystals were collected, washed with cold methanol and dried under vacuum. Elemental analysis indicated the stoichiometric formula of $[Hg_2(\mathbf{L^1})_2](ClO_4)_4 \cdot 2H_2O$.

Figure 123. Crystals photograph of **9.**

Yield	23 mg, 72%
$C_{50}H_{44}Cl_4Hg_2N_8O_{18}$	1587.92 g.mol^{-1}
Calc.[%]	Hg 25.26, Cl 8.93, C 37.82, H 2.79, N 7.06, O 18.14
Found [%]	Hg 25.70, Cl 8.30, C 37.60, H 3.80, N 7.30, O 17.90
ESI-MS (MeOH)	m/z = 477 $[Hg(\mathbf{L^1})_2]^{2+}$, 594 $[Hg(\mathbf{L^1})_2 + 3(DMSO)]^{2+}$, 1053 $[Hg(\mathbf{L^1})_2 + ClO_4]^+$

IR Spectroscopy data

Vibration frequency $\tilde{\nu}$ (cm^{-1})	Intensity†, band form‡	Assignment [150]
3458	m, br	C−H_{ph} stretch
3111−3040	w, sr	C−H_{py} stretch
2926	w, sr	C−H_{im} stretch
2842	w, sr	C−H_{ali} stretch
1634	m, sp	C=N_{im} stretch
1504−1444	m, sp	C−C_{arom} stretch
1096	s, sp	C−N_{py} stretch

† vs = very strong, s = strong, m = medium, w = weak
‡ br = broad, sp = sharp, sr = shoulder

$[Hg_2(\mathbf{L^3})_2]$ $(ClO_4)_4$ (**10**)

Mercury(II) perchlorate monohydrate (15.98 mg, 0.04 mmol) in acetonitrile (1 ml) was layered on the top of a methanolic solution (1 ml) containing ligand $\mathbf{L^3}$ (15.0 mg, 0.04 mmol). Light-yellow crystals of the title compound were formed by slow diffusion of diethylether into the resulting solution after 3 days. The crystals were collected, washed with cold methanol and dried under vacuum. Elemental analysis indicated the stoichiometric formula of $[Hg_2(\mathbf{L^3})_2](ClO_4)_4 \cdot 10H_2O$.

Yield	31 mg, 88%
$C_{48}H_{56}Cl_4Hg_2N_8O_{26}S_2$	1768.12 g.mol^{-1}
Calc.[%]	C 32.61, H 3.19, N 6.34, S 3.63
Found [%]	C 32.28, H 2.53, N 6.85, S 3.18

ESI-MS (MeOH) m/z = 495 $[Hg(\mathbf{L^3})_2]^{2+}$, 612 $[Hg(\mathbf{L^3})_2 + 3(DMSO)]^{2+}$, 1089 $[Hg(\mathbf{L^3})_2 + ClO_4]^+$

IR Spectroscopy data

Vibration frequency $\tilde{\nu}$ (cm^{-1})	Intensity†, band form‡	Assignment [150]
3440	m, br	C−H_{ph} stretch
3083−3035	w, sr	C−H_{py} stretch
2972	w, sr	C−H_{im} stretch
1633	m, sp	C=N_{im} stretch
1485−1446	m, sp	C−C_{arom} stretch
1266−1198	w, sp	C−S stretch
1100	s, sp	C−N_{py} stretch

† vs = very strong, s = strong, m = medium, w = weak
‡ br = broad, sp = sharp, sr = shoulder

$[Mn_2(\mathbf{L^1})_3](ClO_4)_4$ (**11**)

Manganese(II) perchlorate hexahydrate (9.56 mg, 0.026 mmol) in methanol (1 ml) was layered on the top of a acetonitrile solution (1 ml) containing ligand $\mathbf{L^1}$ (15.0 mg, 0.04 mmol). Orange-red crystals (Figure 124) of the title compound were obtained by slow diffusion of diethylether into the resulting overnight. The crystals were collected, washed with diethylether and dried under vacuum. Elemental analysis indicated the stoichiometric formula of $[Mn_2(\mathbf{L^1})_3](ClO_4)_4 \cdot 2H_2O$.

Figure 124. Crystals photograph of **11**.

Yield	21 mg, 94%
$C_{75}H_{64}Cl_4Mn_2N_{12}O_{18}$	1673.07 g.mol^{-1}
Calc.[%]	C 53.84, H 3.86, N 10.05
Found [%]	C 54.07, H 3.29, N 9.93
ESI-MS (MeOH)	m/z = 446 $[Mn_2(\mathbf{L^1})_3(ClO_4)_4]^{3+}$, 591 $[Mn(\mathbf{L^1})_3]^{2+}$,718 $[Mn_2(\mathbf{L^1})_3(ClO_4)_2]^{2+}$

IR Spectroscopy data

Vibration frequency ṽ (cm^{-1})	Intensity†, band form‡	Assignment [150]
3436	m, br	C−H_{ph} stretch
3100−3066	w, sr	C−H_{py} stretch
1630	m, sp	C=N_{im} stretch
1494−1443	s, sp	C−C_{arom} stretch
1244−1198	s, sp	C−H_{ali} deformation
1093−1014	s, sp	C−N_{py} stretch

† vs = very strong, s = strong, m = medium, w = weak
‡ br = broad, sp = sharp, sr = shoulder

$[Ni_2(\mathbf{L^2})_3](NO_3)_4$ (**12**)

Nickel(II) nitrate hexahydrate (7.16 mg, 0.025 mmol) in acetonitrile (0.5 ml) was layered on the top of a acetonitrile solution (0.5 ml) containing ligand $\mathbf{L^2}$ (14.0 mg, 0.04 mmol). Orange-red crystals (Figure 125) of the title compound were obtained by slow diffusion of diethylether into the resulting solution after 1 week. The crystals were collected, and dried under vacuum. Elemental analysis indicated the stoichiometric formula of $[Ni_2(\mathbf{L^2})_3](NO_3)_4{\cdot}6H_2O$.

Figure 125. Crystals photograph of **12**.

Yield	13 mg, 61%
$C_{72}H_{66}N_{16}Ni_2O_{21}$	1608.77 g.mol^{-1}
Calc.[%]	C 53.75, H 4.14, N 14.09
Found [%]	C 54.28, H 4.47, N 13.55
ESI-MS (MeOH)	m/z = 437 $[Ni_2(\mathbf{L^2})_3NO_3]^{3+}$, 687 $[Ni_2(\mathbf{L^2})_3(NO_3)_2]^{2+}$, 1436 $[Ni_2(\mathbf{L^2})_3(NO_3)_3]^{+}$

IR Spectroscopy data

Vibration frequency $\tilde{\nu}$ (cm^{-1})	Intensity[†], band form[‡]	Assignment [150]
3435	m, br	C−H_{ph} stretch
3060−3025	w, sr	C−H_{py} stretch
2928	w, sr	C−H_{im} stretch
1627	m, sp	C=N_{im} stretch
1494−1385	s, sp	C−C_{arom} stretch
1243−1199	m, sp	C−O stretch
1164−1021	w, sp	C−N_{py} stretch

[†] vs = very strong, s = strong, m = medium, w = weak
[‡] br = broad, sp = sharp, sr = shoulder

$[Ni_2(\mathbf{L^5})_3](PF_6)_4$ (**13**)

To a solution of $\mathbf{L^5}$ (50.00 mg, 0.112 mmol) in MeOH (5 ml) a methanolic solution (5 ml) of nickel (II) chloride hexahydrate (17.82 mg, 0.074 mmol) was add. The resulting orange-yellow mixture was refluxed for 1 h, cooled to room temperature and treated with methanolic ammonium hexafluorophosphate (excess) to yield an orange-yellow product which was isolated by filtration, washed with cold methanol and dried under vacuum. Addition of water in a saturated acetonitrile solution of the complex (20% acetonitrile solution) afforded single X-Ray quality crystals (Figure 126) overnight. Elemental analysis indicated the stoichiometric formula of $[Ni_2(\mathbf{L^5})_3](PF_6)_4 \cdot H_2O$.

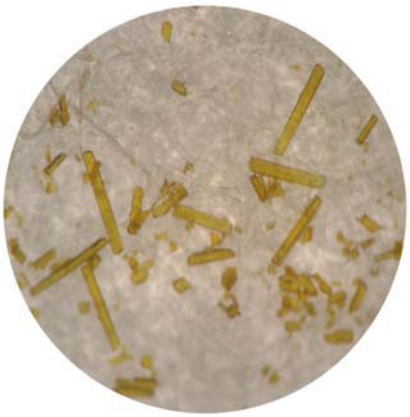

Figure 126. Crystals photograph of **13**.

Yield	67 mg, 87%
$C_{90}H_{86}F_{24}N_{12}Ni_2OP_4$	2048.97 g.mol^{-1}
Calc.[%]	C 52.76, H 4.23, N 8.20
Found [%]	C 52.24, H 4.72, N 8.15
ESI-MS (MeOH)	m/z = 531 $[Ni_2(\mathbf{L^5})_3PF_6]^{3+}$,
	563 $[Ni_2(\mathbf{L^5})_3PF_6 + 3MeOH]^{3+}$,
	965 $[Ni_2(\mathbf{L^5})_3(PF_6)_2 + 6MeOH]^{2+}$
UV/Vis (MeCN)	361 (ε = 36132), 328 (ε = 57200), 286 (ε = 51200) nm

IR Spectroscopy data

Vibration frequency ṽ (cm^{-1})	Intensity†, band form‡	Assignment [150]
3436	m, br	C−H_{ph} stretch
3052−3000	w, sr	C−H_{py} stretch
2932	m, sp	C−H_{im} stretch
2862	m, sp	C−H_{ali} stretch
1631	m, sp	C=N_{im} stretch
1500−1445	m, sp	C−C_{arom} stretch
1057−1020	m, sp	C−N_{py} stretch

† vs = very strong, s = strong, m = medium, w = weak

‡ br = broad, sp = sharp, sr = shoulder

$[Fe_2(\mathbf{L^5})_3](PF_6)_4$ (**14**)

To a solution of $\mathbf{L^5}$ (50.00 mg, 0.112 mmol) in MeOH (5 ml) a methanolic solution (5 ml) of iron(II) chloride tetrahydrate (14.91 mg, 0.075 mmol) was add. The resulting purple mixture was refluxed for 1 h, cooled to room temperature and treated with methanolic ammonium hexafluorophosphate (excess) to yield a purple product which was isolated by filtration, washed with cold methanol and dried under vacuum. Addition of water in a saturated acetonitrile solution of the complex (20% acetonitrile solution) afforded single crystals overnight. Elemental analysis indicated the stoichiometric formula of $[Fe_2(\mathbf{L^5})_3](PF_6)_4 \cdot 3H_2O$

Yield	64 mg, 82%
$C_{90}H_{90}F_{24}Fe_2N_{12}O_3P_4$	2079.30 $g.mol^{-1}$
Calc.[%]	C 51.99, H 4.36, N 8.08
Found [%]	C 51.87, H 4.18, N 8.12
ESI-MS (MeOH)	m/z = 361 $[Fe_2(\mathbf{L^5})_3]^{4+}$, 931 $[Fe_2(\mathbf{L^5})_3(PF_6)_2 + 4MeOH]^{2+}$, 1879 $[Fe_2(\mathbf{L^5})_3(PF_6)_3]^{+}$
UV/Vis (MeCN)	574 (ε = 16800), 521 (ε = 12400), 328 (ε = 48000), 280 (ε = 69600) nm

IR Spectroscopy data

Vibration frequency $\tilde{\nu}$ (cm^{-1})	Intensity†, band form‡	Assignment [150]
3436	m, br	C−H_{ph} stretch
3052−3000	w, br	C−H_{py} stretch
2939	m, sp	C−H_{im} stretch
2862	m, sp	C−H_{ali} stretch
1613	w, sp	C=N_{im} stretch
1500−1443	m, sp	C−C_{arom} stretch
1059−1014	m, sp	C−N_{py} stretch

† vs = very strong, s = strong, m = medium, w = weak

‡ br = broad, sp = sharp, sr = shoulder

Synthesis of compounds 15-20

Compounds **15-20** were synthesized by refluxing methanolic solution containing Schiff base ligands (1 mmol), and $UO_2(NO_3)_2{\cdot}6H_2O$ (1 mmol) for 12 h. The resulting orange-red precipitates were filtered, washed with a cold MeOH, and dried under vacuum. Crystal of **15**, **17**, **18** and **20** suitable for X-ray diffraction studies were obtained by slow diffusion of diethylether into the equimolar methanol/acetonitrile (1:1) (1 mL) solution of $UO_2(NO_3)_2{\cdot}6H_2O$ (0.05 mmol) and the corresponding ligand after one week. Crystals photograph of **17** and **18** are shown in Figure 127. The crystals were collected, washed with ether, and dried under vacuum. IR spectroscopy data are nearly the same in every case.

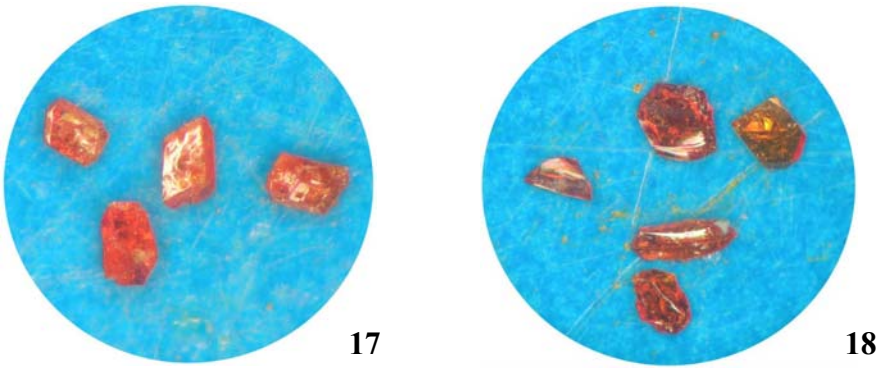

Figure 127. Crystals photograph of **17** and **18**

IR Spectroscopy data of compounds **15-20**

Vibration frequency $\tilde{\nu}$ (cm^{-1})	Intensity†, band form‡	Assignment [150]
3433−3428	m, br	O−H stretch
3158−2853	w, sr	C−H stretch
2427	w, sr	N−H stretch
1654−1637	s, sp	C=N stretch
1385	vs, sp	O−H deformation and C−O stretch
921	s, sp	U=O stretch

† vs = very strong, s = strong, m = medium, w = weak

‡ br = broad, sp = sharp, sr = shoulder

$[UO_2(\mathbf{L}^6)(NO_3)_2]_n$ (**15**)

Yield	27 mg, 73%
$C_{26}H_{20}N_4O_{11}U$	802.49 g.mol^{-1}
Calc.[%]	C 38.91, H 2.51, N 6.98
Found [%]	C 38.95, H 2.37, N 7.01
ESI-MS (MeOH)	m/z = 677 $[UO_2(\mathbf{L}^6) - H]^+$, 740 $[UO_2(\mathbf{L}^6)(NO_3)]^+$, 1085 $[UO_2(\mathbf{L}^6)_2 - H]^+$

^{1}H-NMR (500 MHz, DMSO-d_6, 25 °C, TMS): δ [ppm] = 12.67 (s, 2H, OH···N), 9.12 (s, 2H, CH=N), 7.64 (dd, J = 7.7 Hz, 2H, C_6H_4O), 7.50 (ddd, J = 5.4, 6.7 Hz, 4H, $C_6H_4OC_6H_4$), 7.43 (t, J = 7.9 Hz, 2H, C_6H_4O), 7.13 (ddd, J = 11.9, 8.2, 7.5 Hz, 4H, $C_6H_4OC_6H_4$), 6.98 (m, 4H, C_6H_4O)

$[UO_2(\mathbf{L}^7)(NO_3)_2]_n$ (**16**)

Yield	24 mg, 65%
$C_{27}H_{22}N_4O_{10}U$	800.51 g.mol^{-1}
Calc.[%]	C 40.51, H 2.77, N 7.00
Found [%]	C 40.86, H 2.99, N 6.68
ESI-MS (MeOH)	m/z = 675 $[UO_2(\mathbf{L}^7) - H]^+$, 738 $[UO_2(\mathbf{L}^7)(NO_3)]^+$, 1081 $[UO_2(\mathbf{L}^7)_2 - H]^+$

^{1}H-NMR (500 MHz, DMSO-d_6, 25 °C, TMS): δ [ppm] = 12.73 (s, 2H, OH···N), 9.11 (s, 2H, CH=N), 7.62 (dd, J = 8.7 Hz, 2H, C_6H_4O), 7.35 (m, 10H, C_6H_4O, $C_6H_4OC_6H_4$), 6.96 (m, 4H, C_6H_4O), 4.00 (s, 2H, CH_2)

$[UO_2(\mathbf{L}^8)(NO_3)_2]$ (**17**)

Yield	30 mg, 89%
$C_{22}H_{20}N_4O_{10}U$	738.44 g.mol^{-1}

Calc.[%]	C 35.78, H 2.73, N 7.59
Found [%]	C 35.38, H 3.00, N 7.50
ESI-MS (MeOH)	m/z = 613 $[UO_2(\mathbf{L^8}) - H]^+$, 676 $[UO_2(\mathbf{L^8})(NO_3)]^+$, 771 $[UO_2(\mathbf{L^8})(NO_3)_2 + MeOH + H]^+$, 957 $[UO_2(\mathbf{L^8})_2 - H]^+$
UV/Vis (MeOH)	324 (ε = 17000), 357 (ε = 18600) nm

^{1}H-NMR (500 MHz, DMSO-d_6, 25 °C, TMS): δ [ppm] = 13.01 (s, 2H, OH···N), 8.83 (s, 2H, CH=N), 7.48 (dd, J = 7.6 Hz, 2H, C_6H_4), 7.39 (t, J = 7.6, 7.5 Hz, 1H, C_6H_4), 7.35 (s, 1H, C_6H_4), 7.33 and 6.91 (t, J = 11.2, 7.5 Hz, 4H, C_6H_4O), 7.28 (d, J = 7.7 Hz, 2H, C_6H_4O), 6.87 (d, J = 8.3 Hz, 2H, C_6H_4O), 4.82 (s, 2H, CH_2)

$[UO_2(\mathbf{L^{10}})(NO_3)_2]$ (**18**)

Yield	36 mg, 94%
$C_{30}H_{24}N_4O_{10}U$	838.56 g.mol^{-1}
Calc.[%]	C 42.97, H 2.88, N 6.68
Found [%]	C 42.52, H 2.98, N 6.97
ESI-MS (MeOH)	m/z = 713 $[UO_2(\mathbf{L^{10}}) - H]^+$, 838 $[UO_2(\mathbf{L^{10}})(NO_3)_2 - H]^-$, 1157 $[UO_2(\mathbf{L^{10}})_2 - H]^+$
UV/Vis (MeOH)	310 (ε = 13200), 334 (ε = 13200), 398 (ε = 14800), 420 (ε = 12000) nm

^{1}H-NMR (500 MHz, DMSO-d_6, 25 °C, TMS): δ [ppm] = 13.99 (s, 2H, OH···N), 9.39 (d, J = 14.9 Hz, 2H, CH=N), 8.15 (dd, J = 11.5, 12 Hz, 2H, C_6H_4), 7.82 and 7.70 (d, J = 9.6, 7.3 Hz, 4H, $C_{10}H_6O$), 7.40−7.48 (m, 4H, C_6H_4, $C_{10}H_6O$), 7.38 (d, J = 8.6 Hz, 2H, $C_{10}H_6O$), 7.25 (t, 2H, $C_{10}H_6O$), 6.81 (d, J = 7.3 Hz, 2H, $C_{10}H_6O$), 4.94 (d, J = 9.7 Hz, 4H, CH_2)

$[UO_2(\mathbf{L^{12}})(NO_3)_2]$ (**19**)

Yield	26 mg, 76%
$C_{22}H_{26}N_4O_{10}U$	744.49 g.mol^{-1}
Calc.[%]	C 35.49, H 3.52, N 7.53
Found [%]	C 35.05, H 3.63, N 7.57
ESI-MS (MeOH)	m/z = 619 $[UO_2(\mathbf{L^{12}}) - H]^+$, 679 $[UO_2(\mathbf{L^{12}})(NO_3)]^+$, 970 $[UO_2(\mathbf{L^{12}})_2 - H]^+$
UV/Vis (MeOH)	322 (ε = 4000), 376 (ε = 5200) nm

^{1}H-NMR (500 MHz, DMSO-d_6, 25 °C, TMS): δ [ppm] = 13.12 (s, 2H, OH···N), 8.63 (d, J = 8.7, 2H, CH=N), 7.43 (dd, J = 6.7, 6.6 Hz, 2H, C_6H_4O), 7.26 (ddd, J = 3.3, 7.8, 5.2 Hz, 2H, C_6H_4O), 6.85 (m, 4H, C_6H_4O), 3.52 (d, J = 9.7, Hz, 4H, CH_2), 3.45 (m, 2H, C_6H_{10}), 0.9 and 1.7 (m, 8H, C_6H_{10})

$[UO_2(\mathbf{L^{13}})(NO_3)_2]$ (**20**)

Yield	35 mg, 90%
$C_{30}H_{30}N_4O_{10}U$	844.61 g.mol^{-1}
Calc.[%]	C 42.66, H 3.58, N 6.63
Found [%]	C 42.67, H 3.76, N 6.60
ESI-MS (MeOH)	m/z = 719 $[UO_2(\mathbf{L^{13}}) - H]^+$, 782 $[UO_2(\mathbf{L^{13}})(NO_3)]^+$, 1170 $[UO_2(\mathbf{L^{13}})_2 - H]^+$
UV/Vis (MeOH)	338 (ε = 15400), 395 (ε = 13600), 418 (ε = 10600) nm

^{1}H-NMR (500 MHz, DMSO-d_6, 25 °C, TMS): δ [ppm] = 13.73 (s, 2H, OH···N), 9.25 (t, J = 10.5 Hz, 2H, $C_{10}H_6O$), 8.06 (dd, J = 7.6 Hz, 2H, $C_{10}H_6O$), 7.68 (dd, J = 4.9 Hz, 2H, $C_{10}H_6O$), 7.58 (d, J = 7.7, 2H, CH=N), 7.40 (t, J = 6.9 Hz, 2H, H $C_{10}H_6O$), 7.17 (t, J = 7.2 Hz, 4H, C_6H_{10}), 6.71 (dd, J = 5.9 Hz, 2H, $C_{10}H_6O$), 3.62 (d, J = 8.1 Hz, 4H, CH_2), 3.52 (m, 2H, C_6H_{10}), 1.8 (m, 2H, C_6H_{10}), 1.75 (m, 4H, C_6H_{10}), 0.95 (m, 2H, C_6H_{10})

$[UO_2(\mathbf{L^{21}})(NO_3)_2]$ (**21**)

Uranium(VI) nitrate hexahydrate (50.0 mg, 0.1 mmol) and $\mathbf{L^{21}}$ (49.9 mg, 0.1 mmol) in a mixture acetonitrile-methanol (1:1, 10mL) were refluxed for 6 hours, after which a brown-orange solution was formed. No precipitate or crystals were formed with slow diffusion of diethylether into the resulting solution.

ESI-MS (MeOH) m/z = 833 $[UO_2(\mathbf{L^{21}})(NO_3)]^+$, 864 $[UO_2(\mathbf{L^{21}})(NO_3)$ + MeOH$]^+$

$[UO_2(\mathbf{L^{22}})(NO_3)_2]$ (**22**)

Uranium(VI) nitrate hexahydrate (50.0 mg, 0.1 mmol) and $\mathbf{L^{22}}$ (49.9 mg, 0.1 mmol) in a mixture acetonitrile-methanol (1:1, 10mL) were refluxed for 6 hours, after which a brown-orange solution was formed. No precipitate or crystals were formed with slow diffusion of diethylether into the resulting solution.

ESI-MS (MeOH) m/z = 865 $[UO_2(\mathbf{L^{22}})(NO_3)$ + MeOH$]^+$

$[Eu(\mathbf{L^{21}})(NO_3)_3]$ (**23**)

Europium(III) nitrate pentahydrate (17.1 mg, 0.04 mmol) in acetonitrile (1 ml) was layered on the top of a dichloromethane solution (1 ml) containing ligand $\mathbf{L^{21}}$ (20.0 mg, 0.04 mmol). Light-yellow precipitate was formed by slow diffusion of diethylether into the resulting solution after 1 week, collected and dried under vacuum. Elemental analysis indicated the stoichiometric formula of $[Eu(\mathbf{L^{21}})(NO_3)_3]\cdot H_2O$.

Yield	30 mg, 88%
$C_{32}H_{34}EuN_9O_{10}$	856.63 g.mol^{-1}
Calc.[%]	C 44.87, H 4.00, N 14.72
Found [%]	C 44.48, H 3.38, N 14.77
ESI-MS (MeOH)	m/z = 777 $[Eu(\mathbf{L^{21}})(NO_3)_2]^+$, 840 $[Eu(\mathbf{L^{21}})(NO_3)_3 + H]^+$

[Nd(**L**^{21})$(NO_3)_3$] (**24**)

Neodynium(III) nitrate monohydrate (13.9 mg, 0.04 mmol) in acetonitrile (1 ml) was layered on the top of a dichloromethane solution (1 ml) containing ligand **L**^{21} (20.0 mg, 0.04 mmol). Yellow precipitate was formed by slow diffusion of diethylether into the resulting solution after 1 week, collected and dried under vacuum.

Yield	21 mg, 63%
$C_{32}H_{32}N_9NdO_9$	830.89 g.mol^{-1}
Calc.[%]	C 46.26, H 3.88, N 15.17
Found [%]	C 45.78, H 3.47, N 14.85
ESI-MS (MeOH)	m/z = 766 [Nd(**L**^{21})$(NO_3)_2]^+$, 829 [Nd(**L**^{21})$(NO_3)_3$ + H]$^+$

[Eu(**L**^{23})$(NO_3)_3$] (**25**)

Europium(III) nitrate pentahydrate (12.7 mg, 0.03 mmol) and **L**^{23} (20.0 mg, 0.03 mmol) in acetonitrile (2mL) were stirred at room temperature for 30 minutes. The resulting white solution was left one week undisturbed at room temperature. During this time the evaporation of the solvent induce the formation of white crystalline product of the title compound which was collected and dried under vacuum. Elemental analysis indicated the stoichiometric formula of [Eu(**L**^{23})$(NO_3)_3]\cdot H_2O$.

Yield	23 mg, 75%
$C_{39}H_{38}EuN_{15}O_{10}$	1028.78 g.mol^{-1}
Calc.[%]	C 45.53, H 3.72, N 20.42
Found [%]	C 45.18, H 2.75, N 19.82
ESI-MS (MeOH)	m/z = 780 [Eu(**L**^{23})$_2NO_3]^{2+}$, 949 [Eu(**L**^{23})$(NO_3)_2]^+$

[Yb($\mathbf{L}^{23}$)$(NO_3)_3$] (**26**)

Ytterbium(III) nitrate tetrahydrate (12.8 mg, 0.03 mmol) and $\mathbf{L}^{23}$ (20.0 mg, 0.03 mmol) in acetonitrile (2mL) were stirred at room temperature for 30 minutes. The resulting white solution was left one week undisturbed at room temperature. During this time the evaporation of the solvent induce the formation of white crystalline product of the title compound which was collected and dried under vacuum. Elemental analysis indicated the stoichiometric formula of [Yb($\mathbf{L}^{23}$)$(NO_3)_3$].

Yield	20 mg, 75%
$C_{39}H_{36}N_{15}O_{10}Yb$	1031.84 g.mol^{-1}
Calc.[%]	C 45.50, H 3.52, N 20.36
Found [%]	C 44.97, H 2.89, N 20.04
ESI-MS (MeOH)	m/z = 970 [Yb($\mathbf{L}^{23}$)$(NO_3)_2$]$^+$

6.4 DFT calculation

Density functional theory (DFT) calculations were carried out to optimize the structure of uranyl complexes in solvent, as well as to compare the stability of their isomeric complexes. Geometry optimization and Gibbs energy calculations were performed in solvent at the B3LYP level using CPCM [178] with UAHF radii [179] on the program package Gaussian 03[180]. Small core effective core potentials (ECPs) were used on U, O, C, and N atoms with the corresponding basis sets [181]. For hydrogen we used the 5s functions contracted to 3s [182].

6.5 Liquid –liquid extraction

The liquid–liquid extraction experiments were performed at 23 ± 1 °C in microcentrifuge tubes (2 ml) with a phase ratio $V_{(org)}$:$V_{(aq)}$ of 1:1 (0.5 ml each). The aqueous phase contained $Eu(NO_3)_3$ or $UO_2(NO_3)_2$ (1 x 10^{-4} M), sodium nitrate (5 x 10^{-3} M) as

supporting anion and the zwitterionic buffer systems, MES/$NaNO_3$ (pH 5.4), HEPES/HNO_3 (pH 5.2), or HEPES/NaOH (pH 7.2); As a precaution, the pH of the aqueous phase was monitored before and after each experiment with the aid of an InLab423 pH electrode. The organic phase contained a known concentration of ligand in chloroform (1 x 10^{-2} M). All experiments involved the mechanical shaking of the two-phase system for 60 min (T = 23 ± 1 °C) by which time equilibrium was reached (as established by preliminary experiments). At the end of this time, the phases were separated, centrifuged and the determination of the Eu(III) ions concentration in both phases was carried out radiometrically by γ-radiation of ^{152}Eu with NaI(Tl)-scintillation counter (Cobra II/Canberra-Packard) while that of U(VI) ions in aqueous phase was measured using an ICP-MS (ELAN 9000/Perkin Elmer) spectrometer.

6.6 X-ray single crystal analyses

The X-ray analyses were carried out at the Technical University of Dresden. X-ray diffraction data for **2-5** and **16** was collected on a Bruker-Nonius Kappa CCD with ω and φ scans at 198 K (**2**, **3**), 150 K (**4**, **5**) and 293 K (**16**). Data collections were undertaken with COLLECT [183], cell refinement with Dirax/lsq [184], and data reduction with EvalCCD [185]. Data for structures of $\mathbf{L^1}$, $\mathbf{L^4}$, $\mathbf{L^5}$, **1**, **6-13**, **15**, **17** and **18** were collected in the temperature range 150-203 K with a Bruker AXS Kappa APEX II CCD diffractometer with Oxford Cryosystems coldhead attached. Data integration and reduction were undertaken with SAINT and APEX2 [186, 187] Each structure was solved by direct methods using SHELXS-97 [188]. The diffractometers employed graphite-monochromated Mo-Kα radiation generated from a sealed tube (0.71073 Å). Multi-scan empirical absorption corrections were applied to all data sets using the program SADABS [189]. All structures were refined and extended with SHELXL-97 [190] In general, ordered non-hydrogen atoms with occupancies greater than 0.5 were refined anisotropically. Partial occupancy carbon, nitrogen and oxygen atoms were refined isotropically. Carbon-bound hydrogen atoms were included in idealised positions and refined using a riding model. Oxygen and nitrogenbound hydrogen atoms that were structurally evident in the difference Fouriermap were included and refined with bond

length and angle restraints. The structures were visualized carefully and analyzed using the program DIAMOND version 3.1 [191]. To evaluate the quality of structure model gives the R-value, which indicate the agreement of observed (F_o) and calculated (F_c) F-values. $R1$ is defined by:

$$R1 = \frac{\sum || F_o | - | F_c ||}{\sum | F_o |}$$

The weighted R-factor w$R2$ base on F^2

$$wR2 = \sqrt{\frac{\sum w(F_o^2 - F_c^2)^2}{\sum w(F_o^2)^2}}$$

where the w-value is coming from

$w = 1/[\ \sigma^2(F_o^2) + (aP)^2 + bP]$ with

$P = [(2\ F_c^2 + \max\ (F_o^2,0)]/3$

Another important factor to evaluating the quality of crystal structure refinement is Goodness-of-fit (GooF):

$$GooF = S = \sqrt{\frac{\sum w(F_o^2 - F_c^2)^2}{n - p}}$$

where n is the number of reflections and p the total number of parameters refined. A right structure model normally requires the S value near to 1.

F_o: observed structure factor

F_c: calculated structure factor

σ: standard deviation

Crystal and structure refinement data for all structures are summarised in the crystallographic data section.

7 References

1 J.-M. Lehn, *Pure Appl. Chem.* **1978**, *50*, 871

2 J.-M. Lehn, *Angew. Chem. Int. Ed. Engl*. **1988**, 27, 89

3 J.-M. Lehn, *Pure Appl. Chem.* **1994**, 66, 1961

4 J.-M. Lehn, *Supramolecular chemistry–concepts and perspectives*, VCH, Weinheim, **1995**

5 J. W. Steed, J. L. Atwood, *Supramolecular chemistry*, Wiley, New York, **2000**

6 P. D. Beer, P. A. Gale, D. K. Smith, *Supramolecular chemistry*, Oxford University Press, Oxford, **1999**

7 K. Ariga, T. Kunitake, *Supramolecular chemistry*, *Fundamentals and applications*, Springer, Berlin, Heidelberg, New York, **2006**

8 L. F. Lindoy, I. M. Atkinson, *Self-assembly in Supramolecular Chemistry*, RSC, Cambridge, UK, **2000**

9 F. Vögtle, *Supramolekulare Chemie*, Teubner, Stuttgart, **1992**

10 G. M. Whitesides, J. P. Mathias, C. T. Seto, *Science*, **1991**, 254, 1312

11 A. Klug, *Angew. Chem. Int. Ed. Engl*. **1983**, 22, 565

12 T. Urich, C. M. Gomes, A. Kletzin, C. Frazao, *Science*, **2006**, 311, 996

13 B. J. Holliday, C. A. Mirkin, *Angew. Chem. Int. Ed*. **2001**, 40, 2022

14 L. J. Prins, D. N. Reinhoudt, P. Timmerman, *Angew. Chem. Int. Ed*. **2001**, 40, 2382

15 A. N. Khlobystov, A. J. Blake, N. R. Champness, D. A. Lemenovskii, A. G. Majouga, N. V. Zyk, M. Schröder, *Coord. Chem. Rev*. **2001**, 222, 155

16 S. Leininger, B. Olenyuk, P. J. Stang, *Chem. Rev*. **2000**, 100, 853

17 C. J. Jones, *Chem. Soc. Rev*. **1998**, 27, 289

18 G. R. Desiraju, *Angew. Chem. Int. Ed.* **1995**, 34, 2311

19 B. Moulton, M. J. Zaworotko, *Chem. Rev.* **2001**, 101, 1629

20 J. Aizenberg, D. A. Muller, J. L. Grazul, D. R. Hamann, *Science*, **2003**, 299, 1205

21 A. J. Blake, N. R. Champness, P. Hubberstey, W. S. Li, M. A. Withersby, M. Schroder, *Coord. Chem. Rev.* **1999**, 183, 117

22 D. Whang, S. Jin, Y. Wu, C. M. Lieber, *Nano Lett.*, **2003**, 3, 1255

23 J. C. Love, L. A. Estroff, J. K. Kriebel, R. G. Nuzzo, G. M. Whitesides, *Chem. Rev.* **2005**, 105, 1103

24 C. D. Bain, E. B. Troughton, Y. T. Tao, J. Evall, G. M. Whitesides, R. G. Nuzzo, *J. Am. Chem. Soc.* **1989**, 111, 321

25 D. Witt, R. Klajn, P. Barski, B. A. Grzybowski, *Curr. Org. Chem.* **2004**, 8, 1763

26 J. D. Hartgerink, E. Beniash, S. I. Stupp, *Science*, **2001**, 294, 1684

27 J. D. Hartgerink, E. Beniash, S. I. Stupp, *Proc. Natl. Acad. Sci. USA*, **2002**, 99, 5133

28 C. A. Mirkin, R. L. Letsinger, R. C. Mucic, J. J. Storhoff, *Nature*, **1996**, 382, 607

29 M. Li, H. Schnablegger, S. Mann, *Nature*, **1999**, 402, 393

30 S. J. Park, A. A. Lazarides, C. A. Mirkin, R. L. Letsinger, *Angew. Chem. Int. Ed.*, **2001**, 40, 2909

31 A. M. Kalsin, M. Fialkowski, M. Paszewski, S. K. Smoukov, K. J. M. Bishop, B. A. Grzybowski, *Science*, **2006**, 312, 420

32 S. S. Fan, M. G. Chapline, N. R. Franklin, T. W. Tombler, A. M. Cassell, H. J. Dai, *Science*, **1999**, 283, 512

33 M. Yan, H. T. Zhang, E. J. Widjaja, R. P. H. Chang, *J. Appl. Phys.*, **2003**, 94, 5240

34 B. A. Grzybowski, M. Radkowski, C. J. Campbell, J. N. Lee, G. M. Whitesides, *Appl. Phys. Lett.*, **2004**, 84, 1798

35 C. J. Campbell, B. A. Grzybowski, *Philos. Trans. R. Soc. Lond. Ser. A*, **2004**, 362, 1069

36 M. Fialkowski, A. Bitner, B. A. Grzybowski, *Nat. Mater.* **2005**, **4**, 93

37 Z. D. Cheng, W. B. Russell, P. M. Chaikin, *Nature*, **1999**, 401, 893

38 A. D. Dinsmore, M. F. Hsu, M. G. Nikolaides, M. Marquez, A. R. Bausch, D. A. Weitz, *Science*, **2002**, 298, 1006

39 T. D. Clark, J. Tien, D. C. Duffy, K. E. Paul, G. M. Whitesides, *J. Am. Chem. Soc.* **2001**, 123, 7677

40 T. D. Clark, R. Ferrigno, J. Tien, K. E. Paul, G. M. Whitesides, *J. Am. Chem. Soc.* **2002**, 124, 5419

41 D. H. Gracias, J. Tien, T. L. Breen, C. Hsu, G. M. Whitesides, *Science*, **2000**, 289, 1170

42 M. Boncheva, S. A. Andreev, L. Mahadevan, A. Winkleman, D. R. Reichman, M. G. Prentiss, S. Whitesides, G. M. Whitesides, *Proc. Natl. Acad. Sci. USA*, **2005**, 102, 3924

43 B. A. Grzybowski, A. Winkleman, J. A. Wiles, Y. Brumer, G. M. Whitesides, *Nat. Mater.* **2003**, 2, 241

44 A. Winkleman, B. D. Gates, L. S. McCarty, G. M. Whitesides, *Adv. Mater.*, **2005**, 17, 1507

45 H. J. J. Yeh, J. S. Smith, *IEEE Phot. Tech. Lett.*, **1994**, 6, 706

46 Alien Technology website: http://www.alientechnology.com/products/fsa/.

47 M. J. Heller, J. M. Cable, S. C. Esener, Methods for electronic assembly and fabrication of devices, *U.S. Patent* 6 652 808, **2003**

48 IBM Website: http://www-03.ibm.com/press/us/en/pressrelease/21473.wss.

49 D. G. Grier, *Nature*, **2003**, 424, 810

50 K. E. Strecker, G. B. Partridge, A. G. Truscott, R. G. Hulet, *Nature*, **2002**, 417, 150

51 Y. Robin, K. M. Fromm, *Coord. Chem. Rev*. **2006**, 250, 2127

52 S. R. Batten, R. Robson, *Angew. Chem.* **1998**, 110, 1558

53 C. Janiak, *Dalton Trans.* **2003**, 2781

54 H. Schiff, *Ann. Chem. (Paris)*, **1864**, 131, 118

55 C. D. Meyer, C. S. Joiner, J. F. Stoddart, *Chem. Soc. Rev.* **2007**, *36*, 1705

56 N. Sari, S. Arslan, E. Logoglu, I. Sakiyan, *G. U. J. Sci.*, **2003**, 283

57 S. V. More, D, V. Dongerkhadekar, R. N. Chavan, W. N. Jadhav, S. R. Bhusare, R. P. Pawar, *J. Indian Chem. So*c., **2002**, 79, 768

58 S. K. Sridhar, M. Saravanan, A. Ramesh, *Eur. J. Med. Chem.*, **2001**, 36, 615

59 S. P. Rajendran, R. Karvembu, *Indian J. Chem., Sect. B*, **2002**, 41B, 222

60 U. Calis, M. Yarim, M. Koksal, M. Ozalp, *Arzneimittel-Forschung*, **2002**, 52, 778

61 M. Nagatsuka, H. Ishida, S. Tanaka, Jpn. Kokai Tokkyo Koho JP **2002**, 128, 610, Appl. 316,079/2000

62 A. S. Kabeer, M. A. Baseer, N. A. Mote, Source *Asian J. Chem.*, **2001**, 13, 496

63 S. K. Sridhar, S. N. Pandeya, J. P. Stables, A. Ramesh, *Eur., J. Pharm. Sci.* **2002**, 16, 129

64 S. K. Sridhar, S. N. Pandeya and E. De Clercq, *Bollettino chimico farmaceutico*, **2001**, 140, 302

65 S. K. Sridhar and A. Ramesh, *Indian Drugs,* **2001**, 38, 174

66 S. B Desai, P. B. Desai, K. R Desai, *Heterocycl. Commun.,* **2001**, 7, 83

67 T. H. Tarafder, A. Kasbollah, N. Saravanan, K. A. Crouse, A. M. Ali, K. Tin Oo, *J Biochem Mol Biol Biophys.,* **2002**, 6, 85

68 Z. N. Chohan, S. Kausar, *Chem Pharm Bull* (Japan), **1993**, 41, 951

69 W. Zishan, L. Zhiping, Y. Zhenhuan, *Trans Met Chem*, **1993**, 18, 291

70 M. Nishio, *Weak Hydrogen Bonds*, in (*Encyclopedia of Supramolecular Chemistry,* J.L. Atwood, J.W. Steed (Eds.), Marcel Dekker, New York), **2004**, 1576

71 T. Steiner, *Angew. Chem.* **2002**, 114, 50

72 C. Janiak, *Dalton Trans.* **2000**, 3885

73 B. Antonioli, *Molekulare Architekturen auf Basis von Oligofunktionellen Pyridinliganden*, Doctoral thesis, TU Dresden, **2006**

74 M. A. M. Abu-Youssef, V. Langer, L. Ohrström, *Dalton Trans.* **2006**, 2542

75 N. C. Kasuga, A. Sugie, K. Nomiya, *Dalton Trans.* **2004**, 3732

76 P. Lin, R.A. Henderson, R.W. Harrington, W. Clegg, C.-D. Wu, X.-T. Wu, *Inorg. Chem.* **2004**, 43, 181

77 S. Yamanda, T. Ishida, T. Nogami, *Dalton Trans.* **2004**, 898

78 Huang-Chun Wu, P. Thanasekaran, Chi-Hwe Tsai, Jing-Yun Wu, Sheng-Ming Huang, Yuh-Sheng Wen, Kuang-Lieh Lu, *Inorg. Chem.* **2006**, 45, 295.

79 A. Tesouro Vallina, H. Stoeckli-Evans, *Acta Cryst.* **2001**, E57, m59

80 H. Cheng, D. Chun-Ying, F. Chen-Jie, M. Qing-Jin, *J. Chem. Soc. Dalton Trans.* **2000**, 2419

81 A. V. Zelewsky, *Stereochemistry of Coordination Compounds*, Wiley, Chichester, **1996**

82 R. S.Cahn, C. Ingold, V. Prelog, *Angew. Chem., Int. Ed. Engl.* **1966**, *5*, 385.

83 M. J. Hannon, L. J. Childs, *Supramol. Chem.* **2004**, *16*, 7

84 M. J. Hannon, C. L. Painting, A. Jackson, J. Hamblin, W. Errington, *Chem. Commun.* **1997**, 1807

85 J. Keegan, P. E. Kruger, M. Nieuwenhuyzen, N. Martin, *Cryst. Growth Des*. **2002**, 2, 329

86 M. J. Hannon, C. L. Painting, N. W. Alcock, *Chem. Commun.* **1999**, 2023

87 M. J. Hannon, S. Bunce, A. J. Clarke, N. W. Alcock, *Angew. Chem. Int. Ed.* **1999**, 38, 1277

88 R. Ziessel, A. Harriman, J. Suffert, M.-T. Youinou, A. De Cian, J. Fischer, *Angew. Chem., Int. Ed. Engl.* **1997**, 36, 2509

89 R. Stiller, J.-M. Lehn, *Eur. J. Inorg. Chem.* **1998**, 977

90 G. I. Pascu, A. C. G. Hotze, C. Sanchez-Cano, B. M. Kariuki, M. J. Hannon, *Angew. Chem. Int. Ed.* **2007**, 46, 4374

91 Y. Parajo, J. Malina, I. Meistermann, G. J. Clarkson, M. Pascu, A. Rodger, M. J. Hannon, P. Lincoln, *Dalton Trans.* **2009**, 4868

92 M. J. Hannon, V. Moreno, M. J. Prieto, E. Moldrheim, E. Sletten, I. Meistermann, C. J. Isaac, K. J. Sanders, A. Rodger, *Angew. Chem., Int. Ed.* **2001**, 40, 880

93 M. J. Hannon, I. Meistermann, C. J. Isaac, C. Blomme, J. R. Aldrich-Wright, A. Rodger, *Chem. Commun.* **2001**, 1078

94 I. Meistermann, V. Moreno, M. J. Prieto, E. Moldrheim, E. Sletten, S. Khalid, P. M. Rodger, J. C. Peberdy, C. J. Isaac, A. Rodger, M. J. Hannon, *Proc. Natl. Acad. Sci. USA*, **2002**, 99, 5069

95 E. Molderheim, M. J. Hannon, I. Meistermann, A. Rodger, E. Sletten, *J. Biol. Inorg. Chem*. **2002**, 7, 770

96 M. J. Hannon, A. Rodger, *Pharmaceutical Visions*, **2002**, Autumn Issue, 14

97 A. C. G. Hotze, N. J. Hodges, R. E. Hayden, C. Sanchez-Cano, C. Paines, N. Male, M. K. Tse, C. M. Bunce, J. K. Chipman, M. J. Hannon, *Chem. Biol.* **2008**, 15, 1258

98 For examples of solid-state helical coordination polymers see F. Tuna, J. Hamblin, G. Clarkson, W. Errington, N. W. Alcock, M. J. Hannon, *Chem. Eur. J.* **2002**, 8, 4957 and references therein.

99 F. Tuna, J. Hamblin, A. Jackson, G. Clarkson, N. W. Alcock, M. J. Hannon, *Dalton Trans.* **2003**, 2141

100 L. J. Childs, N. W. Alcock, M. J. Hannon, *Angew. Chem., Int. Ed. Engl.* **2001**, 40, 1079

101 L. J. Childs, N. W. Alcock, M. J. Hannon, *Angew. Chem., Int. Ed. Engl.* **2002**, 41, 4244

102 J. Hamblin, F. Tuna, S. Bunce, L. J. Childs, A. Jackson, W. Errington, N. W. Alcock, H. Nierengarten, A. Van Dorsselaer, E. Leize-Wagner, M. J. Hannon, *Chem. Eur. J.* **2007**, 13, 9286

103 A. Tesouro Vallina, H. Stoeckli-Evans, *Chimia*, **1999**, 53, 342

104 L. B. Or, E. J. Parsons, W. T. Perrington, *Acta Cryst.* **1992**, C48, 2042

105 M. G. B. Drew, V. Felix, V. McKee, G. Morgan, J. Nelson, *Supramol. Chem.* **1995**, 5, 281

106 N. Yoshida, K. Ichikawa, *Chem. Commun.* **1997**, 1091

107 N. Yoshida, K. Ichikawa, M. Shiro, *J. Chem. Soc. Perkin Trans. 2*, **2000**, 17

108 R. Ahuja, A. G. Samuelson, *Cryst. Eng. Comm*, **2003**, 5, 395.

109 A. F. Williams, *pure appl. Chem*. **1996**, 68, 1285

110 A. Rodger, B. *Norden, Circular Dichroism and Linear Dichroism*, Oxford University Press, Oxford, **1997**

111 I. Castro-Rodriguez, K. Olsen, P. Gantzel, K. Meyer, *J. Am. Chem. Soc.* **2003**, 125, 4565

112 T. W. Hayton, J. M. Boncella, B. L. Scott, E. R. Batista, P. J. Hay, *J. Am. Chem. Soc.* **2006**, 128, 10549

113 V. Rericha, M. Kulich, R. Rericha, D. L. Shore, D. P. Sandler, *Environ. Health Persp.* **2006**, 114, 818

114 J. Bruno, R. C. Ewing, *Elements*, **2006**, 2, 343

115 S. Shinkai, H. Koreishi, K. Ueda, T. Arimura, O. Manabe, *J. Am. Chem. Soc.* **1987**, 109, 6371

116 P. D. Beer, G. D. Brindley, O. D. Fox, A. Grieve, M. I. Ogden, F. Szemes, M. G. B. Drew, *J. Chem. Soc. Dalton Trans.* **2002**, 3101

117 A. E. V. Gorden, J. D. Xu, K. N. Raymond, P. Durbin, *Chem. Rev.* **2003**, 103, 4207

118 J. D. Xu, K. N Raymond, *Inorg. Chem.* **1999**, 38, 308

119 M. Sawicki, J. M. Siaugue, C. Jacopin, C. Moulin, T. Bailly, R. Burgada, S. Meunier, P. Baret, J. L. Pierre, F. Taran, *Chem. Eur. J.* **2005**, 11, 3689

120 M. Ephritikhine, *Dalton Trans.* **2006**, 2501

121 K. L. Nash, *Solv. Extract. Ion Exch.* **1993**, 11, 729

122 N. N. Greenwood, A. Earnshaw, *Chemistry of the Elements*, Pergamon Press, Exeter **1984**, 1477–1479

123 M. P. Wilkerson, C. J. Burns, H. J. Dewey, J. M. Martin, D. E. Morris, R. T. Paine, B. L. Scott, *Inorg. Chem.* **2000**, 39, 5277

124 P. D. E. Wilson, *Nuclear Fuel Cycle: From Ore to Waste*; Oxford Science Publications: Oxford, **1996**

125 P. G. Eller, R. A. Penneman, *Inorg. Chem.* **1976**, 15, 2439

126 P. Thuery, N. Keller, M. Lance, J. D. Vigner, M. Nierlich, *New J. Chem.* **1995**, 19, 619

127 C. Drouza, V.Gramlich, M. P. Sigalas, L. Pashalidis, A. D. Keramidas, *Inorg. Chem.* **2004**, 43, 8336

128 B. Saha, K. A. Venkatesan, R. Natarajan, M. P. Antony, P. R. V. Rao, *Radiochim. Acta* **2002**, 90, 455

129 S. K. Sahu, V. Chakravortty, *J. Radioanal. Nucl. Chem.* **1998**, 227, 163

130 J. L. Sessler, P. J. Melfi, G. D. Pantos, *Coord. Chem. Rev.* **2006**, 250, 816

131 M. S. Bharara, K.Strawbridge, J. Z. Vilsek, T. H. Bray, A. E. V. Gorden, *Inorg. Chem.* **2007**, 46, 8309

132 M. Nierlich, J. M. Sabattie, N. Keller, M. Lance, J. D. Vigner, *Acta Crystallogr., Sect. C: Cryst. Struct. Commun.* **1994**, 50, 52

133 E. M. Holt, N. W. Alcock, R. R. Hendrixson, G. D. Malpass, R. G. Ghirardelli, R. A. Palmer, *Acta Crystallogr. Sect. B: Struct. Sci.* **1981**, 37, 1080

134 L. Salmon, P. Thuery, Z. Asfari, M. Ephritikhine, *Dalton Trans.* **2006**, 3006

135 B. Boulet, C.Bouvier-Capely, C.Cossonnet, G. Cote, *Solv. Extract. Ion Exc.* **2006**, 24, 319

136 P. Pfeiffer, T. Hesse, H. Pfitzner, W. Scholl, H. Thielert, *J. Prakt. Chem.* **1937**, 149, 217

137 G. Bandoli, D. A. Clemente, U. Croatto, M. Vidali, P. A. Vigato, *J. Chem. Soc. Dalton Trans.* **1973**, 2331

138 K. Takao, Y. Ikeda, *Inorg. Chem.* **2007**, 46, 1550

139 M. S. Bharara, S. A. Tonks, A. E. V. Gorden, *Chem. Commun.* **2007**, 4006

140 M. S. Bharara, K. Heflin, S. Tonks, K. L. Strawbridge, A. E. V. Gorden, *Dalton Trans.* **2008**, 2966

141 D. J. Evans, P. C. Junk, M. K. Smith, *Polyhedron* **2002**, *21*, 2421

142 U. Casellato, S. Tamburini, P. Tomasin, P. A. Vigato, *Inorg. Chim. Acta*, **2002**, 341 118

143 L. Salmon, P. Thuèry, M. Ephritikhine, *Polyhedron*, **2003**, 22, 2683

144 A. W. Maverick, R. K. Laxman, M. A. Hawkins, D. P. Martone, F. R. Fronczek, *Dalton Trans.* **2005**, 200

145 N. Yoshida, H. Oshio, T. Ito, *J. Chem. Soc. Perkin Trans. 2*, **1999**, 975

146 P. E. Kruger, N. Martin, M. Nieuwenhuyzen, *J. Chem. Soc. Dalton Trans.* **2001**, 1966

147 H. H. Freedman, *J. Am. Chem. Soc.* **1961**, 83, 2900

148 A. A. A. Abu-Hussen, *J. Coord. Chem.* **2006**, 59, 157

149 T. S. Franczyk, K. R. Czerwinski, K. N. Raymond, *J. Am. Chem. Soc.* **1992**, 114, 8138

150 K. Nakamoto, *Infrared and Raman Spectra of Inorganic and coordination compounds; Part A: Theory and Applications in Inorganic Chemistry*. John Wiley & Sons New York, 5th edition **1997**

151 P. V. Rao, C. P. Rao, A. Sreedhara, E. K. Wegelius, K. Rissanen, E. Kolehmainen, *J. Chem. Soc. Dalton Trans.* **2000**, 1213

152 P. A. Giesting, P. C. Burns, *Crystallogr. Rev.* **2006**, 12, 205

153 G. Bandoli, D. A. Clemente, U. Croatto, M. Vidali, P. A. Vigato, *J. Chem. Soc. Chem. Commun.* **1971**, 1330

154 M. T. Weller, M. E. Light, T. Gelbrich, *Acta Crystallogr. Sect. B: Struct. Sci.* **2000**, 56, 577

155 Y. A. Zolotov, *Macrocyclic Compounds in Analytical Chemistry*, John Wiley and Sons, Inc. 1997

156 P. Mühl, K. Gloe, *Chem. Techn*. **1989**, 41, 457

157 J. Rydberg, M. Cox, C. Musikas, G. R. Choppin, *Principles and Practices of Solvent Extraction*, Marcel Dekker, New York, **2004**

158 H. F. Frensdorff, *J. Am. Chem. Soc*. **1971**, 13, 600

159 K. Gloe, P. Mühl, J. Beger, *Z. Chem.* **1988**, 28, 1

160 Y. Takeda, in *Host-Guest Complex Chemistry III*, F. Vögtle, E. Weber (Eds.), Springer, Berlin, **1984**, 121, 1

161 H. Tsukube, H. Furuta, A. Odani, Y. Takeda, Y. Kudo, Y. Inoue, Y. Lin, H. Sakamoto, K. Kumura, in *Comprehensive Supramolecular Chemistry,* Elsevier, Oxford, **1996**, 8, 461

162 K. Gloe, P. Mühl, J. Beger, E. Uhlemann, L. Beyer, *Flüssig-Flüssig-Extraktion von Metallionen mit Coronanden und Podanden – Möglichkeiten und Grenzen*, Wissenschaftliche Berichte, ZFW Dresden **1990**, 43, 83-103

163 M. Petrich, L. Beyer, K. Gloe, P. Mühl, *Anal. Chim. Acta* **1990**, 228, 229

164 G. R. Choppin, in *Principles and Practices of Solvent Extraction*, J. Rydberg, C. Musikas, G. R. Choppin (Eds.), Marcel Dekker, New York, **2004**, 81-107

165 J. Rydberg, G. R. Ghopping, C. Musikas, T. Sekine, in *Principles and Practices of Solvent Extraction*, J. Rydberg, C. Musikas, G. R. Choppin (Eds.), Marcel Dekker, New York, **2004**, 109-201

166 S. Liu, L. Gelmini, S. J. Rettig, R. C. Thompson, C. Orvig, *J. Am. Chem. Soc.* **1992**, 114, 6081

167 L. R. Morss, R. D. Rogers, *Inorg. Chim. Acta*, 255, **1997**, 193

168 R.Wietzke, M. Mazzanti, J-M. Latour, J. Pécaut, *J. Chem. Soc., Dalton Trans.***, 1998**, 4087

169 R.Wietzke, M. Mazzanti, J-M. Latour, J. Pécaut, P-Y. Cordier, C. Madic, *Inorg. Chem.*, **1998**, 37, 6690

170 R. Mirvaliev, M. Watanabe, T. Matsumura, S. Tachimori, K. Takeshita, *J. Nucl. Sci. Technol.*, **2004**, 41, 1122

171 L. Natrajan, J. Pécaut, M. Mazzanti, C. LeBrun*, Inorg. Chem.* **2005**, 44, 4756

172 T. Yamada, S. Shinoda, H. Sugimoto, J. Uenishi, H. Tsukube, *Inorg. Chem.* **2003**, 42, 7932

173 K. Ishimori, M. Watanabe, T. Kimura, T. Yaita, T. Yamada, Y. Kataoka, S. Shinoda, H. Tsukube, *Chemistry Letters*, **2005**, 34,1112

174 A. A. Naiini, W. M. P. B. Menge, J. G. Verkade, *Inorg. Chem.* **1991**, 30, 5009

175 H. B. Tanh Jeazet, Ke. Gloe, T. Doert, O. N. Kataeva, A. Jäger, G. Geipel, G. Bernhard, B. Büchner, Ka. Gloe, *Chem. Commun.* **2010**, 46, 2373

176 G. Geipel , M. Acker , D. Vulpius , G. Bernhard , H. Nitsche , T. Fanghänel , *Spectrochim. Part A* **2004**, *60/1-2*, 417

177 P. de Hoog, P. Gamez, W. L. Driessen, J Reedijk, *Tetrahedron Lett*. **2002**, 43, 6783

178 V. Barone, M. Cossi, *J. Phys. Chem. A*, **1998**, 102, 1995

179 A. Bondi, *J. Phys. Chem.* **1964**, 68, 441

180 M. J. Frisch, G. W. Trucks, H. B. Schlegel, G. E. Scuseria, M. A. Robb, J. R. Cheeseman, J. A. Montgomery, T. Vreven, K. N. Kudin, J. C. Burant, J. M. Millam, S. S. Iyengar, J. Tomasi, V. Barone, B. Mennucci, M. Cossi, G. Scalmani, N. Rega, G. A. Petersson, H. Nakatsuji, M. Hada, M. Ehara, K. Toyota, R.Fukuda, J. Hasegawa, M. Ishida, T. Nakajima, Y. Honda, O. Kitao, H. Nakai, M. Klene, X. Li, J. E. Knox, H. P. Hratchian, J. B. Cross, V. Bakken, C. Adamo, J. Jaramillo, R. Gomperts, R. E. Stratmann, O. Yazyev, A. J. Austin, R. Cammi, C. Pomelli, J. W. Ochterski, P. Y. Ayala, K. Morokuma, G. A. Voth, P. Salvador, J. J. Dannenberg, V. G. Zakrzewski, S. Dapprich, A. D. Daniels, M. C. Strain, O. Farkas, D. K. Malick, A. D. Rabuck, K. Raghavachari, J. B. Foresman, J. V. Ortiz, Q. Cui, A. G. Baboul, S. Clifford, J. Cioslowski, B. B. Stefanov, G. Liu, A. Liashenko, Piskorz, P. I. Komaromi, R. L. Martin, D. J. Fox, T. Keith, M. A. Al-Laham, C. Y. Peng, A. Nanayakkara, M. Challacombe, P. M. W. Gill, B. Johnson, W. Chen, M. W.

Wong, C. Gonzalez, J. A. Pople, *Gaussian 03*, Revision D.01; Gaussian, Inc.: Wallingford, CT **2004**

181 W. Küchle, M. Dolg, H. Stoll, H. Preuss, *J. Chem. Phys.* **1994**, 100, 7535

182 R. Krishnan, J. S. Binkley, R. Seeger, J. A. Pople, *J. Chem. Phys*. **1980**, 72, 650

183 Nonium BV, Delft, The Netherlands **1998**

184 A. J. M. Duisenberg, *J. Appl. Crystallogr.* **1992**, 25, 92

185 A. J. M. Duisenberg, L. M. J. Kroon-Batenburg, A. M. M. Schreurs, *J. Appl. Crystallogr.* **2003**, 36, 220

186 APEX2, Bruker-AXS, Karlsruhe, Germany **2008**

187 SAINT, Bruker-AXS, Karlsruhe, Germany **2008**

188 G. M. Sheldrick, *Acta Crystallogr. Sect. A* **1990**, 46, 467

189 G. M. Sheldrick, *SADABS: Empirical Absorption and Correction Software*, University of Göttingen, Germany, **1999–2003**

190 G. M. Sheldrick, *SHELXL-97: Programs for Crystal Structure Analysis*, University of Göttingen, Germany, **1997**

191 K. Brandenburg, H. Putz, *DIAMOND3.1*, Crystal Impact GbR, Bonn, Germany, **2008**

8 List of abbreviations

AFM	atomic force microscopy
ali	aliphatic
arom	aromatic
CD	circular dichroism spectroscopy
CIC	combustion ion chromatography
CPCM	conductor-like polarizable continuum model
DFT	density functional theory
DNA	deoxyribonucleic acid
DMF	dimethylformamide
DMSO	dimethylsulfoxide
DTA	differential thermal analysis
EA	elemental analysis
ECP	effective core potential
ESI-MS	electrospray- mass spectroscopy
F	figure of merite
HEPES	4-(2-hydroxyethyl)-1-piperazineethanesulfonic acid
ICD	induced circular dichroism
im	imine
ICP-MS	inductive coupled plasma mass spectroscopy
ICP-OES	inductive coupled plasma optical emission spectroscopy
IR	infra red spectroscopy
L	ligand
MES	2-(N-morpholino)ethanesulfonic acid
MLCT	metal to ligand charge transfert
NMR	nuclear magnetic resonance
RT	room temperature
TG	thermogravimetric analysis
TLC	thin layer chromatography
Tris	tris(hydroxymethyl)aminomethane
TRLFS	time resolved laser fluorescence spectroscopy
UV-vis	ultra violet-visible spectroscopy
Z	number of molecule per unit cell

9 Crystallographic data

Bis[4-(2-pyridylmethyleneimino)phenyl]methane (**L**^{1})

Molecular formula	C_{25} H_{20} N_4
Molar mass	376.45 g.mol^{-1}
Crystal system	Monoclinic
Space group	*C*2/c
Cell dimensions	*a* = 26.369(2) Å
	b = 4.687(1) Å
	c = 18.049(3) Å
	$\alpha = 90.00°$, $\beta = 122.22(2)°$, $\gamma = 90.00°$
Cell volume	1887.0(5) Å^3
Calc. density (ρ)	1.325 g cm^{-3}
Z	4
F(000)	792
Diffractometer	Kappa CCD
Crystal Size	0.25 x 0.09 x 0.05 mm
Crystal colour	light yellow
Crystal Habit	polyhedron
Temperature	160(2) K
λ(MoKα)	0.71073
Absorption coefficient (μ)	0.080 mm^{-1}
2θ-range	3.7-58.4°
Total data collected	67317
Unique data	2563 (R_{int} = 0.118)
Observed data (I >2σ(I))	1027
Data/ restraints/ parameters	2563/ 0/ 132
Goodness of fit	0.662
Final *R* indices [I>2σ(I)]	*R*1 = 0.038, w*R*2 = 0.066
R indices (all data)	*R*1 = 0.107, w*R*2 = 0.073
Residual electron density (max/min)	0.13 / −0.16 e$^-$ Å^{-3}

Bis[4-(2-pyridylmethyleneimino)phenyl]amine(**L**^{4})

Molecular formula	$C_{24}\ H_{19}\ N_5$
Molar mass	377.44 g.mol^{-1}
Crystal system	Monoclinic
Space group	*P*2(1)/c
Cell dimensions	*a* = 11.791(2) Å
	b = 15.617(3) Å
	c = 10.952(2) Å
	$\alpha = 90.00°,\ \beta = 101.03(3)°, \gamma = 90.00°$
Cell volume	1979.4(6) Å^3
Calc. density (ρ)	1.267 g cm^{-3}
Z	4
F(000)	792
Diffractometer	Kappa CCD
Crystal Size	0.18 x 0.18 x 0.05 mm
Crystal colour	yellow
Crystal Habit	polyhedron
Temperature	153(2) K
λ(MoKα)	0.71073
Absorption coefficient (μ)	0.078 mm^{-1}
2θ-range	6.22-50.8°
Total data collected	33338
Unique data	3649 (R_{int} = 0.151)
Observed data (I >2σ(I))	2070
Data/ restraints/ parameters	3649/ 0/ 262
Goodness of fit	1.42
Final *R* indices [I>2σ(I)]	*R*1 = 0.075, w*R*2 = 0.090
R indices (all data)	*R*1 = 0.149, w*R*2 = 0.101
Residual electron density (max/min)	0.186 / −0.225 e$^-$ Å^{-3}

Bis[4-(2-pyridylmethyleneimino)phenyl]-1,1-cyclohexane (**L**^{5})

Molecular formula	C_{30} H_{28} N_4
Molar mass	444.56 g.mol^{-1}
Crystal system	Triclinic
Space group	*P*-1
Cell dimensions	*a* = 8.3736(4) Å
	b = 10.8890(5)Å
	c = 14.2453(6) Å
	α = 109.97(2)°, β = 99.11(2)°, γ = 97.57(2)°
Cell volume	1180.93(9) Å^3
Calc. density (ρ)	1.250 g cm^{-3}
Z	2
F(000)	472
Diffractometer	Bruker APEX-II CCD
Crystal Size	0.28 x 0.20 x 0.09 mm
Crystal colour	pale yellow
Crystal Habit	polyhedron
Temperature	173(2) K
λ(MoKα)	0.71073
Absorption coefficient (μ)	0.075 mm^{-1}
2θ-range	4.06-56.24°
Total data collected	19556
Unique data	5591 (R_{int} = 0.036)
Observed data (I >2σ(I))	3860
Data/ restraints/ parameters	5591/ 0/ 308
Goodness of fit	1.308
Final *R* indices [I>2σ(I)]	*R*1 = 0.049, w*R*2 = 0.115
R indices (all data)	*R*1 = 0.078, w*R*2 = 0.127
Residual electron density (max/min)	0.331 / −0.215 e$^-$ Å^{-3}

Complex $\{[Ag(\mathbf{L}^1)](ClO_4)\cdot CH_3CN\}_n$ (**1**)

Molecular formula	$C_{27}H_{23}AgClN_5O_4$
Molar mass	624.82 g.mol^{-1}
Crystal system	Monoclinic
Space group	*P*21
Cell dimensions	a = 12.065(1) Å
	b = 7.984(1) Å
	c = 14.182(1) Å
	α = 90.00°, β = 103.96(1)°, γ = 90.00°
Cell volume	1325.9(1) Å^3
Calc. density (ρ)	1.565 g cm^{-3}
Z	2
F(000)	632
Diffractometer	Bruker APEX-II CCD
Crystal Size	0.50 x 0.08 x 0.04 mm
Crystal colour	yellow
Crystal Habit	needle
Temperature	200(2) K
λ(MoKα)	0.71073
Absorption coefficient (μ)	0.904 mm^{-1}
2θ-range	5.9-60.24°
Total data collected	12321
Unique data	6922 (R_{int} = 0.023)
Observed data (I >2σ(I))	6125
Data/ restraints/ parameters	6922/ 1/ 344
Goodness of fit	1.144
Final *R* indices [I>2σ(I)]	*R*1 = 0.036, w*R*2 = 0.086
R indices (all data)	*R*1 = 0.043, w*R*2 = 0.089
Residual electron density (max/min)	0.79 / −0.40 e$^-$ Å^{-3}

Complex $\{[Ag(\mathbf{L}^2)]ClO_4 \cdot CH_2Cl_2\}_n$ (**2**)

Molecular formula	$C_{25}H_{20}AgCl_3N_4O_5$
Molar mass	670.67 g.mol^{-1}
Crystal system	Orthorhombic
Space group	*Pbca*
Cell dimensions	a = 15.347(7) Å
	b = 14.820(5) Å
	c = 23.269(2) Å
	α = 90.00°, β = 90.00°, γ = 90.00°
Cell volume	5292(3) Å^3
Calc. density (ρ)	1.683 g cm^{-3}
Z	8
F(000)	2688
Diffractometer	Kappa CCD
Crystal Size	0.25 x 0.10 x 0.10 mm
Crystal colour	pale yellow
Crystal Habit	needle
Temperature	198(2) K
λ(MoKα)	0.71073
Absorption coefficient (μ)	1.109 mm^{-1}
2θ-range	6.24-50.80°
Total data collected	68399
Unique data	4858 (R_{int} = 0.061)
Observed data (I >2σ(I))	3544
Data/ restraints/ parameters	4858/ 4/ 344
Goodness of fit	1.071
Final R indices [I>2σ(I)]	$R1$ = 0.044, w$R2$ = 0.086
R indices (all data)	$R1$ = 0.073, w$R2$ = 0.098
Residual electron density (max/min)	0.61 / −0.71 e$^-$ Å^{-3}

Complex $[Ag_2(\mathbf{L}^2)_2](ClO_4)_2$ (**3**)

Molecular formula	$C_{48}H_{36}Ag_2Cl_2N_8O_{10}$
Molar mass	1171.49 g.mol^{-1}
Crystal system	Triclinic
Space group	*P*–1
Cell dimensions	*a* = 9.748(2) Å
	b = 10.58(1) Å
	c = 12.722(3) Å
	α = 85.28(1)°, β = 75.77(2)°, γ = 85.55(1)°
Cell volume	1266.0(4) Å^3
Calc. density (ρ)	1.537 g cm^{-3}
Z	1
F(000)	588
Diffractometer	Kappa CCD
Crystal Size	0.30 x 0.24 x 0.14 mm
Crystal colour	Yellow-green
Crystal Habit	needle
Temperature	198(2) K
λ(MoKα)	0.71073
Absorption coefficient (μ)	0.943 mm^{-1}
2θ-range	6.04-56.00°
Total data collected	48675
Unique data	6045 (R_{int} = 0.07)
Observed data (I >2σ(I))	4221
Data/ restraints/ parameters	6045/ 94/ 326
Goodness of fit	1.036
Final *R* indices [I>2σ(I)]	*R*1 = 0.058, w*R*2 = 0.138
R indices (all data)	*R*1 = 0.092, w*R*2 = 0.153
Residual electron density (max/min)	1.34 / −0.58 e$^-$ Å^{-3}

Complex $[Cu\mathbf{L}^{1}(SO_4)]_6 \cdot 24H_2O$ (**4**)

Molecular formula	$C_{150}H_{168}Cu_6N_{24}O_{48}S_6$
Molar mass	3648.68 g.mol^{-1}
Crystal system	Trigonal
Space group	*R*–3
Cell dimensions	*a* = 23.6595(2) Å
	b = 23.6595(2) Å
	c = 25.3773(4) Å
	$\alpha = 90.00°$, $\beta = 90.00°$, $\gamma = 120.00°$
Cell volume	12302.3(2) Å^3
Calc. density (ρ)	1.43 g cm^{-3}
Z	3
F(000)	5670
Diffractometer	Kappa CCD
Crystal Size	0.25 x 0.15 x 0.15 mm
Crystal colour	green
Crystal Habit	block
Temperature	150(2) K
λ(MoKα)	0.71073
Absorption coefficient (μ)	0.93 mm^{-1}
2θ-range	2.56-62.00°
Total data collected	71838
Unique data	8702 (R_{int} = 0.070)
Observed data (I >2σ(I))	4845
Data/ restraints/ parameters	8702/ 0/ 352
Goodness of fit	0.967
Final *R* indices [I>2σ(I)]	*R*1 = 0.050, w*R*2 = 0.138
R indices (all data)	*R*1 = 0.108, w*R*2 = 0.163
Residual electron density (max/min)	0.91 / –0.52 e$^-$ Å^{-3}

Complex $[Cu\mathbf{L}^2(SO_4)]_6 \cdot 24H_2O$ (**5**)

Molecular formula	$C_{144}H_{156}Cu_6N_{24}O_{54}S_6$
Molar mass	3660.53 g.mol^{-1}
Crystal system	Trigonal
Space group	*R*–3
Cell dimensions	*a* = 23.4688(3) Å
	b = 23.4688(3) Å
	c = 25.3619(5) Å
	$\alpha = 90.00°$, $\beta = 90.00°$, $\gamma = 120.00°$
Cell volume	12097.5(3) Å^3
Calc. density (ρ)	1.49 g cm^{-3}
Z	3
F(000)	5670
Diffractometer	Kappa CCD
Crystal Size	0.40 x 0.20 x 0.20 mm
Crystal colour	dark green
Crystal Habit	needle
Temperature	150(2) K
λ(MoKα)	0.71073
Absorption coefficient (μ)	0.95 mm^{-1}
2θ-range	3.48-63.10°
Total data collected	55153
Unique data	8975 (R_{int} = 0.052)
Observed data (I >2σ(I))	6296
Data/ restraints/ parameters	8975/ 0/ 355
Goodness of fit	1.080
Final *R* indices [I>2σ(I)]	*R*1 = 0.048, w*R*2 = 0.143
R indices (all data)	*R*1 = 0.073, w*R*2 = 0.153
Residual electron density (max/min)	0.89 / –0.55 e$^-$ Å^{-3}

Complex $[Cu\mathbf{L}^3(SO_4)]_6 \cdot 24H_2O$ (**6**)

Molecular formula	$C_{144}H_{156}Cu_6N_{24}O_{48}S_{12}$
Molar mass	3756.89 g.mol^{-1}
Crystal system	Trigonal
Space group	*R*–3
Cell dimensions	*a* = 23.7647(6) Å
	b = 23.7647(6) Å
	c = 25.3824(8) Å
	$\alpha = 90.00°$, $\beta = 90.00°$, $\gamma = 120.00°$
Cell volume	12414.5(6) Å^3
Calc. density (ρ)	1.51 g cm^{-3}
Z	3
F(000)	5814
Diffractometer	Bruker APEX-II CCD
Crystal Size	0.10 x 0.05 x 0.02 mm
Crystal colour	dark brown
Crystal Habit	needle
Temperature	173(2) K
λ(MoKα)	0.71073
Absorption coefficient (μ)	1.00 mm^{-1}
2θ-range	5.10-55.00°
Total data collected	45135
Unique data	6315 (R_{int} = 0.045)
Observed data (I >2σ(I))	4533
Data/ restraints/ parameters	6315/ 0/ 353
Goodness of fit	1.086
Final *R* indices [I>2σ(I)]	*R*1 = 0.054, w*R*2 = 0.138
R indices (all data)	*R*1 = 0.084, w*R*2 = 0.158
Residual electron density (max/min)	1.09 / –0.62 e$^-$ Å^{-3}

Complex $[Cu_6(\mathbf{L^2})_{3.6}(\mathbf{L^3})_{2.4}(SO_4)_6] \cdot 22.5H_2O$ (**7**)

Molecular formula	$C_{144}H_{132}Cu_6N_{24}O_{50.1}S_{8.4}$
Molar mass	3672.11 g.mol^{-1}
Crystal system	Trigonal
Space group	*R*–3
Cell dimensions	a = 23.3536(9) Å
	b = 23.3536(9) Å
	c = 25.5051(7) Å
	α = 90.00°, β = 90.00°, γ = 120.00°
Cell volume	12046.6(7) Å^3
Calc. density (ρ)	1.483 g cm^{-3}
Z	3
F(000)	5508
Diffractometer	Bruker APEX-II CCD
Crystal Size	0.19 x 0.06 x 0.02 mm
Crystal colour	rod
Crystal Habit	green brown
Temperature	173(2) K
λ(MoKα)	0.71073
Absorption coefficient (μ)	0.977 mm^{-1}
2θ-range	4.34-50.00°
Total data collected	23340
Unique data	4708 (R_{int} = 0.038)
Observed data (I >2σ(I))	3576
Data/ restraints/ parameters	4708/ 0/ 348
Goodness of fit	1.093
Final *R* indices [I>2σ(I)]	*R*1 = 0.051, w*R*2 = 0.130
R indices (all data)	*R*1 = 0.072, w*R*2 = 0.146
Residual electron density (max/min)	0.91 / –0.40 e$^-$ Å^{-3}

Complex $[Hg_2(\mathbf{L^2})_2(ClO_4)_3(H_2O)_2]ClO_4 \cdot CH_3CN$ (**8**)

Molecular formula	$C_{50}H_{43}Cl_4Hg_2N_9O_{20}$
Molar mass	1632.91 g.mol^{-1}
Crystal system	Monoclinic
Space group	$P2_1/c$
Cell dimensions	a = 15.647(1) Å
	b = 25.801(1) Å
	c = 14.115(1) Å
	α = 90.00°, β = 106.39(2)°, γ = 90.00°
Cell volume	5466.8(6) Å^3
Calc. density (ρ)	1.984 g cm^{-3}
Z	4
F(000)	3176
Diffractometer	Bruker APEX-II CCD
Crystal Size	0.30 x 0.21 x 0.03 mm
Crystal colour	yellowish-orange
Crystal Habit	platelet
Temperature	150(2) K
λ(MoKα)	0.71073
Absorption coefficient (μ)	5.893 mm^{-1}
2θ-range	2.72-53.60°
Total data collected	80874
Unique data	11612 (R_{int} = 0.121)
Observed data (I >2σ(I))	8026
Data/ restraints/ parameters	11612 / 0/ 758
Goodness of fit	0.971
Final R indices [I>2σ(I)]	$R1$ = 0.037, w$R2$ = 0.073
R indices (all data)	$R1$ = 0.063, w$R2$ = 0.076
Residual electron density (max/min)	1.42 / −2.35 e$^-$ Å^{-3}

Complex $[Mn_2(\mathbf{L}^1)_3](ClO_4)_4$ (**11**)

Molecular formula	$C_{75}H_{60}Cl_4Mn_2N_{12}O_{16}$
Molar mass	1637.03 g.mol^{-1}
Crystal system	Monoclinic
Space group	*C*2/c
Cell dimensions	*a* = 26.2845(13) Å
	b = 10.1267(7) Å
	c = 26.9289(13) Å
	$\alpha = 90.00°$, $\beta = 92.688(4)°$, $\gamma = 90.00°$
Cell volume	7159.9(7) Å^3
Calc. density (ρ)	1.519 g cm^{-3}
Z	4
F(000)	3360
Diffractometer	Bruker APEX-II CCD
Crystal Size	0.48 x 0.26 x 0.14 mm
Crystal colour	orange
Crystal Habit	block
Temperature	170(2) K
λ(MoKα)	0.71073
Absorption coefficient (μ)	0.581 mm^{-1}
2θ-range	3.02-53.52°
Total data collected	26609
Unique data	7572 (R_{int} = 0.101)
Observed data (I >2σ(I))	3264
Data/ restraints/ parameters	7572 / 0/ 492
Goodness of fit	0.875
Final *R* indices [I>2σ(I)]	*R*1 = 0.050, w*R*2 = 0.089
R indices (all data)	*R*1 = 0.118, w*R*2 = 0.096
Residual electron density (max/min)	0.58 / −0.54 e$^-$ Å^{-3}

Complex $[Ni_2(\mathbf{L^2})_3](NO_3)_4 \cdot 2.5H_2O$ (**12**)

Molecular formula	$C_{72}H_{59}N_{16}Ni_2O_{17.5}$
Molar mass	1545.72 g.mol^{-1}
Crystal system	Monoclinic
Space group	$P2_1/c$
Cell dimensions	a = 19.791(3) Å
	b = 17.748(2) Å
	c = 20.561(3) Å
	α = 90.00°, β = 108.280(10)°, γ = 90.00°
Cell volume	6857.4(16) Å^3
Calc. density (ρ)	1.489 g cm^{-3}
Z	8
F(000)	3168
Diffractometer	Bruker APEX-II CCD
Crystal Size	0.36 x 0.30 x 0.12 mm
Crystal colour	Orange-red
Crystal Habit	needle
Temperature	173(2) K
λ(MoKα)	0.71073
Absorption coefficient (μ)	0.634 mm^{-1}
2θ-range	3.1-49.34°
Total data collected	11557
Unique data	11557 (R_{int} = 0.130)
Observed data (I >2σ(I))	3062
Data/ restraints/ parameters	11557/ 6/ 941
Goodness of fit	0.560
Final R indices [I>2σ(I)]	$R1$ = 0.049, w$R2$ = 0.081
R indices (all data)	$R1$ = 0.167, w$R2$ = 0.096
Residual electron density (max/min)	0.63 / −0.55 e$^-$ Å^{-3}

Complex $[Ni_2(\mathbf{L^5})_3](PF_6)_4 \cdot 0.9H_2O$ (**13**)

Molecular formula	$C_{90}H_{85.8}F_{24}N_{12}Ni_2O_{0.9}P_4$
Molar mass	2047.17 g.mol^{-1}
Crystal system	Monoclinic
Space group	$P2_1/c$
Cell dimensions	a = 16.9404(12) Å
	b = 22.2935(12) Å
	c = 25.5257(19) Å
	α = 90.00°, β = 105.902(2)°, γ = 90.00°
Cell volume	9271.1(11) Å^3
Calc. density (ρ)	1.466 g cm^{-3}
Z	4
F(000)	4188
Diffractometer	Bruker APEX-II CCD
Crystal Size	0.18 x 0.06 x 0.04 mm
Crystal colour	Orange-yellow
Crystal Habit	platelet
Temperature	203(2) K
λ(MoKα)	0.71073
Absorption coefficient (μ)	0.577 mm^{-1}
2θ-range	3.18-36.40°
Total data collected	31936
Unique data	6571 (R_{int} = 0.134)
Observed data (I >2σ(I))	3942
Data/ restraints/ parameters	6571/ 0/ 688
Goodness of fit	0.891
Final R indices [I>2σ(I)]	$R1$ = 0.051, w$R2$ = 0.103
R indices (all data)	$R1$ = 0.096, w$R2$ = 0.116
Residual electron density (max/min)	0.32 / −0.50 e$^-$ Å^{-3}

Complex $\{[UO_2(\mathbf{L}^6)(NO_3)_2]\}_n$ (**15**)

Molecular formula	$C_{26}H_{20}N_4O_{11}U$
Molar mass	802.5 g.mol^{-1}
Crystal system	Monoclinic
Space group	*C*2/c(\a0\g)0s
Cell dimensions	*a* = 12.145(5) Å
	b = 14.256(6) Å
	c = 16.438(8) Å
	$\alpha = 90.00°$, $\beta = 107.23(1)°$, $\gamma = 90.00°$
Cell volume	2718(2) Å^3
Calc. density (ρ)	1.96 g cm^{-3}
Z	4
F(000)	1536
Diffractometer	Bruker APEX-II CCD
Crystal Size	0.10 x 0.04 x 0.03 mm
Crystal colour	orange red
Crystal Habit	rod
Temperature	180(2) K
λ(MoKα)	0.71073
Absorption coefficient (μ)	6.04 mm^{-1}
2θ-range	3.44-51.76°
Total data collected	24408
Unique data	7903 (R_{int} = 0.077)
Observed data (I >2σ(I))	4346
Data/ restraints/ parameters	7903/ 2/ 576
Goodness of fit	1.42
Final *R* indices [I>2σ(I)]	*R*1 = 0.051, w*R*2 = 0.051
R indices (all data)	*R*1 = 0.113, w*R*2 = 0.057
Residual electron density (max/min)	2.29 / −1.92 e$^-$ Å^{-3}

Complex $[UO_2(\mathbf{L}^{8})(NO_3)_2]$ (**17**)

Molecular formula	$C_{22}H_{20}N_4O_{10}U$
Molar mass	738.45 g.mol^{-1}
Crystal system	Triclinic
Space group	*P*–1
Cell dimensions	a = 9.4710(14) Å
	b = 9.5100(11) Å
	c = 15.251(2) Å
	α = 72.170(9)°, β = 89.361(15)°, γ = 70.700(10)°
Cell volume	1228.0(3) Å^3
Calc. density (ρ)	1.997 g cm^{-3}
Z	2
F(000)	704
Diffractometer	Kappa CCD
Crystal Size	0.38 x 0.28 x 0.19 mm
Crystal colour	orange-red
Crystal Habit	polyhedron
Temperature	293(2) K
λ(MoKα)	0.71073
Absorption coefficient (μ)	6.673 mm^{-1}
2θ-range	6.30-60.04°
Total data collected	67317
Unique data	7136 (R_{int} = 0.039)
Observed data (I >2σ(I))	6461
Data/ restraints/ parameters	7136 / 0/ 334
Goodness of fit	1.112
Final *R* indices [I>2σ(I)]	*R*1 = 0.021, w*R*2 = 0.047
R indices (all data)	*R*1 = 0.028, w*R*2 = 0.049
Residual electron density (max/min)	1.32 / −1.22 e$^-$ Å^{-3}

Complex $[UO_2(\mathbf{L}^{10})(NO_3)_2]$ (**18**)

Molecular formula	$C_{30}H_{24}N_4O_{10}U$
Molar mass	838.56 g.mol^{-1}
Crystal system	Monoclinic
Space group	*C*2 / *c*
Cell dimensions	*a* = 31.190(6) Å
	b = 11.082(2) Å
	c = 17.951(4) Å
	$\alpha = 90.00°$, $\beta = 113.32(3)°$, $\gamma = 90.00°$
Cell volume	5698(2) Å^3
Calc. density (ρ)	1.955 g cm^{-3}
Z	8
F(000)	3232
Diffractometer	Bruker APEX-II CCD
Crystal Size	0.14 x 0.11 x 0.03 mm
Crystal colour	orange-red
Crystal Habit	polyhedron
Temperature	160(2) K
λ(MoKα)	0.71073
Absorption coefficient (μ)	5.765 mm^{-1}
2θ-range	2.84-53.60°
Total data collected	31794
Unique data	6059 (R_{int} = 0.075)
Observed data (I >2σ(I))	4212
Data/ restraints/ parameters	6059 / 0/ 406
Goodness of fit	0.802
Final *R* indices [I>2σ(I)]	*R*1 = 0.027, w*R*2 = 0.045
R indices (all data)	*R*1 = 0.052, w*R*2 = 0.048
Residual electron density (max/min)	0.79 / −0.83 e$^-$ Å^{-3}

Complex $[UO_2(\mathbf{L}^{13})(NO_3)_2]$ (**20**)

Molecular formula	$C_{30}H_{30}N_4O_{10}U$
Molar mass	844.61 g.mol^{-1}
Crystal system	Triclinic
Space group	*P*–1
Cell dimensions	a = 11.107(1) Å
	b = 11.424(3) Å
	c = 13.060(2) Å
	α = 112.12(2)°, β = 90.06(1)°, γ = 101.07(1)°
Cell volume	1501.7(5) Å^3
Calc. density (ρ)	1.859 g cm^{-3}
Z	2
F(000)	812
Diffractometer	Bruker APEX-II CCD
Crystal Size	0.15 x 0.07 x 0.04 mm
Crystal colour	orange-red
Crystal Habit	polyhedron
Temperature	198(2) K
λ(MoKα)	0.71073
Absorption coefficient (μ)	5.469 mm^{-1}
2θ-range	6.10-54.00°
Total data collected	50574
Unique data	6550 (R_{int} = 0.066)
Observed data (I >2σ(I))	5640
Data/ restraints/ parameters	6550/ 0/ 406
Goodness of fit	1.060
Final *R* indices [I>2σ(I)]	*R*1 = 0.032, w*R*2 = 0.060
R indices (all data)	*R*1 = 0.045, w*R*2 = 0.064
Residual electron density (max/min)	1.18 / −1.06 e$^-$ Å^{-3}

10 Publications and conference contributions

Publications stemming from this work

1) H. B. Tanh Jeazet, Ke. Gloe, T. Doert, O. N. Kataeva, A. Jäger, G. Geipel, G. Bernhard, B. Büchner, and Ka. Gloe

"Self-assembly of neutral hexanuclear circular copper(II) meso-helicates: topological control by sulfate ions"

Chem. Commun.. **2010**, 46, 2373-2375.

2) H. B. Tanh Jeazet, T. Doert, O. N. Kataeva, S. Tsushima, Ke. Gloe, G. Geipel, G. Bernhard and K. Gloe

"Novel U(VI) complexes of bis(o-hydroxyaryl)imine ligands: Synthesis, X-ray structures, and DFT calculations"

FZD – IRC Annual Report **2008**, 17.

3) H. B. Tanh Jeazet, Ke. Gloe, G. Geipel, G. Bernhard and K. Gloe

"Solvent extraction of U(VI) by bis(o-hydroxyaryl)imine and amine ligands"

FZD – IRC Annual Report **2008**, 18.

4) H. B. Tanh Jeazet, M. Wenzel, Ke. Gloe, G. Geipel, G. Bernhard, Ka. Gloe

"New tripodal polyamines as potential extracting agents for lanthanides and actinides"

FZD – IRC Annual Report **2007**, 29.

5) H. B. Tanh Jeazet, A. Jäger, O. Kataeva, Ke. Gloe, G. Geipel, G. Bernhard, B. Büchner, K. Gloe

"Novel expanded circular helicates formed by copper(II) sulfate and bis-pyridylimine ligands"

FZD – IRC Annual Report **2007**, 30.

6) H. B. Tanh Jeazet, A.Jäger, A. Heine, M. Wenzel, Ke. Gloe, G. Geipel, G. Bernhard, K. Gloe

"The architecture of self-assembled silver (I) complexes with bis-pyridylimine ligands: from coordination polymers to molecular boxes"

FZD – IRC Annual Report **2007**, 31.

Manuscripts in Preparation

7) H. B. Tanh Jeazet, Ke. Gloe, T. Doert, A.Jäger, A. Heine, M. Wenzel and Ka. Gloe

"The architecture of self-assembled silver (I) complexes with bis-pyridylimine ligands: from coordination polymers to molecular boxes"

8) H. B. Tanh Jeazet, Ke. Gloe, T. Doert, O. N. Kataeva, S. Tsushima, G. Geipel, G. Bernhard and Ka. Gloe

"Novel U(VI) complexes of bis(o-hydroxyaryl)imine ligands: synthesis, X-ray structures, extraction studies and DFT calculations"

9) H. B. Tanh Jeazet, Ke. Gloe, T. Doert, G. Bernhard and Ka. Gloe

"Crystal structure of bis[4-(2-pyridylmethyleneimino)phenyl]amine ligand"

Publications not stemming from this work

7) S. Hoffman, H. B. Tanh Jeazet, P. W. Menezes, Y. Prots and R. Kniep

"Na3PbII[B(O3POH)4]: An alkali-metal lead borophosphate with heterocubane-like units Na_3PbO_4"

Inorg. Chem. **2008**, *47*, 10193-10195.

8) H. B. Tanh Jeazet, P. W. Menezes, S. Hoffman, Y. Prots and R. Kniep

"Crystal structures of lead(II) cobalt(II) (monophosphate-hydrogenmonoborate-monophosphate), PbCo[BP2O8(OH)], and lead(II) zinc(II) (monophosphate-hydrogenmonoborate-monophosphate), PbZn[BP2O8(OH)]"

Zeitschrift fuer Kristallographie – NCS **2006**, *221*, 431-433.

Conferences

1) Harold B. Tanh Jeazet, Thomas Doert, Kerstin Gloe, Jens Mizera, Karsten Gloe, Margret Acker, Satoru Tsushima, Gert Bernhard

"Novel multifunctional schiff base ligands for UO_2^{2+} binding and extraction"

Invited lecture and paper for the Proceedings, XIX International Solvent Extraction Conference.

Santiago, Chile, 17. – 21. 10. **2011**.

2) K. Gloe, H. B. Tanh Jeazet, K. Gloe, T. Doert, O. N. Kataeva, G. Bernhard

"Coordination behaviour of bis-pyridylimine ligands: polymers, metallamacrocycles and helicates"

Oral presentation, 39. International Conference on Coordination Chemistry

ICCC39, Adelaide, 25-30 July **2010**.

3) Harold B. Tanh Jeazet, Thomas Doert, Kerstin Gloe, Satoru Tsushima, Gerhard Geipel, Karsten Gloe and Gert Bernhard

"Novel U(VI) Schiff Base Complexes: Synthesis, Structural Characterization, and Extraction Studies"

Poster, 16th Radiochemical Conference, April **2010**.

4) Harold B. Tanh Jeazet, Thomas Doert, Kerstin Gloe, Gerhard Geipel, Gert Bernhard and Karsten Gloe

"Neue UO_2^{2+}-Komplexe von Bis(2-hydroxyaryl)imin-liganden: Synthese, Struktur und Extraktionseigenschaften"

Oral presentation, Jahrestreffen des Fachausschusses Extraktion, ProcessNet/Dechema-VDI, 18-19.03.**2010**, Kaiserslautern.

5) Harold B. Tanh Jeazet, Kerstin Gloe, Thomas Doert, Satoru Tsushima, Gerhard Geipel, Gert Bernhard and Karsten Gloe

"Novel U(VI) Complexes of Bis(2-hydroxyaryl)imine Ligands: Synthesis, Structural Characterization, and Extraction Studies"

Poster, GDCh-Wissenschaftsforum Chemie **2009**, Frankfurt am Main.

6) Harold B. Tanh Jeazet, Kerstin Gloe, Gert Bernhard and Karsten Gloe

"Novel Expanded Circular Helicates Formed by Copper(II) Sulfate and Bis-pyridylimine Ligands"

Oral presentation, Mitteldeutsches Anorganiker-Nachwuchs-Symposium (MANS 6) **2008**, Freiberg.

11 Erklärung

Die vorliegende Arbeit wurde zwischen November 2006 und März 2010 unter der wissenschaftlichen Betreuung von Herrn Prof. Dr. Karsten Gloe Fachrichtung Chemie und Lebensmittelchemie der Technischen Universität Dresden, Professur für Koordinationschemie und Herrn Prof. Dr. Gert Bernhard, Direktor Institut für Radiochemie Forschungszentrum Dresden-Rossendorf, Professur für Radiochemie Fachrichtung Chemie und Lebensmittelchemie der Technischen Universität Dresden angefertigt.

12 Versicherung

Hiermit versichere ich, dass ich die vorliegende Arbeit ohne unzulässige Hilfe Dritter und ohne Benutzung anderer als der angegebenen Hilfsmittel angefertigt habe; die aus fremden Quellen direkt oder indirekt übernommenen Gedanken sind als solche kenntlich gemacht. Die

Arbeit wurde bisher weder im Inland noch im Ausland in gleicher oder ähnlicher Form einer anderen Prüfungsbehörde vorgelegt.

Die Promotionsordnung der Fakultät Mathematik und Naturwissenschaften der Technischen Universität Dresden vom 20. März 2000 in der geänderten Fassung vom 18. März 2003 erkenne ich an.

Dresden, 23.06.2010 Harold Brice Tanh Jeazet

13 Scheme of ligand structures

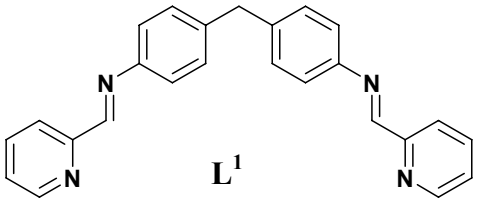

L^1

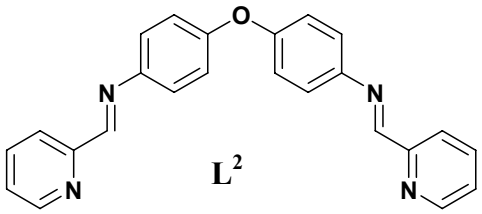

L^2

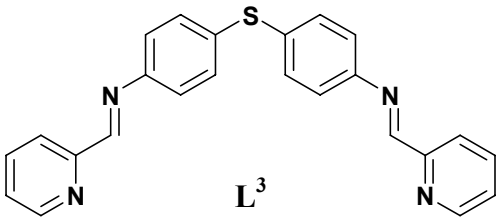

L^3

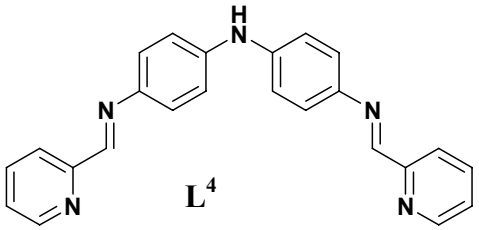

L^4

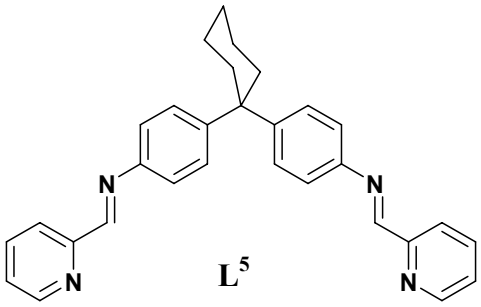

L^5

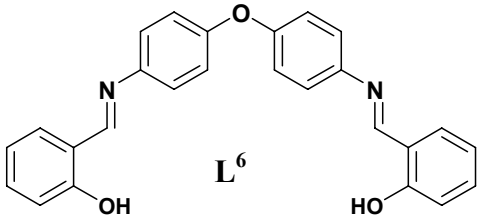

L^6

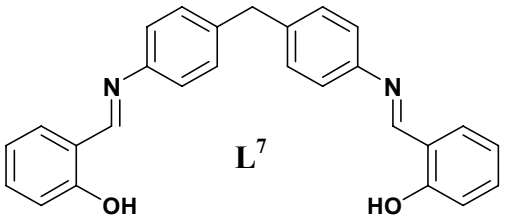

L^7

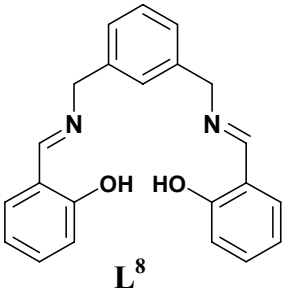

L^8

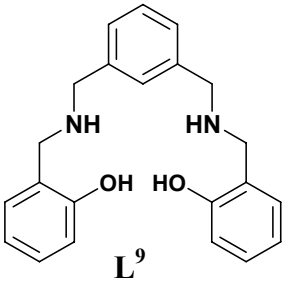

L^9

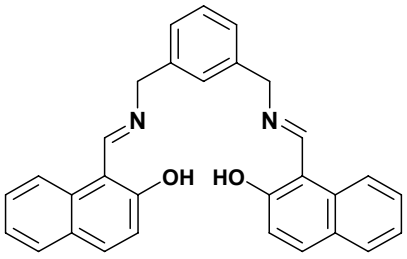

L^{10}

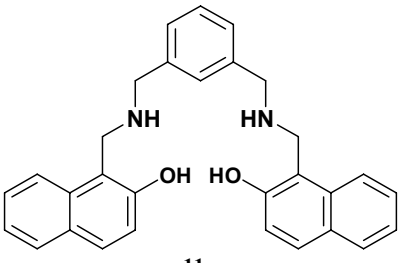

L^{11}

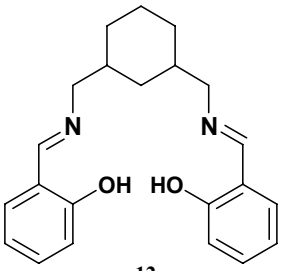

L^{12}

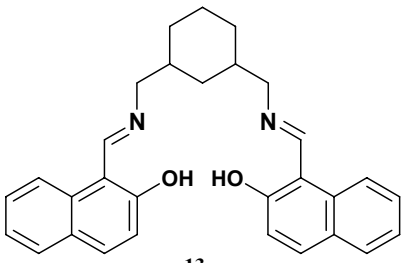

L^{13}

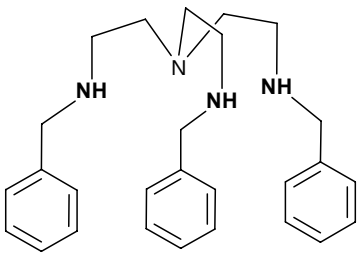

L^{14}

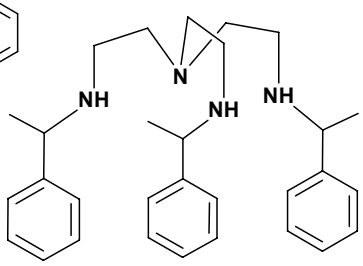

L^{15}

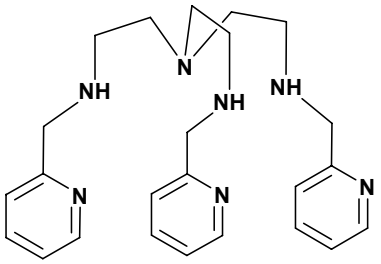

L^{16}

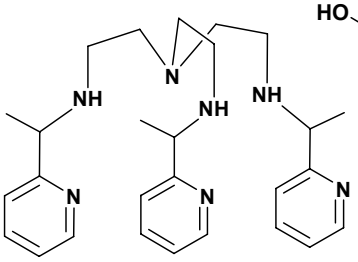

L^{17}

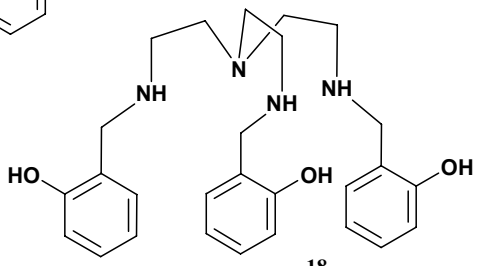

L^{18}

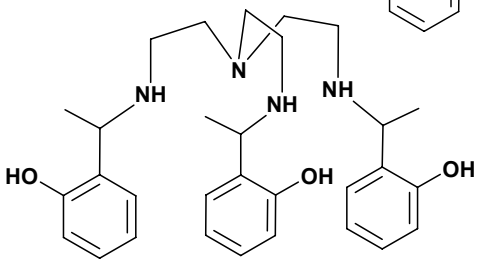

L^{20}

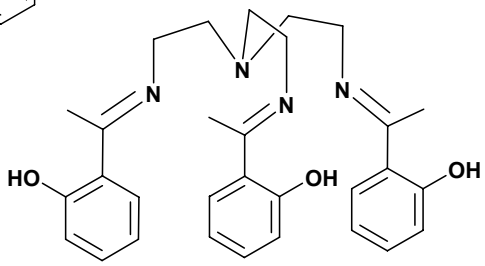

L^{19}

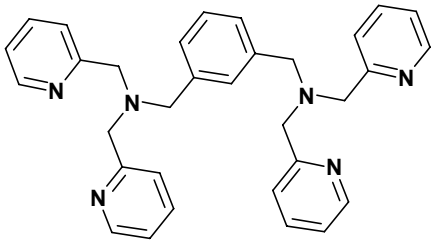

L^{21}

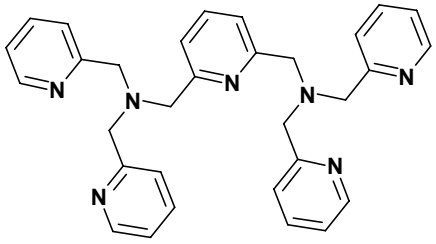

L^{22}

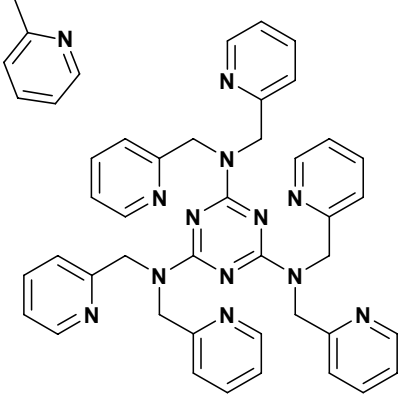

L^{23}